Aeroelastic Tailoring of Aeroplane Wings using Composite Laminates

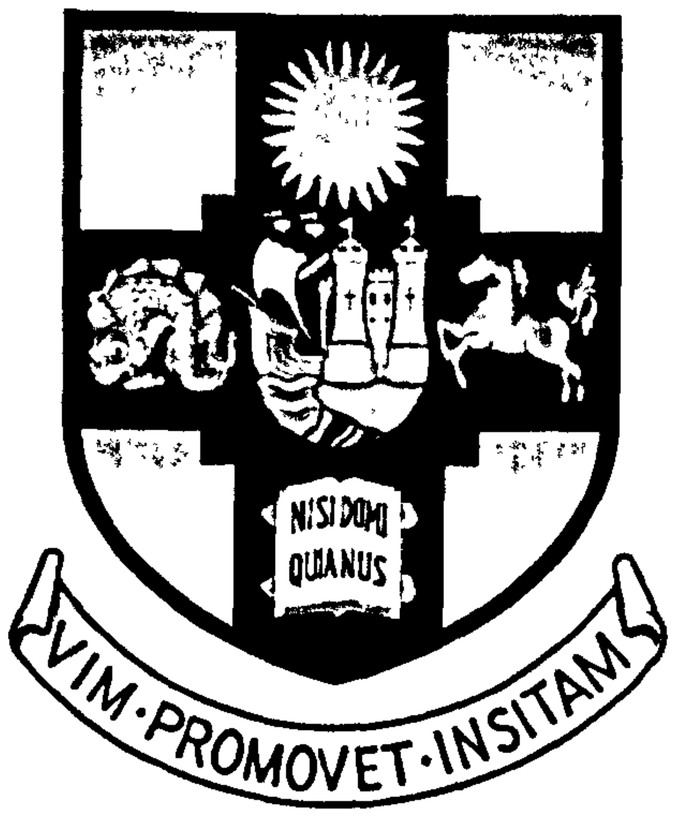

Giacomo Canale

A dissertation submitted to the University of Bristol in accordance with the requirements for award of degree of Doctor of Philosophy in the faculty of engineering.

Department of Aerospace Engineering
November 2010

Abstract

This thesis concerns aeroelastic tailoring, i.e. the discipline that studies the induced deformation of an aeronautical structure, such as wings, tails, or vertical fins, in order to improve a particular aeroelastic performance. Aeroelastic tailoring is achieved here via passive actuation, obtained by exploiting the anisotropy of composite materials.

This research has shown the potential benefits of anisotropic composite laminates for the static and dynamic aeroelastic performances of an aircraft wing, modelled as a thin-walled composite box. A specific kind of anisotropy has been considered: bend-twist coupling effect, obtained using unbalanced and symmetric composite plates.

Two simple models have been developed to study static and dynamic aeroelasticity. Results obtained with the static aeroelastic model have shown that unbalanced composite laminates can be potentially used to improve the flight range of an aircraft. A potential increase of the structural weight of the wing, however, was observed. The static aeroelastic model introduces novel features. Potential improvements of flight range have been identified by exploiting the anisotropy of composite materials. Furthermore, the "optimum" fibre orientation was found by using procedures based on the physical understanding of the problem, rather than optimisation routines.

Results obtained with the dynamic model show that bend-twist coupling has potential to increase the critical flutter speed of a wing. Also, the flutter model presents some points of novelty. A study of the variation of critical flutter speed with the fibre orientations of the laminates of a composite box is given.

Besides the aeroelastic models, two underlying models have been enhanced. The first was the development of a simplified analytical formulation to evaluate the relevant stiffnesses of a composite box, used in both aeroelastic tools, to model the wing. Previously, it has been shown that three stiffnesses mainly control aeroelastic

tailoring: bending, torsional and bend-twist coupling stiffnesses. Models previously presented in the literature for these stiffnesses show a lack of precision when evaluating wing-boxes with different geometries and lay-ups. Consequently, a new model has been formulated and tested by using a commercial finite element code.

The second enhanced model is a new algorithm of combinatorial optimisation to determine the optimum stacking sequence of a composite laminate. It can be used to study plates with fixed thickness and fixed number of ply orientations (i.e. plates whose membrane properties are predetermined). This algorithm gives excellent results when the performance (objective function) to be optimised is strictly related to the flexural stiffness matrix of the laminate.

Acknowledgements

I am indebted to the University of Bristol, to Great Western Research and Airbus UK for making possible this research.

To Dr. Paul Weaver, devoted teacher, painstaking advisor and outstanding engineer must go the primary acknowledgment. His careful criticism and guidance have provided the incentive and confidence necessary to complete this thesis.

Dr. Taqi Khan and Martyn Cantrell, industrial supervisors of this project, must be acknowledged for their suggestions.

Mention must be made of Enrique Herencia, Mark Bloomfield, Michael May, Stephen Daynes, Christophe Thill and Alberto Pirrera. Without their support, I would have been quite far from completing this research.

This thesis is dedicated to my parents.

Author's Declaration

I declare that the work in this dissertation was carried out in accordance with the requirements of the University's Regulations and Code of Practice for Research Degree Programmes and that it has not been submitted for any other academic awards. Except when indicated by specific reference in the text, the work is the candidate's own work.

Work done in collaboration with, or with the assistance of, others, is indicated as such.

Any views expressed in the dissertation are those of the author.

SIGNED...Lyiaome Cenle.....DATE March 24th 2011

Table of contents

List of symbols

$\underline{\underline{A}}, \underline{\underline{B}}, \underline{\underline{D}}$	matrices used in classical lamination theory
A	area of a stringer cross section
A_{dyn}	dynamic matrix
B	bimoment
b	aerodynamic semi-chord
C	chord of a wing box
c_t	specific fuel consumption
C_d	drag coefficient
C_{d0}	zero lift drag coefficient
C_l	lift coefficient
$C_{l\alpha}$	rate of C_l with respect to the angle of attack ($C_l = C_{l\alpha} * \alpha$)
c	aerodynamic chord of an airfoil
D	drag
d	distance between the centre of pressure and the shear centre of an airfoil
E	Young's modulus of an isotropic material
E_1	elastic modulus of a lamina in the axial direction
E_2	elastic modulus of a lamina in the transversal direction
EI	bending stiffness
e_i	bending compliance
$\underline{F}$	vector of generalized forces
F	fitness function to evaluate a heuristic optimisation technique
$F_{x,y,z}$	forces along the X, Y and Z axes
G	shear modulus of an isotropic material
G_{12}	shear modulus of a lamina
GJ	torsional stiffness
g_k	torsional compliance
H	height of a wing box cross section
I	range index
J_{eq}	equivalent torsional moment of inertia of a beam, used for the evaluation

K	bend-twist coupling stiffness
$\underline{\underline{K}}$	stiffness matrix of the beam cross section
k	reduced frequency (used for flutter analysis)
k_a	bend-twist coupling compliance
l	length of a beam
L	lift of a wing
L_0	lift of the rigid wing
M	bending moment (internal load)
$\underline{\underline{M}}$	mass matrix of a beam element
$m(x)$	distribution of twisting moment (as external load) along the span.
m_{eq}	equivalent mass of a beam, used for the evaluation of critical flutter speed
n_l	design load factor
N	moment about Z axis
N_x	axial force per unit of length in a composite laminate
N_y	lateral forces per unit of length in a composite laminate
N_{xy}	shear force per unit of length in a composite laminate
$\underline{\underline{N}}$	matrix of the shape function in a finite element formulation
P	kinetic energy of a system
p	perimeter of the cross section
$\underline{\underline{Q}}$	in plane stiffness matrix in the local axis of a plate
Q_f, Q_t	Lagrangian components of aerodynamic force to study flutter instability.
$q(x)$	distribution of lift: it is a force per unit of length
$q_f(t)$	function describing the time progression of the flexural mode: flexural lagrangian coordinate
$q_t(t)$	function describing the time progression of the torsional mode: torsional Lagrangian coordinate
R	range of the aircraft
S	wing's surface
s, n	circumferential and normal axis of the local frame

T	twisting moment (internal load)
t_v	thickness of the vertical wall of a composite box
t_h	thickness of the horizontal wall of a composite box
U	elastic energy per unit of volume
V	speed induced by a vortex of intensity Γ
V_∞	asymptotic air speed
W	work [J]
$W_{takeoff}$	weight of the aircraft before the take-off
$W_{landing}$	weight of the aircraft when the flight terminates. All the fuel has been consumed.
X, Y, Z	axis of the main frame of a wing box
$\dot{X}, \dot{Y}, \dot{Z}$	speeds measured with respect of the frame X, Y, Z
u, v, w	displacements along X, Y and Z respectively
$\underline{u}$	vector of generalized displacements

Greek Symbols

α	angle of attack
Γ	vortex circulation
γ_{ij}	shear strains in the directions *i-j*
$\underline{\delta}$	generalized vector of nodal displacements
Δ	slope of the main chamber of an airfoil
ε_i	strain in the direction *i*
θ	angle of torsion
Λ	angle of sweep
λ_{eq}	aerodynamic aspect ratio of a wing
$\mu_f(X)$	shape of the first natural mode of a beam
$\mu_t(X)$	shape of the first torsional mode of a beam
ν	Poisson's ratio of an isotropic material
ν_{12}	major Poisson's ratio of a composite material

ξ	fibre angle with the respect of the local frame of the laminate
ξ_0	fibre angle which maximizes bend-twist coupling compliance
ρ	air density
ρ_m	material density
φ	bending angle
Φ	dihedral angle
χ	angle of rotation about the Z axis
ψ	warping function
ω_f	frequency of the first flexural mode
ω_t	frequency of the first torsional mode
Ω	area enclosed by the closed cross section of a beam

List of Figures

Chapter 3

Chapter 4

Chapter 6

Chapter 7

List of Tables

Chapter 1
Introduction

1.1 Motivation

It is well established that, in recent years, composite materials have become extremely important in the construction of aeronautical structures. This is shown by development programs such as the Airbus A350 and the Boeing 787. The reason is simple: strength/weight ratio of composite materials is particularly high, especially when compared with conventional isotropic materials such as aluminium, widely used in the aerospace industry. By using composite materials, it is possible to reduce weight while maintaining structural integrity.

For many years engineers have used such materials without exploiting their full potential. Composite materials have been designed as if they were metals. However, they can be stiffness tailored, which offers the opportunity to explore more designs. Structural deformations can be driven in order to improve some performance measures of the aircraft. Aeronautical structures, such as wings, vertical fins or tails, can be "tailored" by considering their aeroelastic interaction, for example, to reduce the drag, to increase the payload or to increase the range or the endurance.

The main goal of this PhD thesis is to show possible improvements on the static/dynamic aeroelastic performances of a wing, by using anisotropic composite laminates.

1.2 Aeroelastic Tailoring

The discipline which studies materials and geometrical properties of a structure to improve the aeroelastic performances of an aircraft is known as "aeroelastic tailoring". A rigorous definition of aeroelastic tailoring was given for the first time in 1986 by Shirk, Hertz and Weisshaar [1]:

"*Aeroelastic tailoring is the embodiment of directional stiffness into an aircraft structural design to control aeroelastic deformation, static or dynamic, in such a fashion as to affect the aerodynamic and structural performance of that aircraft in a beneficial way*".

In order to have a better understanding, it can be affirmed that similarities exist between aeroelastic tailoring and active control methodology. Aeroelastic tailoring is a passive form of control, in the sense that no external energy source is used directly. It uses a form of pre-programmed control law to modify the behaviour of a structural system. In this analogy, the aeroelastically tailored structure is both sensor and actuator; the control law is embedded within the structure in the form of materials constitutive relations.

1.2.1 Bend-twist coupling

One of the main instruments of aeroelastic tailoring of a wing is the structural anisotropy, in particular the "bend-twist coupling" effect. When an isotropic structure is loaded with a bending moment, only a flexural deformation is shown. When the same structure is loaded with a twisting moment, only a torsional deformation is observed. Consider the structure shown in Figure 1.1: a planar surface representing the top skin of a forward swept wing. Stiffening elements, indicated by straight dark lines, represent either directional plies or/and metallic stringers for the reinforcement. The main load acting on the wing is a bending moment arising from the lift distribution along the span. Consequently, the top surface, shown in Figure 1.1, is subjected to compression. These compressive loads will prefer to be transferred along a path that follows the stiffener directions. On the other hand, a "left over" component remains to be balanced. This component will force the surface to twist. The effect is accentuated when an identical surface is placed beneath (bottom surface of the wing, Figure 1.2) and it is subjected to tension. The wing therefore shows twisting deformation besides flexure when loaded in bending and vice versa.

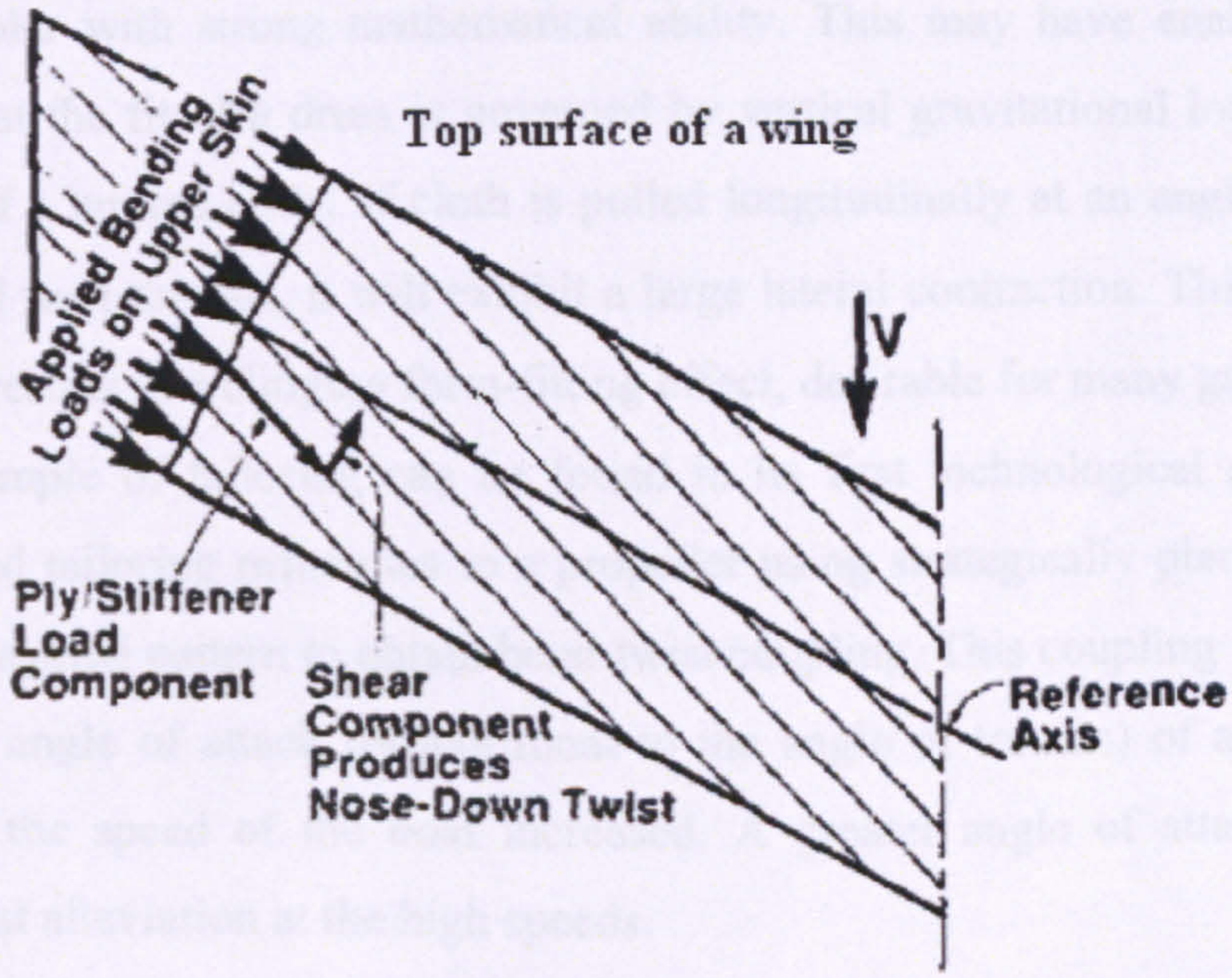

Figure 1.1: The physical meaning of bend-twist coupling [1] explained by using the top surface of a wing subjected to compression loads coming from bending.

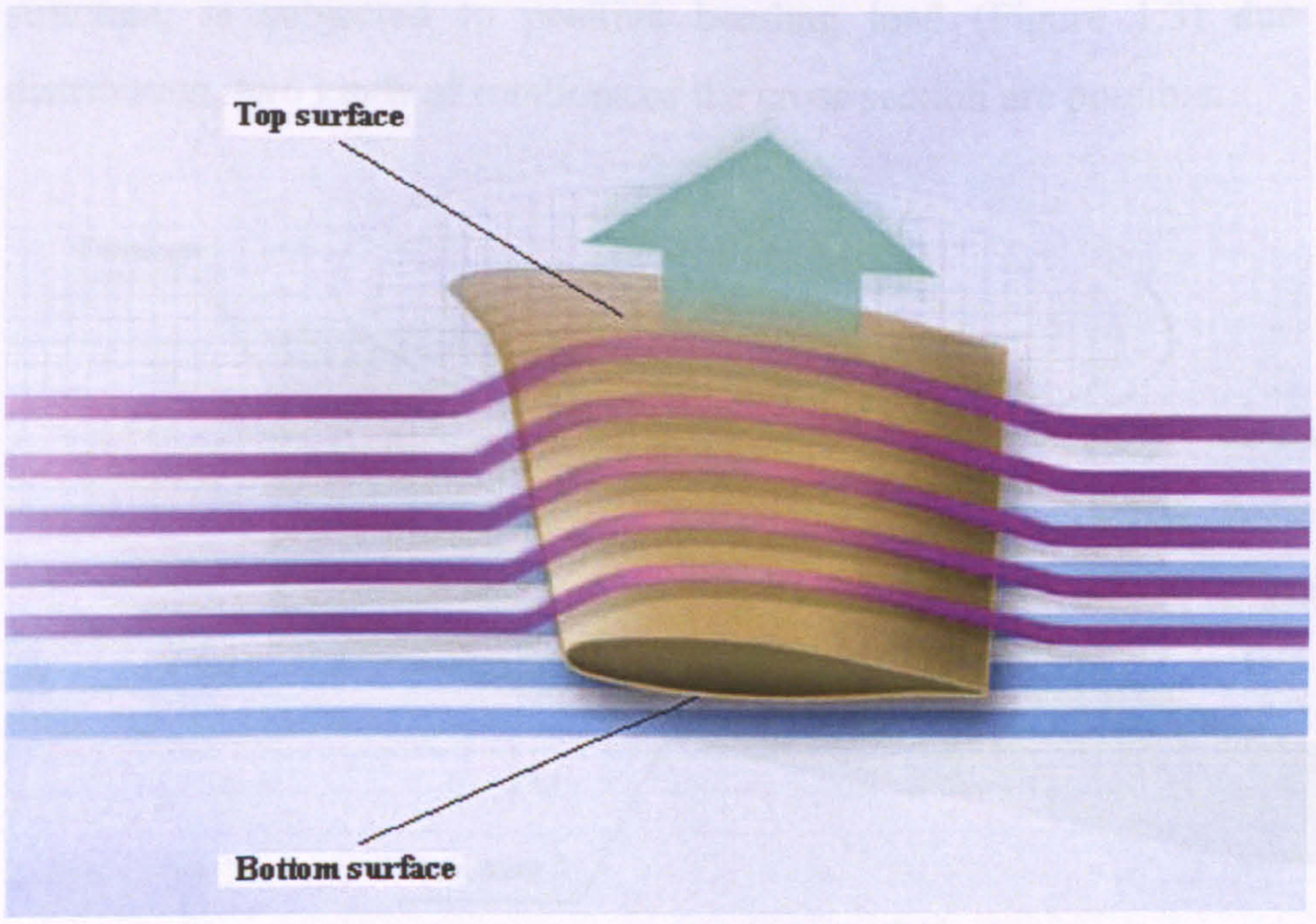

Figure 1.2: Top and bottom surfaces of a wing.

The use the of anisotropy to tailor a structure, however, was not originally thought of for aeronautical applications, as remarked by Weisshaar [2]. In the 1920's a Paris dressmaker, Madame Madeleine Vionnet, perfected the "bias cut". She was reputed

to be a scholar with strong mathematical ability. This may have enabled her to recognize that the fit of a dress is governed by vertical gravitational loads and the movement of a human body. If cloth is pulled longitudinally at an angle of 45° to the warp and weft threads, it will exhibit a large lateral contraction. This Poisson's ratio effect, results in a clinging form-fitting effect, desirable for many garments.

Another example of tailoring can be found in its first technological application. Munk applied tailoring principles to a propeller using strategically placed wooden fibres in a diagonal pattern to obtain bend-twist coupling. This coupling was used to increase the angle of attack (proportional to the angle of torsion) of a propeller's blade when the speed of the boat increased. A greater angle of attack, in fact, avoided thrust alleviation at the high speeds.

Bend-twist coupling is therefore a relatively simply but powerful concept and many applications are possible in aeronautics. When a wing, or more generally a structure, is subjected to positive bending load (Figure 1.3) due to the lift distribution, two kinds of rotations of the cross section are possible.

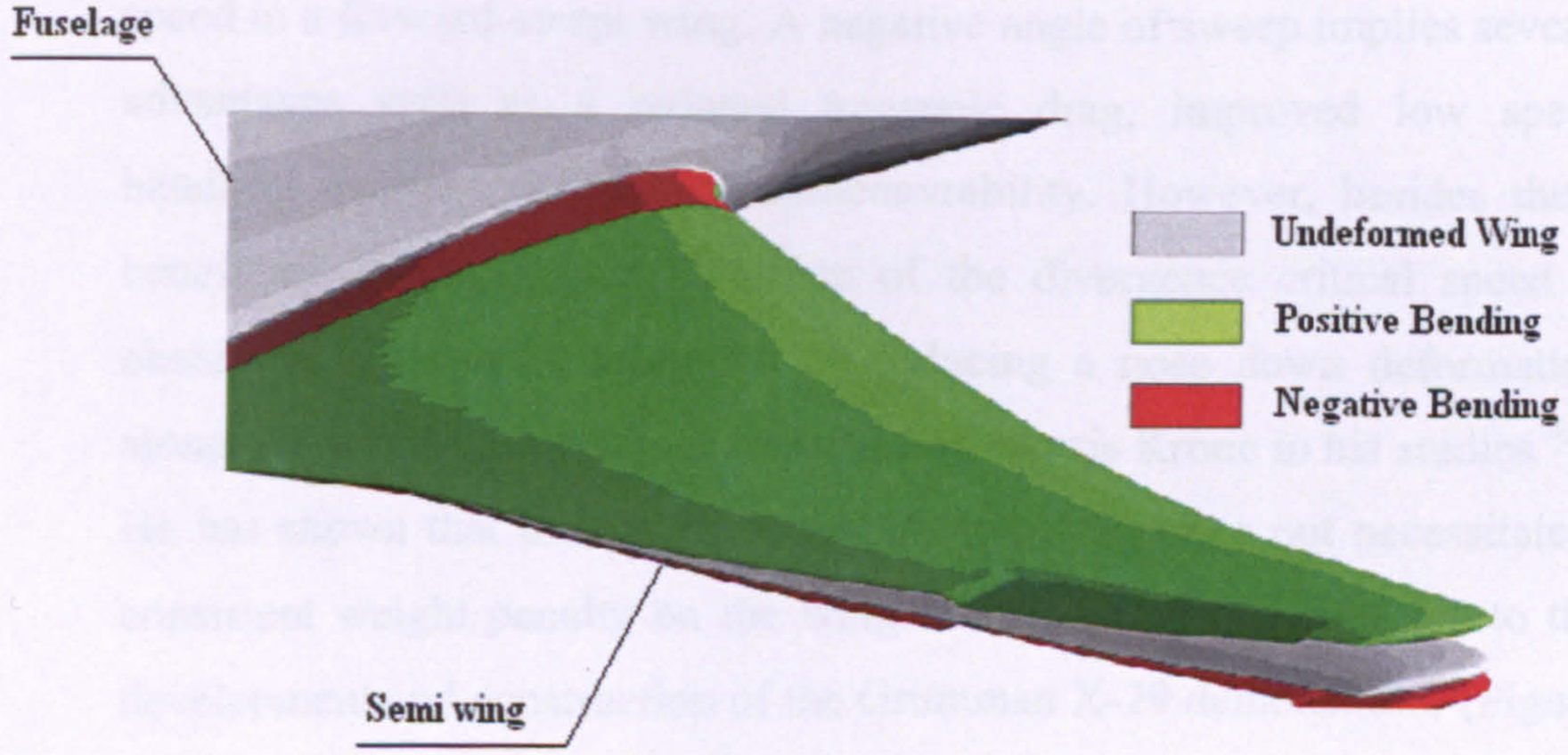

Figure 1.3: Bending deformation of an aircraft wing arising from the lift force distribution.

1. A rotation "nose up", which tends to increase the angle of attack.
2. A rotation "nose down", which tends to decrease the angle of attack.

An example of "nose up" deformation is shown in Figure 1.4.

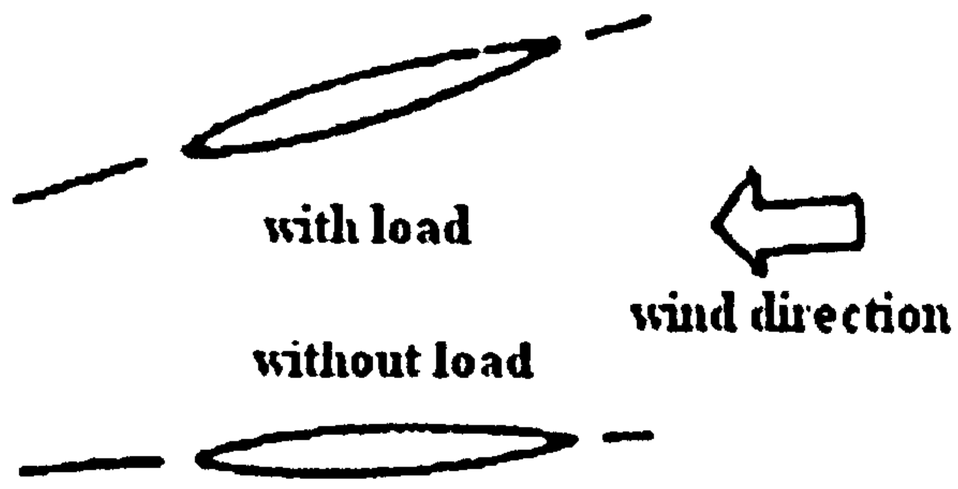

Figure 1.4: An example of "nose up" deformation.

Both "nose up" and "nose down" deformations can be induced along the length of a structure in order to improve performance. The structure, in other words, can be tailored: its deformation can be driven to improve the performance of the whole aircraft at a range of flight condition. Several examples of aeroelastic tailoring, by using bend-twist coupling, can be thought of for the aerospace industry:

1. A global nose down effect can be used to increase the critical divergence speed in a forward-swept wing. A negative angle of sweep implies several advantages such as a reduced transonic drag, improved low speed handling qualities and higher manoeuvrability. However, besides these beneficial effects, also a reduction of the divergence critical speed is observed [3]. It can be mitigated by inducing a nose down deformation along the span of the wing, as remarked by Norris Krone in his studies [4, 5]. He has shown that the use of composite materials does not necessitate a consistent weight penalty on the wing. The research of Krone led to the development and construction of the Grumman X-29 demonstrator (Figure 1.5).

Figure 1.5: Grumman X-29 [1].

2. A global nose up effect can be used to increase the critical flutter speed.
3. Both "nose up" and "nose down" effects along the span can reduce root bending moment while the global value of lift remains unchanged. An example is shown in Figure 1.6.

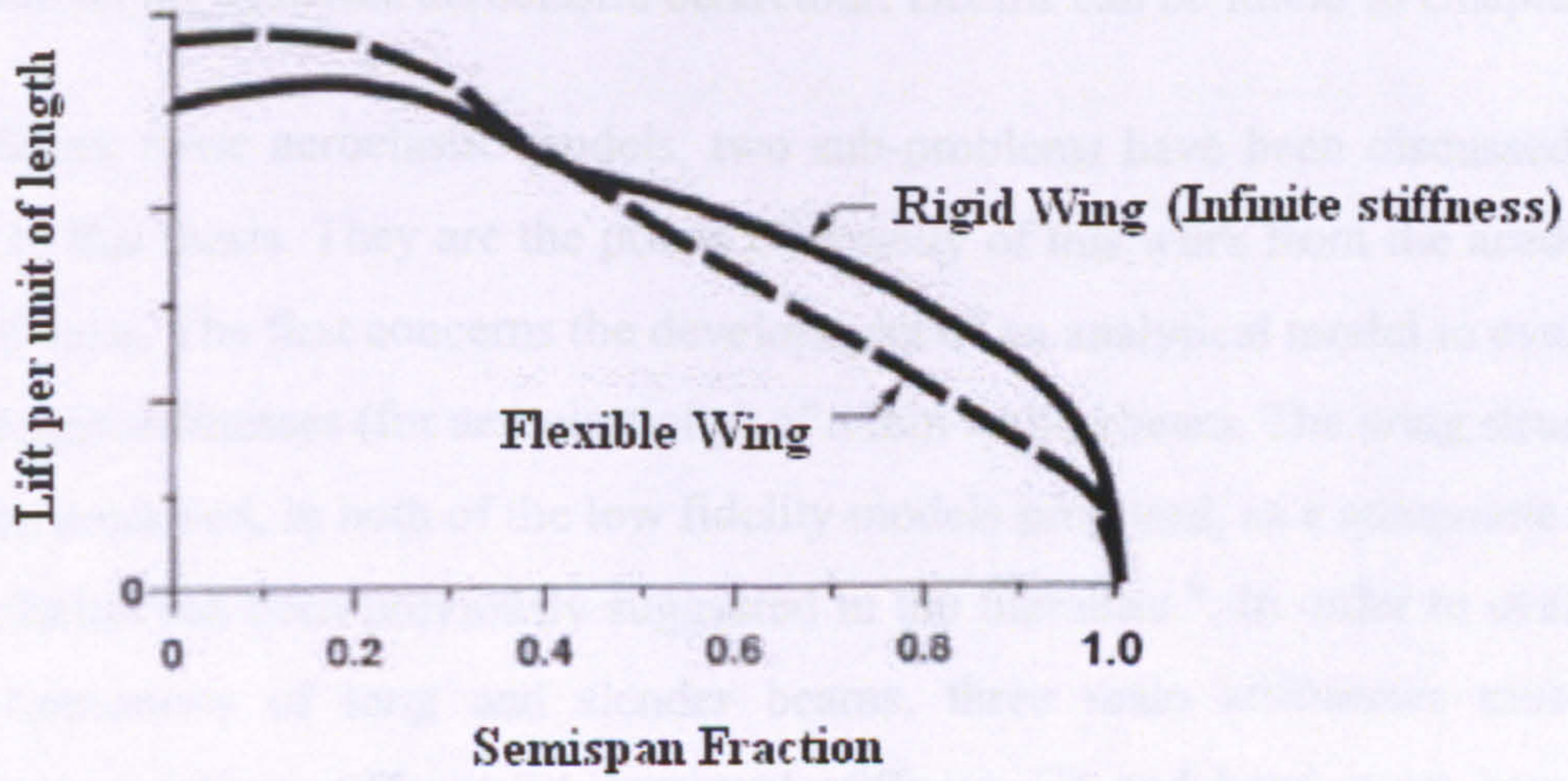

Figure 1.6: Reduction of the bending moment at the root of the wing [2].

1.3 Research goals and overview

As mentioned in section 1.1, the main goal of this thesis is to show how composite materials can be used to improve the aeroelastic performance of an aircraft. Two performance metrics have been chosen for this work.

The first one is the range, i.e. the maximum distance that an aircraft can cover with a fixed amount of fuel. This choice has been suggested by Airbus UK, one of the sponsors of this project. The reason is quite simple: an improvement, even small, in the range can imply strong financial savings. A "low fidelity" static aeroelastic model (i.e. a model that does not contain all the structural and aerodynamic details, but that is able to describe the main physical phenomena and parameters involved) has been prepared and implemented to show the potential benefits induced by the use of bend-twist coupling. Such coupling has been obtained by using symmetric, yet unbalanced composite laminates. The model is described in detail in Chapter 4.

The second performance metric chosen is critical flutter speed. A low fidelity flutter model has been prepared to show the benefit induced by unbalanced composite laminates on the dynamic aeroelastic behaviour. Details can be found in Chapter 6.

To facilitate these aeroelastic models, two sub-problems have been discussed and solved in this thesis. They are the points of novelty of this work from the academic point of view. The first concerns the development of an analytical model to evaluate the relevant stiffnesses (for aeroelasticity) of a thin walled beam. The wing structure has been modelled, in both of the low fidelity models proposed, as a composite box. This solution has been previously suggested in the literature [6]. In order to evaluate the deformations of long and slender beams, three main stiffnesses must be calculated: bending stiffness *EI*, torsional stiffness *GJ* and bend twist coupling stiffness *K*. Many analytical models are already presented in the literature [7-19], but a lack of precision in the prediction of numerical results for structures with different geometries and lay-ups has been observed. Consequently, a new analytical model is discussed in detail in Chapter 3.

The second sub-problem concerns the development of a new algorithm for composite lay-up optimisation. When composite boxes are designed for aeroelastic purposes, the effects of the stacking sequence of each laminate wall can be neglected [20]: the aeroelastic design is affected mainly by the membrane properties. However, once the volume fractions of the fibres are determined, the stacking sequence of each panel can be studied in order to maximize some performances strictly related to the $\underline{\underline{D}}$ matrix, without affecting the $\underline{\underline{A}}$ matrix (the definition of these matrices can be found in reference [21]). Compressive bucking loads, or natural vibration frequencies, are useful examples. Once volume fractions and possible orientations have been pre-determined, the evaluation of the optimum stacking sequence is a combinatorial problem. As such, a new optimisation algorithm has been developed and discussed in Chapter 7.

Conclusions and ideas for future work are described in section 8.

1.3.1 Main contributions of the work

The new analytical model developed for the evaluation of *EI*, *GJ* and *K* is simple and easy to implement. It provides better results than the other models previously presented in the literature.

The new optimisation algorithm proposed in this thesis provides better performances in terms of stacking sequences and CPU running time when compared to the existing permutative optimisation techniques, such like permutative GA and Branch and Bound.

Potential benefits of structural couplings, such as bend-twist coupling, obtained with anisotropic composite laminates, have been shown by studying some aeroelastic performances of aeroplane wings, such as range and flutter.

1.3.2 Publications

Canale G., Weaver P. M., Herencia J. E., "Aeroelastic Tailoring of a Wing Box in Subsonic Compressible Regime", 19th Conference on Adaptive structures and Technology, Ascona 6-9 October 2008.

Canale G., Weaver P. M., "A simple model to evaluate aeroelastic tailoring of a wing box", Proceedings of Royal Aeronautical Society Conference on Aircraft structural design, Liverpool, (2008).

Canale G., Weaver P. M. "Simplified and accurate stiffnesses of a prismatic and anisotropic thin walled box", Thin Walled Structures (under revision).

1.3.3 Chapters outline

The research work contained in this thesis is organized as follows:

Chapter 2 contains a literature review on aeroelastic tailoring, composite beam models and combinatorial stacking sequence optimisation.

Chapter 3 contains the formulation of a new analytical model to evaluate relevant stiffnesses of composite boxes for aeroelastic tailoring.

Chapter 4 describes the static aeroelastic tool. It contains results and comments on the aeroelastic tailoring to improve the range.

Chapter 5 describes the advantages and limitations of the low fidelity static aeroelastic model. Stiffnesses of a composite box are compared with those of a real wing like structure.

Chapter 6 contains some consideration on the critical flutter speed of composite wings.

Chapter 7 describes a new combinatorial algorithm of lay up stacking sequence optimisation. It can be applied to panels with a fixed number of plies and fixed thickness.

Chapter 8 summarises the contributions made by this research and presents suggestions for future work.

Chapter 2
Background

2.1 Introduction

In this Chapter, contributions to aeroelastic tailoring research application presented in the literature are described and critiqued. In the low fidelity aeroelastic models presented in this thesis, the wing has been represented as a thin walled beam. Since one of the goals of this research is the development of an analytical model to evaluate the relevant stiffnesses of a composite box, an "excursus" of the most important existing models of composite beams is included. Analogously, the literature detailing combinatorial stacking sequence optimisation of composite plates, with a fixed number of layers, has been reviewed.

2.2 A survey on aeroelastic tailoring

Aeroelastic tailoring belongs to a wider discipline known as aircraft morphing. An aircraft follows specific mission profiles which generally consist of: take-off, climb, cruise, descent and landing. To specify the performances requirements of the vehicle, design points are chosen within each part of the mission and then the best compromise performance among the possible configurations is selected. It is, therefore, evident that the result is an aircraft which is not optimal for any of the given design points [22]. Off-design flight conditions have significant aerodynamic and structural drawbacks such as increased drag penalty and excessive deformation[23]. These conditions are not only true both for long distance transport aircraft, where the large quantities of fuel burnt in-flight lead to a considerable change in the aircraft mass and aerodynamic requirements, but also for fighter aircraft, where the manoeuvrability requirements constrain most of the performance characteristics. It is evident that the ability of adapting the wing shape to different flight conditions would limit these problems and also it would give a single aircraft the capability to achieve multi-objective mission roles thus reducing the operational costs of having several aircraft, each suited to a different type of mission.

However, from current trends [24] in this research area, it is clearly evident that the practical realisation of a morphing structure is a particularly demanding goal with substantial effort still required. This is primarily due to the need of any proposed morphing airframe to simultaneously fulfil the contradictory requirements of flexibility and stiffness. If, on one hand, for low speed aircraft, it is always possible to rely on the elasticity of the material to achieve small deformations by means of simple actuators, on the other hand this solution is not applicable to high speed aircraft because of the imposed stiffness and strength requirements. Actuation would require a relatively large power consumption and lead to an unacceptable weight penalty. The most efficient solutions adopted so far, consist of complex assemblies of rigid bodies hinged to the main structure and actuated. This technique, though reliable, introduces discontinuities in the aerodynamic surface as well as in the structure and places limitations on manoeuvrability and efficiency. This produces non-optimal design for many flight conditions. These reasons explain why in recent years many projects have focused on realising morphing technologies.

Aeroelastic tailoring can be considered as a part of more generic morphing technologies. It was originally focused on aeroelastic instabilities such as divergence or flutter. It is now referred to the technologies adopted to drive the deformation of a structure in such a way as to improve the general performance of the aircraft. Two ways to perform aeroelastic tailoring exist: active and passive actuation.

In this thesis, according to the definition of Weisshaar, reported in Chapter 1, with the term "aeroelastic tailoring" only passive actuation will be sought.

2.2.1 Active actuation

Aeroelastic tailoring via active activation is a multidisciplinary technology that integrates air vehicle aerodynamics, active controls, and structural aeroelastic behaviour to maximize air vehicle performance. It employs wing aeroelastic

flexibility for a net benefit through use several kind of actuators. Literature provides several examples of aeroelastic tailoring via active actuation by using leading and trailing edge control surfaces activated by a digital flight control system or by varying the position/stiffness/angle of the spars. Moreover, shape memory alloys and piezoelectric actuators have been investigated.

Flick [25] at al proposes to control both leading and trailing edges to aeroelastically shape a high aspect ratio wing in order to design a lighter structure by satisfying flutter and strength constraints. A more flexible wing with active leading edges has been optimised by Voracek et al [26] in order to improve roll efficiency. Other authors have shown the potential benefits of adaptive internal structures [27, 28]. Aeroelastic tailoring has been obtained, in other words, by rotating the spars and by changing their position in the wing box.

Actuation has been obtained also by using shape memory alloys (SMA) [29]. They are metallic alloys that undergo solid-to-solid phase transformations induced by appropriate temperature/stress change during which they can recover their original, un-deformed shape. Their fundamental property for engineering applications is therefore the shape memory effect, obtained when inelastic strains existing in the material are recovered by applying a thermal load. In other words, the original shape is regained upon heating. Shape memory effect is useful for actuation and it has already been applied in the propulsion systems engineering [29]. Wires or beams made of shape memory alloys, moreover, when recovering their original configuration, can be used to actuate the trailing edge to deform the wing in order to improve aeroelastic performances [30]. Strelec et al [31] have used shape memory alloys wires to effectively change the shape of an airfoil while Sofla et al [32] developed a series of SMA flexural structures which could be used to deform wing boxes for shape morphing. Balta et al [33] used SMA wires to develop an adaptive aircraft winglet. A different and interesting structural implementation of SMA actuation is found in a patent [34] pertaining to actuation of the wing main spar. Here the active elements are placed inside tubular spars would be used to extend or retract a telescopic portion of the wing in the spanwise direction. SMA have the advantage

to provide actuation force during shape recovery, however, the difficulty to quickly cooling components limits the use in frequency applications. Furthermore, the amount of thermal energy required for actuation is much larger than the mechanical output and plastic accumulation during several cycles may degrade the material [29].

The piezoelectric effect, on the other hand, was discovered in 1880 by the Curie brothers [35]. The importance of this effect is due to the conversion of mechanical into electrical energy and vice versa. When an electric field is applied to a free layer made of piezoelectric material, the material of the layer will exhibit a displacement from its original location, similar to a thermal expansion of a freely heated elastic strip. On the other hand, an electric field emerges within the piezoelectric layer when it is deformed by an actuator. When the surface of the bonded layer is mounted with metallic electrodes, this latter piezoelectric effect can be used for the sensing of the deformation. When a piezoelectric layer is used for both, sensing and actuating, it is called a self-sensing layer [36]. Because the bonded piezoelectric layers are integral to the structure, which may be connected with an automatic control agency, it becomes possible to design structures able to react upon external disturbances. Both static and dynamic performances of a structure can be improved with such actuation. Four parameters can be used to obtain the optimal design: the position of the actuators, their size, orientation and the applied voltage [36]. Chee et al[37], for example, developed an algorithm to find the optimal orientation of the actuators in order to obtain the desired deformation of a composite plate. They performed a quasi-static study, since they were only interested in the final shape of the structure. Shape control is not only possible for plates, but also for slender beams [38]. An useful analytical model to describe the deformation of beams with embedded piezoelectric actuators, moreover, is described by Cesnik and Palacios [39]. Piezoelectric materials have been used to reduce vibrations and to increase the critical flutter speed [40-44]. The effect of sensors and actuators is analogous to an increase in the structural stiffness, but, and this is a key advantage, without a significant increase of the structural weight. Piezoelectric actuation, however, does

show two non-negligible disadvantages: the cost and their susceptibility to damage and malfunction induced by external electric fields.

2.2.2 Passive actuation

Aeroelastic tailoring can be described, as mentioned before, as passive actuation: the aircraft wing will adapt itself to improve its performance during the designed flight conditions. The mechanism of passive actuation is the structural coupling, caused by the anisotropy of the material. There are three main types of structural couplings used for aeroelastic tailoring and examples of their use have been shown in the literature. They are:

- Bend-twist coupling [45]
- Extension-twist coupling [45]
- Extension-bending coupling [45]

Bend-twist coupling has already been introduced and explained in Chapter 1. When a structure is subjected to a bending load, beside the bending deformation, also an angle of torsion is observed and vice versa. An important parameter to describe the bending behaviour of a structure is the bending stiffness *EI*. It can be interpreted, as it will be discussed more in detail in Chapter 3, as the bending moment arising in a cross section when a unitary bending deformation is applied. In the same way, torsion is described by the stiffness *GJ*. It can be interpreted as the twisting moment arising in the cross section when a unitary twisting deformation is applied. Bend-twist coupling is fully described by the stiffness *K*. In analogy with *EI* and *GJ*, it can be interpreted as the twisting moment arising in a cross section when a unitary bending deformation is applied.

Bend-twist coupling can be easily obtained in a wing when top and bottom skins (Figure 1.2) are built with laminates having their fibres oriented with an angle ξ with respect to the main frame of the structure *X, Y, Z*, as shown in Figure 2.1.

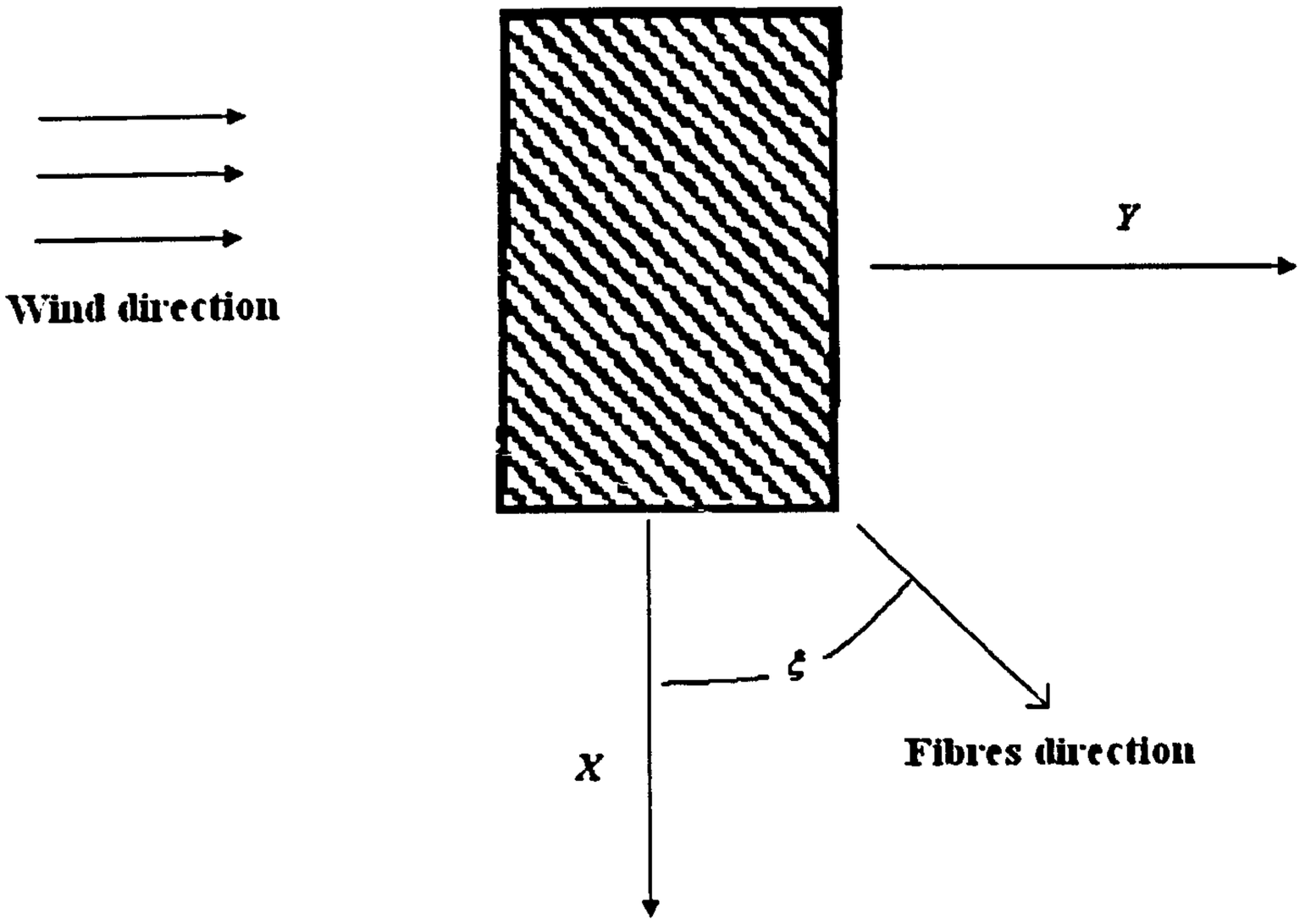

Figure 2.1: Fibre direction in the top and bottom skins of a wing in order to obtain bend-twist coupling (nose up).

Extension-twist coupling is a similar concept. When an isotropic structure is loaded with an axial load, only axial and transverse deformation is obtained. In a composite structure, if the anisotropy is exploited, when an axial load is applied, besides the axial and transverse deformation, a twisting deformation also exists (and vice versa). In a composite wing, this effect can be obtained when the top skin is constructed with fibres oriented with an angle ξ with respect to the structural axes and the bottom skin with an angle $-\xi$. When an axial load is applied, the top and bottom skins tend to shear in opposite directions, and therefore, an angle of twist is observed.

An analogous explanation can be given for the extension-bending effect: when an axial load is applied, besides the axial deformation of the structure, bending is measured. This effect could be observed, for example, in a composite box of rectangular cross section, with top and bottom laminates orthotropic and vertical walls made with fibres oriented with angles ξ with respect to the local reference system of the walls.

All three of these different kinds of anisotropy can be used in a beneficial way in aeroelasticity. However, the most effective, for aircraft wing design is the bend-twist coupling effect. Consequently, it has been chosen as the means for aeroelastic tailoring when developing the static and dynamic low fidelity models, presented in Chapter 4 and 6 respectively.

Several authors have already demonstrated the potential benefits of all structural couplings described in this section with many examples, not only regarding aircrafts. Soykasap and Hodges [45] showed how aeroelastic tailoring can improve the performance of a tilt-rotor (Figure 2.2).

Figure 2.2: Tilt-rotor.

A tilt-rotor is a complex machine as it is able to perform vertical take-off and landing as a helicopter and, on the other hand, it is able to fly with uniform horizontal cruise as an aeroplane. In their paper, the authors implemented a multi-objective optimisation to design a rotor blade able to improve the performance of the machine both in hovering and uniform horizontal flight. They found that the benefit of extension-twist coupling is greater than the beneficial effects from bend-twist coupling. They have also shown the existence of a marginally small beneficial effect from the extension-bending coupling. Their result is reasonable because the centrifugal force is the prevalent load in a tilt rotor blade.

Similar findings apply to a helicopter blade. Consequently, extension-twist coupling is the most relevant anisotropic effect to improve aeroelastic performance in this case also [46]. However, Ganguli and Chopra [47] showed the importance of bend-twist coupling in the design: they used a global "nose down" effect to reduce the vibratory hub loads and bending moments.

Bend-twist coupling is particularly useful also for HAWT (Horizontal Axis Wind Turbine) blades, shown in Figure 2.3. Lobitz and Laino [48] used a global "nose down" effect to reduce the stresses at the hub of the blade and to increase the fatigue life of the structure. They also show how this effect can be used to increase the average power produced by the wind turbine in a day. This is possible because a global "nose down" effect avoids the stall of a slender and flexible blade and increases the aerodynamic efficiency. Lobitz and Veers [49], when studying the effect of a global "nose up" or a global "nose down" on the wind turbine blade, also noted some negative aspects. They found that bend-twist coupling affects the frequencies of the first natural modes, making their values converge. Such studies have been also confirmed by Weissahaar and Foist [50]. On the other hand, they showed the following potential benefits of aeroelastic tailoring of a wind turbine blade:

- A global "nose down" effect is beneficial to avoid divergence. In other words, critical divergence speed is increased because the rotation of the generic cross section tends to decrease the angle of attack.
- A global "nose up" has beneficial effects on the critical flutter speed. The coupled modes induce the same behaviour obtained when the centre of mass is shifted in the direction of the leading edge of the blade, and then in the direction of the aerodynamic centre [51]. It is well-known that this effect is beneficial for flutter [52]. "Nose up" fibres induce, in other words, the same effect of moving the flexural axis to the aerodynamic centre, reducing aeroelastic coupling. The effect is also similar to a fictive increase of the torsional stiffness.

Figure 2.3: Horizontal Axis Wind Turbine (HAWT).

Previous results on the global nose up effect have also been confirmed for aeroplane wings by the work of Sarigul-Klijn and Oguz [53] and by Green [54].

One fundamental design parameter of a civil aircraft is the angle of sweep, denoted in this thesis by the symbol Λ (Figure 2.4). A wing with positive angle of sweep (aft-swept), when loaded in bending, shows a nose down deformation, i.e. an overall reduction of the angle of attack. The opposite effect is obtained with a forward-swept wing [55-57].

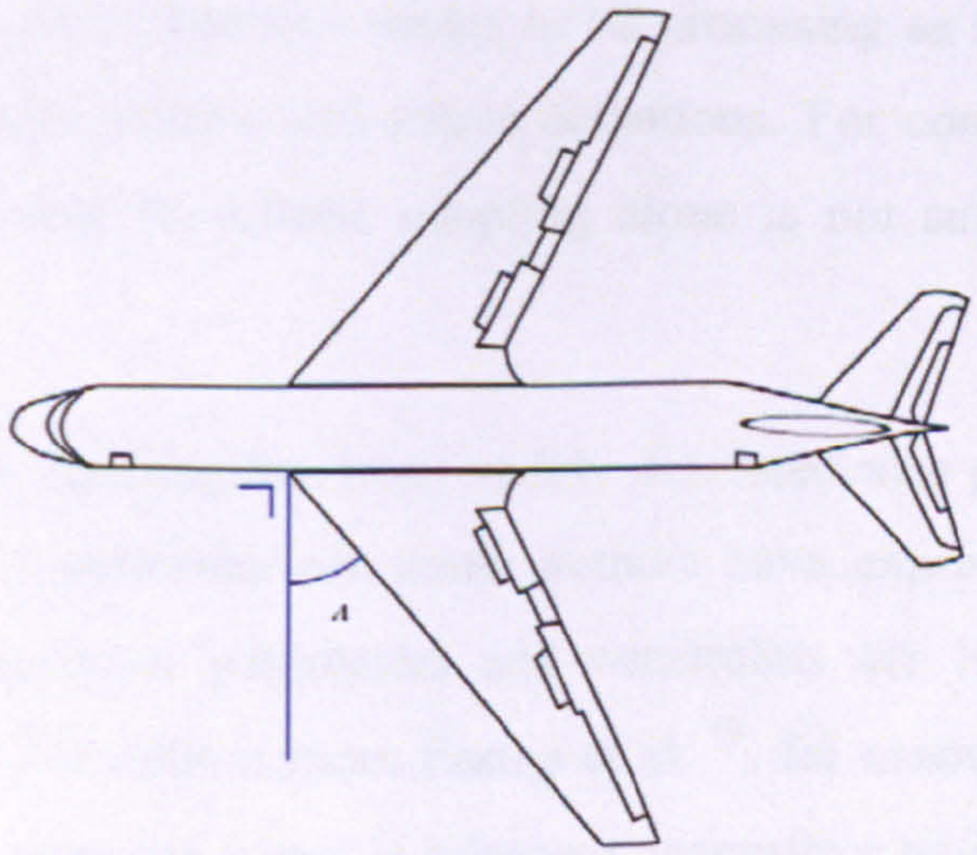

Figure 2.4: A positive angle of sweep.

An aft swept wing can also show a reduced critical flutter speed when compared with an unswept wing with the same properties [51], while a forward-swept wing shows a lower value of the critical divergence speed [51].

The bend-twist coupling effect, given by the anisotropy of composite materials, can be used to tailor effects related to the presence of the angle of sweep. In other words, a nose up effect induced by the elastic properties can be used to increase the critical flutter speed of aft-swept wings [54]. A nose down effect can be used to increase the critical divergence speed of a forward swept wing [55], as already implemented for the X-29, mentioned in Chapter 1.

Weisshaar and Duke [58] suggest that, in order to improve a particular performance of the aircraft, for example to reduce the drag, a combination of passive aeroelastic tailoring and actively controlled actuators can be used. They first design a stiffness tailored wing able to deform, in such a way, as to produce a nearly (but not exact) elliptical lift distribution. This implies a low value of drag, but not the minimum value possible, obtainable only with an exact elliptical distribution of lift. In the second step of their work, they introduce and design active controls on the wing surface. Such active devices, coupled with laminate stiffness tailoring, can further reduce induced drag by using small actuator deformations. These actuator arrays include ailerons, leading edges surfaces, active chord wise chambering or advanced controlling devices. This approach seems to be promising as it tends to overcome the limitations of both passive and active actuations. For complex geometries, in fact, they conclude that the elastic coupling alone is not sufficient to reach the desired goals.

Although aeroelastic tailoring has been widely discussed as a potential mechanism to improve aircraft's performances, some authors have expressed their concerns, especially when numerous parameters and constraints are introduced in to the structural design and/or optimisation. Eastep et al. [59], for example, suggest that the optimal weight of composite wings is relatively insensitive to the orientation of the

laminate lay-up when the wing is subjected to multiple structural constraints, such as strength, roll reversal velocity and minimum critical flutter speed.

Other authors, however, disagree with the results proposed by Eastep et al. and show that structural weight can be optimised even when numerous constraints are included. Herencia, Weaver and Friswell [60], for example, impose buckling constraints, whose importance is emphasised as well as strength and manufacturing constraints. They also show that a potential reduction of induced drag can be obtained by using unbalanced composite laminates. A small weight penalty, however, is observed.

2.3 A review of thin walled beams models

It is both complexity in composite design and market competition that makes aircraft manufacturers continuously demand rapid but efficient methods and tools: low fidelity models, to reduce computational time, in the preliminary design phase. Furthermore, low fidelity models provide a clear understanding of the physical phenomena involved in the analysis.

In both static and dynamic aeroelastic tools, which will be discussed in Chapter 4 and 6, a structural model and an aerodynamic model of a wing are developed. Since the main task of this work is to investigate the influence of anisotropic composite materials on the aeroelastic behaviour, more attention is paid in this chapter to the structural models previously presented in literature. In particular, this section is dedicated to thin walled beam theories, more suitable (in the opinion of the author) to wing models.

An example of thin walled beam is shown in Figure 2.5.

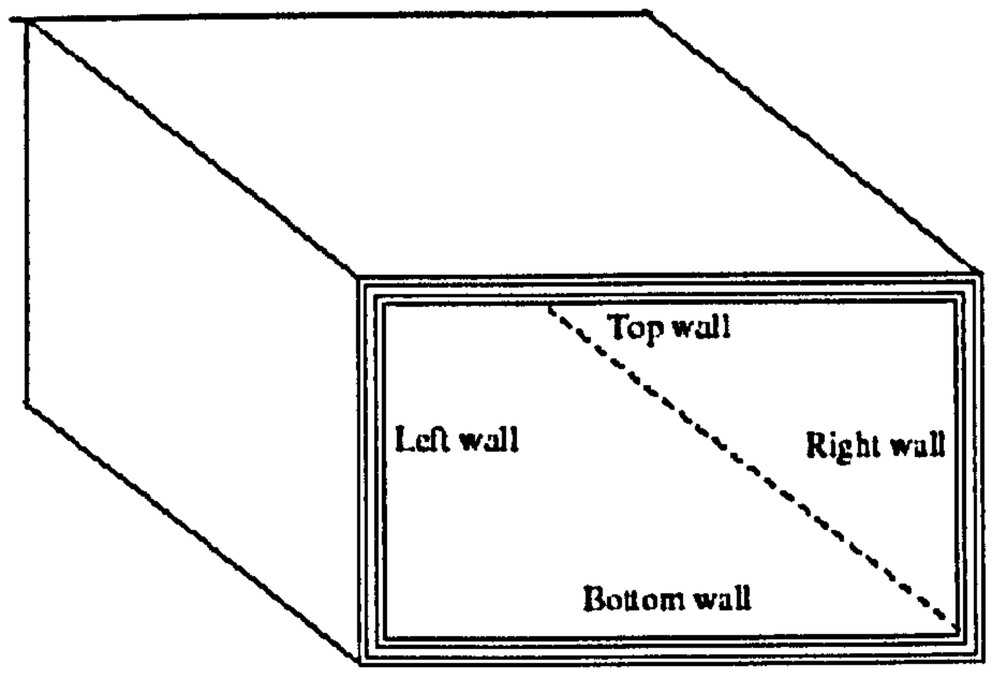

Figure 2.5: A prismatic thin walled composite beam.

Several models have been presented in literature. They can be divided in to two main categories: numerical models and analytical models. The difference between these approaches is explained as follows. The essential common element of the numerical models (typically finite element analysis) is structural discretization. Displacements of the whole structure are written as a function of displacements of certain points, called nodes. Displacements of all the points of a structure, located between the nodes are interpolated with shape functions, usually polynomial (linear, quadratic and so on). In other words, the following relation can be written:

$$\underline{u} = \underline{\underline{N}}\,\underline{\delta} \tag{2.1}$$

where

$\underline{u}$ is the vector of displacements

$\underline{\delta}$ is the vector containing nodal displacements

$\underline{\underline{N}}$ is a matrix containing the shape functions.

In the analytical models, on the other hand, the displacement field is written as a function of continuous variables representing the coordinates and the degree of freedom of the system.

Many numerical models of beams can be found in the literature. Some of them show a relatively simple formulation [49, 61] and they can be easily translated into a

computer code. However, they are no more precise or more efficient than analytical models. Therefore, when a simple system with few beams has to be studied, analytical models are more suitable and more practical. On the other hand, numerical models become of crucial importance to study complex beam systems, with an increased number of uni-dimensional elements with different orientations and boundary conditions. An example of this type of problem is the design of pipe lines of a chemical or nuclear plant [62]. The literature also offers examples of complex and detailed numerical beam theories, including those of Giavotto [63] and Yu [64]. These kinds of numerical models are generally precise, but they are computationally expensive and their implementation is often complex.

The use of analytical models seems more appropriate for the low fidelity aeroelastic models presented in this thesis, since the wing is represented as a cantilevered beam. Numerous analytical formulations of thin-walled beams have been proposed previously. In the following sections, an outline of the most important and most cited is provided. Particular attention has been paid to the following aspects:

1. The stiffness formulation of each model has been carefully considered. Three stiffnesses, in fact, are fundamental for aeroelastic tailoring and have been considered in this thesis:

EI	bending stiffness
GJ	torsional stiffness
K	bend-twist coupling stiffness

Axial deformation and lag-bending, are negligible in a wing-type structure[2, 58]. Also pure shear deformation can be neglected because the wings studied are generally long and slender.

2. The models reviewed are suitable for engineering applications and results presented in the relevant papers have been reproduced in this thesis.

Considering these two points, some models have not been included in this review. The model of Wu and Sun [7], for example, has been discarded because of its complexity and because the final stiffness formulation is not explicitly reported in their work. The work of Massa and Barbero [8] has also been discarded because, although the bending and twisting stiffnesses are expressly calculated, no coupling term is considered. The model of Rand [9], on the other hand, provides a clear physical explanation of the composite beam behaviour and an educating insight into the coupling mechanisms. However, constitutive equations are written only for some simple cases. Loads are restricted only to a tip axial force and a tip torque. Beams walls are constructed only with a single composite layer. Fundamentals of the general formulation are explicitly explained, but the development is left to the reader.

For all of the models considered, the main reference frame used is shown in Figure 2.6. It is placed at the geometric centre of each cross section. Axes are denoted by *X, Y, Z.* The circumferential coordinate, located in the middle line of the contour of the cross section, is denoted with *s*.

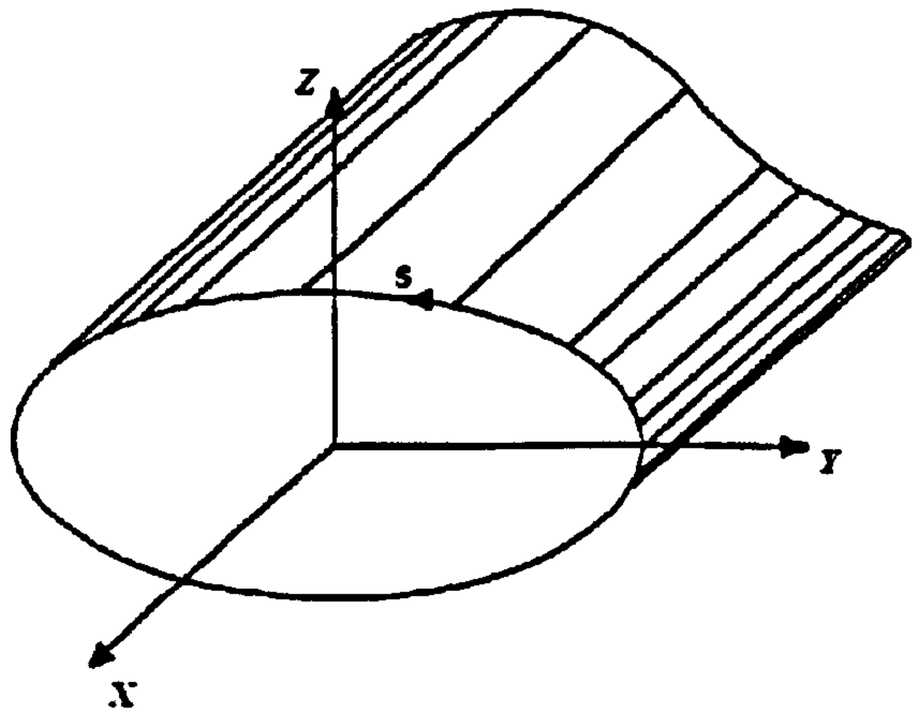

Figure 2.6: Global frame used in the description of all the analytical models.

2.3.1 The model of Hwu and Tsai [10]

It is probably the simplest among the models reviewed and probably the least accurate. However, it is important for one reason: it is the only model where the effects of structural components such as stringers, webs and ribs are explicitly considered.

Unfortunately, webs and the top and bottom skins are not modelled together as a part of a unique structure. The hypothesis proposed by Bruhn [65] in his book is in fact adopted: different structural components react separately to different kinds of loads. Stringers and top and bottom skins are supposed to react to the bending, torsion and axial loads, while webs are supposed to react only the shear stresses coming from the vertical force F_z. Bending, torsional and bend-twist coupling stiffnesses are calculated by means of the classical lamination theory [21]. They are expressed as terms of the $\underline{\underline{D}}$ matrix only. The reference plane $Z = 0$ for the evaluation of such a matrix is not located at the middle surface of each laminate but in the middle surface of the whole cross section (Figure 2.7), to guarantee the evaluation of global properties.

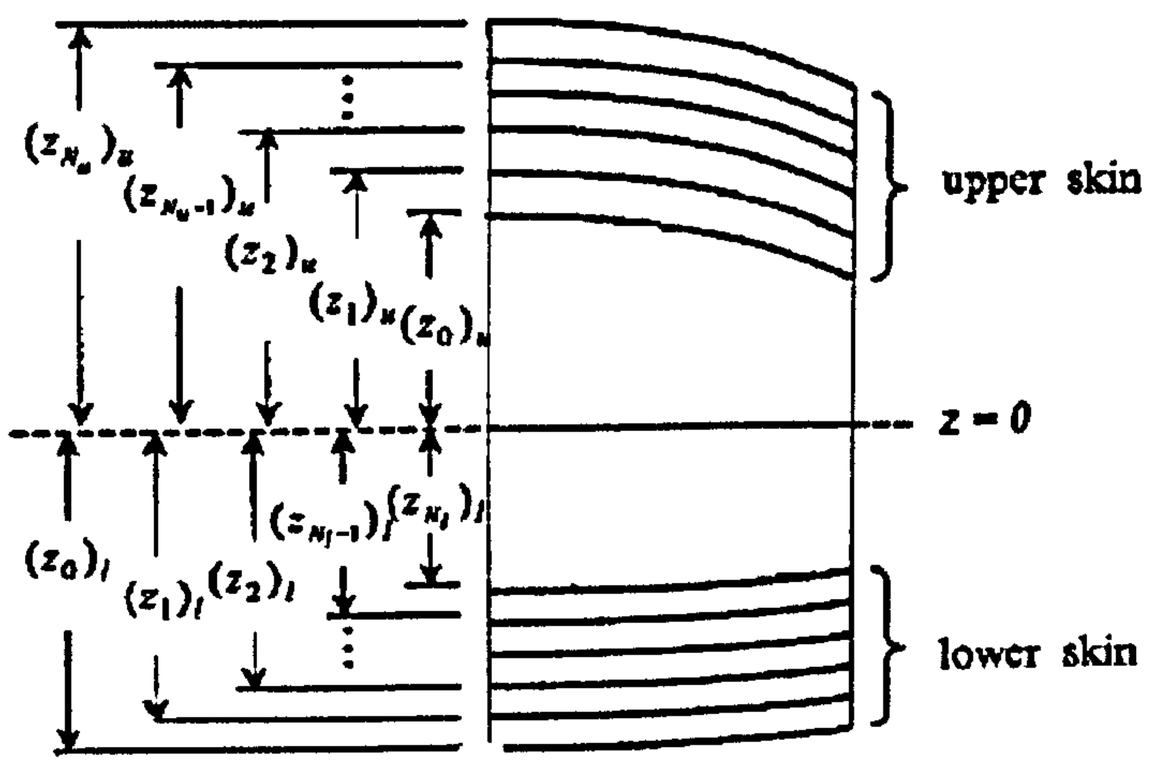

Figure 2.7: The axis $Z = 0$ for the global $\underline{\underline{D}}$ matrix evaluation, in the model of Hwu and Tsai.

These assumptions made by the authors lead to inaccurate evaluations of stiffnesses and deformations, even when analyzing a simple wing box. There are two main reasons for the inaccuracies. The first one concerns the vertical walls of a beam, that, even when short, they give a non-negligible contribution to the bending and torsional stiffnesses. The second one involves the most effective way to evaluate the stiffnesses of a thin-walled beam. In all other models considered in this section, membrane properties are used for each wall. However, in this formulation, the authors consider a thin walled beam as a plate and calculate its stiffnesses by using a global $\underline{\underline{D}}$ matrix.

This paper, however, is mentioned in this review because a clear and simple method to model the stringers is presented. Stringers are normally placed in the internal part of the top and bottom skin (Figure 2.8).

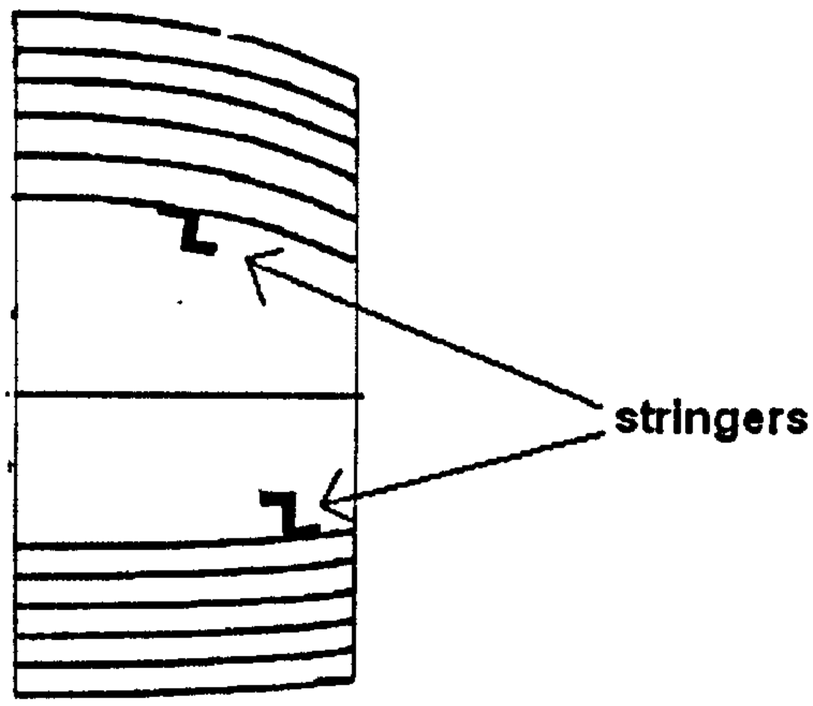

Figure 2.8: The position of the stringers in a wing cross section.

The two layers containing the stringers can be considered as two additional laminae of composite. The elastic properties of a lamina are:

E_1	elastic modulus in the axial direction
E_2	elastic modulus in the transverse direction
G_{12}	shear modulus
v_{12}	major Poisson's ratio

Elastic properties of a smeared "pseudo-lamina" containing the stringers can be evaluated by using the rule of mixture as follows:

$$E_{1pl} = \frac{E_s A_s}{A_t}$$

$$\nu_{12pl} = \frac{\nu_s A_s}{A_t} \qquad (2.2)$$

$$G_{12pl} = 0$$

$$E_{2pl} = 0$$

where

E_{1pl} is the axial elastic modulus of the pseudo-lamina made by stringers and empty spaces between them

E_{2pl} is the transverse elastic modulus of the pseudo-lamina made by stringers and empty spaces between them

G_{12pl} is the shear modulus of the pseudo-lamina

ν_{12pl} is the Poisson's ratio of the pseudo-lamina

A_s is the total area occupied by the stringers of a pseudo lamina

A_t is the total area of the pseudo-lamina

E_s, is the Young's modulus of a stringer

ν_s is the Poisson's ratio of the stringers

Once properties of Eqn. 2.2 are know, the stiffness matrix of a pseudo-lamina can be readily evaluated. The pseudo-lamina is only one layer that can be finally added to the complete laminate in order to evaluate the overall stiffness matrix $\underline{\underline{D}}$.

2.3.2 The model of Kim and White [11]

The formulation of Kim and White is precise and suitable to evaluate complex deformations of beams with a high degree of anisotropy. Furthermore, thin and thick walled composite beams can be analysed because both primary and secondary warping effects are included.

Generally, when a twisting moment is applied to the beam tip, besides the twisting deformation, a non-uniform axial displacement field is observed. In other words, points of the cross section tend to deform out of their original plane (Figure 2.9). This phenomenon is particularly evident in beams with open sections.

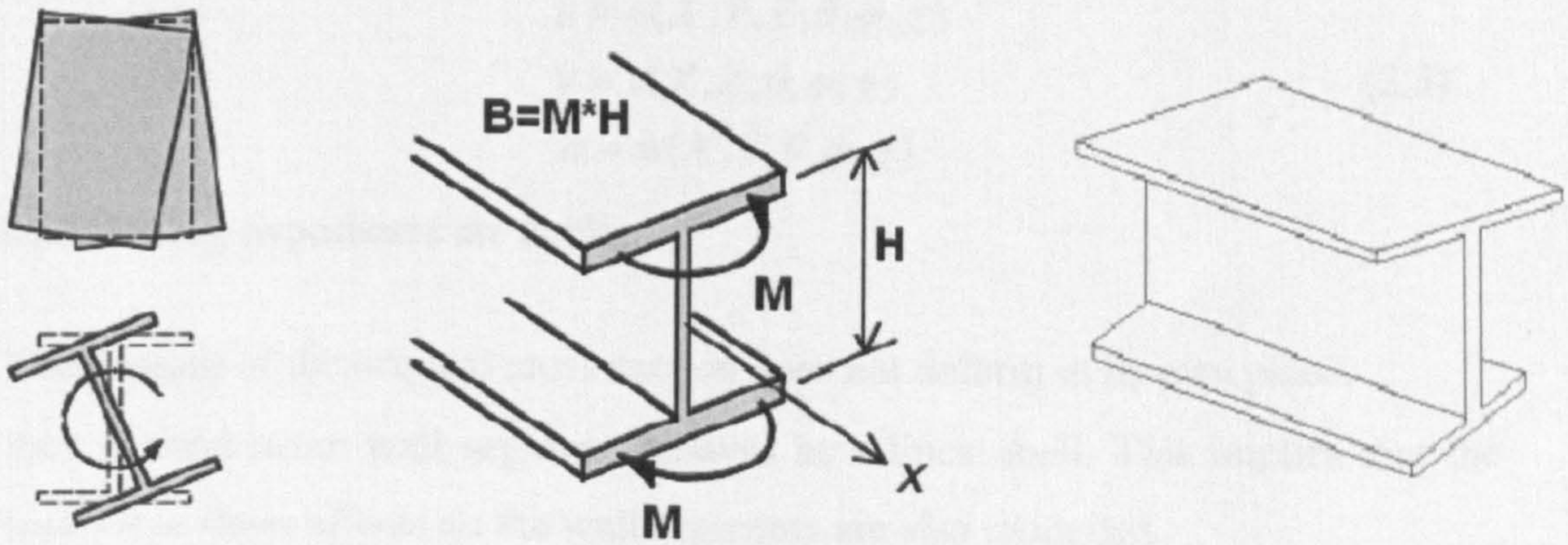

Figure 2.9: The phenomenon of warping.

This effect is usually modelled by means of an equivalent action, known as "bimoment" denoted in this thesis with the symbol *B*. It is the product of a moment *M* with the cross's section height *H*. Two opposite moments *M* are acting on the top and bottom parts of the cross section. They tend to induce out-of-plane displacements on the cross section (Figure 2.9).

Out-of-plane displacements of a cross section, induced by a torsional load, can affect, in certain cases, the final deformation of a beam, especially if a high level of anisotropy exists. Furthermore, if such phenomenon is prevented, additional longitudinal stresses are induced. Also aeronautical structures can be affected by restrained warping, due, for example, to the presence of ribs.

Two kinds of warping have been modelled by Kim and White. The primary warping refers to the out of plane displacements of the mid lines of each wall. If the walls are particularly thick, out of plane displacements are observed with the respect to the mid line of each wall. This effect is the secondary warping.

Consider the model's formulation, in terms of constitutive equations and stiffnesses. A displacement field is written as a function of the rigid body translations u_0, v_0, w_0, representing the rigid displacements of the cross section along the axes X, Y and Z, and as a function of the rotations (θ, φ, χ) about such axes. In other words, a displacement field is written as a function of six kinematic variables:

$$\begin{aligned} u &= u(X,Y,Z,\theta,\varphi,\chi) \\ v &= v(X,Z,\theta,\varphi,\chi) \\ w &= w(X,Y,\theta,\varphi,\chi) \end{aligned} \tag{2.3}$$

The following hypotheses are applied:

- The contour of the original cross section does not deform in its own plane.
- Any general beam wall segment behaves as a thick shell. This implies that the transverse shear effects on the wall segments are also modelled.

Once the displacement field in the global coordinate system is known, the strain field can be evaluated using the definition (Eqn. 2.4):

$$\begin{aligned} \varepsilon_x &= \frac{\partial u}{\partial x} \\ \gamma_{xy} &= \frac{\partial u}{\partial y} + \frac{\partial v}{\partial x} \\ \gamma_{xz} &= \frac{\partial u}{\partial z} + \frac{\partial w}{\partial x} \end{aligned} \tag{2.4}$$

The following condition (Eqn. 2.5) must be satisfied to ensure the non-deformability of the cross section:

$$\varepsilon_z = \varepsilon_y = \gamma_{yz} = 0 \tag{2.5}$$

A local frame of reference is considered in every wall segment of the cross section. The axes are respectively:

n	Normal to the wall, directed from the internal to the external part of the cross section.
s	Tangential to the wall.
x	Coincident with the *x* axis of the main frame.

The centre of each local frame (Figure 2.10) is located at the centre line of each wall segment. For each lamina, in the local frame, the following relation between the local stresses and strains can be written:

$$\begin{bmatrix} \sigma_x \\ \tau_{xs} \\ \tau_{nx} \end{bmatrix} = \begin{bmatrix} Q_{xx} & Q_{xxs} & Q_{xnx} \\ Q_{xxs} & Q_{xs} & Q_{xsnx} \\ Q_{xnx} & Q_{nxxs} & Q_{nx} \end{bmatrix} \begin{bmatrix} \varepsilon_x \\ \gamma_{xs} \\ \gamma_{nx} \end{bmatrix} \tag{2.6}$$

where

σ_x	is the axial stress
ε_x	is the axial strain
τ_{ij}	is the tangential stress in the direction *i-j*
γ_{ij}	is the tangential strain in the direction *i-j*
$\underline{\underline{Q}}$	is the local stiffness matrix

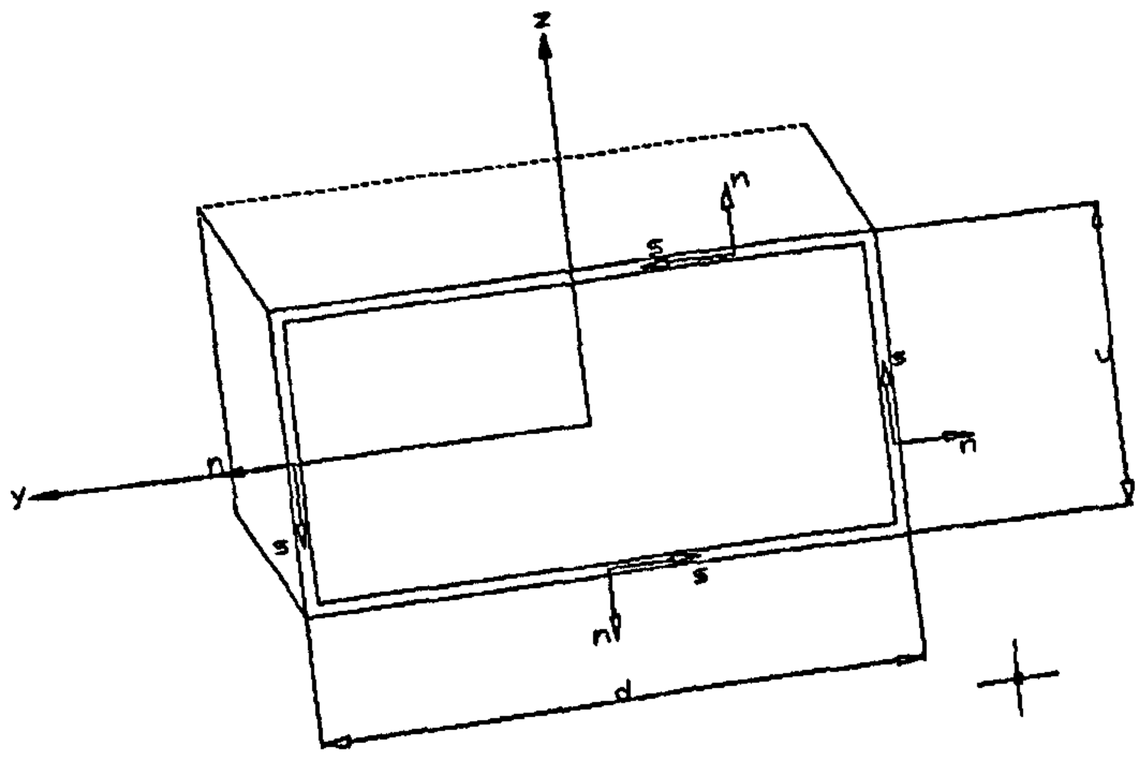

Figure 2.10: The local frame of each wall.

A coordinate transformation can be used to express the global stress vector $\begin{bmatrix} \sigma_x \\ \tau_{xy} \\ \tau_{xz} \end{bmatrix}$

as a function of the local stresses of each wall segment. Constitutive equations in the global coordinates can be finally written. They must be six, the same number as kinematic variables. They are represented by:

$$
\begin{aligned}
F_x &= \iint \sigma_x \, dydz \\
F_y &= \iint \tau_{xy} \, dydz \\
F_z &= \iint \tau_{xz} \, dydz \\
T &= \iint \left[\left(y - \frac{\partial \psi}{\partial z} \right) \tau_{xz} - \left(z + \frac{\partial \psi}{\partial y} \right) \tau_{xy} \right] dydz + \frac{\partial}{\partial x} \iint \psi \sigma_x \, dydz \\
M &= - \iint \sigma_x z \, dydz \\
N &= - \iint \sigma_x y \, dydz
\end{aligned}
\tag{2.7}
$$

where

F_x, F_y, F_z	are the internal forces along the axes *X*, *Y* and *Z*, related to the external loads applied.
T, M, N	are the internal moments about the axes *X*, *Y* and *Z*.
Ψ	is the warping function modelling both primary and secondary effect.

Substituting the global stresses into Eqn. 2.7 and integrating, the system of equation is obtained in terms of u_0, v_0, w_0, θ, φ, χ . Such a system can be solved accounting for the boundary conditions.

This model is readily translated into a computer code and becomes highly effective, in comparison with other models, when beams with thick walls are studied. Stiffness expressions are explicitly provided.

2.3.3 The model of Rehfield et al [12]

An assumed displacement field is also used by Rehfield et al. as a starting point to develop their model. Displacements u, v and w are written as functions of three rigid body translations, three rotations and one warping function, considered explicitly as a kinematic variable. From this displacement field, strains are evaluated and referred to the local frame of each wall of the cross section. Such local strains can be substituted in the local constitutive equations of each section of the contour, which can be written as:

$$\begin{bmatrix} N_x \\ N_{xs} \end{bmatrix} = \begin{bmatrix} A_{11} - \dfrac{A_{12}^{\,2}}{A_{22}} & A_{16} - \dfrac{A_{26}A_{12}}{A_{22}} \\ A_{16} - \dfrac{A_{26}A_{12}}{A_{22}} & A_{66} - \dfrac{A_{26}^{\,2}}{A_{22}} \end{bmatrix} \begin{bmatrix} \varepsilon_x \\ \gamma_{xs} \end{bmatrix} \tag{2.8}$$

From Eqn 2.8, three assumptions are clear:

- The cross section maintains its shape after the deformation, consequently the circumferential deformation is: $\varepsilon_s = 0$.
- Local curvatures of the shells are neglected. Only the membrane properties are therefore considered.
- Any general beam wall segment behaves as a thin shell.

Global constitutive equations can be written as follows:

$$\begin{aligned} (F_x, M, N, B) &= \oint N_x (1, z, -y, \psi) ds \\ (F_y, F_z, T) &= \oint N_{xs} \left(\frac{dy}{ds}, \frac{dz}{ds}, \frac{2\Omega}{p} \right) ds \end{aligned} \tag{2.9}$$

where

Ω	is the area enclosed by the cross section
p	is the perimeter of the cross section
ds	is the infinitesimal element of the contour
B	is the "bimoment"

Substituting Eqn. 2.8 into Eqn. 2.9 and integrating, a general equation is obtained relating the vector of the internal forces with the vector of the kinematic unknown. In other words, an expression:

$$\underline{F} = \underline{\underline{K}}\,\underline{u} \tag{2.10}$$

is obtained, where

$$\underline{u} = \begin{bmatrix} \dfrac{\partial u}{\partial x} \\ \gamma_{xy} \\ \gamma_{xz} \\ \dfrac{\partial \vartheta}{\partial x} \\ \dfrac{\partial \varphi}{\partial x} \\ \dfrac{\partial \chi}{\partial x} \\ \dfrac{\partial^2 \vartheta}{\partial x^2} \end{bmatrix} \quad \text{and} \quad \underline{F} = \begin{bmatrix} F_x \\ F_y \\ F_z \\ T \\ M \\ N \\ B \end{bmatrix}$$

and $\underline{\underline{K}}$ is a stiffness matrix.

Rehfield and the co-authors remark on the existence of two non classical effects of anisotropic composite beams. The first one is the shear-bending coupling, shown in beams with a circular cross section. The configuration analysed is a CUS (Circumferentially Uniform Stiffness), where the contour is built with only one kind of laminate, wrapped all around the cross section. Rehfield proves that when a CUS configuration is loaded with a bending moment, a displacement along the Y axis is observed.

The second non-classical effect investigated is warping. It has been observed that, when warping is restrained and the beam is loaded in torsion, the tip shows a smaller angle of twist. In other words, torsional stiffness GJ is greater when restrained warping exists. However, this effect is increasingly negligible as the

beam becomes longer and more slender. Analytical expressions, functions of geometric and elastic characteristics of the cross-section, are provided to establish when such effects can be neglected. Analytical formulae to evaluate stiffnesses are explicitly provided.

2.3.4 The model of Librescu and Song [13]

The model developed by Librescu and Song is analogous to the model of Rehfield et al. and to the model of Kim and White. A displacement field is written with respect to the global coordinates system. The following assumptions are made:

1. The original shape of each cross section is assumed to remain unchanged after the deformation.
2. Transverse shear effects are incorporated. Shear strains γ_{xz} and γ_{xy} are assumed to be uniform in each cross section.
3. Both the primary and secondary warping are considered, as in the theory developed by Kim and White.

Once the displacement field has been written, the strain field in each local frame is evaluated and used in a 3-D constitutive expression as

$$\underline{\sigma_{loc}} = \underline{\underline{Q}}\,\underline{\varepsilon_{loc}} \tag{2.11}$$

where

$\underline{\sigma_{loc}} = \begin{bmatrix} \sigma_x \\ \sigma_s \\ \tau_{xs} \\ \sigma_n \\ \tau_{xn} \\ \tau_{ns} \end{bmatrix}$ is the vector of local stresses

$$\underline{\varepsilon_{loc}} = \begin{bmatrix} \varepsilon_x \\ \varepsilon_s \\ \gamma_{xs} \\ \varepsilon_n \\ \gamma_{xn} \\ \gamma_{ns} \end{bmatrix}$$ is the vector of local strains

The constitutive equations exhibit a 3-D dependence, and this is a point of novelty with respect to the theory of Rehfield. They are reduced to equivalent 1-D dependence in two steps. The first step, yields the 2-D constitutive equations, similar to those used by Rehfield (Eqn. 2.8), done by integration of their original form through the laminate thickness. The second step, resulting in the final 1-D form, consists of a further integration along the mid-line contour of the cross section of the beam. Explicitly derived stiffness terms include *EI* and *GJ* and coupling terms.

This paper [13] also considers a CUS configuration. Results obtained are in agreement with those presented by Rehfield et al. An important fact is remarked upon: a theory that does not consider restrained warping risks overestimation of twisting deformation. It is shown quite clearly in the paper, for example, that the divergence speed of a beam with free warping is lower than the divergence speed of the same wing with restrained warping.

A point of novelty is emphasised by Librescu and Song: shear deformation cannot be neglected without precise investigation of the structure. Even in a slender beam, such an effect can influence the final deformation if a high level of anisotropy exists. However, according to their analysis, the difference in results between a structure including shear deformation and the same structure studied without shear deformation is only 2% (wings with moderate angle of sweep). Furthermore, the performance used for the comparison is the critical divergence speed of a swept wing (modelled as a beam), which is extremely sensitive to small bending and torsional deformations.

2.3.5 The model of Chandra and Chopra [14]

The model of Chandra and Chopra is also built on an "ad hoc" displacement field. The basic assumptions of this theory are:

- The contour (mid-line of the plate segments) of a cross section does not deform in its plane.
- A general plate segment of the beam is governed by classical lamination theory. This implies that the transverse shear deformation of the plate segment is not accounted for.

The last point is significant and merits further explanation. In order to simplify the implementation of the model, i.e. its translation into a computer code, it is desirable to have the opportunity to use classical lamination theory as it is, as a ready tool. Computer codes of classical lamination theory, in fact, are already available and the implementation of new programs is therefore not needed. This intuition has been already used in the model of Rehfield, but only the membrane properties have been considered.

In the model of Chandra and Chopra, classical lamination theory also includes the effects of local curvatures. The authors demonstrate that neglecting the local bending curvature, for example, may lead to large errors in the prediction of the structural response. Two identical beams, built with non-symmetrical laminates and showing bend-twist coupling, are compared. In the first one, membrane properties only (Rehfield approach) are considered while in the second both membrane properties and local curvatures (Chandra and Chopra approach) are retained. A bending load is applied to the tip of both the beams and bending and twisting deflections are measured. Concerning the induced twist (bend-twist coupling effect) no difference is shown. However, the beam of Chandra and Chopra, which includes the effects of $\underline{\underline{B}}$ and $\underline{\underline{D}}$ matrices, shows a greater bending deformation. This effect is accentuated for open cross section beams and for beams with non-symmetrical laminates but it becomes negligible for closed cross section beams.

Also in this work, as in the previous described, the authors consider the effects of transverse shear and the effects of restrained warping. Concerning the restrained warping, they define a parameter depending on the geometrical characteristics of the beam and on the elastic couplings. If this parameter is greater than some reference values, the effect of warping cannot be neglected. This usually happens in beams with open cross section.

The influence of transverse shear deformation on the structural response occurs in two ways: the direct transverse shear and the effect via transverse shear related coupling. The latter can be obtained in a composite box, for example, when unbalanced symmetric laminates are used to build the vertical walls. The direct transverse shear effect is controlled mainly by the slenderness ratio of the beam and its cross sectional details. It can be neglected only in short beams.

2.3.6 The theory of Berdichevsky et al. [15]

Many of the theories presented in literature are developed from an assumed displacement field. Berdichevsky et al. disagree with this approach and propose to use a variational method in order to find the equilibrium equations.

The starting point is therefore the strain energy of a thin walled beam. It is written from the 2-D energy of a shell component of each wall. Energy density is:

$$U = \frac{1}{2} \underline{\varepsilon_{ij}} \underline{\underline{E_{ij}}} \underline{\varepsilon_{ij}} \tag{2.12}$$

where $\underline{\varepsilon_{ij}}$ is a vector containing the local strains, measured with respect of the local reference of each wall. They are first evaluated by applying the strains definition to the displacements u, v and w (unknown) and then substituted in the energy density (Eqn. 2.12). The global energy functional can then be written as follows:

$$I = \iint U dx ds - W_{ext} \tag{2.13}$$

where

W_{ext} is the work made by the external forces

A correct displacement field is obtained after minimizing this functional. In the first step, strains with a lower order of magnitude are neglected. Such hypothesis is called "zero order" approximation. The minimization of the energy functional leads to equations containing the displacement field. After this first iteration, the following result is obtained:

$$\begin{aligned} u &= u_0 \\ v &= v_0 - Z\vartheta(X) \\ w &= w_0 + Y\vartheta(X) \end{aligned} \tag{2.14}$$

where θ is the angle of torsion. The zero order approximation is not accurate: the bending angle is not even considered. Three correction functions f_1, f_2, f_3, as yet unknown, are added to the displacement field as follows:

$$\begin{aligned} u &= u_0 + f_1(x,s) \\ v &= v_0 - Z\vartheta(x) + f_2(x,s) \\ w &= w_0 + Y\vartheta + f_3(x,s) \end{aligned} \tag{2.15}$$

Strains are again evaluated and substituted into the energy functional of Eqn. 2.13. A new minimization is performed. The iterative process is stopped when the new corrective terms become negligible with respect to the previous ones. An asymptotical correct displacement field is finally obtained. Starting from it, global constitutive equations can be readily obtained.

2.3.7 The model of Kollar and Pluzsik [16,17]

The model of Kollar and Pluzsik is based mainly on matrix analysis and classical lamination theory. It can be applied only when the cross-section is made of straight segments. Four global kinematic variables are considered, the axial displacement of

the beam, curvatures about Y and Z axis and the angle of torsion. A global system of four equations in four unknown is obtained at the end. The resulting stiffness matrix is consequently square and of order four.

The fundamental idea of the model is quite simple: in the global coordinate system (X, Y, Z), forces and moments acting on the whole cross section are the sum of forces and moments acting on all the wall segments. A local coordinate system is used in each k-th wall, together with the global frame. They are shown in Figure 2.11.

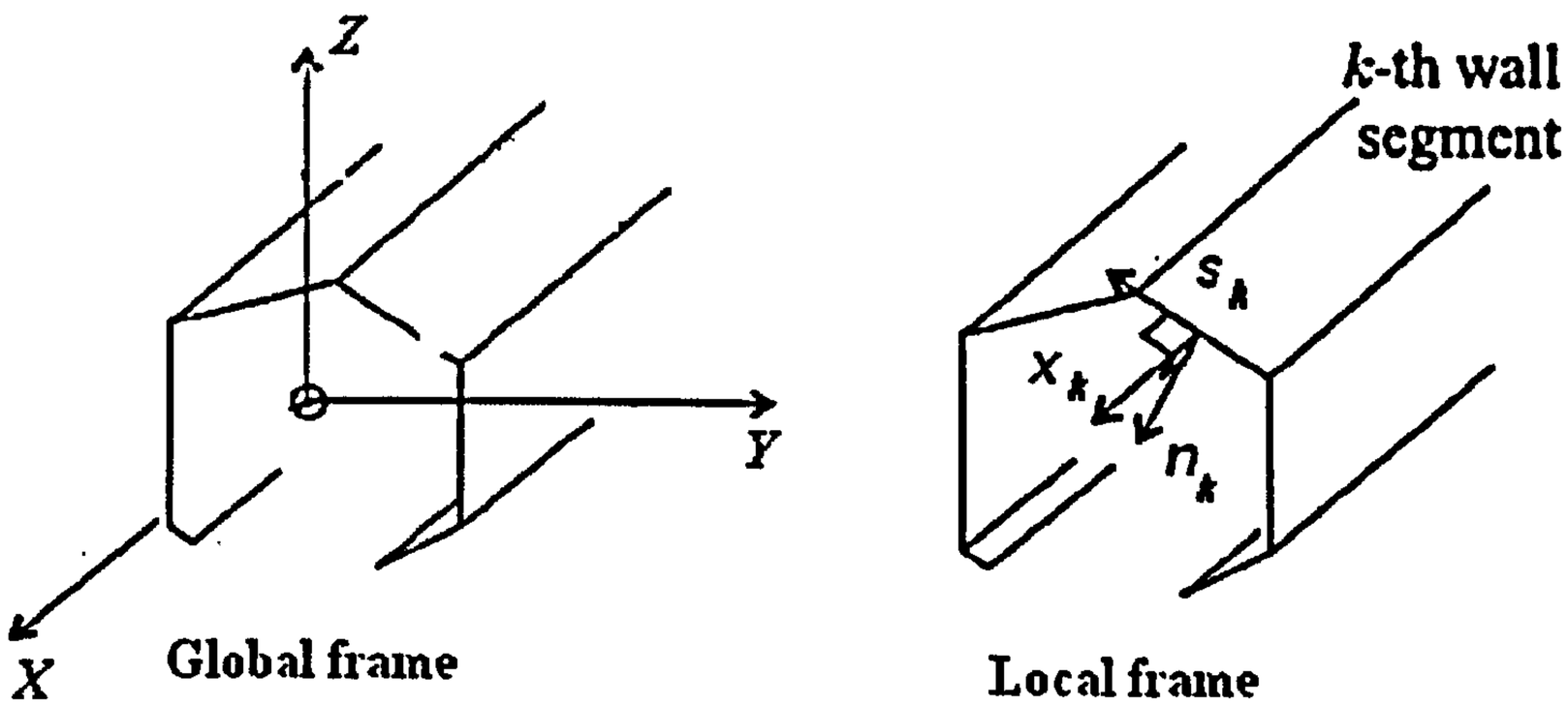

Figure 2.11: Coordinate systems used in the model of Kollar and Pluzsik.

The model is originally developed for open cross sections. Four steps are required:

1. Strains in each wall are expressed in terms of global kinematic variables.
2. Forces and moments in each wall segment are determined from the strains of each segment by using classical lamination theory.
3. Resultant axial force, moments and torque acting on the axis of the beam are determined from the forces and moments acting in each wall.
4. The stiffness matrix is established by relating global internal forces to the global displacements. The final expression of the model is $\underline{F} = \underline{\underline{K}}\underline{u}$.

The first part of the theory, as already mentioned, is suitable for open sections, but it can be easily adapted to a closed cross section. If a closed section were cut lengthwise, the two cut edges would move relative to each other, as shown in

Figure 2.12. In the uncut beam this deformation is prevented by the force X_1, the bending moment X_2, and two transverse forces X_3 and X_4 along the cut.

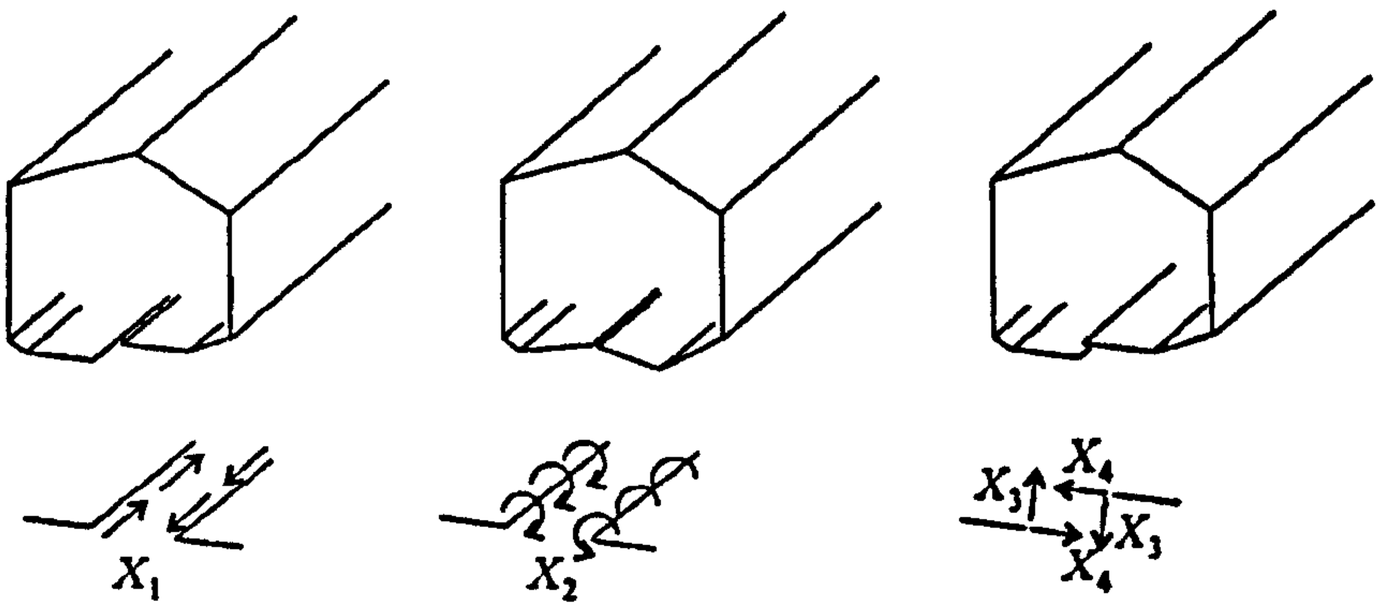

Figure 2.12: Forces and moments that arise to maintain the shape of a closed section.

As the deformation caused by transverse shear is neglected and the circumferential stress is supposed to be zero, X_3 and X_4 shown in Figure 2.12 can be neglected. Unknown X_1 and X_2 can be determined from compatibility equations.

Finally, the system of constitutive equations is obtained in the matrix form $\underline{F} = \underline{\underline{K}}\underline{u}$ for a closed cross section. Displacements and forces are considered with respect to the centroid, i.e. that point located in such a way that the beam's axis remains straight if a simple axial load is applied. Analytical formulae to locate it are explicitly provided.

This model presents some significant advantages:

- Classical lamination theory can be used as a "black box" in order to determine the forces inside each wall segment.
- Structural differences between an open and a closed section are clearly explained.
- A possibility of a centroid which differs from the geometric centre of the section is considered and explicit formulation to evaluate it is provided.

Two effects are neglected by Kollar and Pluzsik: shear deformation and warping. The effects of the shear deformations on the final deformation are negligible in slender beams. Concerning warping, it cannot be neglected when dealing with open beams. However, and it is an important result, the warping can be neglected for a long closed section cantilevered beam. This result, according to the authors, is independent of the slenderness of the beam.

2.3.8 The model of Lemanski and Weaver [18]

This model does not provide a complete theory to evaluate the deformation of a beam. The work is focused, instead, on the evaluation of the bend-twist coupling stiffness *K*, which is the most critical stiffness to be evaluated for aeroelastic purposes. The formulation is valid only for rectangular cross sections (Figure 2.13).

The stiffness *K* is calculated analytically by considering moments and forces that arise in each part of the cross-section when a deformation is induced. *K* can be thought, according to its mathematical definition, in two different ways. It is the twisting moment that arises in a box when a unitary bending curvature is applied. On the other hand, it is also the bending moment that arises when a unitary twisting curvature is applied to the cross-section.

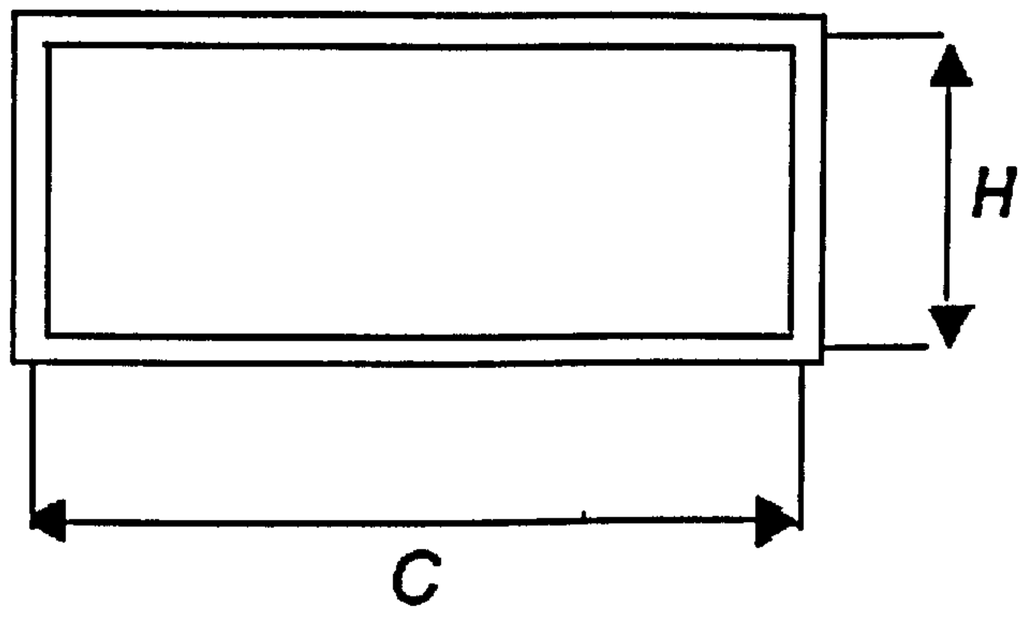

Figure 2.13: The wing-box in the model of Lemanski and Weaver.

The first step in the analysis is to apply a unitary bending deflection to the structure and to assume a deformed shape of the cross-section. Forces and moments consequently arising in each horizontal and vertical wall are calculated with

classical lamination theory. Starting from these forces and moments, a twisting moment can be determined. This induced twisting moment is the stiffness K.

This formulation is found to be precise and based on physical understanding. Further comments and analyses are provided in Chapter 3.

2.3.9 The model of Johnson, Vasiliev and Vasiliev [19]

The analysis of thin-walled beams can be generally performed following two main methods: the displacement formulation, where the starting point is an assumed displacement field, or of the strain formulation, where the starting point is an assumed strain field.

In contrast, these authors propose the use of a stress formulation: the shear flow, used in the local constitutive equation of each wall, is determined from a differential equation of equilibrium. Its integration does not impose any restrictions on the manner in which the wall stiffness varies along the cross sectional contour. Furthermore, the stress formulation does not require assumptions concerning the warping function.

The key points of the theory can be summarised as follows:

- An expression of the strain ε_x of the axial direction is assumed.
- Displacements v and w are assumed.
- Equilibrium equations are written for an infinitesimal element (Fig 2.14) of the beam: local shear flow τ_{xy} is expressed as a function of the axial stress σ_x.
- The stress component in the Y direction (σ_y) is neglected.

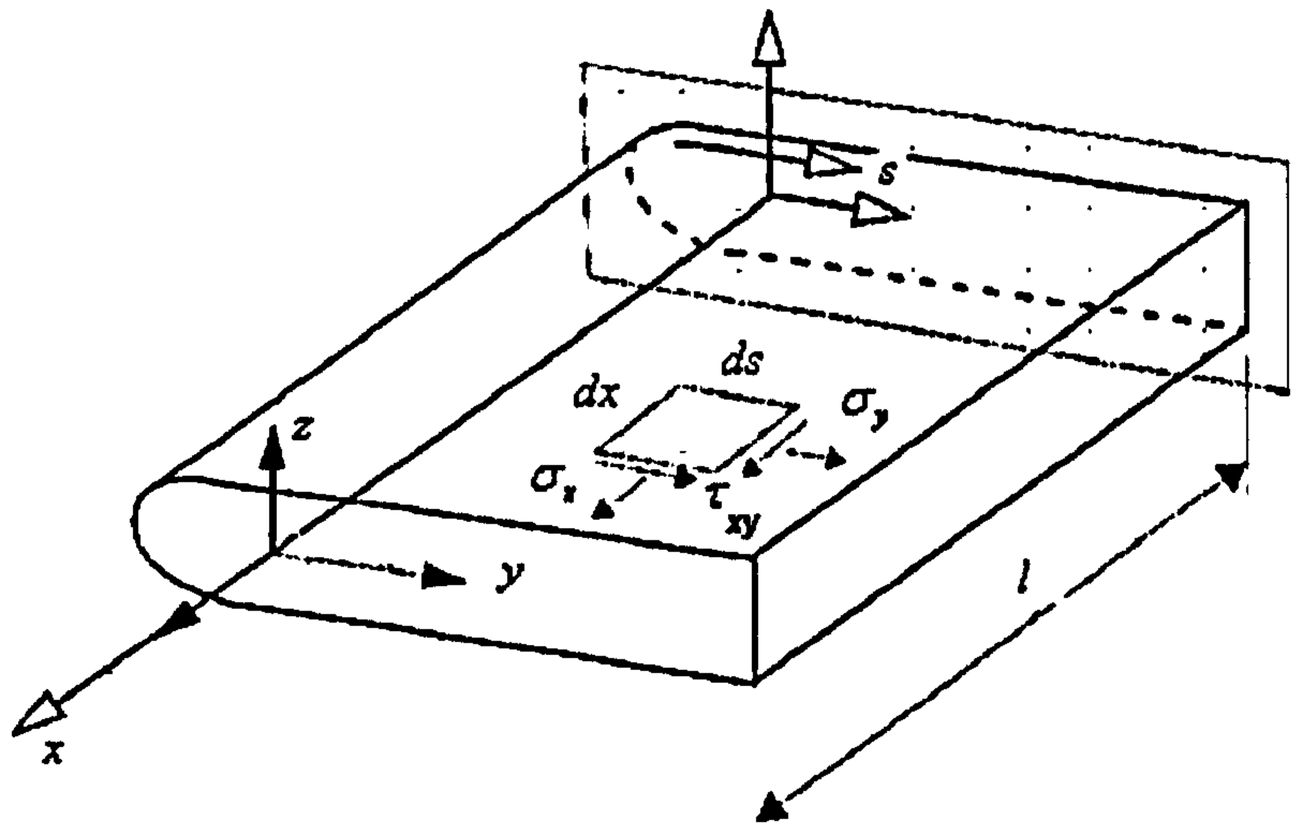

Figure 2.14: The stress formulation is founded on the equilibrium of an infinitesimal element.

Equilibrium is studied and global constitutive equations are written in matrix form at the end. Stiffness expressions are explicitly reported and explained in the paper.

This model presents a relatively high level of complexity; therefore its potential use in this research was deemed to be limited.

2.3.10 A comparison of the models in terms of *EI*, *GJ* and *K*

The models described in this Chapter have been compared in terms of stiffnesses *EI*, *GJ* and *K*, with the only exception being the formulation of Hwu and Tsai. It has not been included in this comparison because its level of accuracy is not sufficient, as already remarked upon in section 2.3.1. The comparison has been completed by adding the results of a FE model, which will be fully described in Chapter 3.

A rectangular cross-section (Figure 2.13) has been chosen to test the models. It is representative of a composite wing box. Its height is 0.3 m, whilst its chord is 0.6 m. The thicknesses of both horizontal and vertical walls are 0.006 m.

Elastic properties of one composite lamina are presented in Table 2.1.

Table 2.1: Elastic properties of the composite material.

E_1	181 GPa
E_2	10.3 GPa
G_{12}	4.55 GPa
ν_{12}	0.28

Vertical walls are kept orthotropic. They are built with one single layer with 0° fibres. Horizontal laminates are identical and built with one layer whose fibres orientation can vary from 0° to 90° with respect to the global frame of reference. Such geometry and properties have been chosen because it is possible to obtain bend-twist coupling. As previously remarked, this effect has been chosen in this thesis as a mechanism to show the potential benefits of aeroelastic tailoring.

A convergence analysis has been performed to find the optimal discretization of the FE model. A complete discussion can be found in Chapter 3. The mesh used for the analyses has been compared with a "high density" mesh, having 100% more elements. It has been observed that the results do not change. Results of the torsional stiffness *GJ* are as shown in Figure 2.15. Analogous results have obtained when studying also *EI* and *K*.

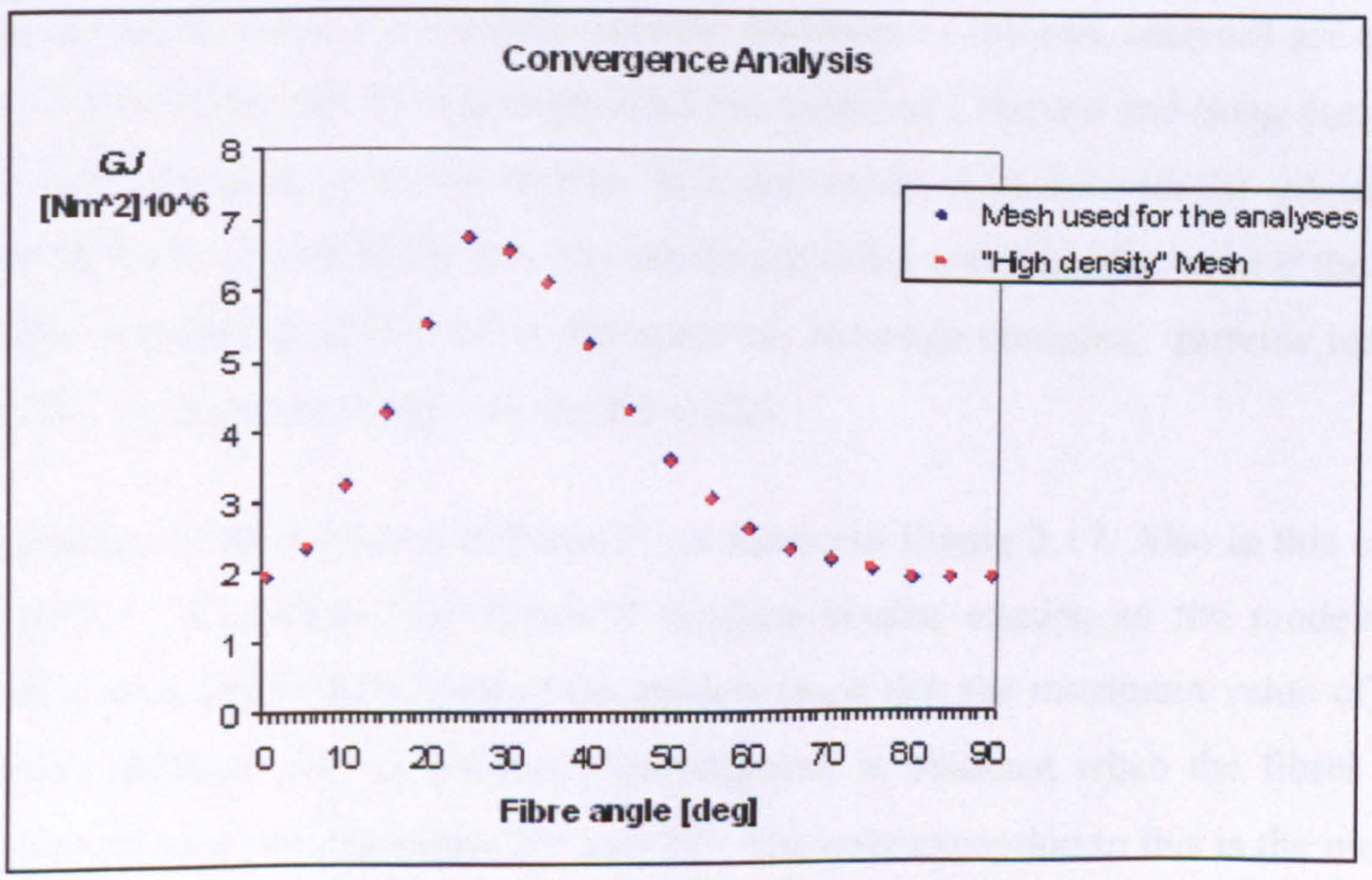

Figure 2.15: Convergence analysis.

A comparison of the bending stiffness *EI*, from various theories, is shown in Figure 2.16.

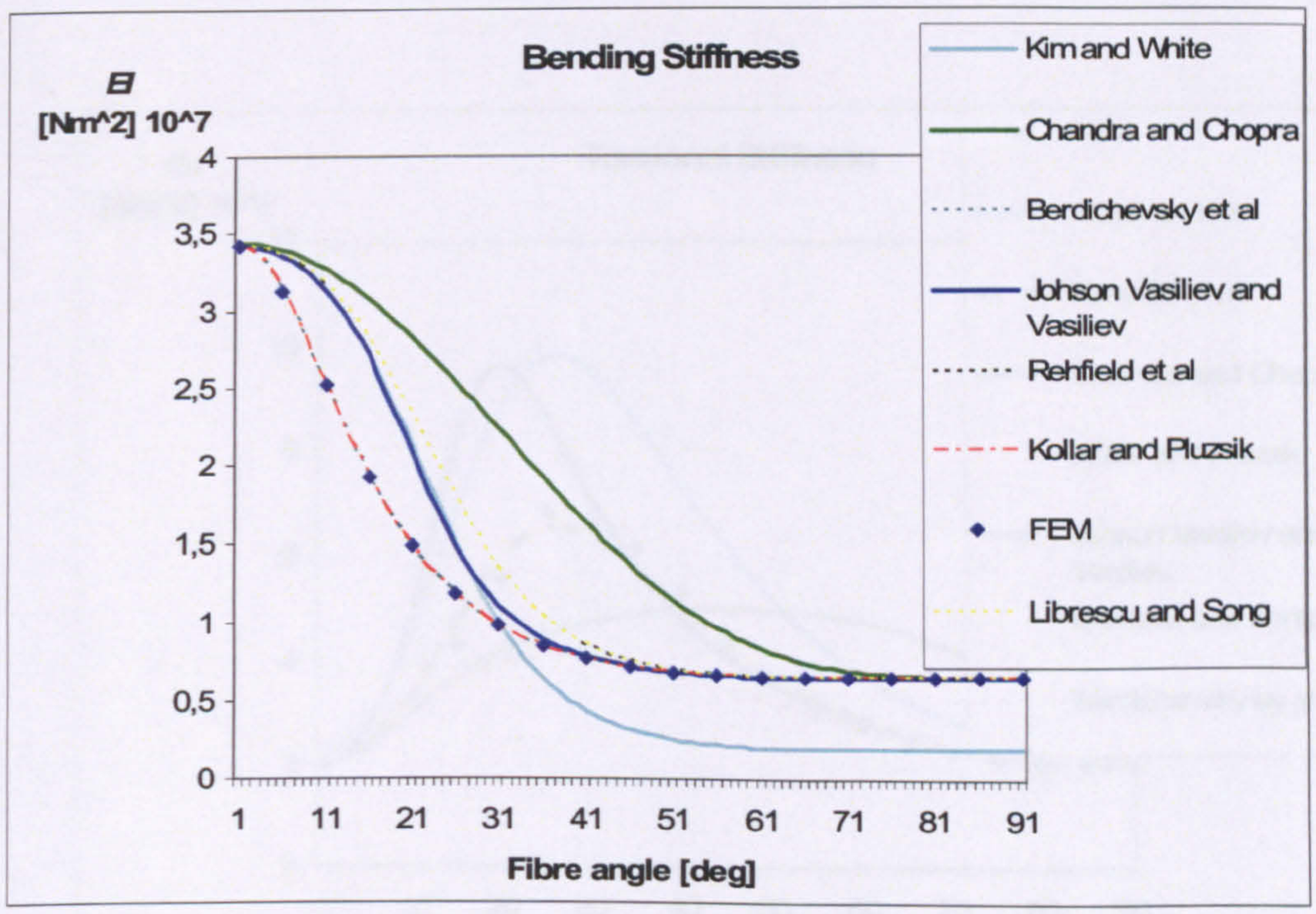

Figure 2.16: Comparison of the bending stiffness *EI*.

It is interesting to observe that the models of Librescu and Song and Rehfield et al. produce similar results. It happens because the walls of the box analysed are quite thin. Consequently, the 3D dependence of the model of Librescu and Song does not have significant impact on the results. Also the results obtained with the models of Berdicevsky et al. and Kollar and Pluzsik do not differ significantly, even if the two theories are quite different. Such formulations, although complex, provide results very close to those obtained with the FE model.

Comparison of the torsional stiffness *GJ* is shown in Figure 2.17. Also in this case, the models of Librescu and Rehfield produce similar results, so the models of Berdichevsky and Kollar. Most of the models show that the maximum value of the torsional stiffness, for the geometry investigated, is obtained when the fibres are placed with an angle ξ between 20° and 25°. The only exception to this is the model of Chandra and Chopra, which predicts the maximum value when the fibres are

orientated at 45 deg. Results of the FEM, for this geometry, are very close to those predicted by the models of Rehfield and Librescu.

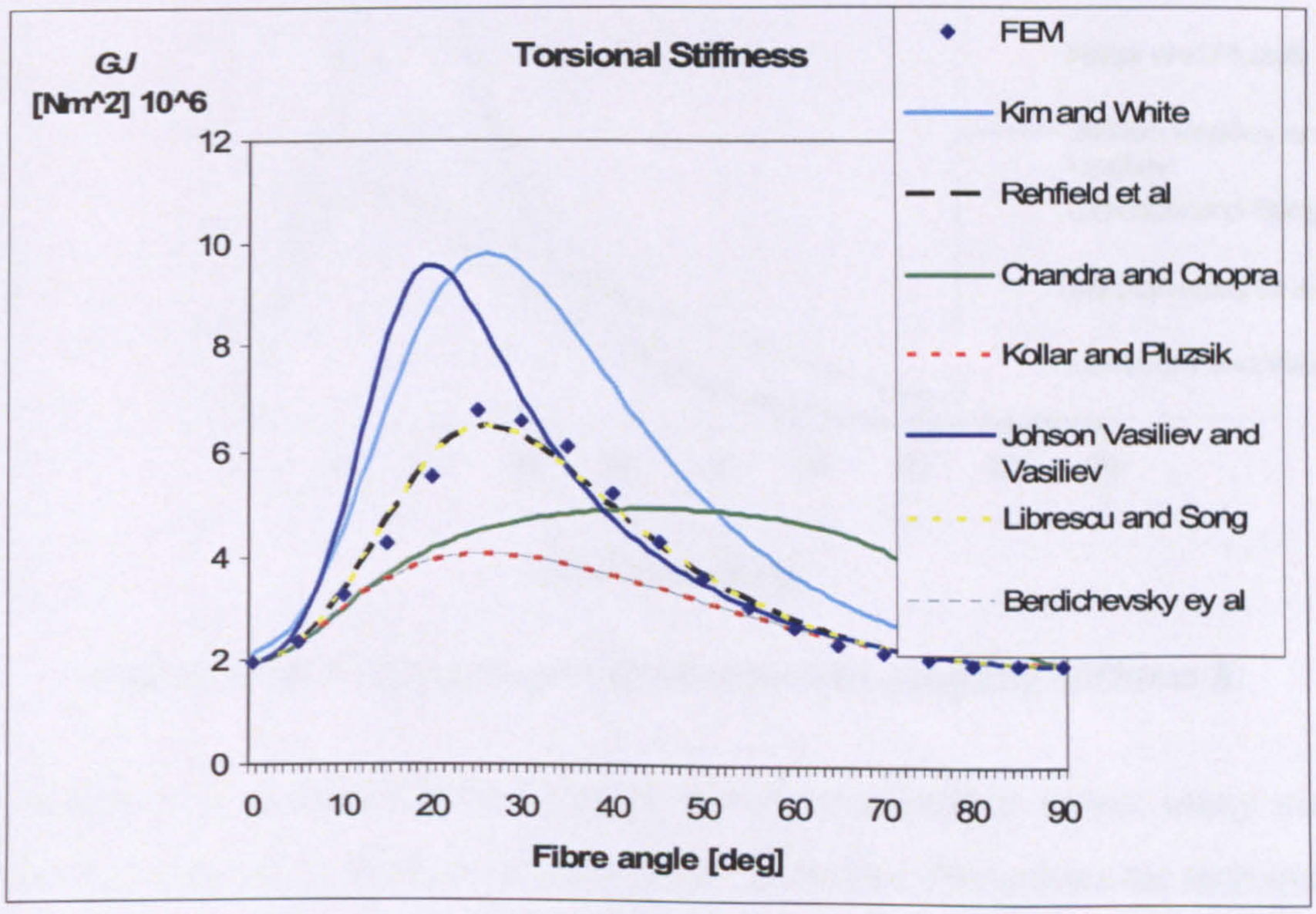

Figure 2.17: Comparison of the torsional stiffness *GJ*.

A comparison of the bend-twist coupling stiffness K is shown in Figure 2.18. The models of Librescu and Rehfield are identical. The models of Lemanski and Weaver, Berdichevsky and Kollar and Pluzsik give approximately the same results and they are in accordance to those obtained by using the FE approach.

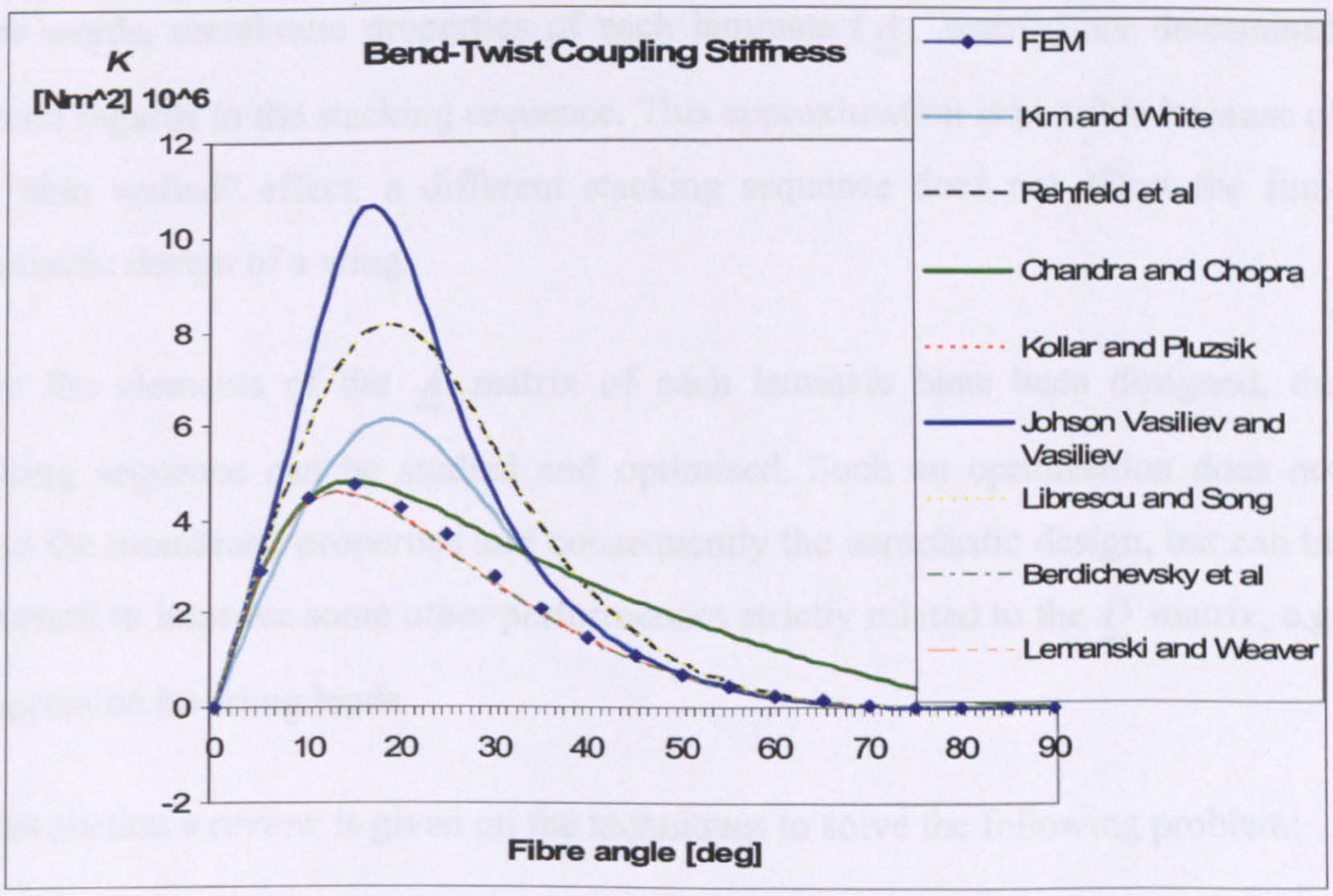

Figure 2.18: Comparison of the bend-twist coupling stiffness *K*.

The comparison proposed in this section shows an important result: many models have been proposed in the literature, but their collective predictions are ambiguous. While, for this geometry, the models of Kollar and Berdichevsky are able to produce good results for *EI* and *K* and incorrect results for *GJ*, the opposite can be affirmed for the models of Rehfield and Librescu. Moreover, a point of disadvantage for the models of Kollar and Berdichevsky is their complexity.

A simplified but precise model to evaluate the important stiffnesses of a composite box has been developed as part of this research. It will be presented in Chapter 3. Results for several geometries and lay-up configurations will be discussed and compared with the finite element model.

2.4 Combinatorial stacking sequence optimisation of composite laminates

In many practical applications, the design of composite laminates for aeroelastic purposes is performed in two steps. In the first one, volume fractions of different composite fibres are determined to optimise a particular aeroelastic performance. In

other words, membrane properties of each laminate ($\underline{\underline{A}}$ matrix) are determined without regards to the stacking sequence. This approximation is possible because of the "thin walled" effect: a different stacking sequence does not affect the final aeroelastic design of a wing.

Once the elements of the $\underline{\underline{A}}$ matrix of each laminate have been designed, the stacking sequence can be studied and optimised. Such an optimisation does not affect the membrane properties and consequently the aeroelastic design, but can be important to improve some other performances strictly related to the $\underline{\underline{D}}$ matrix, e.g. compression buckling loads.

In this section a review is given on the techniques to solve the following problem:

- To find the "optimum" stacking sequence of a laminate with fixed number of total layers and fixed number of layers with a specific orientation. As an example consider a laminate whose maximum number of layers is 80 where 20 layers must be oriented at 45°, 20 at 90° and 40 at 0°.

Some attempts to solve such problems with conventional gradient based methods have been performed [66, 67] in the past. The optimal ply angles obtained by these continuous optimisation methods were rounded to appropriate integer values that finally resulted in a non-optimal design. These results, together with the permutative and discrete nature of the problem, suggest that heuristic techniques may be more appropriate.

One of the most popular heuristic optimisation methods is the Genetic Algorithm: a guided random search technique working on a design population. This technique was inspired by Darwinian Evolution Theory. Among the papers presented in the literature [68-72], the work of Liu et al is particularly useful because the authors developed some "ad hoc" operators to make the algorithm suitable for a permutative problem. Their work is described as follows. It will be particularly

useful as a basis for comparison of results presented in Chapter 7, where a new optimisation technique developed as part of this thesis is presented.

2.4.1 Genetic Algorithms for permutative problems [72]

Each individual of the population represents a possible design, i.e. a stacking sequence. An example of an individual with 10 plies is shown in Figure 2.19. Fixed percentages of fibres must be respected; therefore the laminate is formed, in this example, by four 0° layers, two 90° layers and four 45° layers.

[45 /45 /0 /0 /90 / 45 /0 /0 /45 /90]

Figure 2.19: An example of stacking sequence.

The algorithm, as a standard GA, is based on four basic operations:

- Determination of an initial population of stacking sequences.
- Selection of parents among the best individuals of the population.
- Crossover: two parents generate children that will form the next generation.
- Mutation: after a fixed number of generations, a random element is modified.

The algorithm starts with an initial population of *n* randomly selected elements. The number of stacking sequences forming the initial population is an important parameter to tune. If its value is too high the CPU running time increases without an appreciable improvement of results. On the other hand, if the number of elements of the initial population is too low, the algorithm is not able to converge, i.e. there will be not any improvement in the population.

Once the initial population is selected, each element is evaluated by using a fitness function. The best individuals, in terms of fitness function, have more chance to survive and to transmit their genes to their children.

The procedure used to select the parents of the next generation is a simulated roulette wheel, with each element being assigned to a sector of the wheel with an

area proportional to its fitness. That is, with n elements having fitness values of F_i, with $i = 1, 2, ...n$, the *i-th* element gets a fraction r_i, of the wheel, where

$$r_i = \frac{F_i}{\sum_{j=1}^{n} F_j} \tag{2.16}$$

Within a computer code, the roulette wheel can be implemented by generating a random number a between 0 and 1, and then selecting the *i-th* design when

$$R_{i-1} \leq a < R_i \tag{2.17}$$

where $R_0 = 0$ and

$$R_i = \sum_{j=1}^{i} r_j \tag{2.18}$$

The following example clarifies the entire procedure. Imagine having an initial population formed by six elements, i.e. six different stacking sequences, whose fitness values are respectively:

$$[F_1, F_2, F_3, F_4, F_5, F_6] = [0.35 \;\; 0.60 \;\; 0.38 \;\; 0.55 \;\; 0.45 \;\; 0.15]$$

It implies (Eqn. 2.16) that the values of r_i are

$$r_i = \; [0.14 \; 0.24 \; 0.15 \; 0.22 \; 0.18 \; 0.07]$$

Values of coefficients R_i, boundaries of each part of the selection wheel, are calculated according to Eqn. 2.18. The following results are obtained:

$$[R_0, R_1, R_2, R_3, R_4, R_5, R_6] = [0 \;\; 0.14 \;\; 0.38 \;\; 0.53 \;\; 0.75 \;\; 0.93 \;\; 1]$$

Six random numbers are generated to select the best individual of the initial population. These six random numbers are gathered in the same vector denoted with the symbol a as follows:

$$a = [0.2825 \; 0.7123 \; 0.1560 \; 0.9217 \; 0.6120 \; 0.3471]$$

The first number $a(1)$ is 0.2825 and it is such that $R_1<a(1)<R_2$. Therefore, the second stacking sequence, corresponding to the fitness function F_2 is selected as a parent. Parents selected are therefore stacking sequences [2 4 2 5 4 2]. Design stacking sequence 2 is more successful because it shows the best value of fitness function.

Once pairs of parents are selected, the mating of the pairs involves a random process called crossover. The simplest crossover used in the standard genetic algorithms [21] (single point crossover) begins by generating a random integer b between 1 and l-1, where l is the string length. This number defines a cut-off point in each of the two strings and separates each into two substrings. To be more precise parent 1 will be cut at point b. Parent 2 will be cut at the point l-b. The right segment of parent 1 becomes the left segment of child 2 and the left segment of parent 2 becomes the right segment of child 1. An example is given in Figure 2.20. The cut-off point is $b = 3$.

Parent 1
[0\90\45\0\0\90\45\0\45\45],

Parent 2
[0\0\0\90\45\45\45\0\45\90],

Random cut off number selected is $b=3$

Parent 1 is broken as follows
[0\90\45\0\0\90\45] and [0\45\45]

Parent 2 is broken as follows
[0\0\0] and [90\45\45\45\0\45\90]

Children are consequently

Child 1
[90\45\45\45\0\45\90\0\45\45],

Child 2
[0\0\0\0\90\45\0\0\90\45],

Figure 2.20: An example of single point crossover.

Child 1 and Child 2 are not able to respect the established fixed percentage of fibre angles, consequently, they are not suitable for combinatorial optimisation. Child 2,

for example, has got six layers oriented at 0 degrees instead of four. This kind of crossover, widely used for standard algorithms, cannot be used for stacking sequence optimisation of panels with fixed thickness and fixed percentage of orientations.

A different crossover must be considered for these kinds of problems, as suggested by Liu et al [72]. It is called gene-rank crossover. It is based on the imitation of the process used to average the rankings that two judges give to a group of contestants. Each laminate can be viewed as a ranking of the set of plies forming the laminate itself, and gene-rank crossover averages two rankings (parents) to generate a new vector (child).

Consider the simple case with three elements [45 0 90]. The first judge denotes them as 45-first, 0-second, 90-thrird, in short-hand [45 0 90]. The second judge ranks them as 45-second, 0-third, 90-first, or [90 45 0]. Two weights W_1 and W_2 can be associated to each ranking, representing the respective influence of the judges $W_1+W_2=1$. In a computer program, they are implemented as two uniformly distributed random numbers in the interval [0, 1]. The final ranking is then obtained by summing the weighted rank of each individual:

45	W_1*1+W_2*2
0	W_1*2+W_2*3
90	W_1*3+W_2*1

If, for example $W_1 = 0.4$ and $W_2=0.6$, the following values are obtained for the vector above [1.6, 2.6, 1.8], corresponding to the final ranking of [45 90 0].

There is a fundamental difference between the single-point crossover and a gene-rank one. In the first algorithm, two parents generate two children. In the second one, two parents generate only one child. It means that each parent must mate twice to keep constant the dimension of the population. All the strings selected to reproduce must mate with other two elements of the population that are randomly selected.

Once a new generation is born, the selection process is repeated as well as the gene-rank crossover. The algorithm stops when both the following conditions are reached:

- A fixed number of generation must be examined
- The average fitness of the generation *i* is lower than the average fitness of the generation *i-1*. It means that the population is not improving further.

After a given number of iterations, a standard permutation can be also introduced in the procedure. This permutation has the same role as a mutation in a standard GA.

Genetic Algorithms often give good results, but their primary limitation is the increased number of iterations that are performed.

2.4.2 PSO and ACO

Good results can be obtained with two other heuristic techniques: Particle Swarm Optimisation (PSO) and Ant Colony Optimisation (ACO).

Particle swarm optimization [73] is a stochastic, population-based computer algorithm. It is a type of swarm intelligence based on social principles and social learning that enables a person to maintain cognitive consistency. People solve problems by talking with other people about them, and as they interact their beliefs, attitudes, and behaviours change. The changes could, typically, be depicted as the individuals move towards one another in a socio-cognitive space. PSO simulates this kind of social optimisation. For a given problem a fitness function is defined. In our case, it is either the natural frequency of a plate [74], or the compressive buckling load. A communication structure or social network is also defined, assigning neighbours for each individual to interact with. Then a population of individuals defined as random guesses for the problem solutions is initialized. These individuals are candidate solutions. They are also known as the particles, hence the name particle swarm. An iterative process, to improve these candidate solutions, is

set in motion. The particles iteratively evaluate the fitness of the candidate solutions and remember the location where they had their best success. The individual's best solution is called the particle best or the local best. Each particle makes this information available to their neighbours. They are also able to see where their neighbours have had success. Movements through the search space are guided by these successes, with the population usually converging, by the end of a trial, on a problem solution better than that of non-swarm approach using the same methods.

The swarm is typically modelled by particles in multidimensional space that have a position and a velocity. These particles fly through hyperspace and have two essential reasoning capabilities: their memory of their own best position and knowledge of the global or their neighbourhood's best. In an optimization problem, problems are formulated so that "best" simply means the position with the greatest objective value. Members of a swarm communicate good positions to each other and adjust their own position and velocity based on these good positions.

As the swarm iterates, the fitness of the global best solution improves (decreases for minimization problem). It is possible that all particles, being influenced by the global best, eventually approach the global best, and a converged solution is found.

Suresh et al [75], use particle swarm intelligence in multi-objective constrained optimisation: their goal is the maximization of bend-twist coupling stiffness of a composite box beam, while maintaining almost the same values of bending stiffness and torsional stiffness required by the design. The design variable vector used has the following form:

$$DV = [H \quad C \quad \xi_1 \quad \xi_2 \quad \xi_3 \quad . \quad . \quad \xi_n]$$

where

H is the height of the wing box

C is the chord of the wing box

ξ_i is the *i*-th ply orientation on *n* plies. The number of plies is fixed a priori. The number of layers with a specific discrete orientation is not fixed. However, this constraint can be easily added.

Suresh et al claim better performances and CPU running time compared to standard genetic algorithms.

ACO [76] appears to be even more suitable for problems of combinatorial optimisation. In the real world, ants (initially) wander randomly, and upon finding food return to their colony while laying down pheromone trails. If other ants find such a path, they are likely not to keep travelling at random, but to instead follow the trail, returning and reinforcing it if they eventually find food. With increased time, however, the pheromone trail starts to evaporate, thus reducing its attractive strength. The more time it takes for an ant to travel down the path and back again, the more time the pheromones have to evaporate. A short path, by comparison, gets marched over faster, and thus the pheromone density remains high as it is laid on the path as fast as it can evaporate. Pheromone evaporation has also the advantage of avoiding convergence to a locally optimal solution. If there were no evaporation at all, the paths chosen by the first ants would tend to be excessively attractive to the following ones. In that case, the exploration of the solution space would be constrained. Thus, when one ant finds a good (i.e., short) path from the colony to a food source, other ants are more likely to follow that path, and positive feedback eventually leads all the ants following a single path.

The idea of the ant colony algorithm is to mimic this behaviour with "simulated ants" walking around the graph representing the problem to solve.

Aymeric and Serra [77] applied ACO to find the optimum stacking sequence to maximize the compression buckling load of a simply supported composite plate with fixed thickness. A strength constraint was also included. If the number of possible ply orientations (for example 0, +45, -45 and 90 degrees) that can be used in the laminate is denoted with *m* and the number of layers is denoted with *n*, a

matrix $\underline{\underline{RT}}$ (routing table) n times m is prepared. The element i-j of this matrix contains the probability that the i-th layer is occupied by the j-th ply angle orientation.

At the beginning of analysis, this matrix is initialized with the same value in each position. An initial random laminate is selected and its fitness function evaluated. During each iteration the generic element of the routing table is updated as follows:

$$RT_{ij} = \frac{ph_{ij}}{\sum_{m} ph_{ij}} \tag{2.19}$$

where ph_{ij} is the pheromone trail associated to the j-th orientation in the i-th layer. Its value is related to the fitness function. A new candidate solution is then constructed by randomly choosing the j-th orientation for the i-th position according to the probabilities of the routing table. At the end of the assembly phase, pheromone evaporation is simulated by means of a linear relation step dependent.

In the work of Aymeric and Serra, the amount of pheromone deposited ph_{ij} is directly proportional to the fitness function: the compression buckling critical load. The authors chose to follow an elitist strategy: pheromone values are updated only when the solution generated in the current iteration is better or equal to the best solutions found since the start of the search. The pheromone evaporation, however, is always carried out, at any step. It is worth noting that such a pheromone reinforcement mechanism induces a strong exploitation of the past search experience. The inspection process thus becomes heavily guided towards regions of the solution space characterized by components contained in high quality solutions found during the previous explorations. This effect, while usually improving algorithm performance, may however limit the exploration of the less promising regions of the domain.

Aymeric and Serra claim that ACO obtains the same performances as a GA in terms of stacking sequences, but it requires less CPU running time to converge. Also other authors claim excellent results obtained by using Ant Colony for stacking sequence

optimisation. Manan et al [78], for example, have used this technique to optimise flutter and divergence speed of a composite laminate. Stacking sequences obtained with ACO give better average results than GA and PSO.

2.4.3 Some considerations on the heuristic techniques

Heuristic techniques are often used in industry because they are able to produce good results and because of their relative simplicity. From the optimisation point of view one of the main advantages of evolutionary techniques is that they do not have much mathematical requirements. They are 0-order methods: all they need is the evaluation of an objective function. Beside the advantages, heuristic techniques such as GA and ACO already shown have three basic limitations [79]:

1. They often provide "practical solutions", but it is difficult to obtain the global optimum. This is exactly the same limitation often attributed to gradient based techniques.
2. They are computational expensive. In other words, they may require several iterations to obtain the result.
3. It is difficult to use them with constraints.

Considering all the reasons reported above, a new deterministic technique will be proposed in Chapter 7.

2.5 Conclusions

Contributions to aeroelastic tailoring previously presented in the literature have been discussed and commented upon in this Chapter. Particular attention has been given to passive actuation mechanisms, obtained by means of structural couplings.

A literature survey has also been performed for composite beams analytical models and stacking sequence combinatorial optimisation of plates.

Concerning analytical models, several theories have been reviewed and compared. Particular attention has been dedicated to the global constitutive equations and to the formulation of the relevant stiffnesses for aeroelastic tailoring: *EI*, *GJ* and *K*.
Concerning the combinatorial problems, the literature on the optimisation techniques of plates with fixed thickness and fixed number of plies with a specific orientation has been reviewed.

In the following chapters, the novel work developed in this thesis will be discussed.

Chapter 3
The analytical model to evaluate the fundamental stiffnesses for aeroelastic analyses

3.1 Introduction

The aeroelastic tools described in the following chapters include a structural model in order to evaluate the deformations. A beam model has been used. This approach has proven itself to be effective in a variety of engineering applications. In aeroelastic studies, beam models have been used to reveal important trends and generally, rectangular cross sections have been used to model wing boxes [56, 80].

Accurate values of stiffnesses are required as input to the structural model for aeroelastic analysis. In order to obtain appropriate deformations, the evaluation of *EI, GJ* and *K* must be as accurate as possible. However, a correct evaluation of the stiffnesses of a composite beam is not a trivial problem: a fact confirmed by the number of different formulations presented in the literature. Such models often show a lack of precision when cross sections with different geometries and unbalanced lay-ups are analysed. The effect of anisotropy can render current methods inaccurate for specific geometries.

In this chapter, a simplified and precise model is proposed to evaluate bending and torsional stiffnesses of a prismatic, anisotropic, thin-walled symmetrical box, whose vertical walls are orthotropic. Bending and torsional stiffnesses are derived by using physical reasoning and validated with respect to finite element analysis. Stiffnesses *EI* and *GJ* are, in other words, calculated by exploiting their mathematical definition. They represent, in fact, bending and twisting moment obtained in a cross section when unitary bending and torsional deformation are respectively applied.

Numerical results are commented upon and compared with other models presented in the literature. Good accuracy has been obtained for structures with different geometries and lay-ups. No other model, to the knowledge of the author, is able to provide the same level accuracy for the structure analysed being, at the same time, simple and easy to translate into a computer code.

3.2 Evaluation of bend-twist coupling stiffness *K*

A prismatic thin-walled box is shown in Figure 3.1. Its global coordinate system is the same used for all other model presented in this thesis and it is shown in Fig. 3.2. It is denoted by *X, Y, Z*, and it is located in the geometrical centre of the cross section, denoted by *O*.

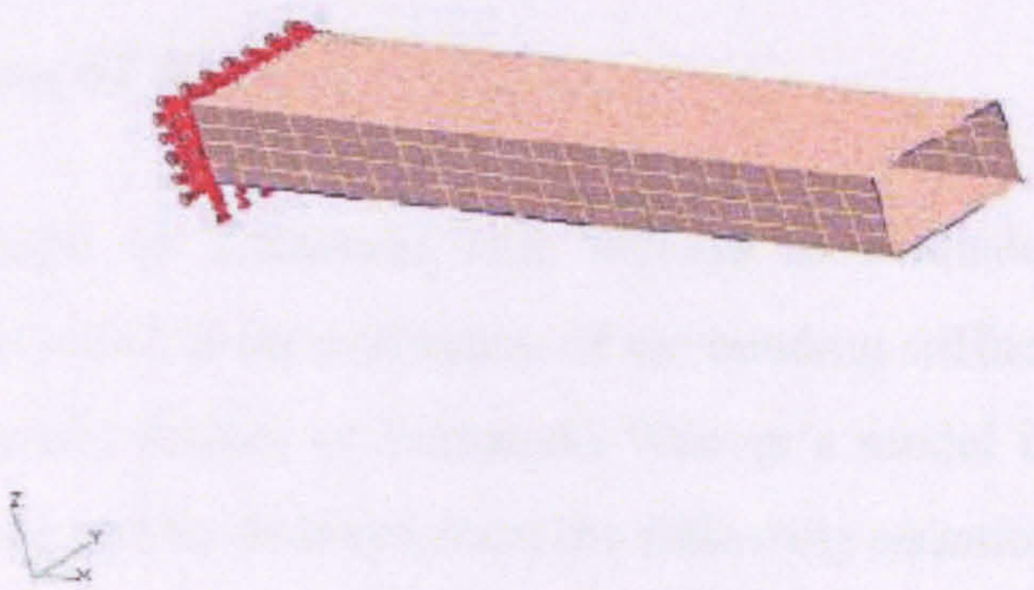

Figure 3.1: An example of prismatic thin-walled composite box.

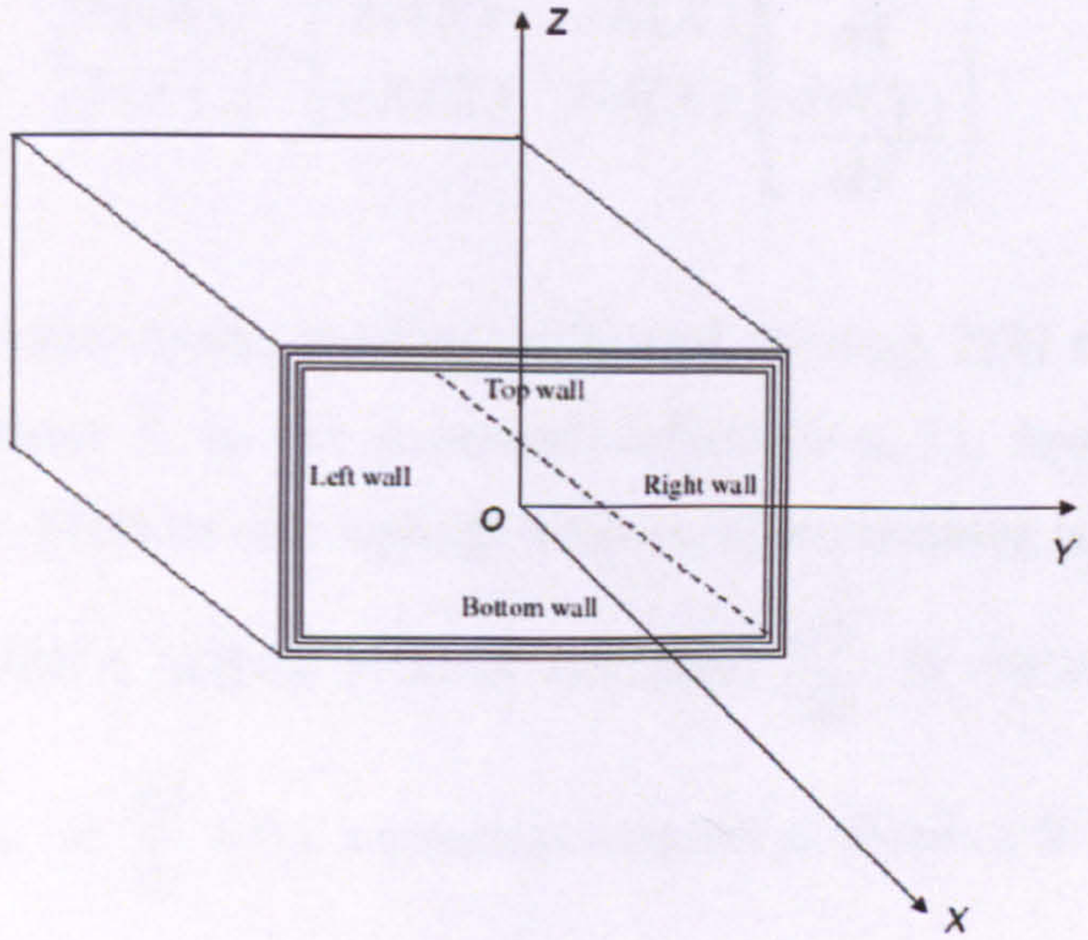

Figure 3.2: The global frame *X, Y, Z* of the box.

Concerning bend-twist coupling stiffness, *K*, the analytical predictions of Lemanski and Weaver are relatively accurate, simple and based on physical reasoning. Their results have been investigated and reproduced as part of this work. An example is

shown in section 3.5. No further discussion on the stiffness K is therefore needed. The same cannot be said for bending and torsional stiffnesses, as formulae presented in the literature are not able to provide sufficient accuracy when cross sections of different geometries and lay-ups are analysed. Therefore, a model able to predict accurate results is required. The approach used by Lemanski and Weaver[18] to calculate K is extended to evaluate the bending stiffness EI of a symmetric composite thin-walled box. A new analytical formula is also proposed to evaluate GJ.

3.3 Evaluation of *EI*

The strategy used by Lemanski and Weaver to evaluate bend-twist coupling stiffness K is extended to the evaluation of the bending stiffness EI.

The most important feature of Lemanski-Weaver's model is the definition of the stiffness K, which can be deduced form the following equation (Eqn. 3.1).

$$\begin{bmatrix} M(X) \\ T(X) \end{bmatrix} = \begin{bmatrix} EI(X) & -K(X) \\ -K(X) & GJ(X) \end{bmatrix} \begin{bmatrix} \dfrac{d\varphi(X)}{dX} \\ \dfrac{d\theta(X)}{dX} \end{bmatrix} \tag{3.1}$$

It relates the internal loads, bending $M(X)$ and twisting $T(X)$ moments along the spanwise coordinate X, to the structural deformation, i.e. bending angle φ and twisting angle θ. Bend twist coupling stiffness is the twisting moment arising in a cross section when a unitary bending curvature $\frac{d\varphi}{dx}$ is applied. When $\frac{d\varphi}{dx}=1$, (without twisting, i.e. $\frac{d\vartheta}{dx}=0$), a torsional moment is obtained from Eqn. 3.1 as:

$$T = -K\frac{d\varphi}{dx} \tag{3.2}$$

The numerical value of the stiffness therefore coincides with the twisting moment arising in the walls of the cross section. Similar reasoning can be used to evaluate

EI: as the bending moment arising in the cross section when the same unitary bending deformation is applied.

Consider a hollow box shown in Fig. 3.3. The box is symmetrical, such that the top and bottom laminates are identical. It is noted that the vertical walls are made from balanced laminates, as unbalanced laminates here do not induce bend-twist coupling of the box. it's the geometrical characteristics are denoted by:

C	is the length of the horizontal wall
H	is the length of the vertical wall
t_v	is the thickness of the vertical wall
t_h	is the thickness of the horizontal wall

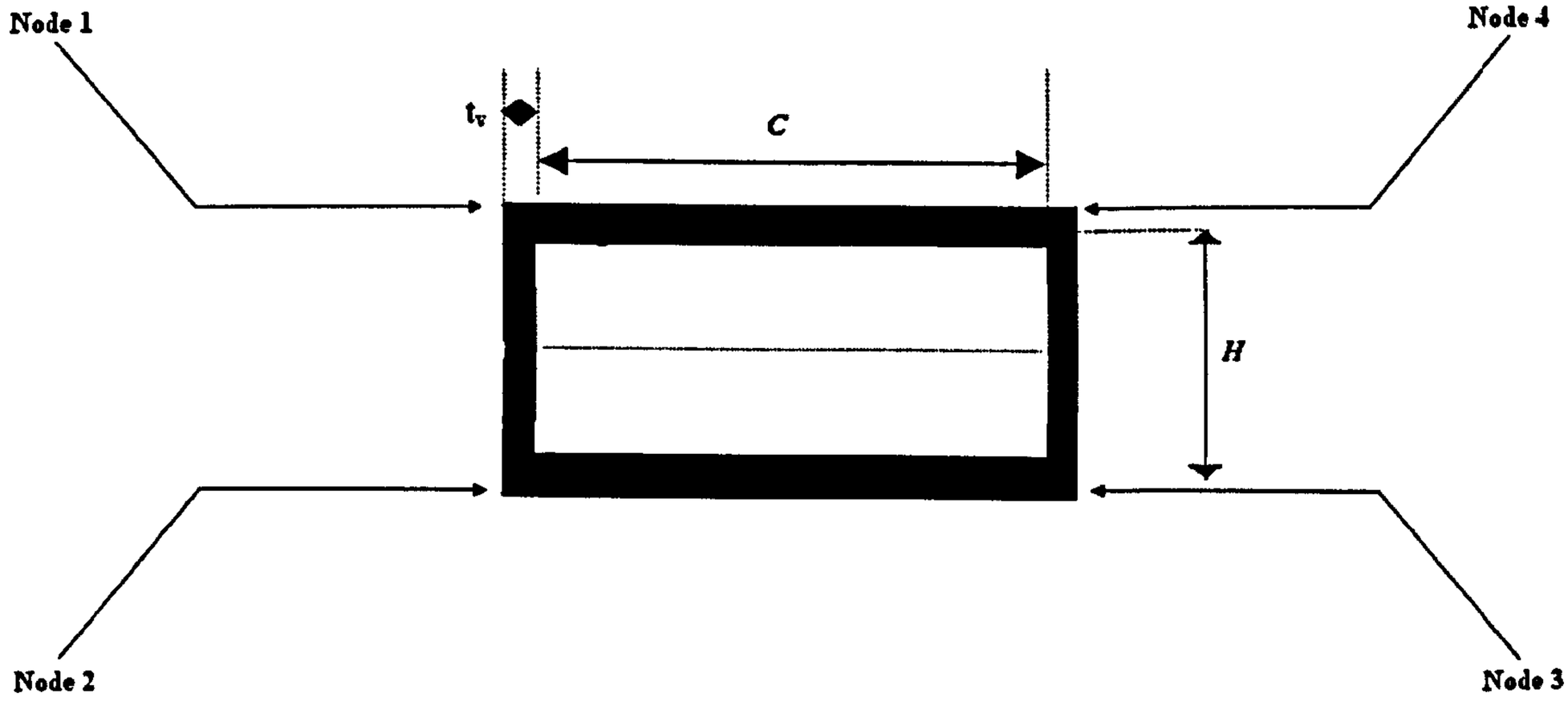

Figure 3.3: Geometric characteristics of a box cross section.

Firstly, a unitary bending deformation $\frac{d\varphi}{dx} = 1$ is applied. On the top wall of the box, if the material is orthotropic and the stiffness of vertical walls negligible, strains are given by

$$\begin{aligned} \varepsilon_x &= \frac{d\varphi}{dx}\frac{H}{2} = \frac{H}{2} \\ \varepsilon_y &= -\nu_{xy}\varepsilon_x \\ \gamma_{xy} &= 0 \end{aligned} \tag{3.3}$$

where

ε_x axial strain

ε_y transversal strain

γ_{xy} shear strain

ν_{xy} major Poisson's ratio of composite laminate

The strains of Eqn. 3.3 are written with respect to the local coordinates x, y of the laminate, shown in Fig. 3.4.

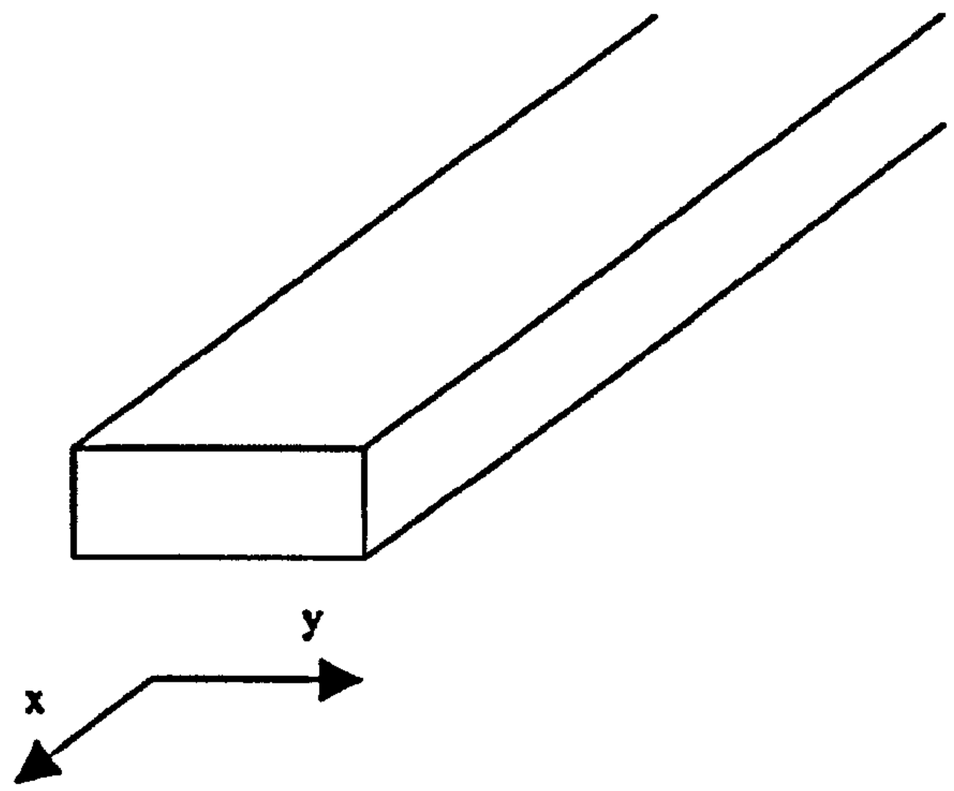

Figure 3.4: Local coordinates x, y in a laminate wall.

Forces per unit of length corresponding to these strains are:

N_x axial force per unit length of horizontal laminate

N_y lateral forces per unit length of horizontal laminate

N_{xy} shear force per unit length of horizontal laminate

and are evaluated by using Classical Lamination Theory [81]. As the box is made of laminated composite materials and the presence of vertical walls constrains the deformation of horizontal laminate, the strain field (Eqn. 3.3) requires modification. Two corrective terms Δ_1 and Δ_2 are added for the following reasons:

1 Lateral deformation ε_y of the horizontal laminate is constrained by the vertical walls and depends not only on the characteristics of the laminate itself but also on the elastic properties of the vertical walls.

2 Shear deformation γ_{xy} of the laminate exists; otherwise no bend/twist coupling effect could be measured.

The strain field of the horizontal laminate is re-written as

$$\varepsilon_x = \frac{H}{2}$$

$$\varepsilon_y = -\nu_{xy}\varepsilon_x + \Delta_1 = -\frac{A_{12}}{A_{22}}\varepsilon_x + \Delta_1 \tag{3.4}$$

$$\gamma_{xy} = \Delta_2$$

where A_{ij} is the membrane stiffnesses of the top laminate. The terms Δ_1 and Δ_2 are unknown. Two algebraic equations are needed to determine them. The first equation can be written evaluating displacement δ of Node 1, shown in Figure 3.5.

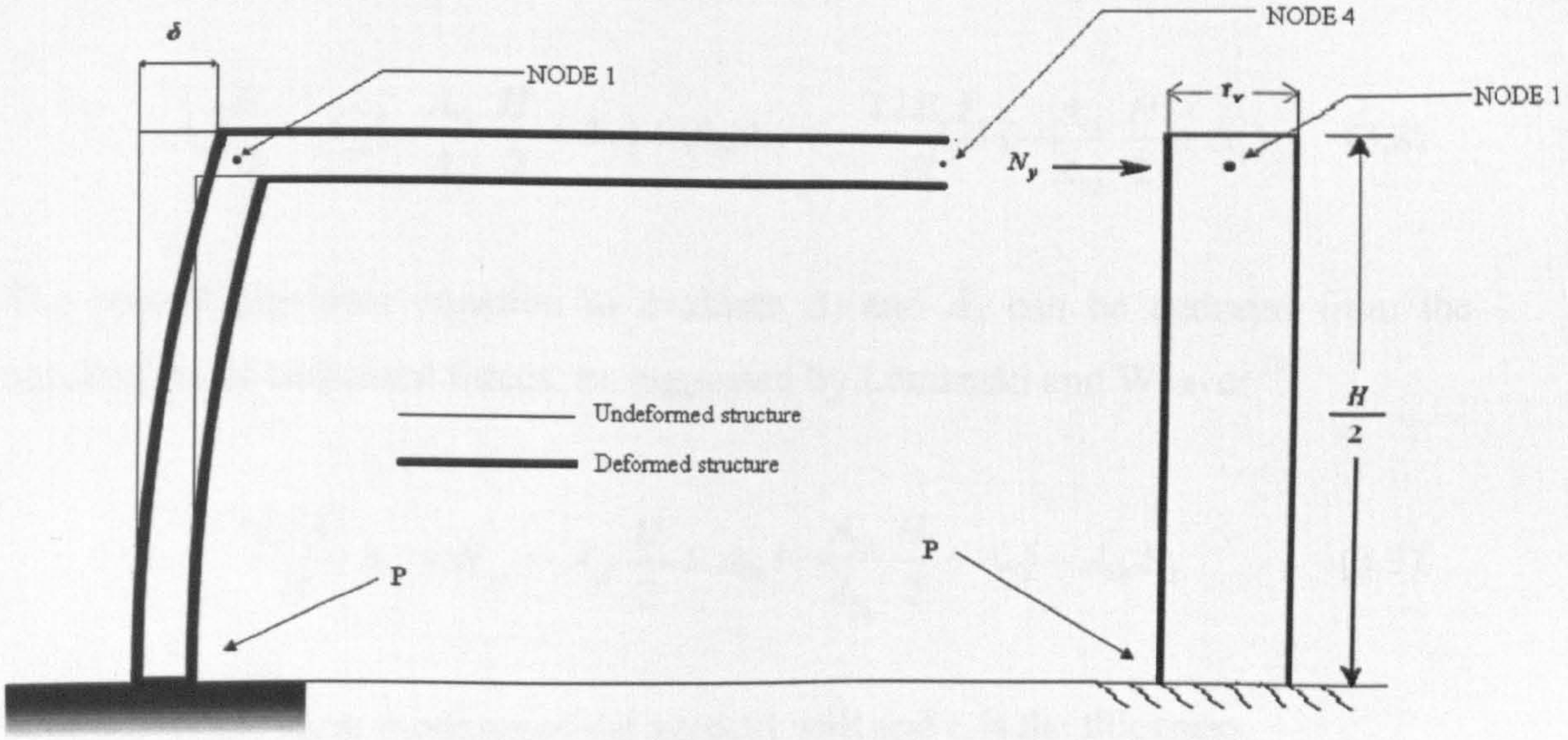

Figure 3.5: Displacement δ of Node 1. It is a local horizontal displacement of the top laminate and a local vertical displacement of the vertical wall, whose idealisation is shown on the right part of the figure.

Node 1 can be thought as a part of the horizontal laminate. Therefore, as the box is symmetric, the following equation can be written

$$2\delta = -\varepsilon_y C = \frac{A_{12}}{A_{22}}\frac{H}{2}C - \Delta_1 C \tag{3.5}$$

On the other hand, Node 1 is also part of the vertical wall. Its deflection can be calculated by modelling half of the vertical wall as a cantilevered beam, as shown in Fig. 3.5. Rotations and displacements of the middle point of vertical walls (point *P* of Figure 3.5) are assumed to be zero [18]. Displacement, δ, is therefore that of a cantilever beam:

$$\delta = -\frac{N_y H^3 C}{24 E_v I_v} \tag{3.6}$$

where N_y is found directly from Classical Lamination Theory,

$$N_y = A_{12}\varepsilon_x + A_{22}\varepsilon_y + A_{26}\gamma_{xy} \tag{3.7}$$

and $E_v I_v$ is the bending stiffness of the vertical walls.

If Eqn. 3.7 is substituted in to Eqn. 3.6 and combined with Eqn. 3.5, then:

$$A_{12}\frac{H}{2} + A_{22}(-\frac{A_{12}}{A_{22}}\frac{H}{2} + \Delta_1) + A_{26}\Delta_2 = -\frac{12 E_v I_v}{H^3}(-\frac{A_{12}}{A_{22}}\frac{H}{2} + \Delta_1) \tag{3.8}$$

The second algebraic equation to evaluate Δ_1 and Δ_2 can be deduced from the equilibrium of tangential forces, as suggested by Lemanski and Weaver [18]:

$$\frac{G_v t_v C}{H}\Delta_2 = N_{xy} = A_{16}\frac{H}{2} + A_{26}(-\frac{A_{12}}{A_{22}}\frac{H}{2} + \Delta_1) + A_{66}\Delta_2 \tag{3.9}$$

where G_v is the shear modulus of the vertical wall and t_v is the thickness.

An algebraic system comprising two equations (Eqns. 3.8-3.9) in two unknowns Δ_1 and Δ_2 is obtained and is readily solved. Once Δ_1 and Δ_2 are calculated, they are substituted in to Eqn. 3.4. and the strain field of the top laminate is completely defined.

Concerning vertical walls, their local coordinates system x_v, y_v is shown in Fig. 3.6.

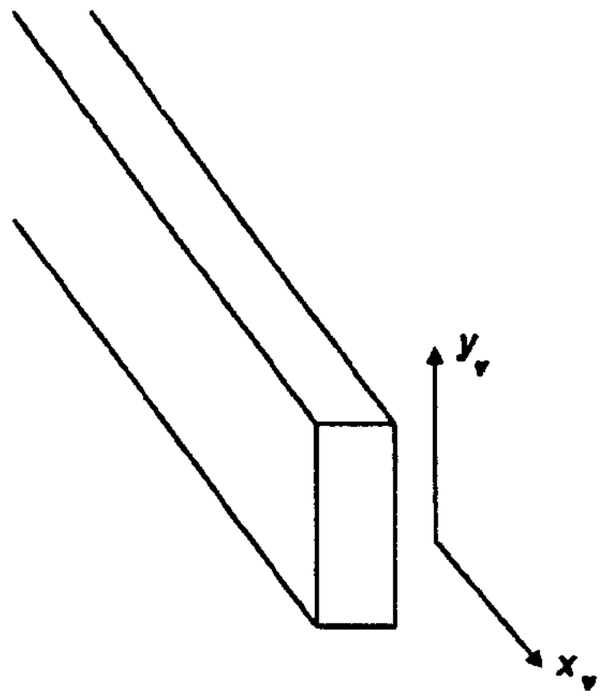

Figure 3.6: Local coordinates of vertical walls.

Consequently, x_v and x, are coincident and they have the same direction as the global axis X. Forces per unit of length of vertical walls are

N_{xv} is the axial force per unit length.

N_{yv} is the lateral force per unit length

N_{xyv} is the shear force per unit length

while corresponding strains are

ε_{xv} is the axial strain

ε_{yv} is the lateral strain

γ_{xyv} is the shear deformation

As EI is the bending moment arising in the cross section when a unitary bending curvature is applied, it can be calculated as the bending moment with respect to the global Y axis,

$$EI = \oint \overline{N}_x Z d\overline{C} \tag{3.10}$$

where

$d\overline{C}$ is the infinitesimal element of the contour

$\overline{N}_x$ is the axial force per unit length in the global reference. It includes contributions from both N_x and N_{xv}.

Eqn. 3.10 can be divided into two components, those from the horizontal and those from vertical walls. The contribution from the top and bottom laminates is:

$$EI_{hozizontal} = N_x CH \tag{3.11}$$

where

$$N_x = A_{11}\varepsilon_x + A_{12}\varepsilon_y + A_{16}\gamma_{xy} \tag{3.12}$$

and the strains of Eqn. 3.12 are found from Eqn. 3.4. Now consider half of the vertical wall to evaluate the second component. The strain ε_{xv}, for simple bending, is a linear function of the global coordinate Z:

$$\varepsilon_{xv} = Z \quad \text{with } 0 \le Z \le \frac{H}{2} \tag{3.13}$$

Consequently, the contribution of the vertical walls to the bending stiffness can be assumed to be:

$$EI_{vertical} = 4\int_0^{H/2} E_v t_v Z^2 dZ = \frac{1}{6} E_v t_v H^3 \tag{3.14}$$

where t_v is the thickness of vertical walls. The final expression of bending stiffness EI is:

$$EI = N_x CH + \frac{1}{6} E_v t_v H^3 \tag{3.15}$$

3.4 Evaluation of torsional stiffness *GJ*

In this section, a model to predict the torsional stiffness GJ is presented. This model gives good results for several wall length ratios and different lay-ups.

The starting point is the formula developed by Librescu and Song [13]. It has been chosen among several formulations because it shows two good characteristics:

- It is quite accurate, especially if compared to the other models investigated.
- Its formulation is relatively straightforward. Other models, such as that due to Kollar and Pluzsik [16, 17] or Berdichevsky [15] et al, for example, contain more information and are more involved to implement.

The initial formula proposed by Librescu and Song can be re-arranged as follows:

$$GJ = f(H,C)\Omega\left[HA_{66}^{v} + C\left(A_{66} - \frac{A_{26}^2}{A_{22}}\right)\right] \tag{3.16}$$

where

A_{ij}^{v} are the terms of the membrane matrix of the orthotropic vertical wall

Ω is the area enclosed by the contour of the cross section

$$f(H,C) = \frac{4\Omega}{(H+C)^2}$$

There are two contributions to the torsional stiffness:

- the contribution given by the vertical walls:

$$GJ_{vertical} = f(H,C)\Omega HA_{66}^{v}$$

- the contribution given by the top and bottom laminates:

$$GJ_{horizontal} = f(H,C)\Omega C\left(A_{66} - \frac{A_{26}^2}{A_{22}}\right)$$

Using Lemanski and Weaver's approach, the stiffness GJ can be thought as the twisting moment arising in a cross section when a unitary twisting curvature is applied. The forces per unit of length arising on the vertical and horizontal walls are derived from Eqn.3.16, as

$$N_{xyv} = f(H,C)HA_{66}^{v}$$
$$N_{xy} = f(H,C)C\left(A_{66} - \frac{A_{26}^2}{A_{66}}\right) \tag{3.17}$$

These forces per unit length are usually not equal and they are constant along the walls. This fact implies a discontinuity of the tangential forces per unit of length at the corners of the cross sections, as shown in the example of Figure 3.7.

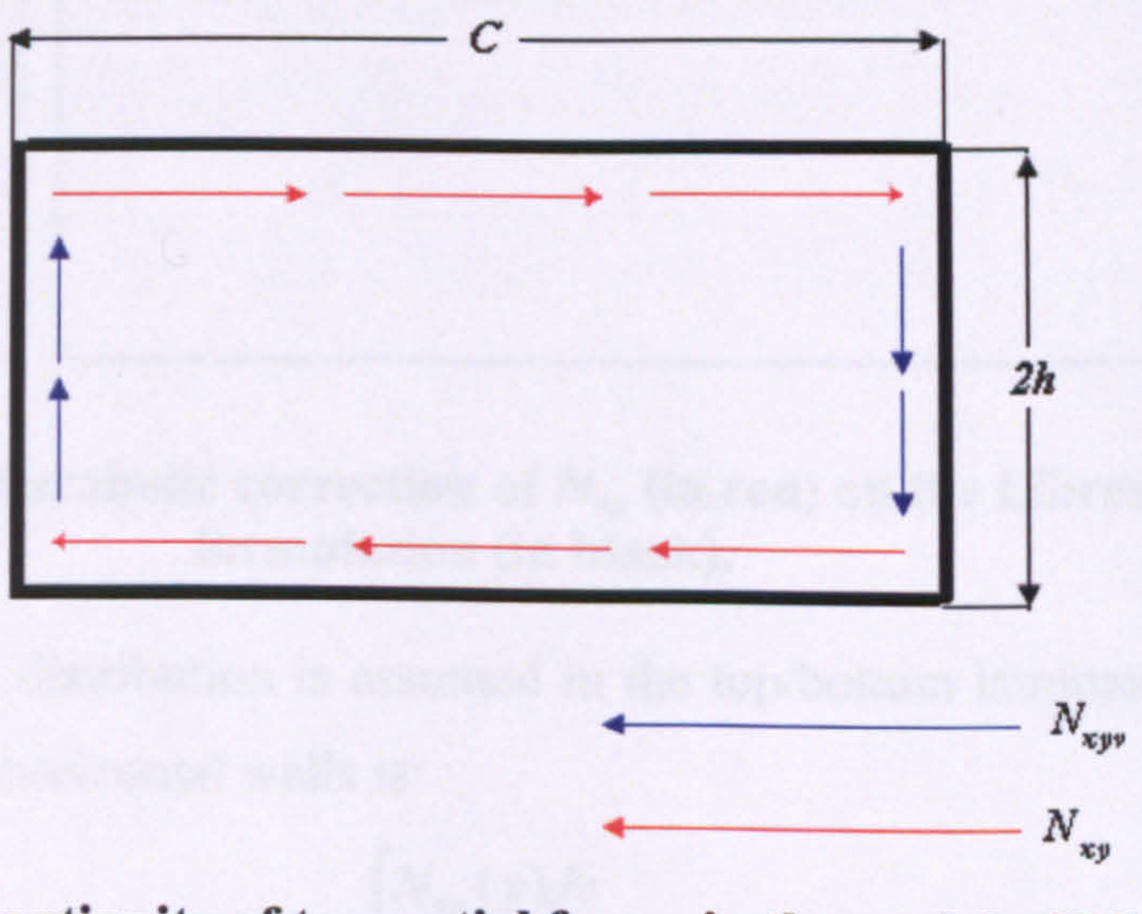

Figure 3.7. Discontinuity of tangential forces in the model of Librescu and Song.

The shear continuity at the corners is imposed by assuming a parabolic distribution, in the horizontal or in the vertical laminates, of force per unit length. For example, when N_{xy} is greater than N_{xyv}, the shear flow of the top/bottom laminate will be assumed to vary parabolically: its value at the corner will be equal to N_{xyv}, and its maximum value, at the middle of the wall, will be equal to N_{xy} (Figure 3.8). In other words, the shear flow of the horizontal laminates is now a parabolic function $N_{xy}(y)$, where y is the local axis of the laminate, shown in Figure 3.4. An analogous distribution occurs when N_{xyv} is greater than N_{xy}. In this case, the shear flow of the vertical laminates is assumed to vary parabolically.

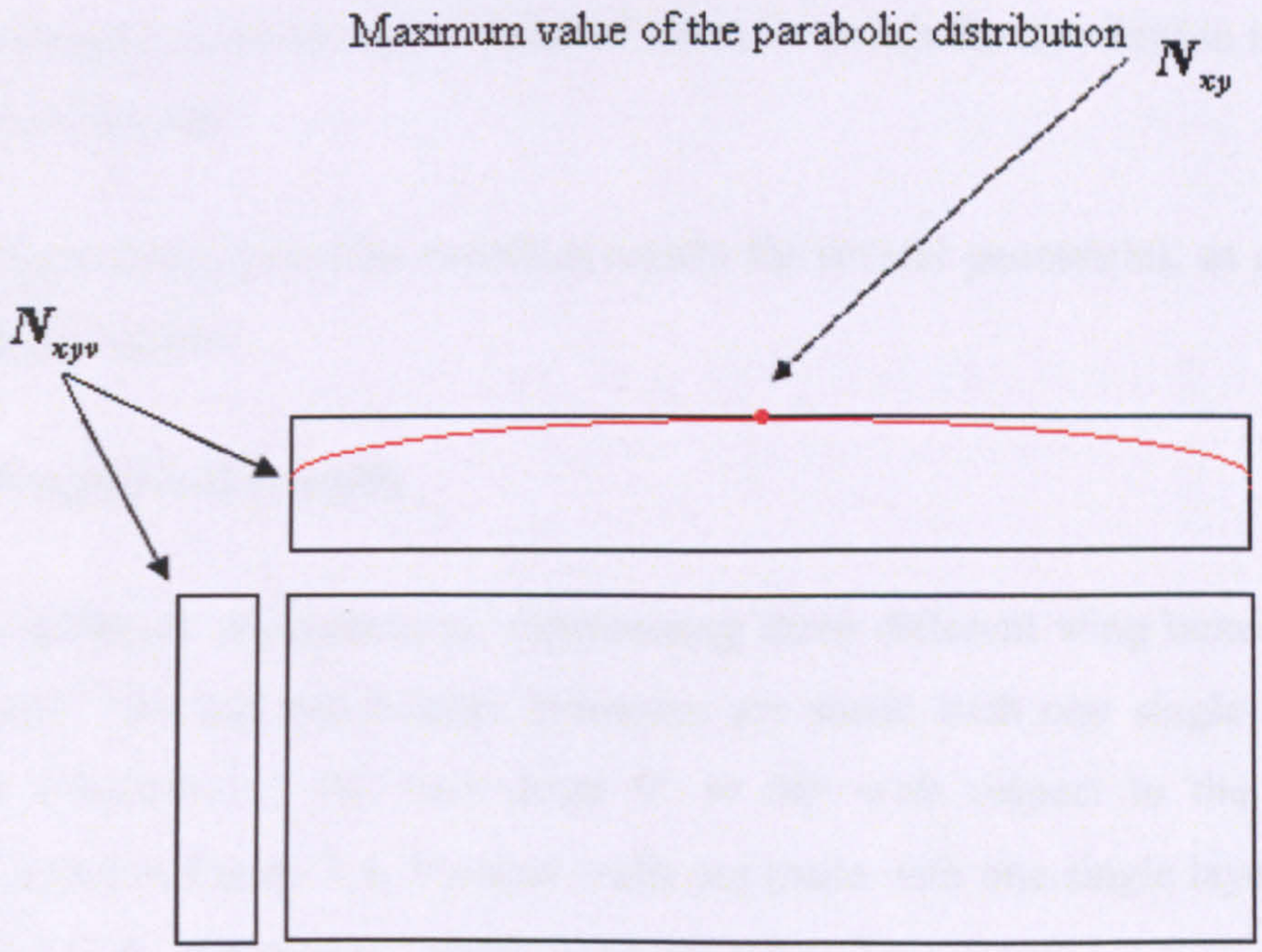

Figure 3.8. Parabolic correction of N_{xy} (in red) on the Librescu formulation (in black).

When a parabolic distribution is assumed in the top/bottom laminates, the average shear flow of the horizontal walls is:

$$N_{xy}^{*} = \frac{\int_{w} N_{xy}(y)dy}{C} \tag{3.18}$$

The stiffness GJ can be therefore evaluated with Bredt's formula [82]:

$$GJ = 2\Omega N_c \tag{3.19}$$

where

N_c is an average expression of the shear flow along all the contour found from

$$N_c = \frac{N_{xy}^{*} C + HN_{xyv}}{H + C} \tag{3.20}$$

An analogous formula can be deduced when the parabolic distribution is assumed in the vertical walls.

This formulation provides excellent results for several geometries, as shown in the following section.

3.5 Numerical results

Three different cross-sections, representing three different wing boxes, have been analyzed. The top and bottom laminates are made with one single layer whose fibres orientation ξ can vary from 0° to 90° with respect to the local frame represented in Figure 3.4. Vertical walls are made with one single layer with fibres oriented at 0°. Appropriate elastic properties are:

$E_1 = 181$ GPa
$E_2 = 10.3$ GPa
$G_{12} = 4.55$ GPa
$\nu_{12} = 0.28$

These three cross sections have different wall lengths, but the same shape (rectangular) and the same area enclosed by the contour. Geometrical properties are reported in Table 3.1.

Table 3.1: Geometric properties of three different boxes.

Wing Box Type	Length of vertical walls [m]	Length of horizontal walls [m]	Thickness of vertical walls [m]	Thickness of horizontal walls [m]
Representative Wing Box	0.3	0.6	0.006	0.006
Square Wing Box	0.424	0.424	0.006	0.006
Tall Wing Box	0.6	0.3	0.006	0.006

Finite element analysis (FE) using Patran/Nastran [83] was performed to validate the results. Shell elements of composite materials have been used. The longer laminate has been divided in 8 elements while 6 elements have been used for the shorter

wall. The span, 4 meters long, has been divided in 20 elements. A convergence analysis has been performed in order to verify that a larger number of elements does not induce any change in the results. Results are shown in Figure 3.9: the stiffness EI of a representative composite box has been studied by using three different meshes: a "low density" mesh, a "high density" mesh and the mesh used in this work. The number of elements used for these three kind of meshes are shown in Table 3.2.

Table 3.2: Meshes used in the convergence analysis.

Mesh Type	Number of elements along the span	Number of elements along the long laminate	Number of elements along the short laminate
"Low density"	10	4	3
"High density"	40	16	12
Mesh chosen for the analyses	20	8	6

When a "low density" mesh is used, the stiffness is overestimated as suggested by Bathe [84]. A "high density" mesh, on the other hand, is not necessary. It produces, in fact, the same results of the reference mesh used for the analyses.

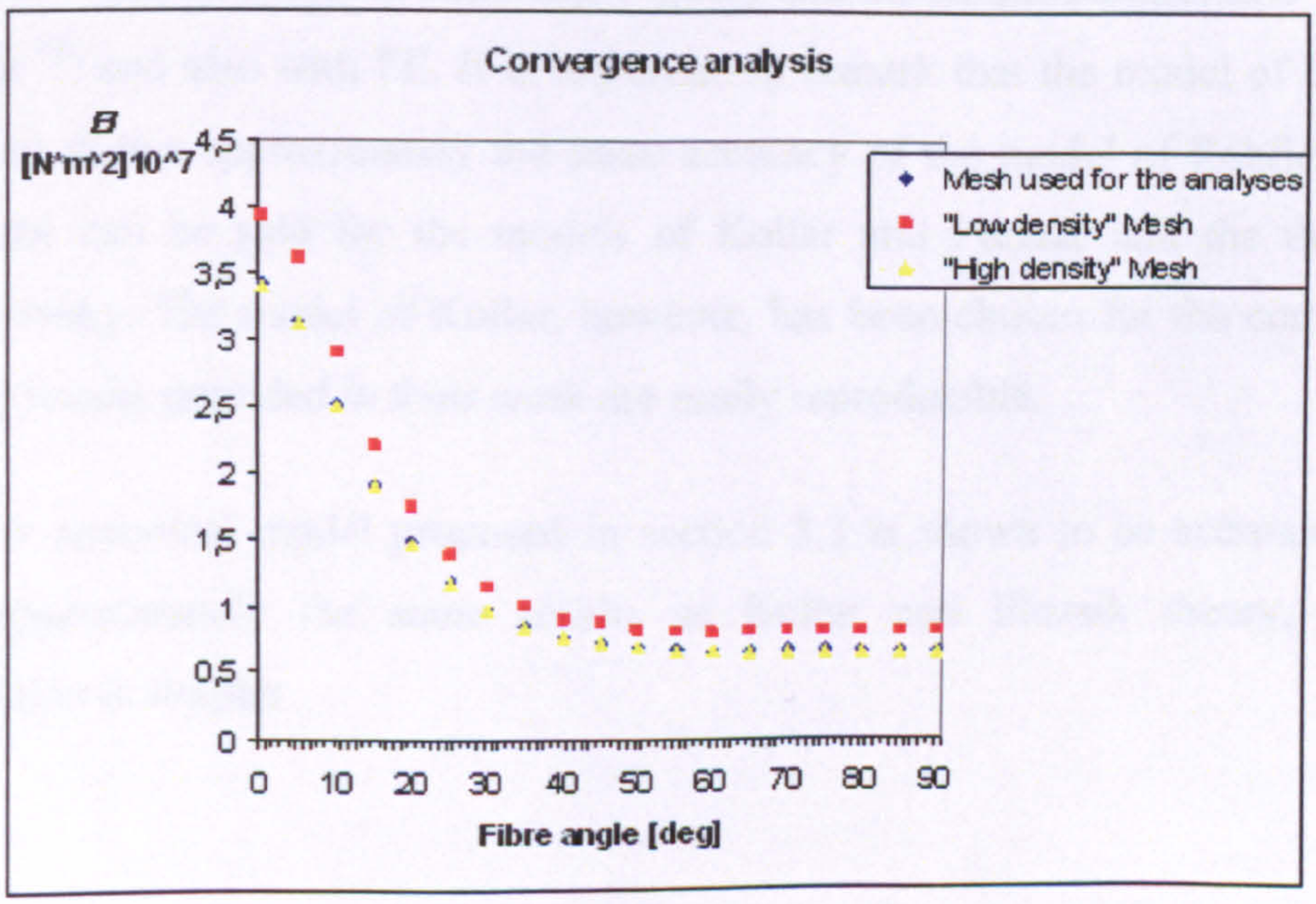

Figure 3.9: Convergence analysis.

The following steps are needed to obtain bending and torsional stiffnesses.

- A unitary bending moment is applied to the tip of the beam.
- Bending and twisting deformations are measured in a cross section located at the middle span of the beam: sufficiently far from the tip and root, in order to avoid the effects of local deformations. The ensuing rates of bending and twisting deformations, due to a unitary bending moment, represent bending and bend/twist coupling compliances. In symbols they can be denoted with e_i and k_a respectively.
- A unitary twisting moment is applied to the tip of the wing with no bending moment.
- Twisting deformation is measured and consequently twisting compliance, denoted with g_k.
- Once all the compliances are known, they can be put in the matrix form:

$$\begin{bmatrix} e_i & k_a \\ k_a & g_k \end{bmatrix}$$

- The inverse of the compliance matrix is the stiffness matrix of Eqn.3.1.

Results for *EI* of unbalanced boxes are shown in Figure 3.10-3.12. The analytical model presented here has been compared with three other different models (Kollar and Pluzsik theory, Librescu and Song's theory and the simple parallel axis theorem [82]) and also with FE. It is important to remark that the model of Librescu and Song shows approximately the same accuracy of the model of Rehfield et al. The same can be said for the models of Kollar and Pluzsik and the theory of Berdichevsky. The model of Kollar, however, has been chosen for the comparison because results provided in their work are easily reproducible.

The new analytical model proposed in section 3.3 is shown to be accurate and it gives approximately the same results as Kollar and Pluzsik theory, but its formulation is simpler.

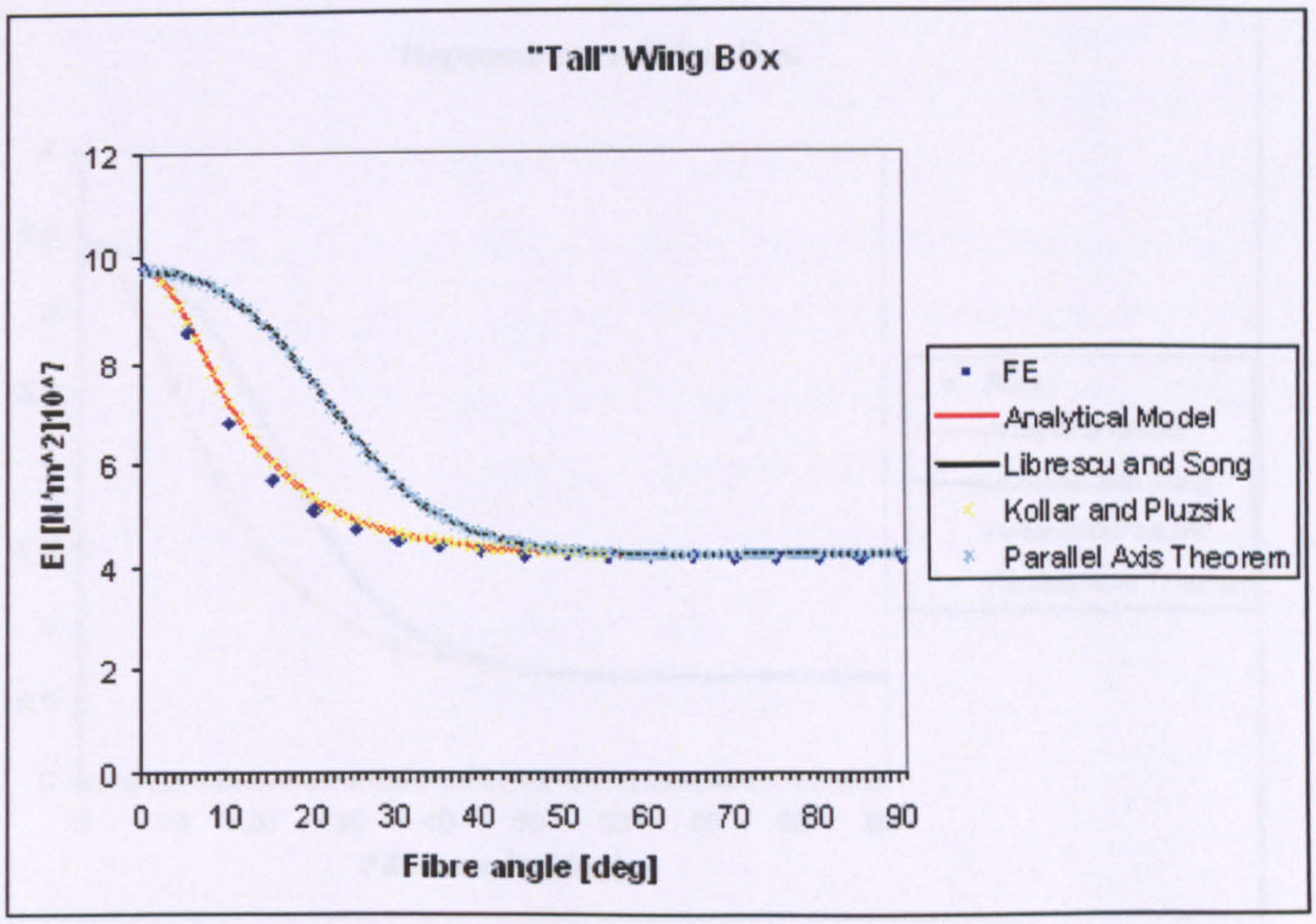

Figure 3.10: *EI* for the "tall" unbalanced composite wing box. Fibre angles vary from 0 to 90 degrees.

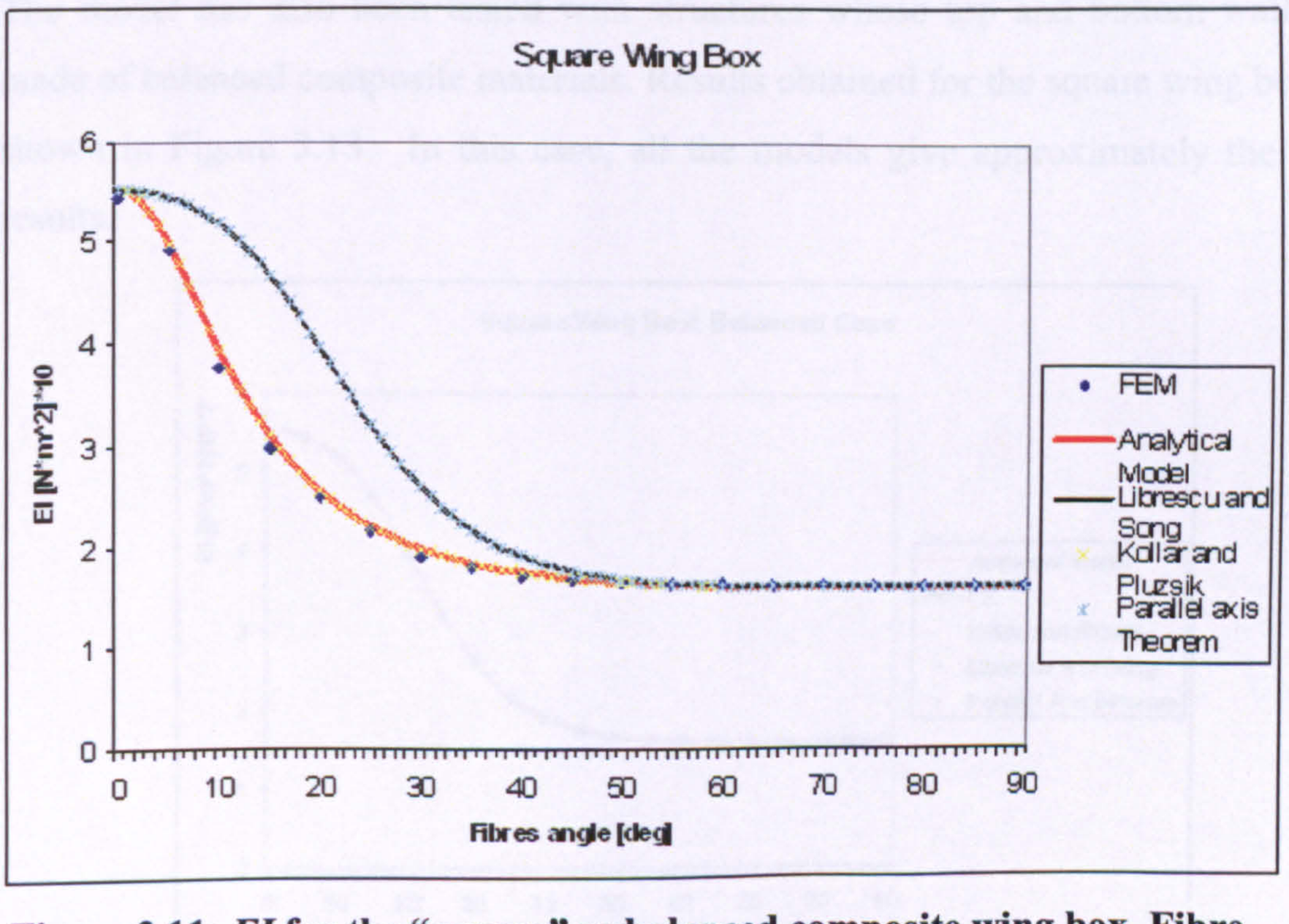

Figure 3.11: *EI* for the "square" unbalanced composite wing box. Fibre angles vary from 0 to 90 degrees.

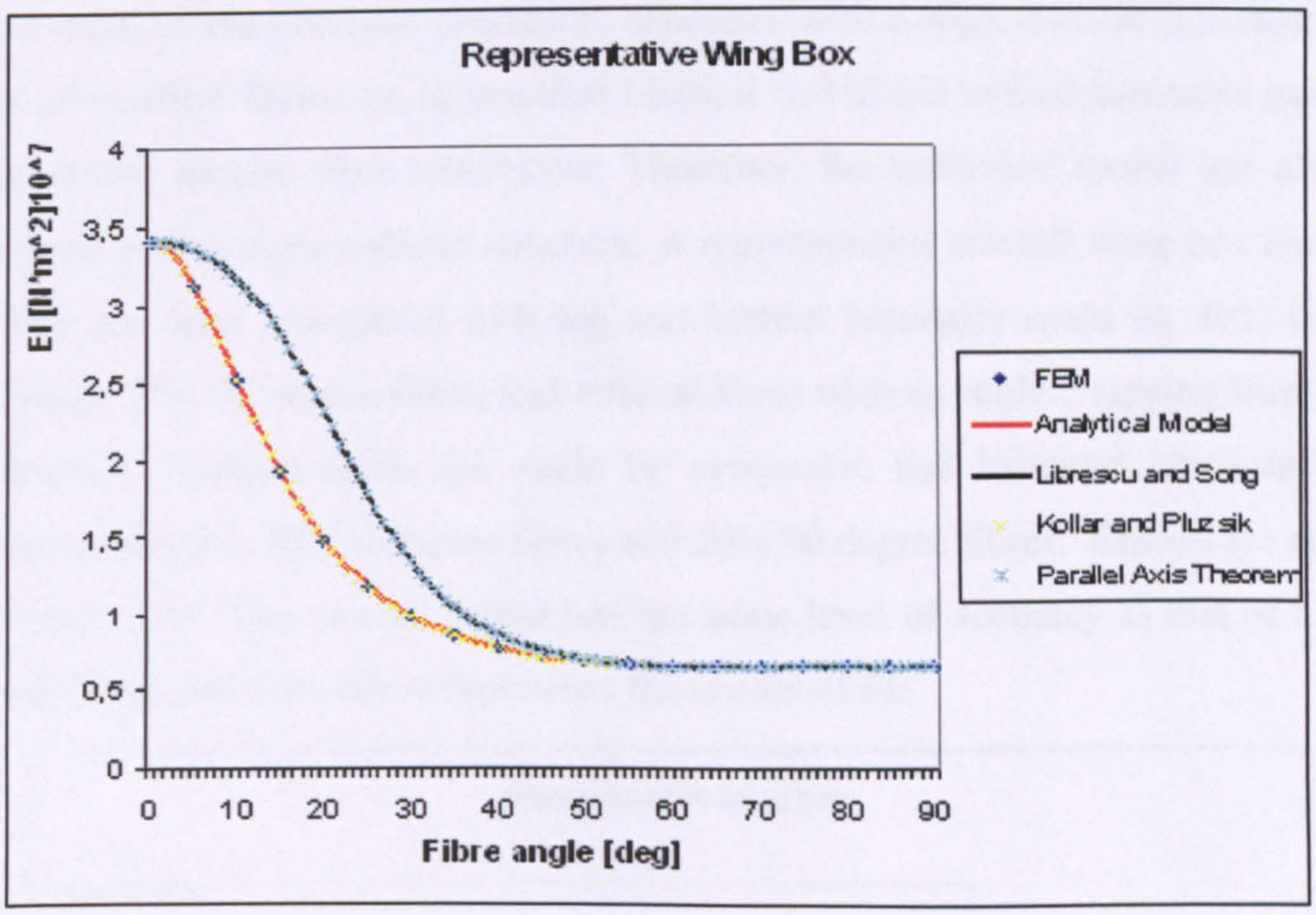

Figure 3.12: *EI* for the representative unbalanced composite wing box. Fibre angles vary from 0 to 90 degrees.

The model has also been tested with structures whose top and bottom walls are made of balanced composite materials. Results obtained for the square wing box are shown in Figure 3.13. In this case, all the models give approximately the same results.

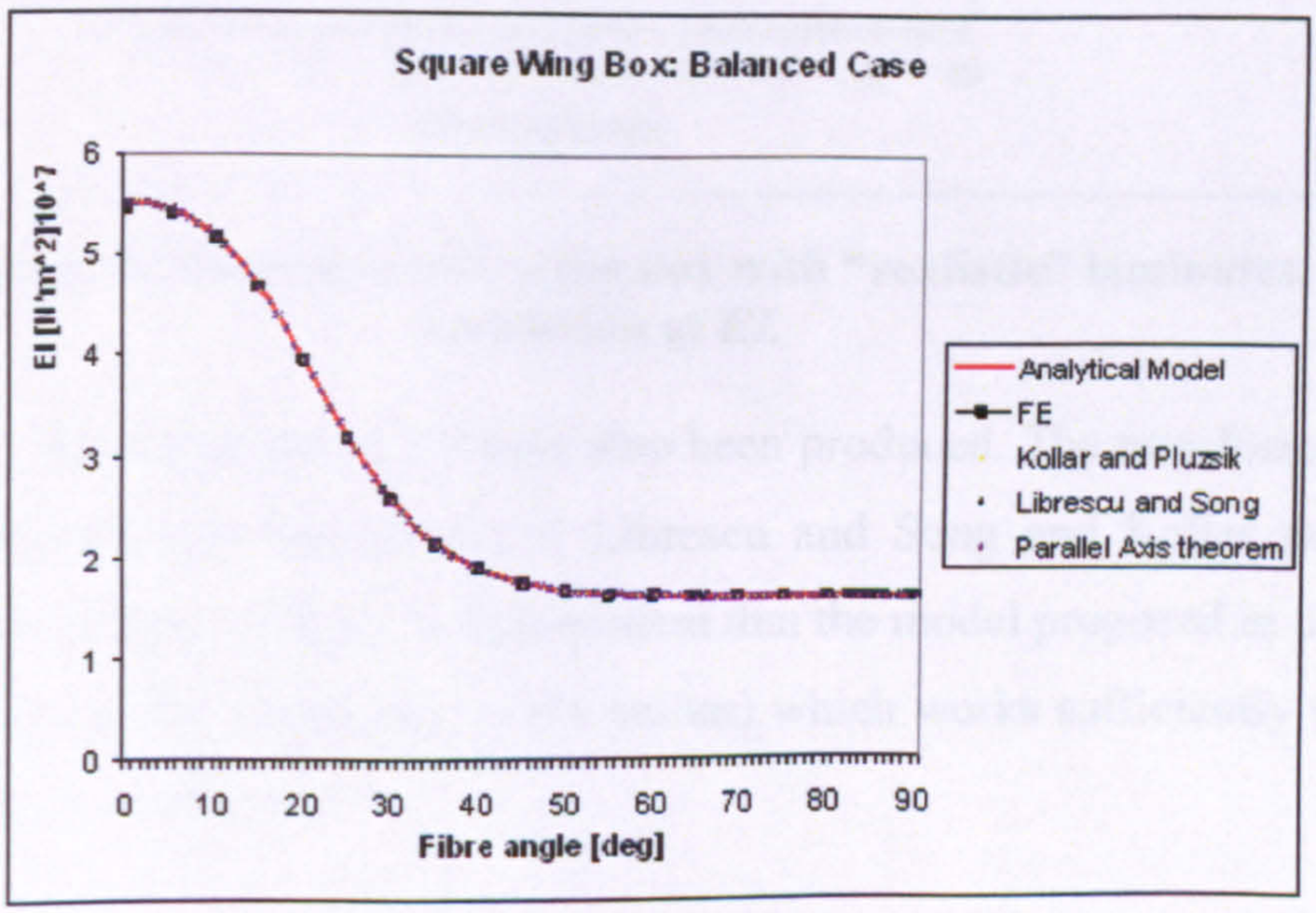

Figure 3.13. *EI* for the "square" balanced composite wing box. Fibre angles vary from 0 to 90 degrees.

In most of the previous examples, structures with a high level of anisotropy have been studied. However, in practical cases, it is difficult to find laminates made with only one unique fibre orientation. Therefore, the analytical model has also been tested with a more realistic structure. A representative aircraft wing box (see Table 3.1) has been considered with top and bottom laminates made by 40% 0 degree fibres, 20% 90 degree fibres and 40% of fibres with an angle ξ varying from 0 to 90 degrees. Vertical walls are made by symmetric and balanced laminates whose composition is 80% 0 degree fibres and 20% 90 degree fibres. Results are shown in Figure 3.14. The current model has the same level of accuracy as that of Librescu and Song and it is able to reproduce the results of FE.

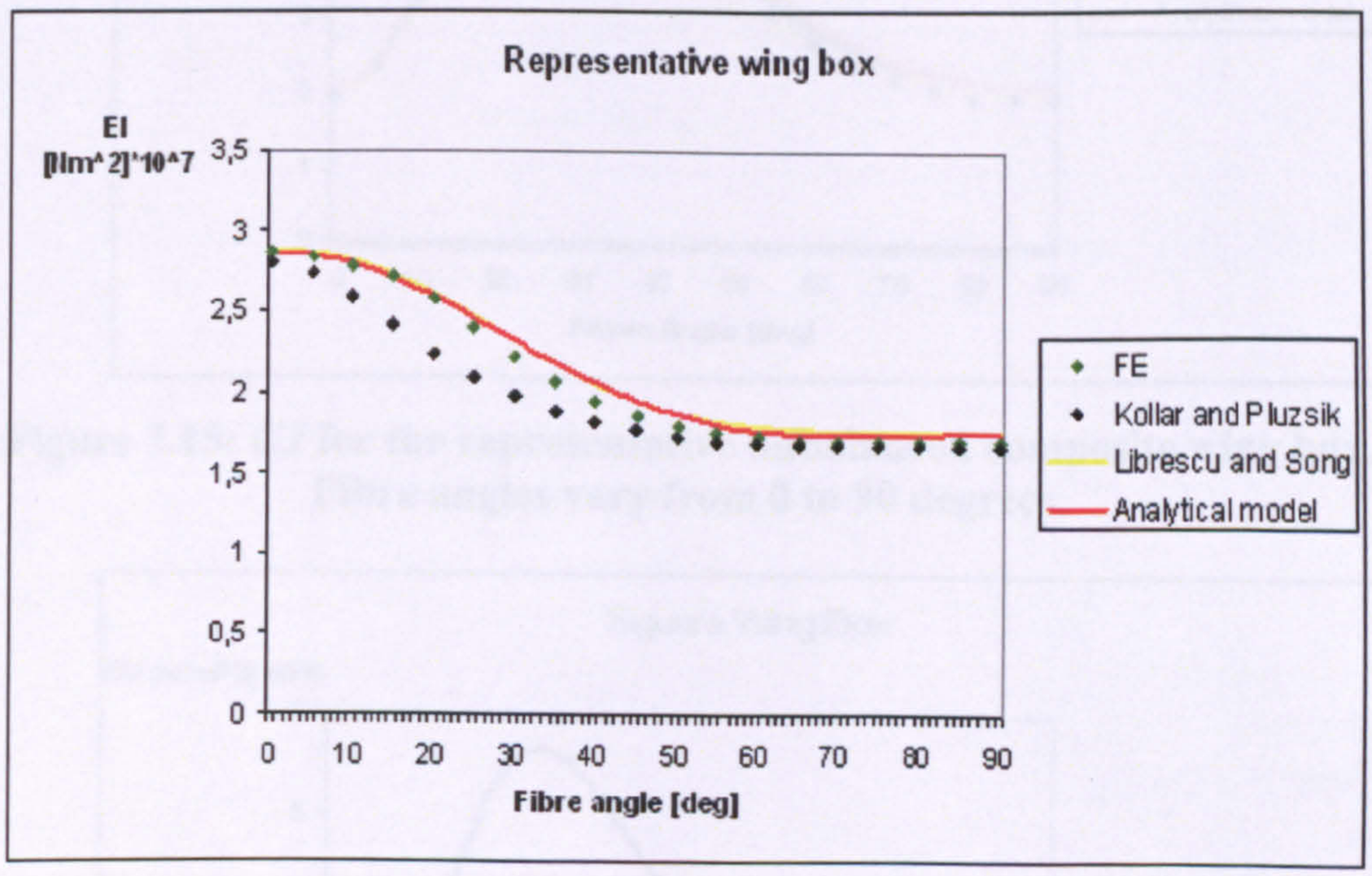

Figure 3.14: Representative wing box with "realistic" laminates. Validation of *EI*.

Results for the evaluation of *GJ* have also been produced. The new formulation has been compared with the models of Librescu and Song and Kollar and Pluzsik, respectively (Figure 3.15-3.17). It is evident that the model proposed in this paper is the only one (to the knowledge of the author) which works sufficiently well for all three different geometries.

Also for the validation of *GJ*, a representative aircraft wing box with lay-up outlined previously has been analysed. Results are shown in Figure 3.18. In this

case, the model of Kollar and Pluzsik underestimates the stiffness. The current formulation is in accordance with the FE and is slightly more accurate than the model of Librescu and Song.

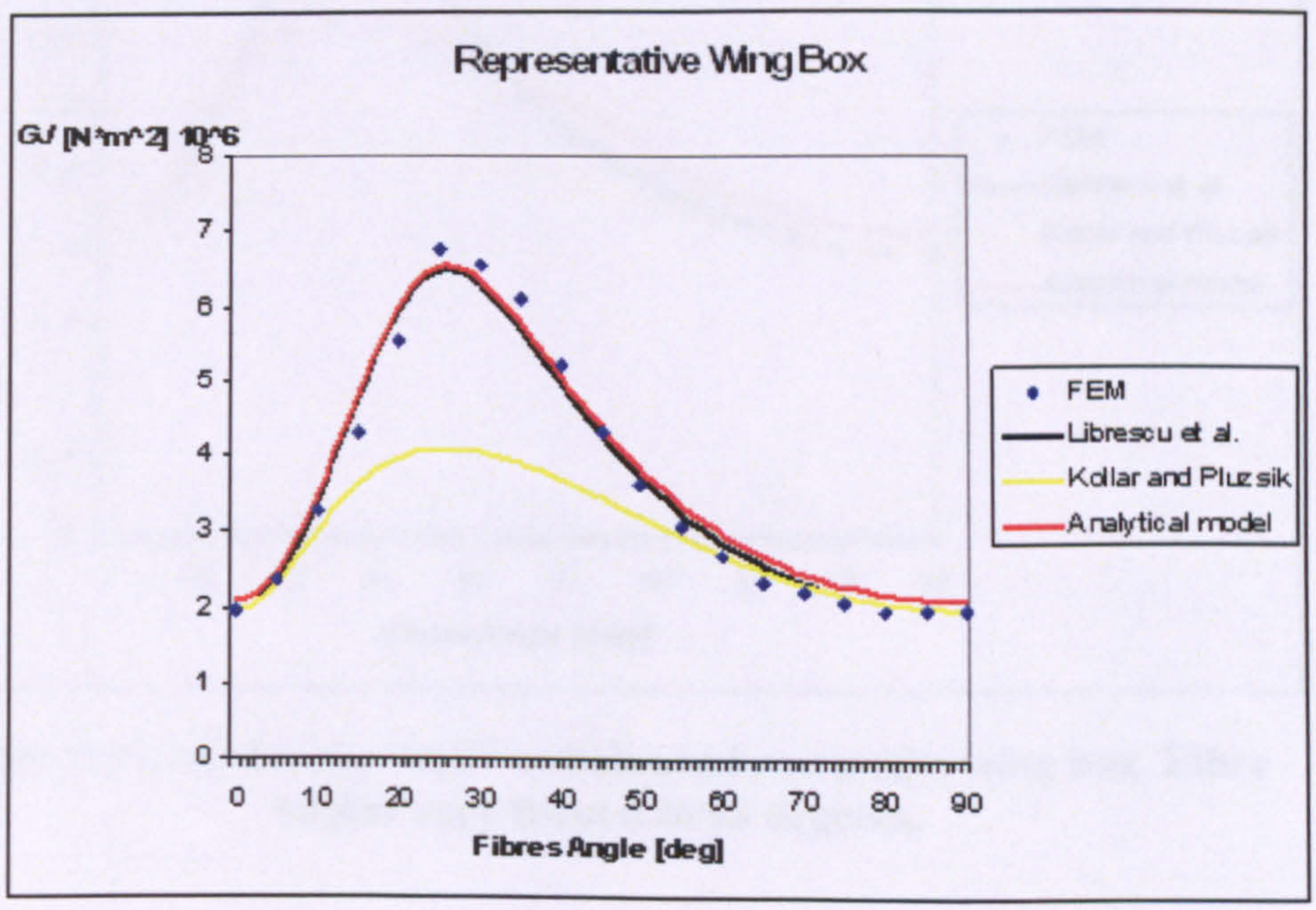

Figure 3.15: *GJ* for the representative unbalanced composite wing box. Fibre angles vary from 0 to 90 degrees.

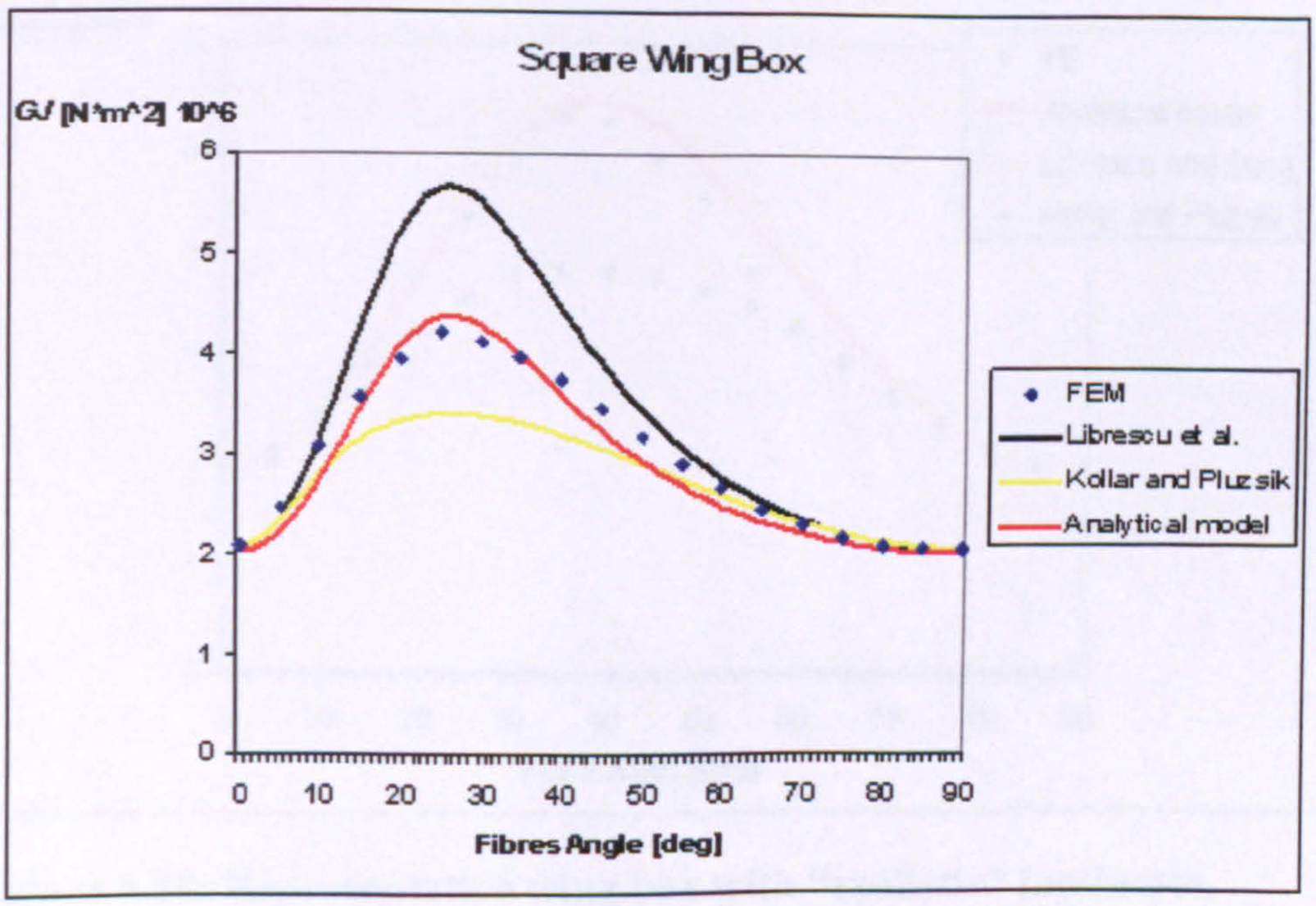

Figure 3.16: *GJ* for the "square" unbalanced composite wing box. Fibre angles vary from 0 to 90 degrees.

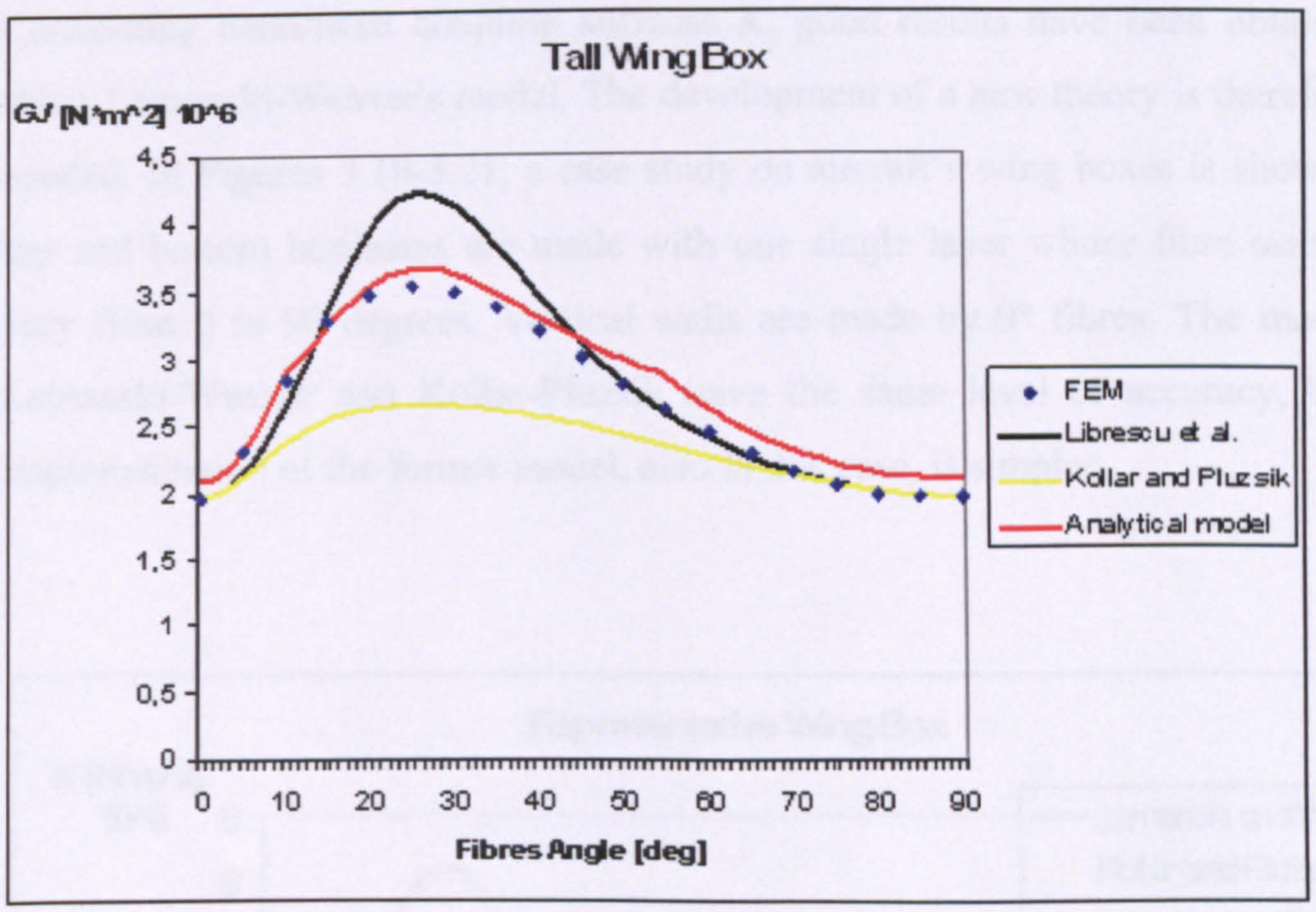

Figure 3.17: *GJ* for the "tall" unbalanced composite wing box. Fibre angles vary from 0 to 90 degrees.

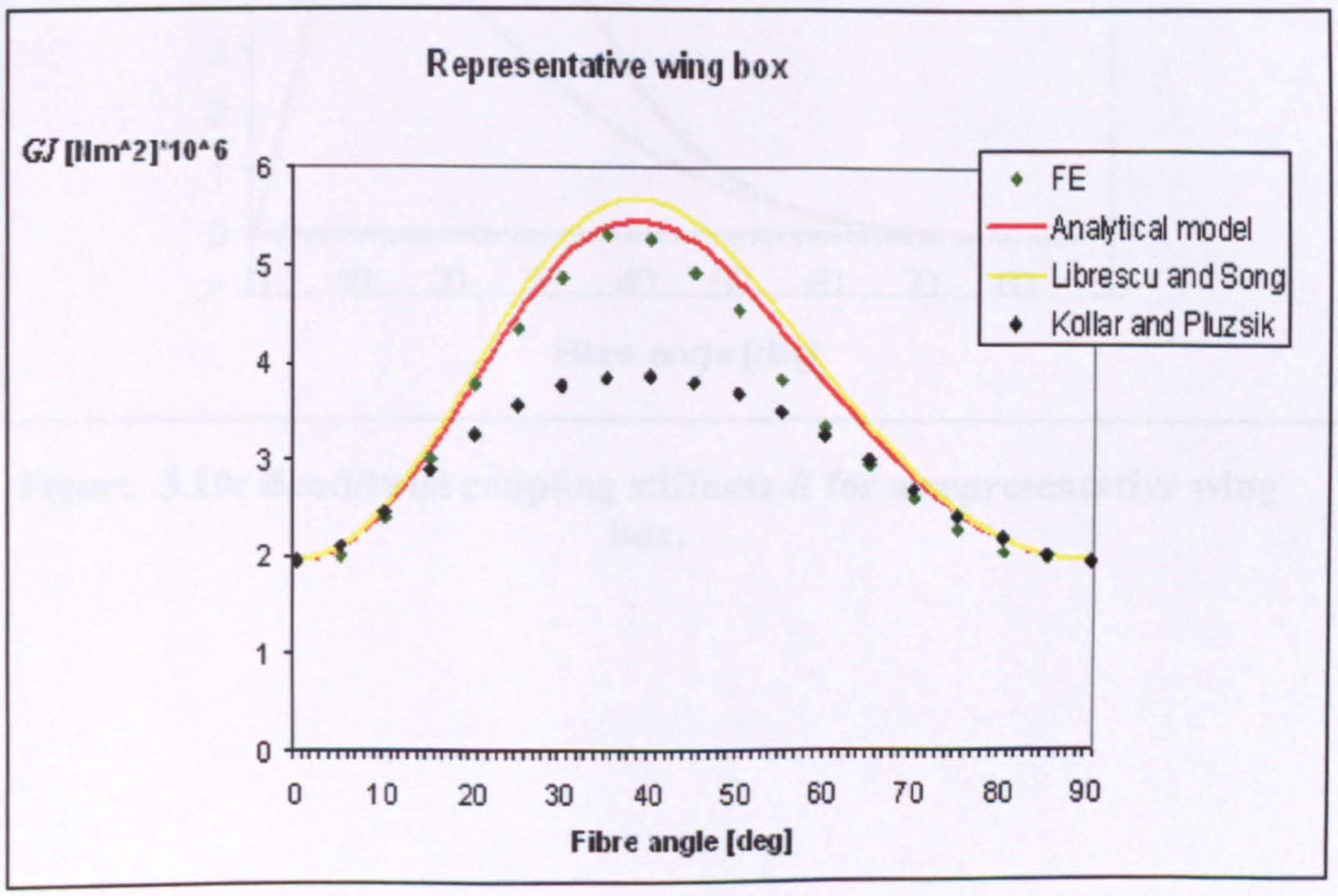

Figure 3.18: Representative wing box with "realistic" laminates. Validation of *GJ*.

Concerning bend/twist coupling stiffness *K*, good results have been obtained by using Lemanski-Weaver's model. The development of a new theory is therefore not needed. In Figures 3.19-3.21, a case study on aircraft's wing boxes is shown. The top and bottom laminates are made with one single layer whose fibre orientation vary from 0 to 90 degrees. Vertical walls are made by 0° fibres. The models of Lemanski-Weaver and Kollar-Pluzsik have the same level of accuracy, but the implementation of the former model, also in this case, is simpler.

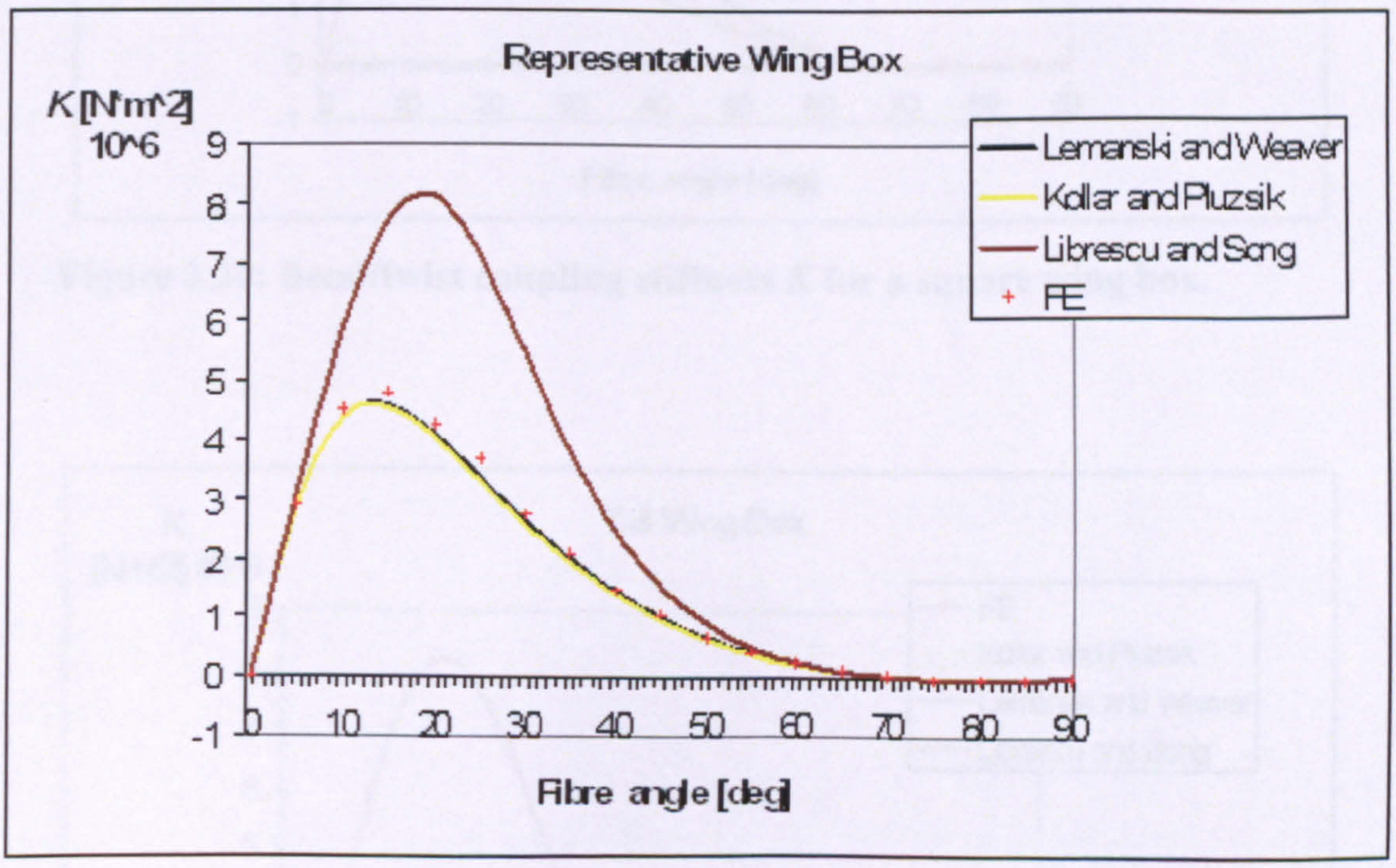

Figure 3.19: Bend/twist coupling stiffness *K* for a representative wing box.

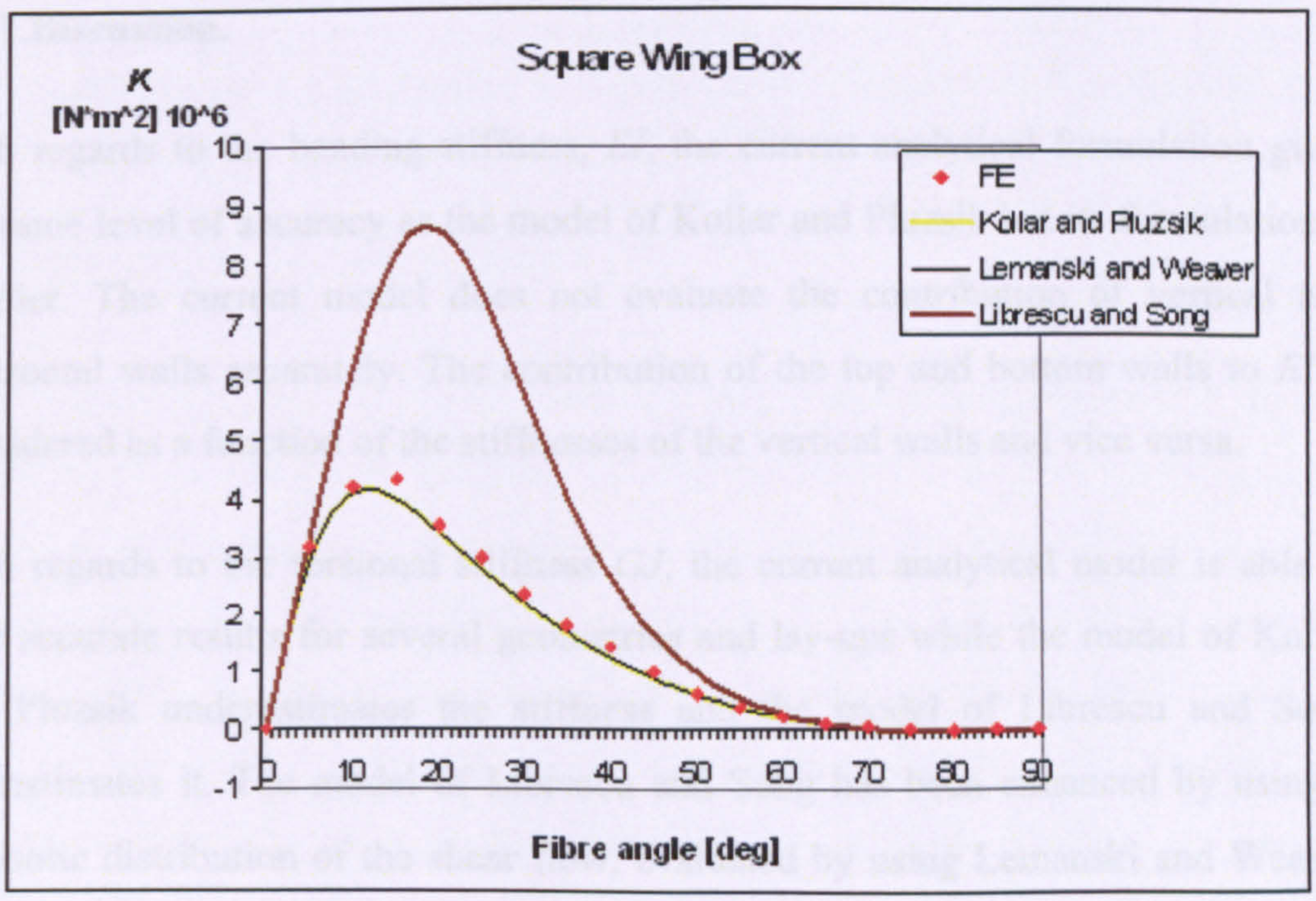

Figure 3.20: Bend/twist coupling stiffness *K* for a square wing box.

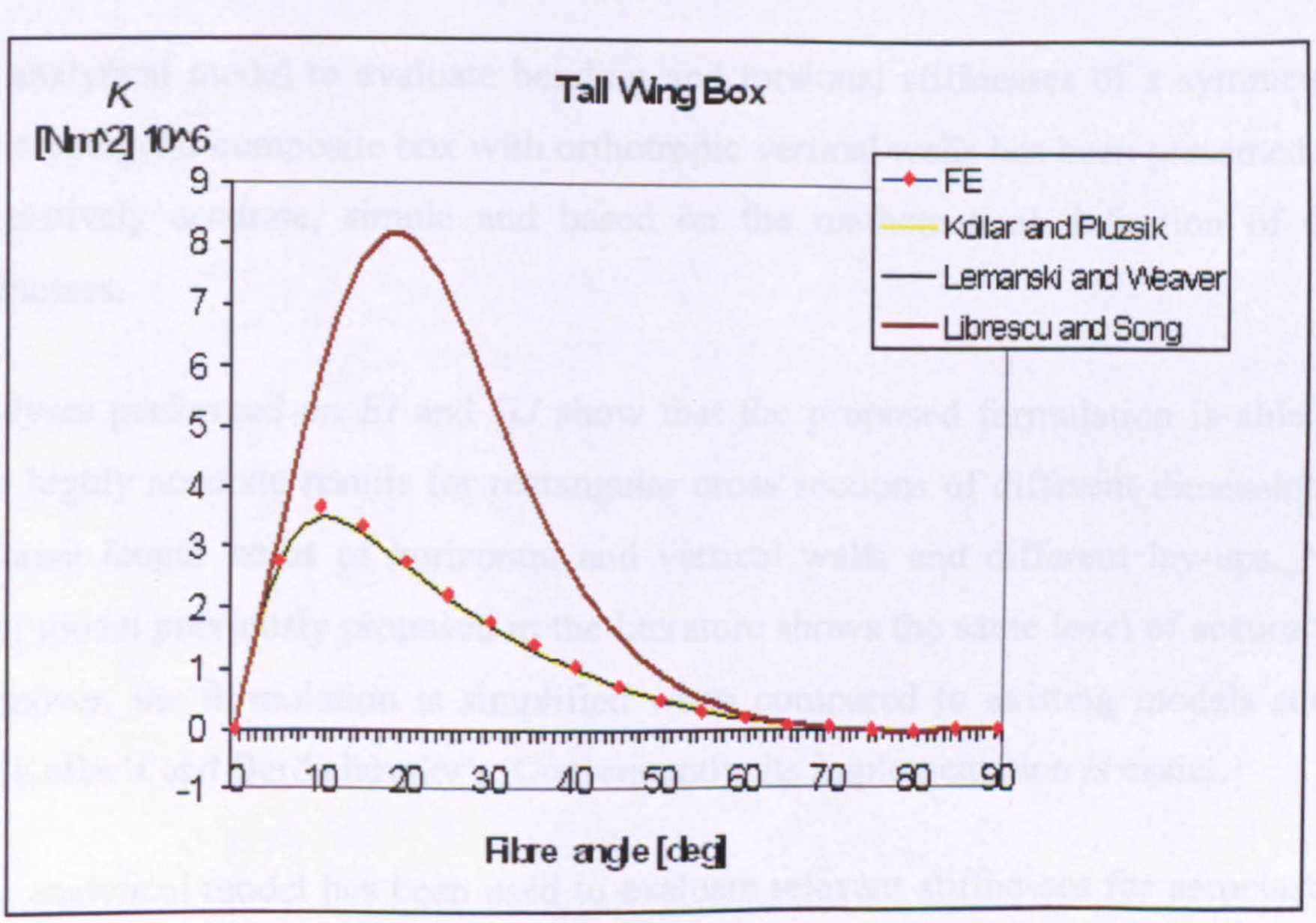

Figure 3.21: Bend/twist coupling stiffness *K* for the "tall" wing box.

3.5.1 Discussion.

With regards to the bending stiffness, *EI*, the current analytical formulation gives the same level of accuracy as the model of Kollar and Pluzsik but its formulation is simpler. The current model does not evaluate the contribution of vertical and horizontal walls separately. The contribution of the top and bottom walls to *EI* is considered as a function of the stiffnesses of the vertical walls and vice versa.

With regards to the torsional stiffness *GJ*, the current analytical model is able to give accurate results for several geometries and lay-ups while the model of Kollar and Pluzsik underestimates the stiffness and the model of Librescu and Song overestimates it. The model of Librescu and Song has been enhanced by using a parabolic distribution of the shear flow, evaluated by using Lemanski and Weaver approach.

3.6 Conclusions

An analytical model to evaluate bending and torsional stiffnesses of a symmetric and rectangular composite box with orthotropic vertical walls has been presented. It is relatively accurate, simple and based on the mathematical definition of the stiffnesses.

Analyses performed on *EI* and *GJ* show that the proposed formulation is able to give highly accurate results for rectangular cross sections of different dimensions, different length ratios of horizontal and vertical walls and different lay-ups. No other model previously proposed in the literature shows the same level of accuracy. Moreover, the formulation is simplified when compared to existing models such like Kollar's and Berdichevsky's. Consequently, its implementation is easier.

This analytical model has been used to evaluate relevant stiffnesses for aeroelastic tailoring. It has been integrated as part of the structural model of the static and dynamic aeroelastic tools described in Chapters 4 and 6.

Chapter 4
A static aeroelastic model to evaluate the benefits of unbalanced laminates on aircraft's range

4.1 Introduction to aeroelasticity

Aeroelasticity studies the interactions between three different kinds of forces: aerodynamic action, elastic response and forces of inertia. This discipline does not concern only aeronautics, where aeroelastic phenomena are observed in wings, tails, engine blades, but also civil and mechanical structures. There is the infamous collapse of the Tacoma bridge, due to flutter instability caused by a wind of only 18 m/s. The images of this disaster clearly show torsional deformation coupled with flexural motion; the same flutter instability that can be observed in a wing. Furthermore, aeroelastic phenomena and instabilities can also be observed in the piping systems of chemical/electrical plants. The fluid-structure interaction is driven by the internal flow, which can cause instability as divergence and flutter [85].

Aeroelasticity was born as an area of analysis in the early 1920s to solve problems strictly related to the aeroplane [86]. Aeroelastic instabilities, even if not known and recognized, have been faced by engineers since the origin of the flight. The cause of the failure of the early attempts of the Wright brothers, for example, was due to divergence. The use of the bi-wing plane was a technical solution used to increase the torsional stiffness and thus avoid divergence, but it was not enough to avoid flutter in the tail wing, when a greater flight speed was reached. The research of Lanchester [87] proves the usefulness of engineers in finding solutions for such problems.

The introduction of the mono-wing with the use of low damping metallic structures (instead of wood) coupled with reduced thicknesses, high aspect ratio wings and the increase of the flight speed have induced further aeroelastic instabilities, including buffeting and transonic buffeting. The latter effect is observed when the aerodynamic stream leaving the wing surrounds the tail. The presence of the vortex generates periodic motions in the tail itself. If the torsional natural frequency is

similar to the frequency of the aerodynamic forces, resonance is observed. Transonic buffeting is strictly related to the transonic flight regime. The flow on the top surface of the wing is partially supersonic and partially subsonic. At a point close to the trailing edge of the airfoil, the stream returns to being subsonic, passing through a shock wave. This shock wave is not able to remain stable at a particular location and it starts to oscillate. This oscillation is transmitted to the structure, which can be significantly damaged.

As the technology progressed, especially with the advent of high speed flight, the effects of high temperatures on structures became important. It was the birth of aero-thermo-elasticity. Such a discipline is important in spacecraft engineering, especially in the return mission. In modern design, engineers have often used control system to reduce or avoid the negative effects of the structural deformations, as already mentioned in Chapter 2. Sometimes the action of the feedback control system, together with other forces, can induce anomalous responses or even instabilities. The discipline studying such phenomena is called aero-thermo-servo-aeroelasticity [88, 89].

Aeroelastic phenomena regarding an aircraft's structure in the subsonic regime can be divided into two main categories: static and dynamic aeroelasticity. Dynamic aeroelasticity is mainly related to the flutter instability and limit cycle oscillation. It is described in more detail in Chapter 6. Static aeroelasticity, on the other hand, studies the interaction of only two forces: aerodynamic action and elastic response. In other words, forces are applied sufficiently slowly that consequent accelerations and forces of inertia can be neglected.

4.1.1 Static aeroelasticity

There are three phenomena generally studied in the static aeroelasticity of a wing [90]:

- Aeroelastic divergence.
- Reversal of aileron control.
- Lift alleviation.

Divergence is caused by the existence of a distance between the point of application of the lift (centre of pressure) and the shear centre of each airfoil (Figure 4.1).

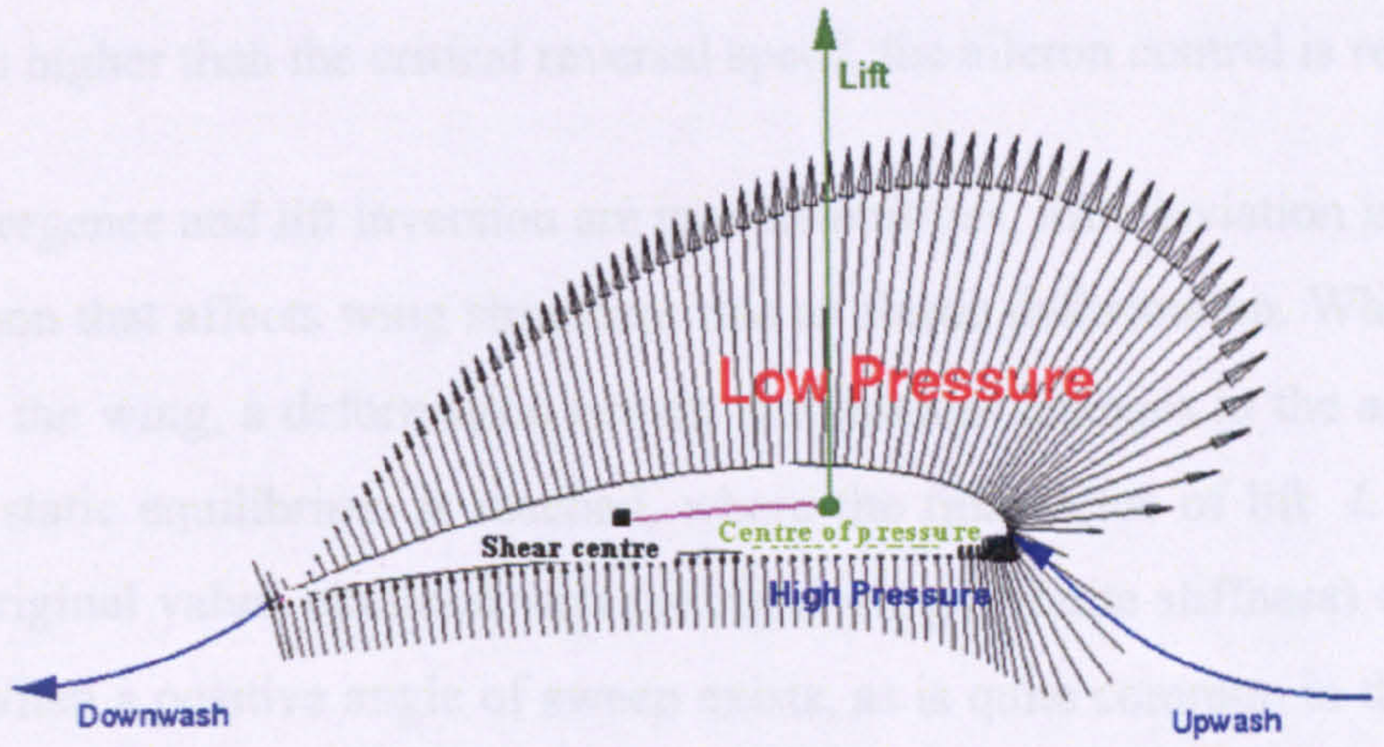

Figure 4.1: Distance between the centre of pressure and the shear centre in a generic airfoil.

This distance causes a torque about the shear centre. This torque must be equilibrated by the elastic reaction. However, the torque induces a rotation of the cross section that tends to increase the angle of attack. When this happens, the lift increases as well, as does the torque. When the elastic reaction is not able to withstand the torque, an instability occurs.

Reversal of aileron control is caused by an analogous mechanism. A simplified description is provided as follows. When an aileron is actuated downwards (Figure 4.2), an additional lift ΔL is induced, thus producing a rolling moment. This force is applied on the aileron and creates an additional torque ΔT about the shear centre of the airfoil, that tends to twist the wing "nose down".

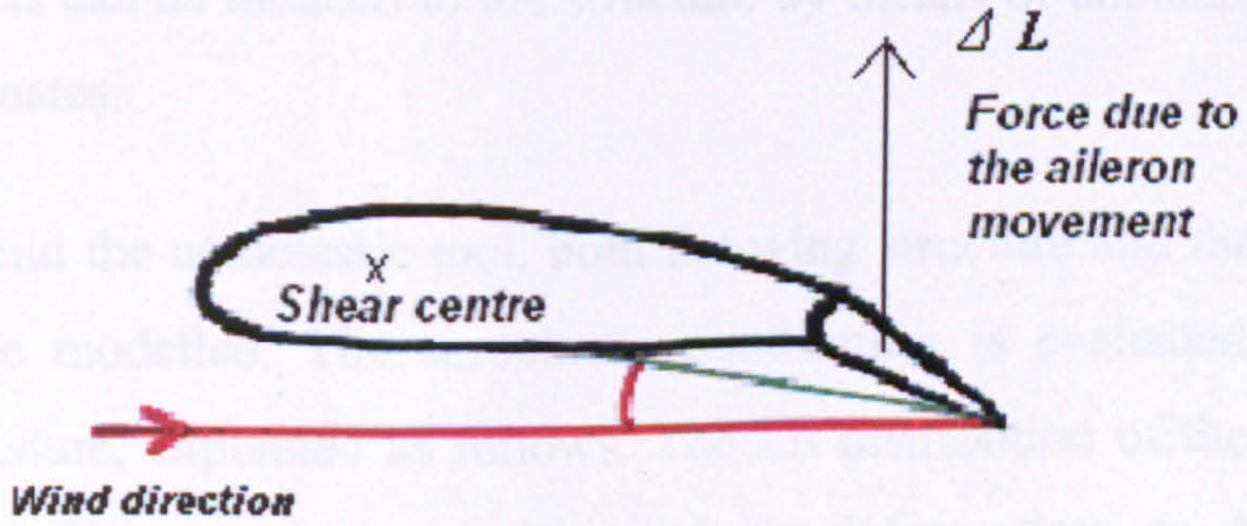

Figure 4.2: Aileron actuation (downwards).

The angle of attack therefore decreases, so the lift over the semi-wing, reducing the rolling moment. An asymptotic air speed may exist at which the aileron becomes completely ineffective. This speed is known as aileron reversal speed. When the airspeed is higher than the critical reversal speed, the aileron control is reversed.

While divergence and lift inversion are two instabilities, lift alleviation is a common phenomenon that affects wing structures due to elastic deformation. When a load is applied to the wing, a deformation occurs that induces changes in the aerodynamic forces. A static equilibrium is reached, where the final value of lift L is different from its original value, obtained with the rigid wing (infinite stiffness) and denoted with L_0. When a positive angle of sweep exists, as is quite common in the design of a civil aircraft, $L < L_0$: the lift is therefore attenuated, as already discussed in Chapter 2. Despite the nature of the phenomenon, the new value of the lift coefficient can be lower or greater than L_0, depending on the values of design parameters.

4.2 The static "low fidelity" aeroelastic model

A low fidelity static aeroelastic model has been developed. It will be described in detail in this section. It can be used for two purposes:

1. To evaluate the lift of the deformed wing, by calculating the final aeroelastic equilibrium.
2. To show the potential benefits of anisotropic composite materials on aircraft's range. A simple distribution of "nose up" and/or "nose down" effects can be induced to the structure by means of unbalanced composite laminates.

In order to build the aeroelastic tool, both the wing structure and the aerodynamic loads must be modelled. The aeroelastic equilibrium is evaluated by using an iterative procedure, explained as follows. The lift distribution of the rigid wing is first calculated. This aerodynamic action induces deformations on the wing. Such deformation induces changes on the span wise distribution of the angles of attack

and, consequently, on the aerodynamic loads. New deformations must therefore be calculated and this procedure continues until convergence.

The iterative procedure has been preferred to the solution of the coupled system, where the aerodynamic-elastic equations are solved simultaneously, because less CPU running time is required.

4.2.1 The structural model

Wing structures are complex assemblages of interconnected structural elements. The challenge is to develop a model able to satisfy the special demands of a conceptual\preliminary design, where understanding is of prime importance. The structural model must be simple enough to provide quick solutions and, at the same time, sufficiently complex to display features such as span-wise lift distribution and the essential effects of laminated wing design. The wing is therefore modelled as a one-dimensional beam. It is assumed to be sufficiently slender that the pure shear deformation and the effects of restrained warping can be neglected, as suggested by Kollar and Pluzsik [16, 17]. Only three stiffnesses need therefore to be considered:

EI	bending stiffness
GJ	torsional stiffness
K	bend-twist coupling stiffness

The stiffnesses will be considered coincident with those of a rectangular box (Figure 2.13), as previously suggested by Weisshaar [56] and Patil [6]. This introduces simplifications into the model without affecting the physical meaning of the results. In Chapter 5, these assumptions will be discussed comparing the stiffnesses of a composite box with those of a real wing like structure.

The structure is loaded with a distribution of lift per unit of length $q(x)$, which is calculated with an aerodynamic model. Once this quantity is known from the aerodynamic tool, internal loads can be calculated. They are:

M(x) is the bending moment distribution

T(x) is the twisting moment distribution

They can be simply evaluated from [82]:

$$\frac{d^2M(X)}{dX^2} = -q(X) \tag{4.1}$$

$$\frac{dT(X)}{dX} = m(X) \tag{4.2}$$

where

m(x) is the distribution of twist per unit of length

At each cross section *X* of the wing, the following relationship exists between *m* and *q*:

$$m(X) = q(X)d(X) \tag{4.3}$$

where

d(X) is the distance between the centre of pressure and the shear centre of each airfoil.

Internal loads can be used to evaluate the deformations by means of a linear analytical model, as already suggested by Weisshaar [2, 56]. The model chosen for this work is that proposed by Librescu and Song [13]. Its general formulation of seven equations is reduced to a system of only two equations: bending and torsional equilibria. As already mentioned, in fact, axial forces, shear deformations, lag moment and warping can be neglected. Only three stiffnesses are therefore considered: *EI*, *GJ* and *K*. The model, as already shown in Chapter 3, can be written in matrix form as follows:

$$\begin{bmatrix} M(X) \\ T(X) \end{bmatrix} = \begin{bmatrix} EI(X) & -K(X) \\ -K(X) & GJ(X) \end{bmatrix} \begin{bmatrix} \frac{d\varphi(X)}{dX} \\ \frac{d\theta(X)}{dX} \end{bmatrix} \tag{4.4}$$

The wing can be divided into segments along the span direction to facilitate the analysis. Equation 4.4 can be solved numerically by using the finite difference approach [91]. The two semi-wings are considered such as cantilevered: rotations and displacements are blocked at the root.

Stiffnesses *EI*, *GJ* and *K*, are properties of the whole cross section. They must be calculated from the geometric and elastic properties of each wall. The analytical model described in Chapter 3 has been used for such purpose. It therefore plays a key role in the structural model.

The wing box used in the aeroelastic model is prismatic and symmetric. The cross section is rectangular. The top and bottom laminates are constructed with 44% of fibres orientated at zero degrees with respect to the local axis. The reason is simple: the main load in a wing is the bending moment and zero degrees fibres maximize bending strength. 12% of the laminate fibres are oriented with an angle of 90 degrees. These are present because, generally, a moment caused by the drag force (lag moment) exists. Its direction is orthogonal to the main bending moment. In order to obtain bend-twist coupling, 44% of fibres are orientated with an angle ξ (Figure 2.1), positive or negative, depending on whether "nose up" or "nose down" effects are desirable. Vertical walls are orthotropic: 88% of fibres are at 0 degrees and 12% at 90 degrees.

The structural effects induced by the presence of an angle of sweep can also be represented. Rotation of the structural axis of swept wings can be evaluated by means of the method proposed by Weisshaar [56].

4.2.2 The aerodynamic model

An aerodynamic model is required to evaluate the loads acting on the wing in each step of the aeroelastic iterative procedure. Since the aim of this work is the development of a low fidelity model, for the sake of simplicity, the vortex lattice method (VLM) proposed by Bertin [92] has been implemented. The vortex-lattice method is built on the theory of ideal flow, also known as theory of potential flow. Ideal flow is a simplification of the real flow experienced in nature, however, for many engineering applications, such simplified representation has all the properties that are important for from the engineering point of view. The following assumptions [93] are made regarding the problems solved with vortex lattice methods:

- The flow field is incompressible, inviscid and irrotational.
- The lifting surfaces are thin [94]
- The angle of attack is small.

In this thesis, the Prandtl-Glauert correction [92] factor has been introduced to represent the effect of limited compressibility. In this section a detailed description of the model is provided.

The method represents the wing as a surface where a grid of horseshoe vortices is superimposed. The surface is divided into small elements called lattices. In each of them one vortex is imposed and one point is chosen as representative: this point is called the "control point".

Vortices bounding each element, whose magnitude is unknown, induce velocities on all of the control points. Such velocities are calculated by using the Biot-Savart law. A vortex situated on the wing span coincides with the quarter-chord line of the panel and is, therefore, aligned with the local angle of sweep. In a theoretical formulation, the panels where the vortices are applied are located on the main camber surface of the wing and, when the trailing vortices leave the wing, they follow a curved path. However, in many engineering applications, suitable accuracy

can be obtained using linear theory in which straight-line trailing vortices extend downstream to infinity.

In this work, the trailing vortices are assumed to be parallel to the axis of the aircraft. This orientation is chosen because the computation of the influences of the various vortices (influence coefficient that will be formally introduced later) becomes simpler. Furthermore, these geometric coefficients do not change as the angle of attack is changed. Application of the boundary condition, that the flow is tangential to the wing surface at the control point of each of the 2N panels (i.e. there is no flow through the surface), provides a set of simultaneous equations in the unknown vortex circulation strength and induced speeds.

The control point C of each panel is centred span wise on the three-quarter-chord line (Figure 4.3) midway between the trailing-vortex legs. It can be easily demonstrated for a flat plate [92] and the results can be extended to thin airfoils [92].

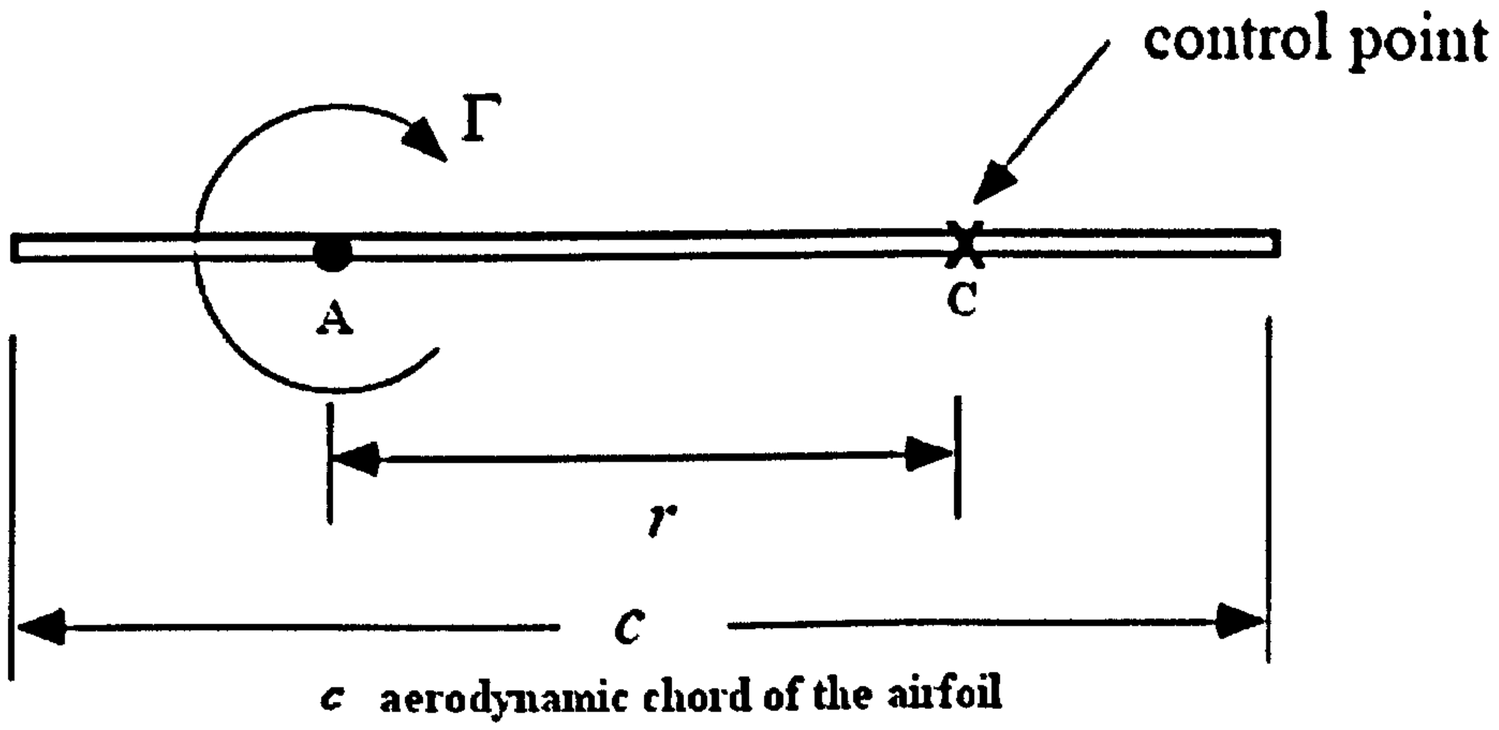

Figure 4.3: Control Point of an airfoil.

Let us calculate the velocity induced on the control point C by a generic vortex filament of strength Γ_n and length dl (Figure 4.4). The velocity can be expressed as:

$$\vec{dV} = \frac{\Gamma_n(\vec{dl} \times \vec{r})}{4\pi r^3} \tag{4.5}$$

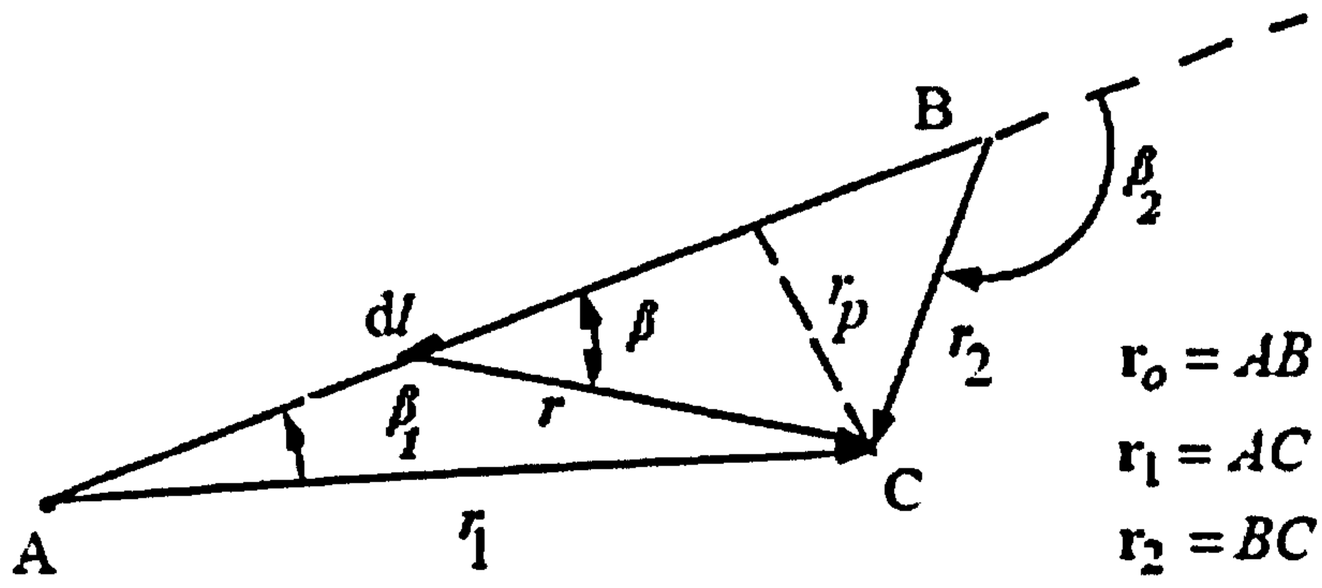

Figure 4.4: Biot-Savart law to determine the velocity induced by a vortex.

The total velocity induced at C by the vortex from A to B could be found by integrating over dl between A and B. Referring to the sketch of Fig. 4.4, the magnitude of the induced velocity on the point C can be expressed in the form:

$$V = \int_A^B \frac{\Gamma_n \sin(\beta) dl}{4\pi r^2} \tag{4.6}$$

The horseshoe vortex is formed by three different components (Figure 4.5):

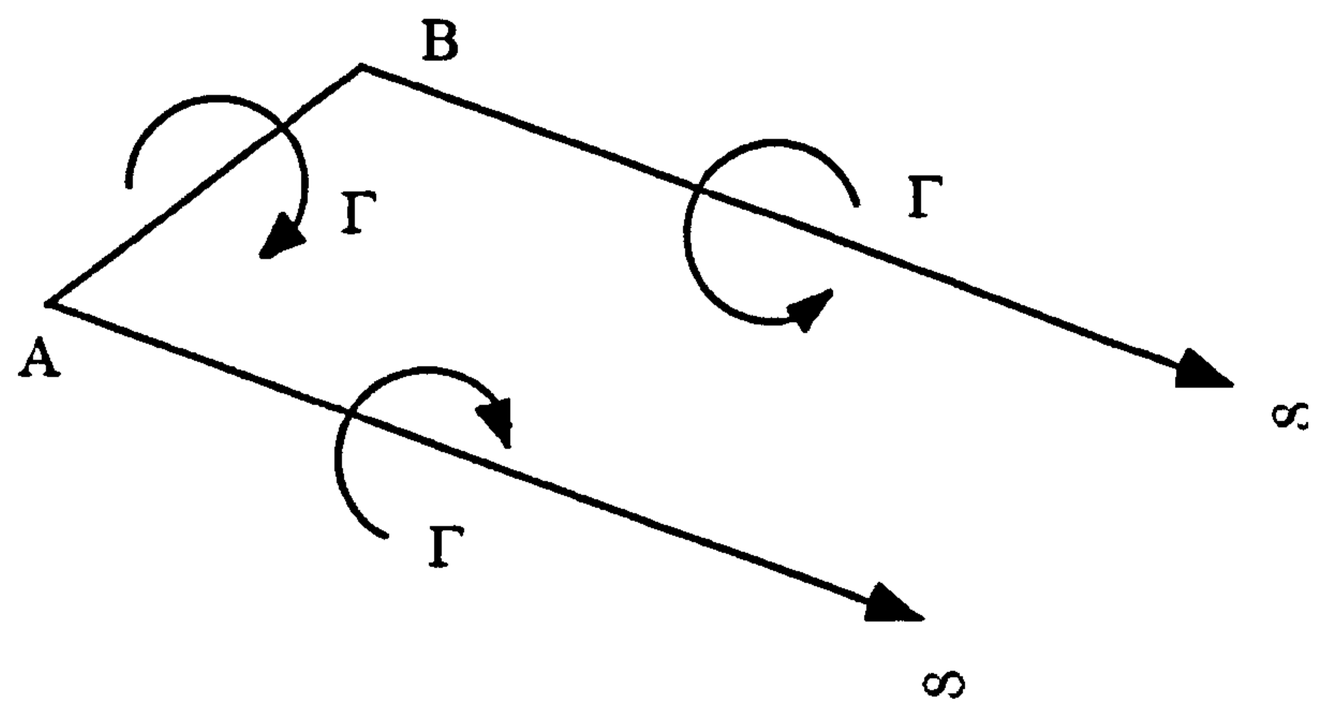

Figure 4.5: "Representative" horseshoe vortex.

A-B	is the vortex contained in each element of the wing surface.
A-∞	is a vortex going from the right edge of the element to infinity.
B-∞	is a vortex going from the left edge of the element to infinity.

Equation 4.5 is used to calculate the effects induced by each vortex separately. Let us start from the segment AB, with the vorticity vector directed from A to B. It can be demonstrated, with some mathematical manipulations, that the magnitude of the induced velocity is:

$$V = \frac{\Gamma_n}{4\pi r_p}\int_A^B \sin\beta d\beta = \frac{\Gamma_n}{4\pi r_p}\left(\cos\beta_1 - \cos\beta_2\right) \qquad (4.7)$$

Let r_0 r_1 and r_2 designate the vectors AB, AC and BC, respectively, as shown in Figure 4.4. Then, the following relations can be written:

$$r_p = \frac{\left|\vec{r}_1 \times \vec{r}_2\right|}{r_0}$$

$$\cos\beta_1 = \frac{\vec{r}_0 \bullet \vec{r}_1}{\left|\vec{r}_0\right|\left|\vec{r}_1\right|} \qquad (4.8)$$

$$\cos\beta_2 = \frac{\vec{r}_0 \bullet \vec{r}_2}{\left|\vec{r}_0\right|\left|\vec{r}_2\right|}$$

Substituting Eqn. 4.8 into Eqn. 4.7 yields, after some mathematical manipulations:

$$\vec{V} = \frac{\Gamma_n}{4\pi}\frac{\vec{r}_1 \wedge \vec{r}_2}{\left|\vec{r}_1 \wedge \vec{r}_2\right|^2}\left[\vec{r}_0 * \left(\frac{\vec{r}_1}{\left|r_1\right|} - \frac{\vec{r}_2}{\left|r_2\right|}\right)\right] \qquad (4.9)$$

As already mentioned, points A and B are representative of the edges of the horseshoe vortex in each element of the wing. Point C is used as the control point. Such control points are used as reference points to calculate the velocity induced by the vortices, the strength of the vortices and, consequently, the local lift and drag. In other words, each element of the wing is associated with its control point that is also used to assign the boundary conditions of the flow. Denote the coordinates of points A, B, C respectively with:

$A=A(x_{1n}, y_{1n}, z_{1n})$

$B=B(x_{2n}, y_{2n}, z_{2n})$

$C=C(x_m, y_m, z_m)$

where

n is an index to denote the n-th panel

m is an index to denote the m-th control point.

The aerodynamic reference frame has the same orientation that the structural frame of reference. It is shown below (Figure 4.6). With the symbols $\vec{i}, \vec{j}, \vec{k}$ are denoted the directions (unitary vectors) along the axes X, Y and Z respectively.

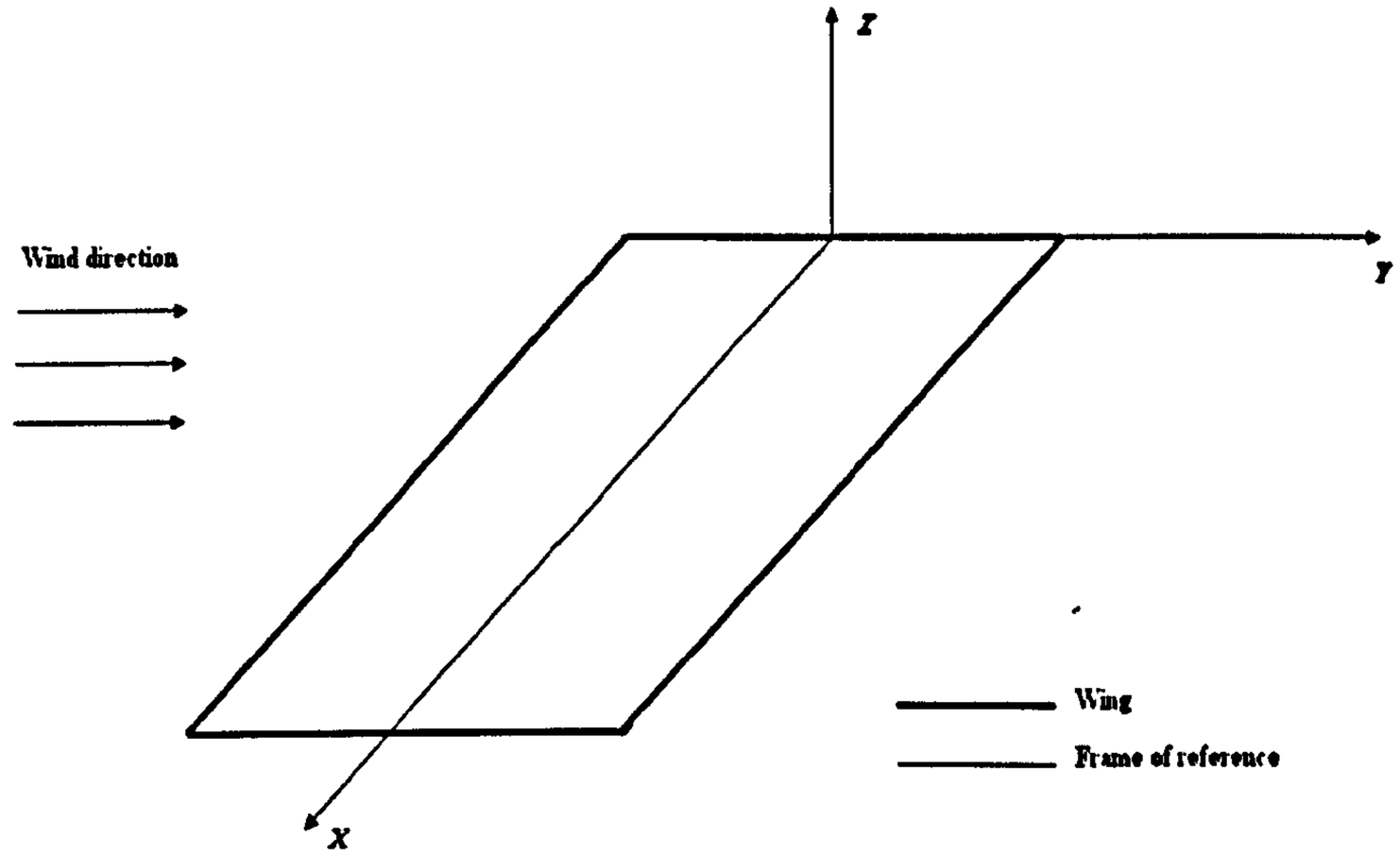

Figure 4.6: Frame of reference of the aerodynamic model.

The velocity induced by the vortex AB, after some mathematical manipulations, can be expressed as a function of the coordinates of the points A, B and C as follows:

$$\vec{V}_{AB} = \frac{\Gamma_n}{4\pi}[Factorial_1][Factorial_2] \tag{4.10}$$

where

$$\begin{aligned} Factorial_1 = \{&-[(x_m - x_{1n})(z_m - z_{2n}) - (x_m - x_{2n})(z_m - z_{1n})]\vec{j} + \\ &[(y_m - y_{1n})(z_m - z_{2n}) - (y_m - y_{2n})(z_m - z_{1n})]\vec{i} + \\ &+[(y_m - y_{2n})(x_m - x_{1n}) - (y_m - y_{1n})(x_m - x_{2n})]\vec{k}\}/\{[(x_m - x_{1n})(z_m - z_{2n}) + \\ &-(x_m - x_{2n})(z_m - z_{1n})]^2 + [(y_m - y_{1n})(z_m - z_{2n}) - (y_m - y_{2n})(z_m - z_{1n})]^2 + \\ &+[(y_m - y_{2n})(x_m - x_{1n}) - (y_m - y_{1n})(x_m - x_{2n})]^2\} \end{aligned} \tag{4.11}$$

and

$$Factorial_2 = \{[(y_{2n}-y_{1n})(y_m-y_{1n})+(x_{2n}-x_{1n})(x_m-x_{1n})+$$
$$+(z_{2n}-z_{1n})(z_m-z_{1n})]/\sqrt{(x_m-x_{1n})^2+(y_m-y_{1n})^2+(z_m-z_{1n})^2}+$$
$$-[(y_{2n}-y_{1n})(y_m-y_{2n})+(x_{2n}-x_{1n})(x_m-x_{2n})+$$
$$+(z_{2n}-z_{1n})(z_m-z_{2n})]/\sqrt{(x_m-x_{2n})^2+(y_m-y_{2n})^2+(z_m-z_{2n})^2}\} \tag{4.12}$$

The vortex starting from the point A to the infinity induces the following velocity:

$$V_{A\infty}=\frac{\Gamma_n}{4\pi}\left[\frac{(z_m-z_{1n})\vec{j}+(y_{1n}-y_m)\vec{k}}{(z_m-z_{1n})^2+(y_{1n}-y_m)^2}\right]\left[1+\frac{(x_m-x_{1n})}{\sqrt{(x_m-x_{1n})^2+(y_m-y_{1n})^2+(z_m-z_{1n})^2}}\right] \tag{4.13}$$

The vortex starting from the point B to the infinity induces the following velocity:

$$V_{B\infty}=\frac{\Gamma_n}{4\pi}\left[\frac{(z_m-z_{2n})\vec{j}+(y_{2n}-y_m)\vec{k}}{(z_m-z_{2n})^2+(y_{2n}-y_m)^2}\right]\left[1+\frac{(x_m-x_{2n})}{\sqrt{(x_m-x_{2n})^2+(y_m-y_{2n})^2+(z_m-z_{2n})^2}}\right] \tag{4.14}$$

At the m-th control point the total velocity, $\vec{V}_{m,n}$, induced by the horseshoe vortex representing the n-th surface element is the sum of the components given by Eqn. (4.10, 4.13, 4.14). Examining these equations it can be seen that,

$$\vec{V}_{m,n}=\vec{C}_{m,n}\Gamma_n \tag{4.15}$$

where the influence coefficients $\vec{C}_{m,n}$ depend on the geometry of the n-th horseshoe vortex and on its distance from the control point of the m-th panel. As the governing equation is linear, the velocities induced by the 2N vortices (N are the vortices of the semi-wing and the wing is symmetric) are added together to obtain the total induced velocity at the m-th control point

$$\vec{V}_m = \sum_{1}^{2N} \vec{C}_{m,n} \Gamma_n \tag{4.16}$$

It is noted that $2N$ equations are obtained, one for each control point. In order to determine the resultant induced velocity of any control point and the strengths Γ_n of the $2N$ horseshoes vortices, the boundary conditions must be applied. The surface is considered as a streamline. In other words, the resultant flow must be tangential to the wing's surface (Figure 4.7).

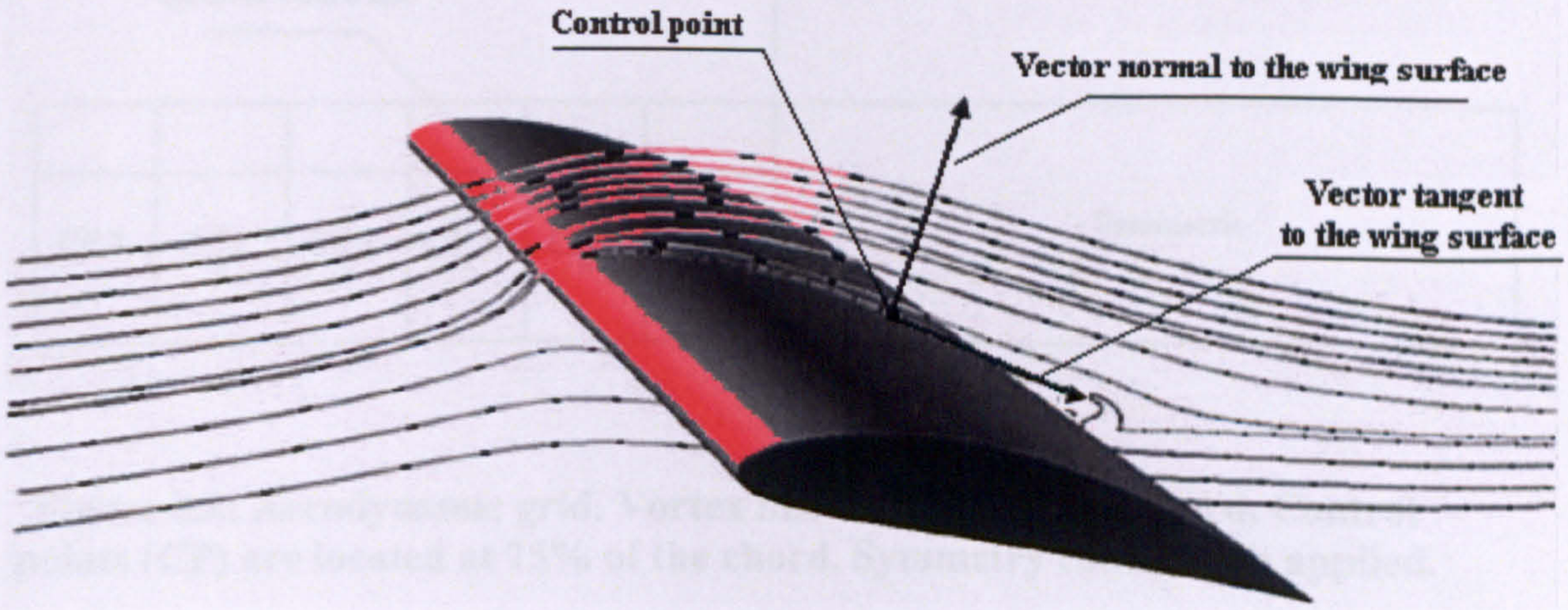

Figure 4.7: Boundary condition applied at the control point. The velocity must be tangent to the wing surface.

By denoting the dihedral angle of the wing with Φ and the slope of the main camber line at the control point by Δ, the boundary condition can be expressed, for each control point as follows:

$$\dot{w}_m + \dot{u}_m \tan\Phi + V_\infty [\alpha - \Delta] = 0 \tag{4.17}$$

where $\dot{w}_m$ and $\dot{u}_m$ are the components of the induced velocity along Z and X axis respectively.

By using Equations 4.16 and 4.17, it is possible to calculate each vortex strength Γ_n. Once these values are known, lift and drag of each element can be easily obtained.

Grid used in this work is shown in Figure 4.8. The wing is symmetric, not only in terms of geometrical properties, but also in terms of vortex magnitude and distribution. Only one panel has been used chordwise. For the vortex lattice method, in fact, it appears important to use a relatively large number of spanwise rows and a relatively small number of chordwise panels [94]. Vortex line is situated at 25 % of the chord. Control points (CP) are situated at 75% of the chord

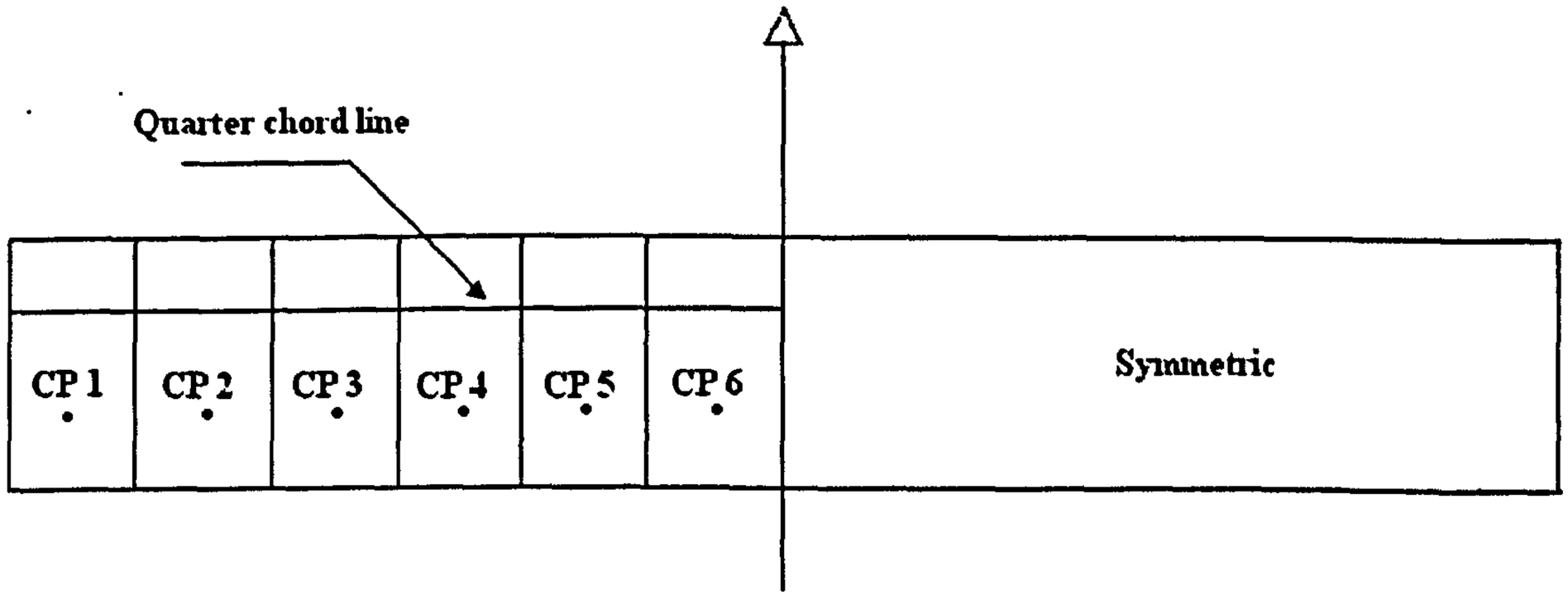

Figure 4.8: Aerodynamic grid. Vortex line is at 25% of the chord. Control points (CP) are located at 75% of the chord. Symmetry condition is applied.

4.2.3 The interaction between the aerodynamic field and the elastic response

A key parameter to study the interactions between the aerodynamic field and the static deformations is the relative position of the wing box inside the airfoil. Of particular relevance, is the distance between the aerodynamic centre and the shear centre of each cross section. It determines the amount of torsion that can be generated by the aerodynamic lift. This distance is requested as input in the aeroelastic tool.

The lift resultant is applied at 25% of the chord [95] of each element of the grid for two reasons:

1. Only subsonic regime has been considered.
2. Only symmetric or quasi-symmetrical airfoils have been used. This assumption does not affect the physical meaning of the results.

The shear centre of the whole airfoil has been assumed to be coincident with that of the wing box. The relative position of a wing box inside the airfoils is shown in Figure 4.9.

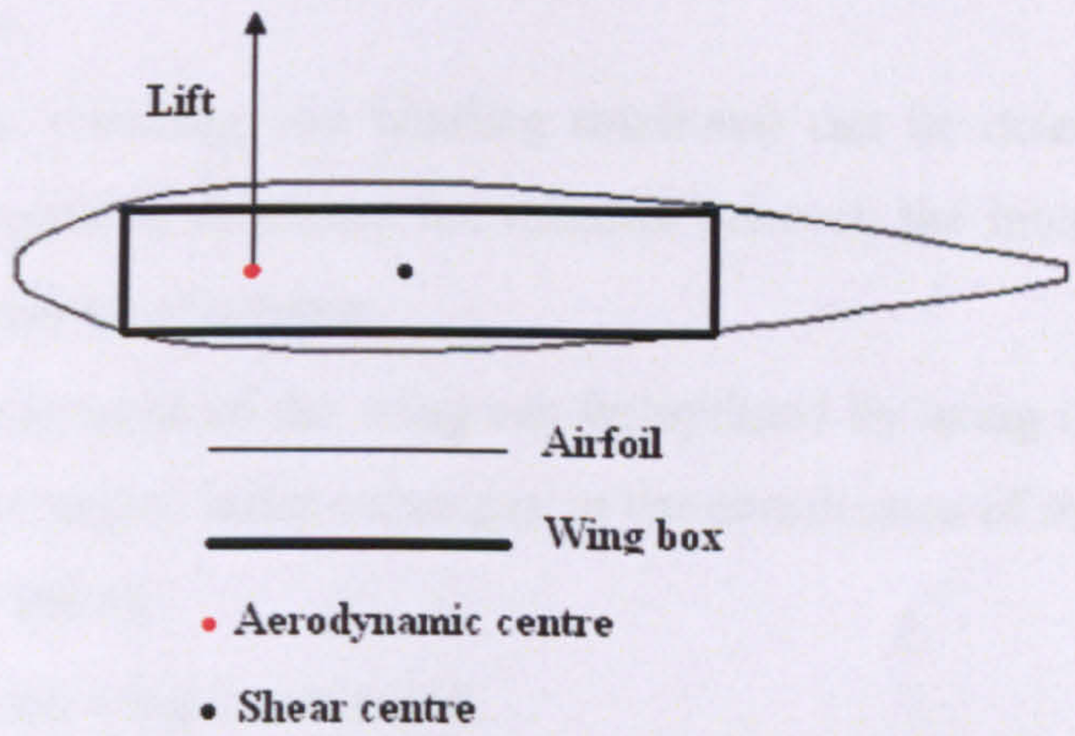

Figure 4.9: Position of the wing box inside each airfoil.

The interaction between the aerodynamic and elastic models can be summarised in the following steps:

- The span wise lift distribution *q(X)* is calculated when the geometric characteristics of the wing and the distribution of angles of attack are known. For each element of the aerodynamic grid (shown in Figure 4.8) a resultant lift is evaluated and applied at 25 % of the chord (Figure 4.10).

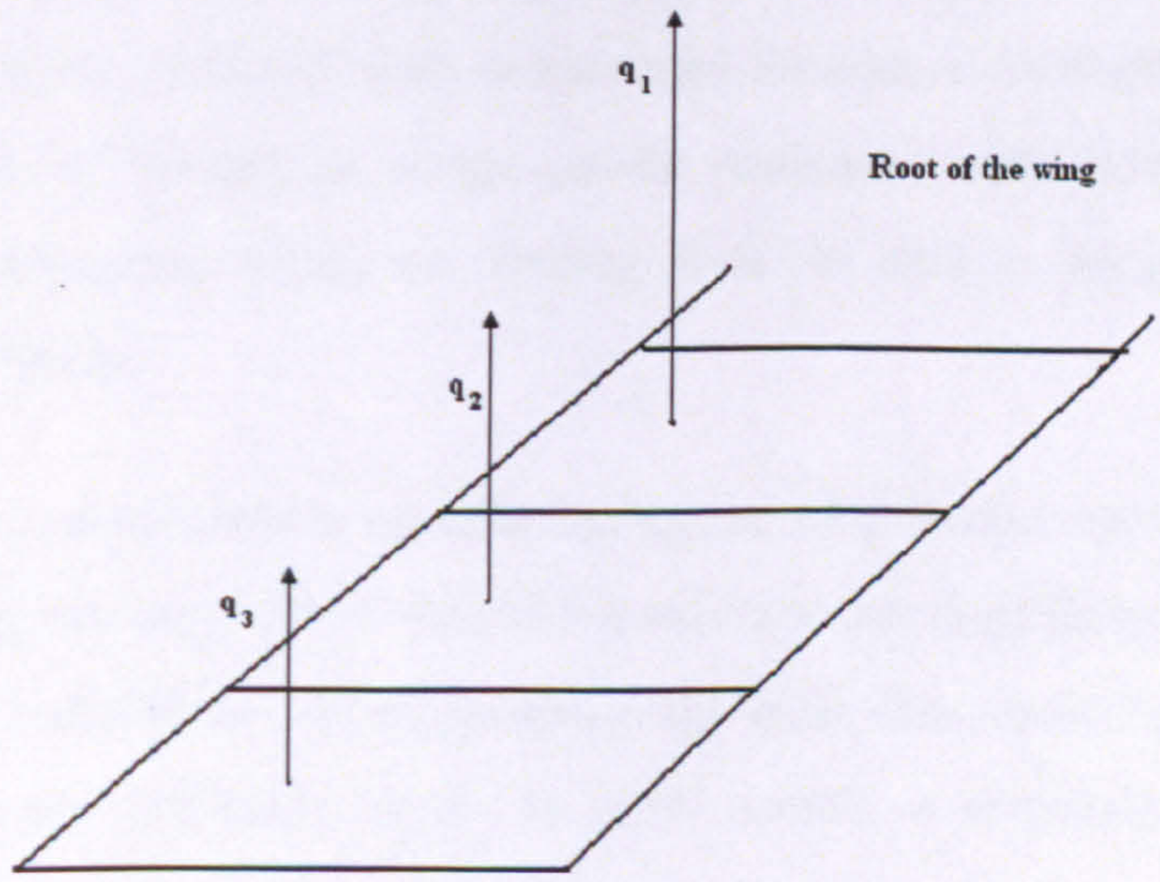

Figure 4.10: Lift distribution *q(X)* along the span. The force is evaluated in each element of the aerodynamic grid and applied at 25% of the chord.

- Once the lift distribution *q(X)* is known, it is possible evaluate the bending moment *M(x)* and the twisting moment *T(x)* by using Eqn. 4.1 and 4.2. Such equations describe the relation between the external loads (lift distribution) and the internal loads.
- The deformations (twisting and bending rotations) can be determined by using Eqn. 4.4. Such equation describes the relation between the internal loads an the structural deformations of a beam.
- Geometric characteristics of the wing can be updated by using the deformations. Bending and twist angles induce changes in the coordinates of the points used by the vortex-lattice theory.
- Lift of the deformed wing is evaluated.
- This procedure is repeated until the deformations obtained are less than 1% of those obtained from the previous calculation.

4.3 The effect of bend-twist coupling on aircraft range

The static aeroelastic tool, developed in Section 4.2, can be used to determine aeroelastic equilibrium and the final deformed shape of several wing topologies, having different elastic distributions of *EI, GJ* and *K* along the span. The model can be particularly useful for investigating potential beneficial effects of anisotropic composite materials, obtained with unbalanced laminates. Performances, range in this case, of several composite wings can be compared with those of a reference structure: an orthotropic wing, i.e. having K=0. In such a wing, no bend-twist coupling effect exists.

Generally, there are potentially an infinite number of different distributions of fibre angles $\xi(x)$ along the span of the wing. This would result in different distributions of "nose up" and "nose down" rotations along the span, that could be investigated in order to obtain the optimum range. In other words, a constrained optimisation problem could be rigorously formulated.

Since the wing box is idealised as rectangular and symmetric, optimisation design variables are thicknesses of vertical walls $t_v(x)$, thicknesses of horizontal walls $t_h(x)$ and fibres angle distribution $\xi(x)$ along the span.

The optimisation can be formulated as follows:

- To find the distribution of vertical thicknesses $t_v(x)$, horizontal thicknesses $t_h(x)$ and fibres angles distribution $\xi(x)$ along the span of the box in such a way as to maximize the range of the aircraft.

The following constraints must be satisfied:

1. Strength constraint: the structure must be able to carry the design load.
2. At the design load, the wing tip's vertical displacement must not exceed 10% of the wing length.
3. In uniform horizontal flight, the lift of the optimised wing must differ by less than 5% with respect to the lift of the reference wing.

The meaning of the first constraint is quite clear: the structure must not fail when subjected to the design load. Tsai-Wu criterion has been used in the ply by ply analysis. The second constraint has been imposed to avoid large deformation of the structure. Numerical value of 10% has been arbitrary chosen together with Airbus UK. The third one has been imposed to avoid large changes in the lift when exploring new stiffness distribution along the span. Numerical value of 5% has been, also in this case, arbitrary chosen.

The problem could be solved by using a commercial optimisation tool. Optimisation algorithms, however, are often used as a "black box" technique, while the first aim of a low fidelity model should be having a good comprehension of the phenomena described. In this case, the formulation of the problem is quite simple. The solution in terms of $t_v(x)$ $t_h(x)$ and $\xi(x)$ can be based on physical understanding. Furthermore, an optimization technique may undergo several iterations until it

reaches an optimum while having a physical understanding of the problem allows a reduction of the number of solution investigated.

For this optimisation, there is no physical reason to have part of the wing with a "nose up" rotation and other parts with a "nose down". Therefore, to obtain a range improvement, a global "nose up" or "nose down" rotation along the entire span is required. Only two kinds of solution are therefore investigated.

4.3.1 Potential solution strategies

Two kinds of solution are investigated to find the optimum range. The first one consists of a constant fibre angle distribution along the span. All of the fibres (44% inside each laminate, as mentioned in section 4.2.1) along the span are oriented with the same angle. Fibre angles within the interval [-45, 45] degrees are investigated, with a step of 5 deg. This type of solution has been suggested by the results obtained with a standard genetic algorithm [21] (GA). An example of such a distribution is shown in Figure 4.11.

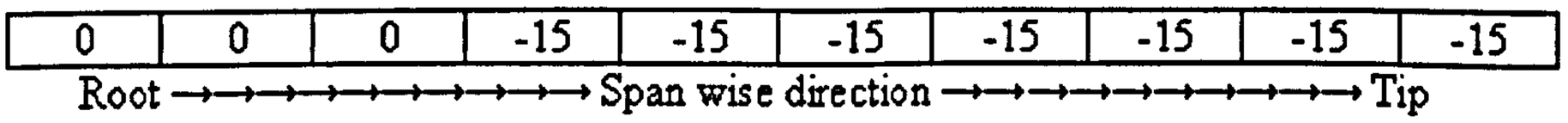

Figure 4.11: Example of constant angle distribution on the top and bottom laminates of the wing box.

The root of the wing, remains orthotropic to guarantee a high level of bending stiffness in that part subjected to the maximum bending load. Consequently, anisotropy is investigated for lengths greater than 30% of the span. This starting point has been arbitrary chosen: it is not far from the root in such a way that the anisotropy can be investigated in the most part of the wing and, on the other hand, the weight increase obtained in the anisotropic wings is moderate. Preliminary analyses have shown that anisotropy in the root of the wing makes a significantly heavier structure yet an excessive weight penalty cannot be accepted. An example will be discussed in section 4.4. In addition, the vertical walls of the wing box are assumed to be orthotropic for two reasons. Orthotropy increases the bending stiffness of the structure. Furthermore, in a realistic wing box, vertical walls are

usually short. If they were considered as anisotropic, their contribution to bend-twist coupling would be in any case negligible.

The second type of solution is a progressive distribution of "nose up" or "nose down" effect along the span of the structure. In order to evaluate this kind of solution, it is necessary to calculate the fibre angle ξ_0 giving the maximum bend-twist compliance, i.e. the angle which gives the maximum "nose up" or "nose down" rotation when a bending load is applied. Such an angle depends on the geometry of the cross section of the wing box, and also on its aspect ratio (*H/C*). The wing, initially orthotropic, is divided into several sections along its span to simplify the analysis. Starting from the section placed at 30% of the span (also in this type of solution the root of the wing remains orthotropic) an amount of bend-twist coupling is given. For the "nose-up" case, fibre angles varying in 5 degrees increments are investigated (or -5 degrees for "nose down" case). An example of this first step of the solution is given in Figure 4.12.

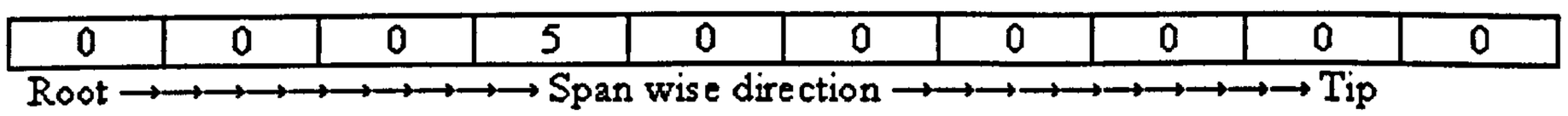

Figure 4.12: Fibre angle distribution at the top and bottom laminates of the wing box: Step 1 of "progressive nose up distribution".

Lift and range are evaluated after the first step. Then, the fibre angle of the same wing segment is increased (or decreased) by 5 degrees and the range is re-evaluated. This process is stopped when the value of fibre angle becomes equal to ξ_0 and consequently the maximum bend-twist compliance is obtained in that particular segment of the wing box. Then, the process is repeated in the neighbouring section and so on. The process terminates when the value ξ_0 is reached in each segment of the wing box. All the steps are shown in Figure 4.13.

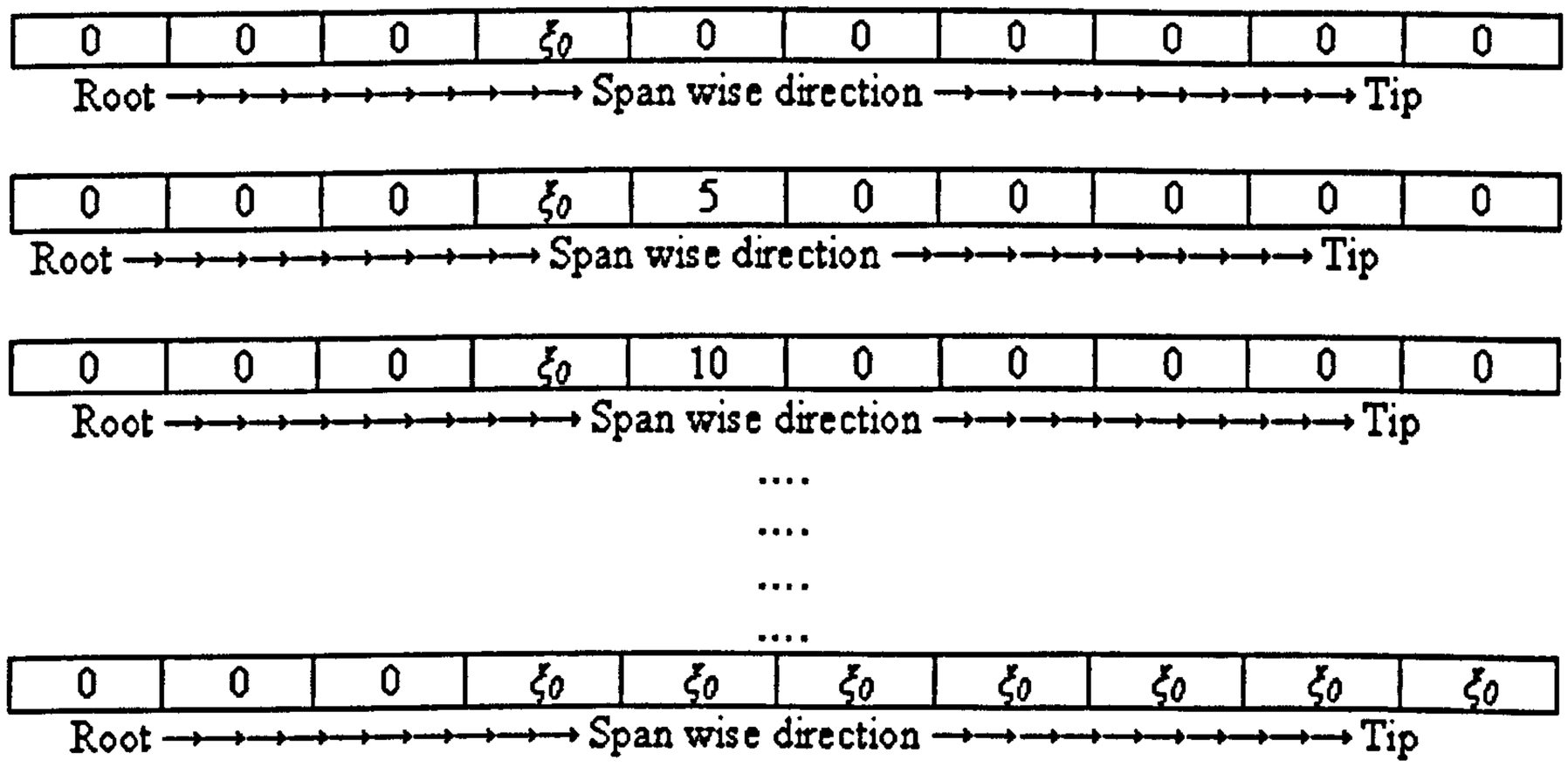

Figure 4.13: Fibre angle distribution at the top and bottom laminates of the wing box: description of progressive fibres angle distribution.

These two kinds of fibre distribution along the span cannot be used without a check on the thickness of the wing box. Each wing investigated, in fact, must be able to carry the design load and to satisfy all of the constraints.

4.3.2 Steps required to complete one analysis

The steps of the whole procedure can be summarised as follows:

- The length of the beam, the aerodynamic chord, the dimensions of the wing box, the distance between the aerodynamic centre and the shear centre, the load factor n_l and the cruise speed of the aircraft are given as input data.
- The orthotropic wing is designed. In other words, minimum thicknesses of the horizontal and vertical walls of the wing box are calculated in such a way that the structure is able to carry a design load $L_{DESIGN} = n_l L$, where L is the lift of uniform horizontal flight obtained after the aeroelastic iteration described in section 4.2.
- All of the evolving anisotropic wing designs, obtained by using one of the potential solution strategies described in section 4.3.1, are sized in such a way that the structure is able to carry the design load L_{DESIGN}. It is the same load previously

used to design the orthotropic wing, and to satisfy the constraints. Thicknesses are increased when the Tsai-Wu [21] failure criterion is not satisfied.

- The range of all wing designs is evaluated and compared with the reference wing.

4.3.3 Range evaluation

Among all the possible performance measures to improve, range has been chosen because it implies heavy financial savings for the airlines. This choice has also been recommended by the sponsor of this PhD project: Airbus UK.

Range is defined as the maximum distance that an aircraft can cover with a fixed amount of fuel. Breguet's formulation [96] has been used for its evaluation. According to this theory, the range of an aircraft moving at constant altitude, angle of attack and specific fuel consumption, can be evaluated by

$$R = \frac{2}{c_T}\sqrt{\frac{2}{\rho S}}\frac{\sqrt{C_l}}{C_d}\left(W_{takeoff} - W_{landing}\right) \tag{4.18}$$

where

R is the aircraft's range

S is the wing surface

c_T is the specific fuel consumption

C_d is the drag coefficient

C_l is the lift coefficient

$W_{takeoff}$ is the weight of the aircraft before the take-off.

$W_{landing}$ is the weight of the aircraft when the flight terminates. All the fuel has been consumed.

Instead of a direct measure of the aircraft's range, for the sake of simplicity, an index I with the same meaning can be used to compare different solutions with the same wing surface, take off and landing weight and specific fuel consumption. It can be written as follows:

$$I = \frac{\sqrt{C_l}}{C_d} = \frac{\sqrt{C_l}}{C_{d0} + \frac{C_l^2}{\lambda_{eq}}} = \frac{\sqrt{L}}{D} \tag{4.19}$$

where

C_{d0} is the zero lift drag coefficient

λ_{eq} is the wing's aerodynamic aspect ratio.

A portion of the lift is evaluated in each element of the aerodynamic grid shown in Figure 4.10 by using the vortex-lattice model. All these forces can be summed and the total lift L therefore obtained.

The drag D can be easily evaluated by using the following formula [97]:

$$D = \frac{1}{2}\rho {V_\infty}^2 S C_d \tag{4.20}$$

where the drag coefficient C_d can be expressed as follows:

$$C_d = C_{d0} + \frac{C_l^2}{\pi \frac{L^2}{S} e} \tag{4.21}$$

The lift coefficient is

$$C_l = \frac{L}{0.5\rho {V_\infty}^2 S}$$

and

e is the Oswald efficiency factor. It depends on the lift distribution and it has been evaluated by using formula presented in the literature [97, 56]

Trim of the aeroplane has not been kept into account.

The total weight of the aircraft ($W_{takeoff}$), used in Eqn. 4.18, has been considered as a constant in every wing. It can be written as:

$$W_{takeoff} = W_{st} + W_{pay} + W_{fuel} \tag{4.22}$$

where

W_{st}	is the structural weight of the aircraft
W_{pay}	is the payload
W_{fuel}	is the weight of the fuel

When a heavier wing is obtained from the optimisation, the structural weight increases. Therefore, the payload is diminished and consequently, a financial penalty is obtained. However, a moderate weight increase of the wing is often negligible in terms of overall aircraft weight. Examples of three aeroplanes, DC8-55, DC10-10, A300B2 [98, 99] can be provided. A 20% increase of the structural weight of the wing, for example, implies 2% increase of the maximum take-off weight. This value is still acceptable. The impact of the wing, in reality, is even less accentuated, since the weight increase is caused only by the wing box. Numerical values are summarised in table 4.1.

Table 4.1: Impact of a 20% heavier wing on the global aircraft weight [92, 93].

Aircraft	Wing weight [kg]	Maximum take off weight [kg]	Impact of a 20% wing weight increase on the aircraft's maximum take off weight
DC8-55	15205	140600	2%
DC10-10	22307	195045	2%
A300B2	20271	165000	2%

Range evaluation would be consequently not affected even if the payload was considered as a constant.

4.4 Numerical examples

An unswept wing box having the technical characteristics reported in Tables 4.2 and 4.3 has been studied.

Table 4.2: Geometric characteristics of airfoil and wing box.

Aerodynamic chord	1.5 m
Wing length	10 m
Angle of attack of cruise	5°
Cruise speed	220 m/s
Design load factor	4
Distance between aerodynamic centre of pressure and shear centre at each cross section	0.1 m
Height of the prismatic wing box	0.3 m
Chord of the prismatic wing box	0.9 m
C_{d0} of the airfoil [96]	0.028
Airfoil curvature at the control point	0°
Air density	0.43 Kg/m^3

Table 4.3: Elastic properties of the composite material.

E_1	181 GPa
E_2	10.3 GPa
G_{12}	4.55 GPa
ν_{12}	0.28

Each semi-wing has been divided in to 10 segments for the analysis. The orthotropic wing, i.e. the reference structure, shows the thicknesses distribution of Figure 4.14. Results are shown for the semi-wing because of the symmetry.

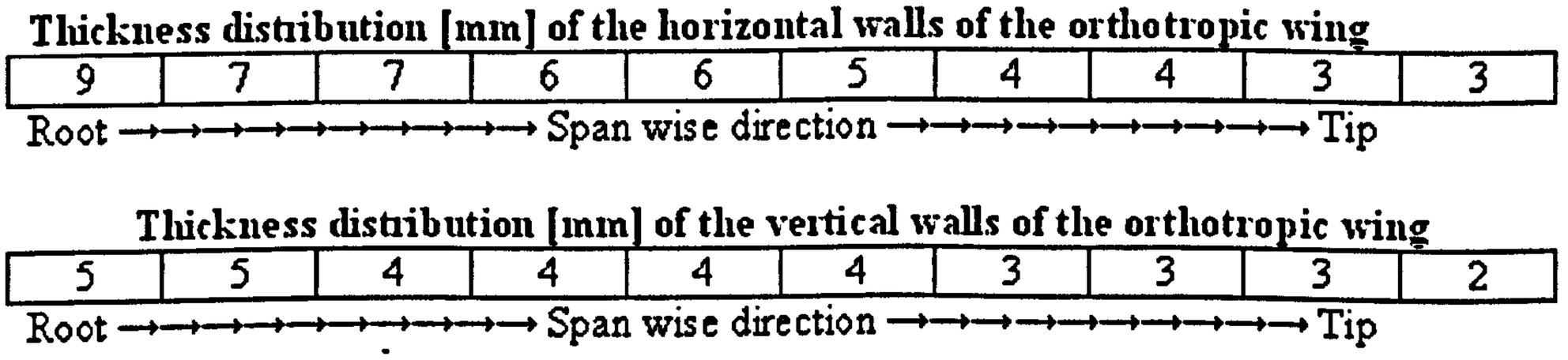

Figure 4.14: Thickness distribution of horizontal and vertical walls for the orthotropic wing. Uniform horizontal flight with an angle of attack of 5°.

The solution (thicknesses and fibre angle distribution) to improve the aircraft's range is shown in Figure 4.15.

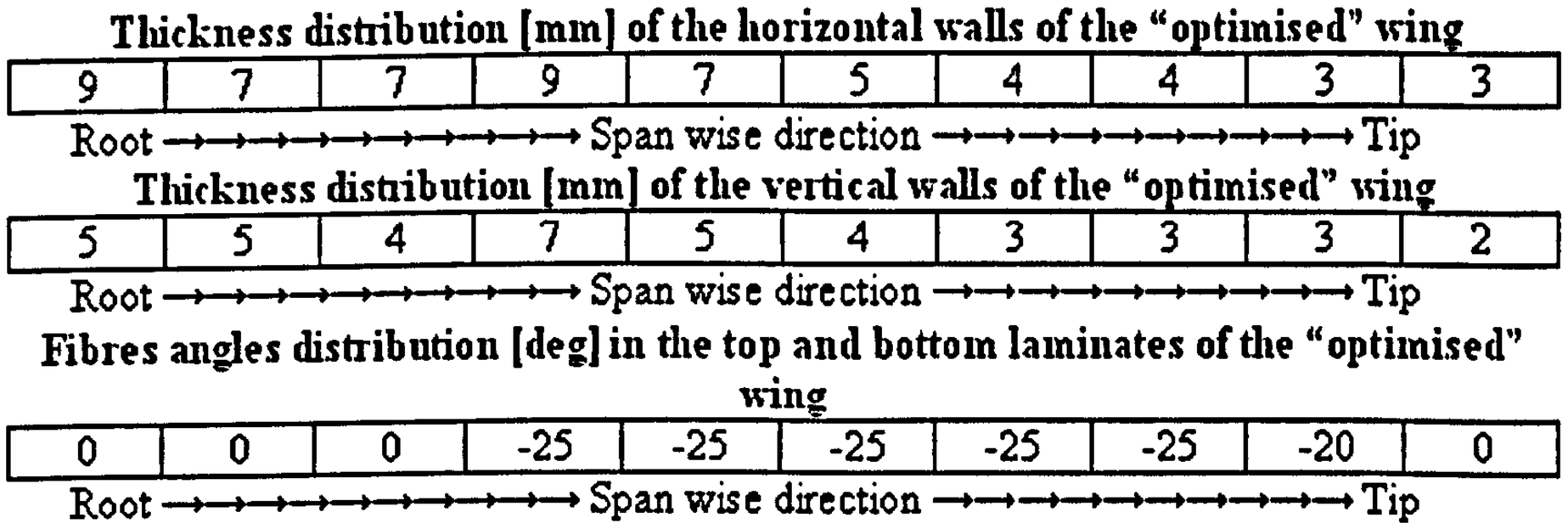

Figure 4.15: Results of the anisotropic wing giving the best range performance. Uniform horizontal flight with an angle of attack of 5°.

The range improvement is found to be 0.8%, but the weight of the "unbalanced composite" structure is 8% greater than the orthotropic one. In this example, a "nose down" rotation is required to obtain an improvement of the index *I* and consequently of the range.

As already explained in section 4.3.1, the potential benefits of anisotropy are investigated starting from a point placed at 30% of the wing. In other words, the root is kept orthotropic. This assumption has been made to avoid unacceptable weight penalties. The analysis is then repeated, allowing the anisotropy at the root of the wing. Results are shown in Figure 4.16.

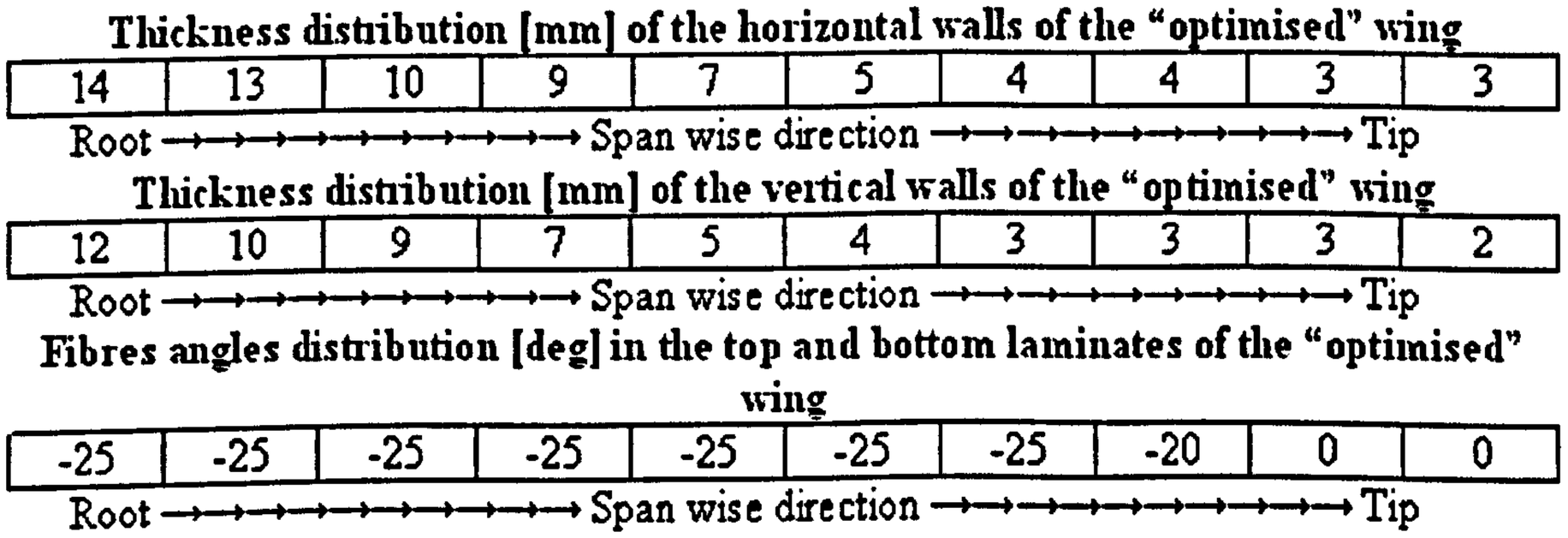

Figure 4.16: Results of the anisotropic wing giving the best range performance. Uniform horizontal flight with an angle of attack of 5°. Anisotropy allowed at the root of the wing.

The range improvement is 2.3%. However, the anisotropic wing is 38.5% heavier than the reference wing. Such weight cannot be accepted.

If the angle of attack of uniform horizontal flight of the same wing is 3° instead of 5, different results are obtained. The orthotropic wing shows the following distribution of thicknesses (Figure 4.17):

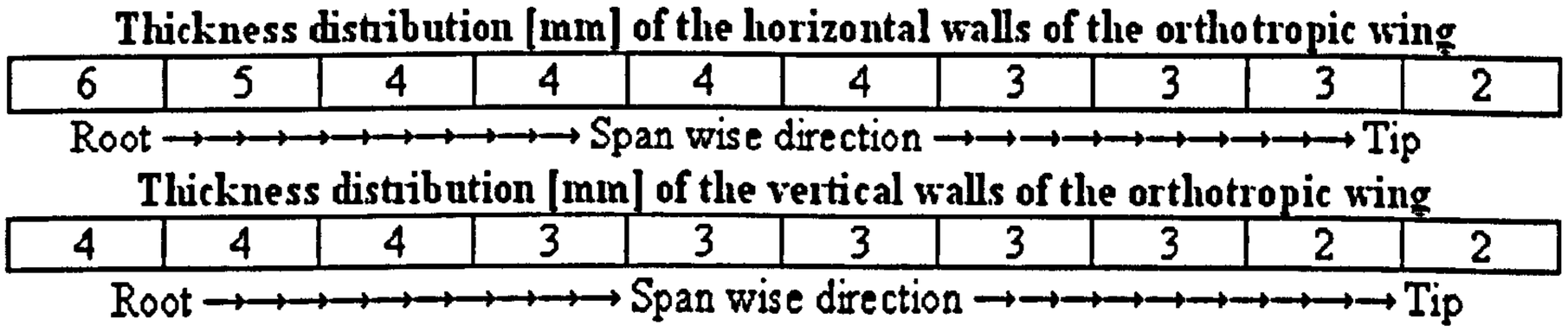

Figure 4.17: Thickness distribution of horizontal and vertical walls for the orthotropic wing. Uniform horizontal flight with an angle of attack of 3°.

Since the angle of attack of uniform horizontal flight is only 3°, the thickness distribution is different and also the kind of bend-twist coupling required to improve the range. A "nose up" rotation is in fact needed. Properties of the "optimised" wing are shown in Figure 4.16.

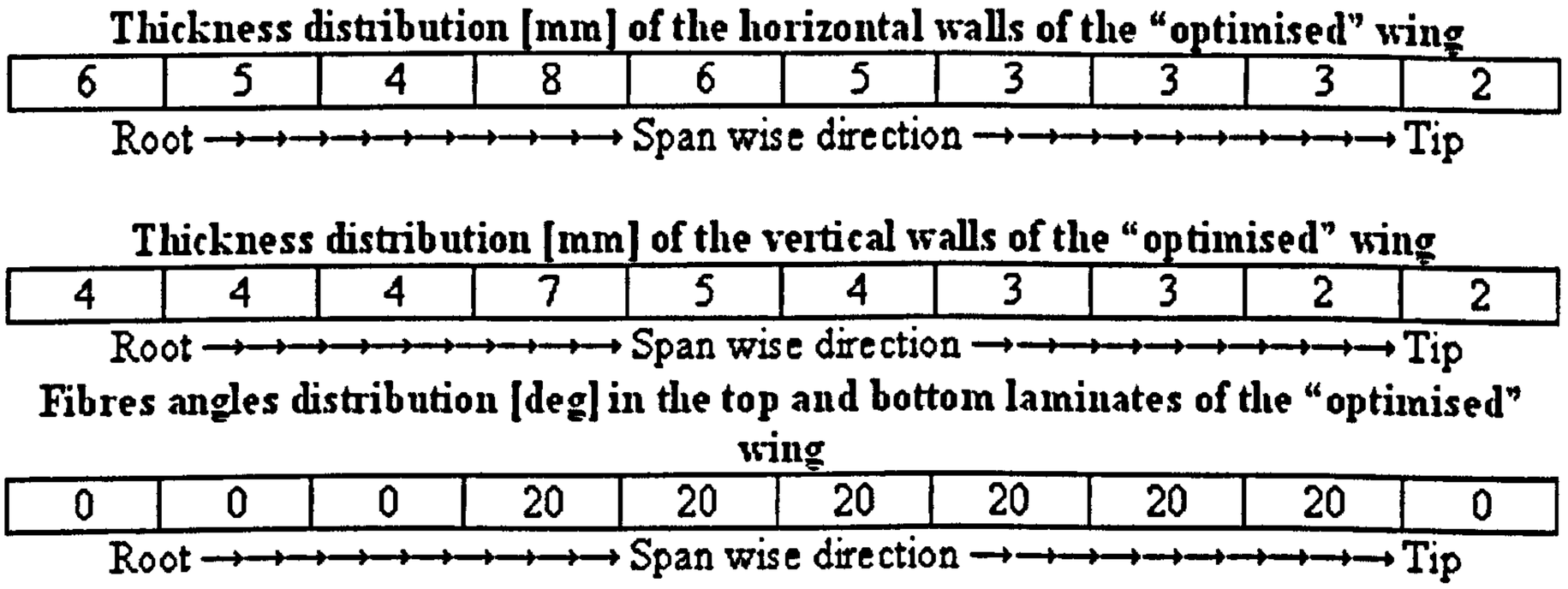

Figure 4.18: Results of the anisotropic wing giving the best range performance. Uniform horizontal flight with an angle of attack of 3°.

Range improvement is 0.5% but a huge increment in the weight (19%) is measured.

4.4.1 Comments on numerical results

After the analyses performed, the following conclusions can be made:

1. Unbalanced laminates can be used to improve the range of the aircraft. The order of magnitude of this improvement, for the cases analyzed, is less than 1%. Even if it appears a relatively poor result, it can imply huge financial savings due to the reduction of fuel consumption [100].
2. In order to carry the same design load of the reference orthotropic wing, the anisotropic structure could be heavier. This fact implies financial losses: part of the lift, in fact, must be used to carry a heavier structure instead of passengers or goods. Of course further investigations should be performed to establish if the savings induced by range improvements are greater then the losses due to a heavier structure.
3. It is important to remark that the percentage of range improvement, although poor, regards the whole aircraft. The percentage of weight increase, although more consistent, concerns the wing only and it is often negligible in terms of aircraft overall weight.
4. A global "nose up" or "nose down" effect is needed to improve aircraft's range, depending on the angle of attack of the rigid wing in uniform horizontal flight (Figure 4.19). The optimum range, is in fact, obtained by maximizing $I=I(C_l)$ (Eqn. 4.19).The corresponding value of C_l is denoted by C_{lmax}. If the design C_l (corresponding to the angle of attack of the rigid wing) lies on the right side of C_{lmax}, a reduction of the angle of attack is required in the deformed wing, in order to maximize the range. Consequently, a "nose down" deformation is needed. On the contrary, a "nose up" deformation is necessary if the initial value of C_l lies on the left of C_{lmax}.

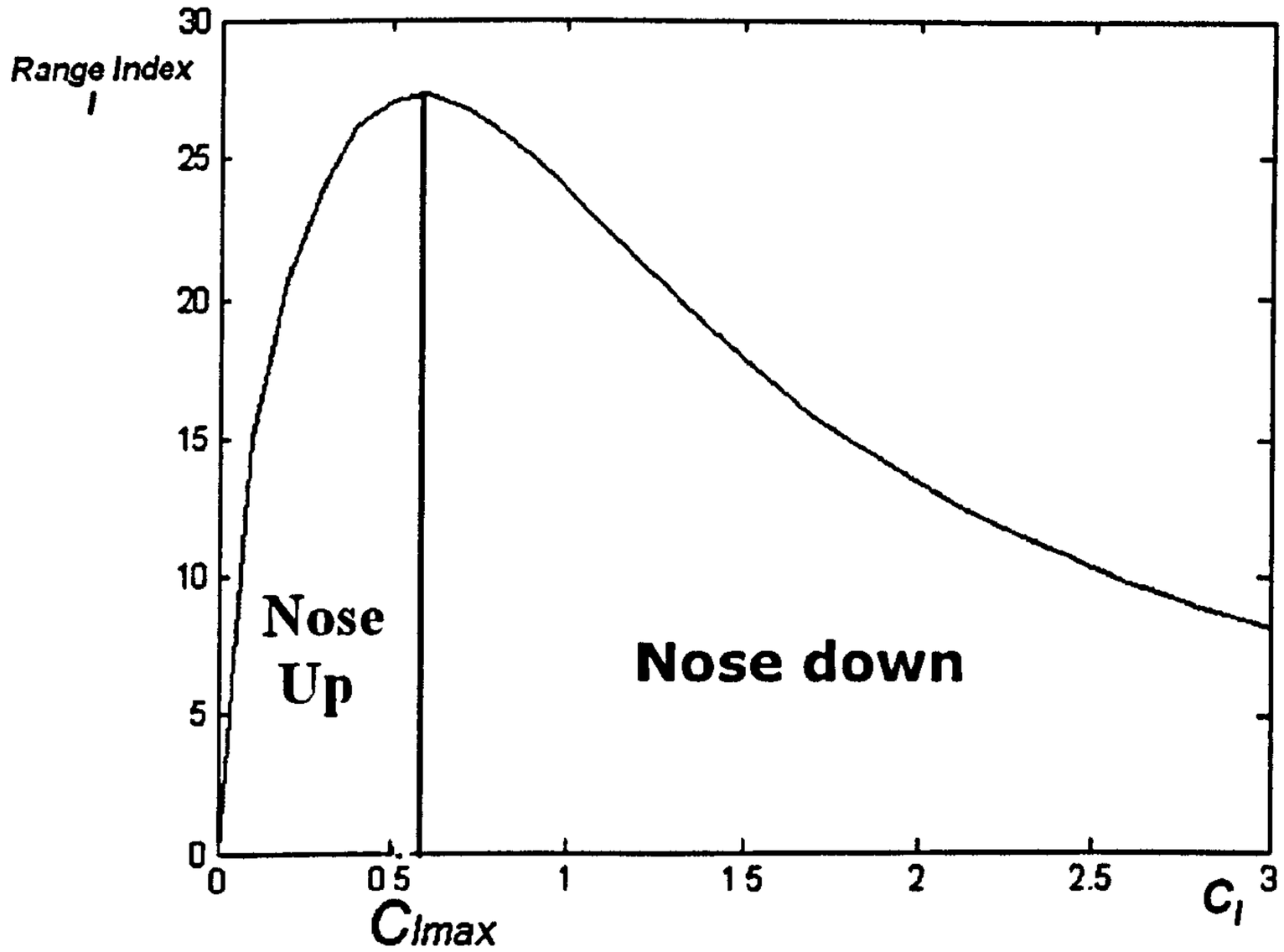

Figure 4.19: Qualitative shape of the function Range Index $I = I(C_l)$. Areas of "nose up" and "nose down" rotation are shown.

4.5 Conclusions

A low fidelity tool has been developed to study the static aeroelastic equilibrium of a wing. The structural part has been modelled by means of a linear analytical beam model. Relevant stiffnesses have been calculated with a novel procedure described in Chapter 3.

The aerodynamic loads have been evaluated by using a vortex-lattice model. The aeroelastic tool has been used to investigate potential improvements on the range induced by unbalanced laminates. Moderate improvements with respect to an orthotropic wing have been measured. However, a weight penalty has also been observed.

Chapter 5
Stiffnesses comparison of a composite box model with a wing like structure

5.1 Introduction

The use of unbalanced composite materials can improve the range of an aircraft but it also induces a negative effect: a heavier wing. It is important, at this point, to understand how the static aeroelastic tool, proposed in Chapter 4, compares with reality. In other words, it is important to understand its limitations, arising from both the aerodynamic and structural models.

From the aerodynamic point of view, the vortex lattice method is widely used by industry to describe not only compressible regimes, but also transonic ones. In this case, correction coefficients, calculated by means of experimental data, are used [101]. This approach has proved itself to be relatively reliable, especially when the height of the wing is negligible with respect to the length.

From the structural point of view it is useful to investigate two aspects. Firstly, it is useful to compare the structural stiffnesses of a composite box with a real wing box, including other components such as stringers, webs and ribs. Secondly, it is important to understand the potential effects of leading and trailing edges on the global stiffnesses of the wing.

5.2 An "equivalent" box to reproduce *EI*, *GJ* and *K* of a real wing like structure.

In order to properly use the static aeroelastic tool, stiffnesses of a real wing structure should be reproduced with sufficient accuracy. It is therefore important to model an "equivalent" box, i.e. a composite box with the same stiffnesses as a real wing.

A comparison between a complete and detailed wing box model and its equivalent box is performed within this section. Airbus UK, the main sponsor of this project,

has provided a wing like structure for such purpose (generic wing box). It is shown in Figure 5.1. This structure is not a complete wing: leading and trailing edges have not been modelled, for example. However, a lot of structural detail such as stringers and ribs are included (Figure 5.1). The structure is not prismatic, like the boxes used in Chapter 4, but this fact does not affect the stiffness evaluation in each cross section.

Questions explored in this thesis include: is it possible to represent such structures simply by using a composite box? Is it possible to match the span wise distribution of all the stiffnesses, *EI*, *GJ* and *K* of a complex structure by using a simplified model?

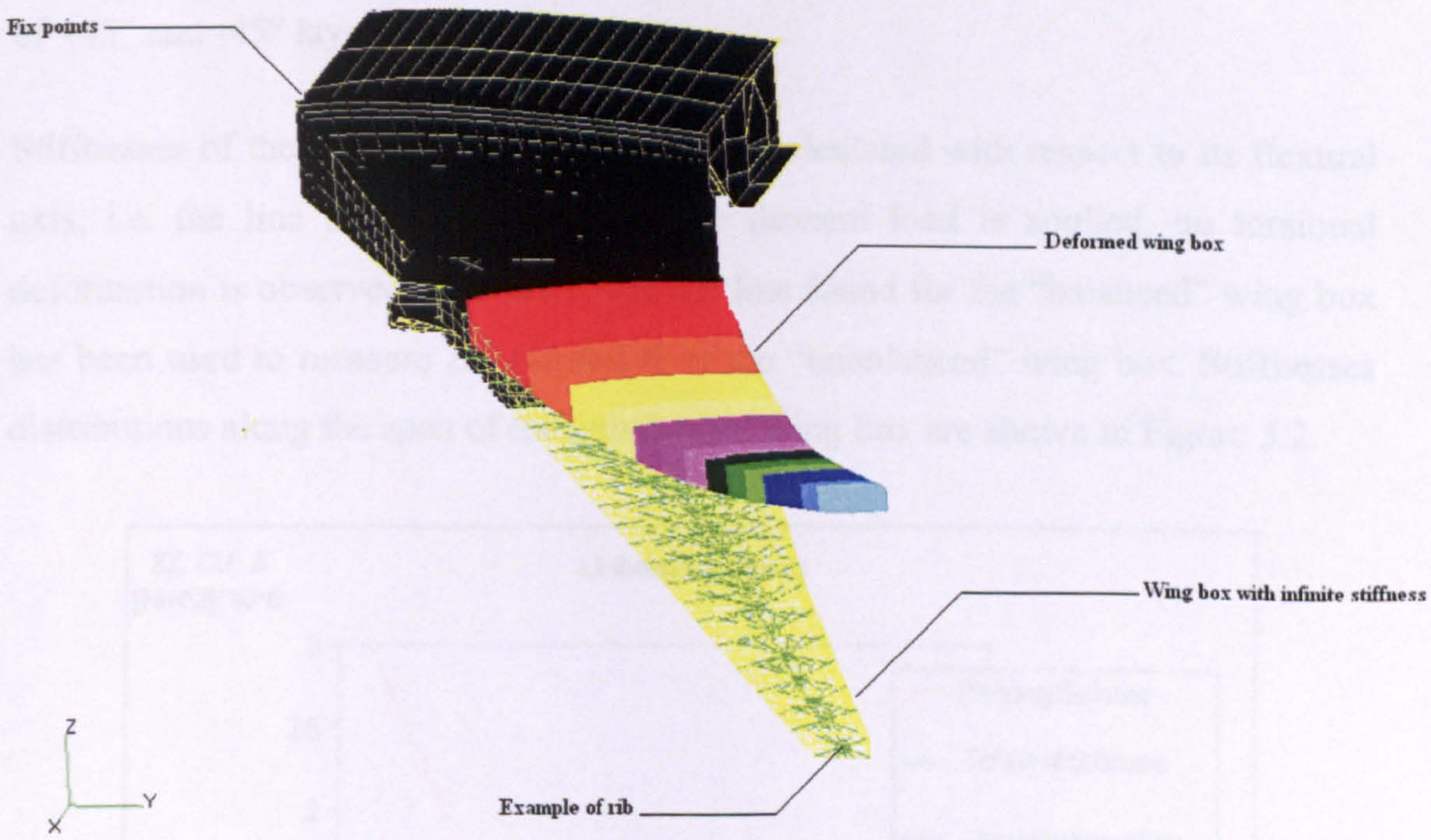

Figure 5.1: An example of a typical, generic wing box used in the aerospace industry.

Analyses with FE models have been performed to answer these questions.

Two different kinds of wing like structure have been analysed. In the first one, the top and bottom skins are made by "unbalanced composite" laminates. These laminates are symmetric and composed of 44% 0 degree fibres, 44% 45 degree

fibres and 12% 90 degree fibres. All fibre angles are with respect to the local frame of each laminate. Vertical walls are built with 0° fibres laminates. Elastic properties of a composite layer are resumed in Table 2.1. The remaining part of the wing box is made of aluminium. As the Young's modulus of aluminium has a lower value than that of the composite laminate, the effects of the remaining structural parts on the global stiffnesses are minimised. If the impact of stringers and ribs on the global stiffnesses are not negligible, it would be even less negligible in a wing built entirely with composites materials.

The second structure is identical to the first one, with the exception that the laminates used for the top and bottom skins have changed. Here, the unbalanced laminates are replaced by the equivalent balanced laminates, i.e. the same number of +45° and -45° layers.

Stiffnesses of the real wing like structure are calculated with respect to its flexural axis, i.e. the line such that, when a pure flexural load is applied, no torsional deformation is observed. The same flexural line found for the "balanced" wing box has been used to measure *EI*, *GJ* and *K* of the "unbalanced" wing box. Stiffnesses distributions along the span of the unbalanced wing box are shown in Figure 5.2.

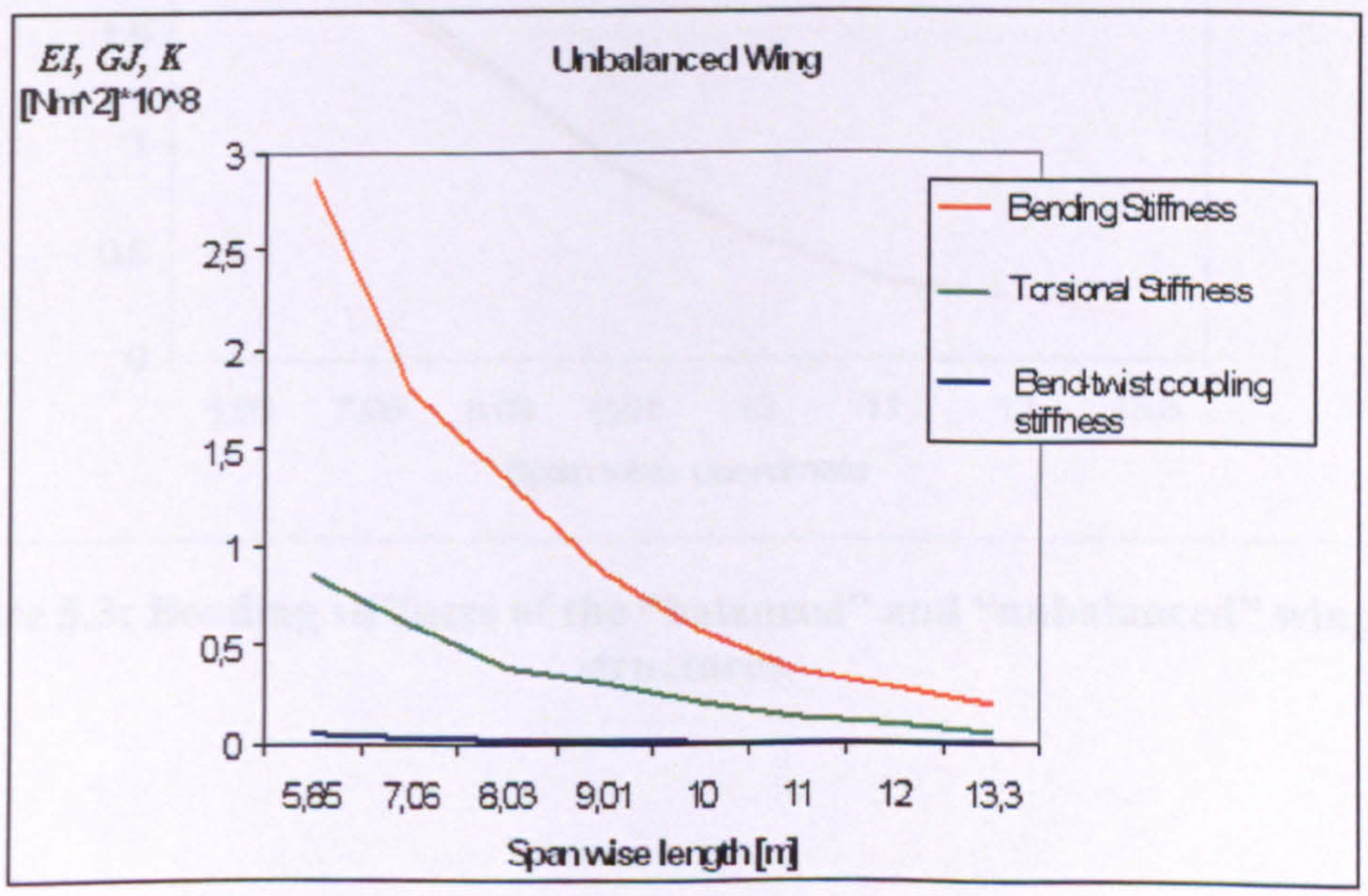

Figure 5.2: Stiffnesses distribution in the "unbalanced" wing like structure.

When the results obtained are compared with those of the balanced wing structure, three observations can be made:

1. Less than 5% difference in the *EI(X)* distribution along the span of the structures exists (Figure 5.3). Such a small difference can be explained as follows. A fibre angle of 45 deg has been used (together with 0 and 90) to build the structure. In the presence of such fibre angles, differences in terms of bending stiffness between balanced and unbalanced structures are not large (refer to Chapter 3, Figures 3.11 and 3.13).
2. Values of *GJ(X)* of the unbalanced composite wing are lower than those measured in the balanced composite wing (Figure 5.4). The unbalanced wing is therefore more deformable when a torsional load is applied.
3. Bend-twist coupling is obtained only when using unbalanced laminates.

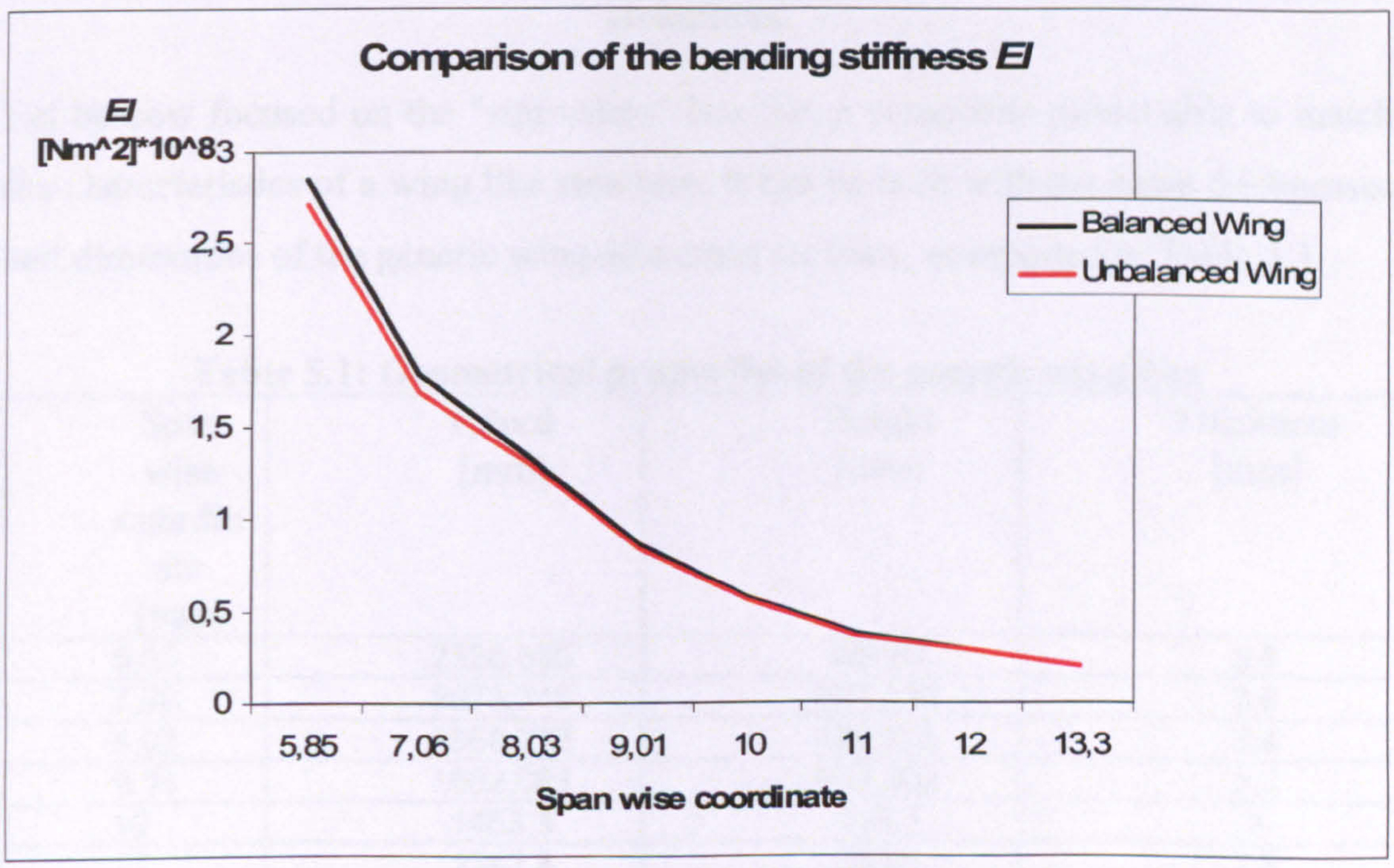

Figure 5.3: Bending stiffness of the "balanced" and "unbalanced" wing like structures.

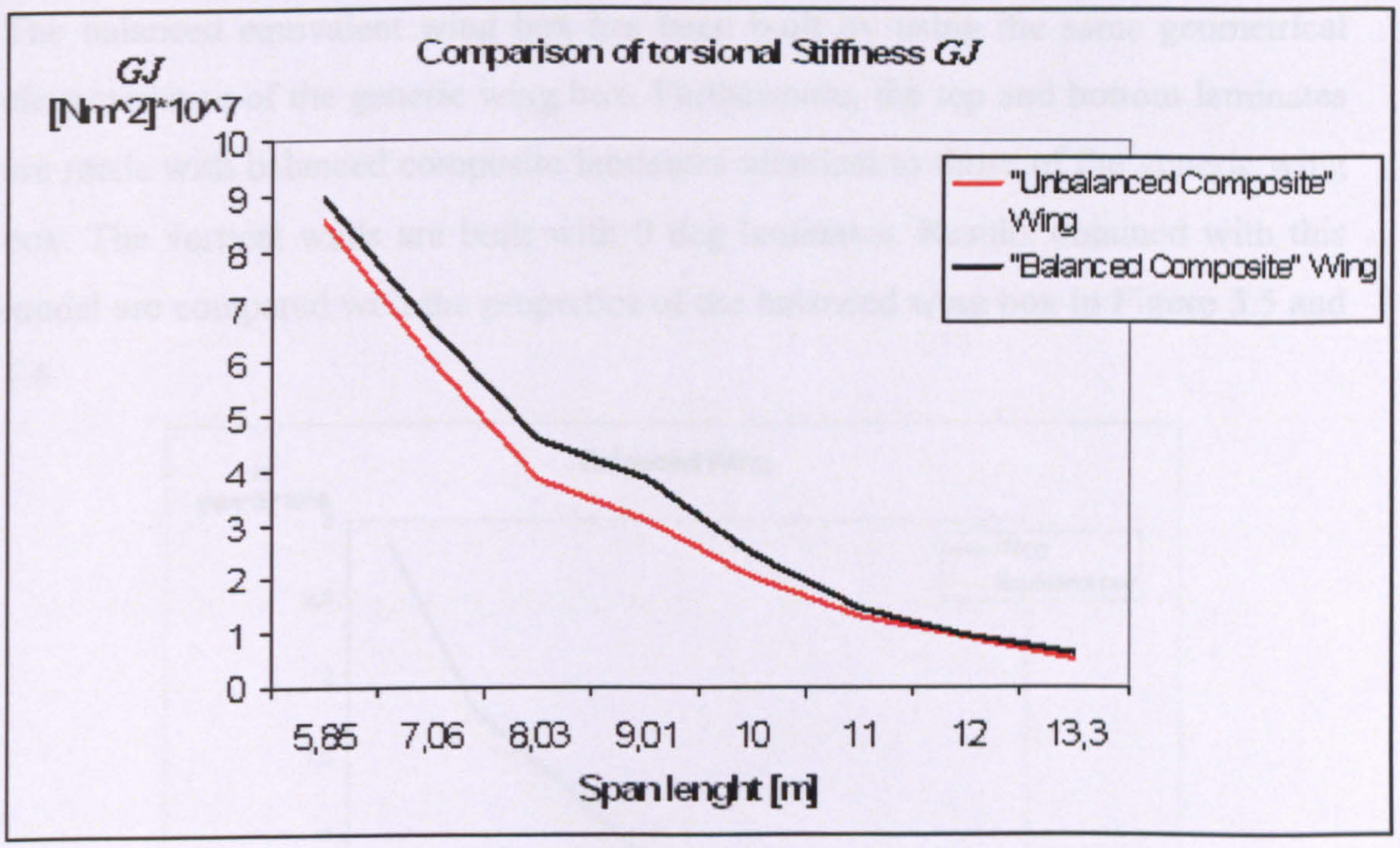

Figure 5.4: Torsional stiffness of the "balanced" and "unbalanced" wing like structures.

Let be now focused on the "equivalent" box, i.e. a composite model able to match the characteristics of a wing like structure. It can be built with the same thicknesses and dimensions of the generic wing-like cross sections, as reported in Table 5.1.

Table 5.1: Geometrical properties of the generic wing box

Span wise coordinate [mm]	Chord [mm]	Height [mm]	Thickness [mm]
5,85	2328,535	696,87	3,8
7,06	2073,346	624,512	3,6
8,03	1868,773	566,506	3,4
9,01	1662,091	507,902	3,2
10	1453,3	448,7	3
11	1242,4	388,9	2,8
12	1031,5	329,1	2,6
13,3	757,33	251,36	2,4

Stiffnesses of equivalent boxes have been calculated by using the model of Canale and Weaver [102], presented in Chapter 3. Two "equivalent" wing boxes have been used for the comparison of balanced and unbalanced cases.

The balanced equivalent wing box has been built by using the same geometrical characteristics of the generic wing box. Furthermore, the top and bottom laminates are made with balanced composite laminates identical to those of the generic wing box. The vertical walls are built with 0 deg laminates. Results obtained with this model are compared with the properties of the balanced wing box in Figure 5.5 and 5.6.

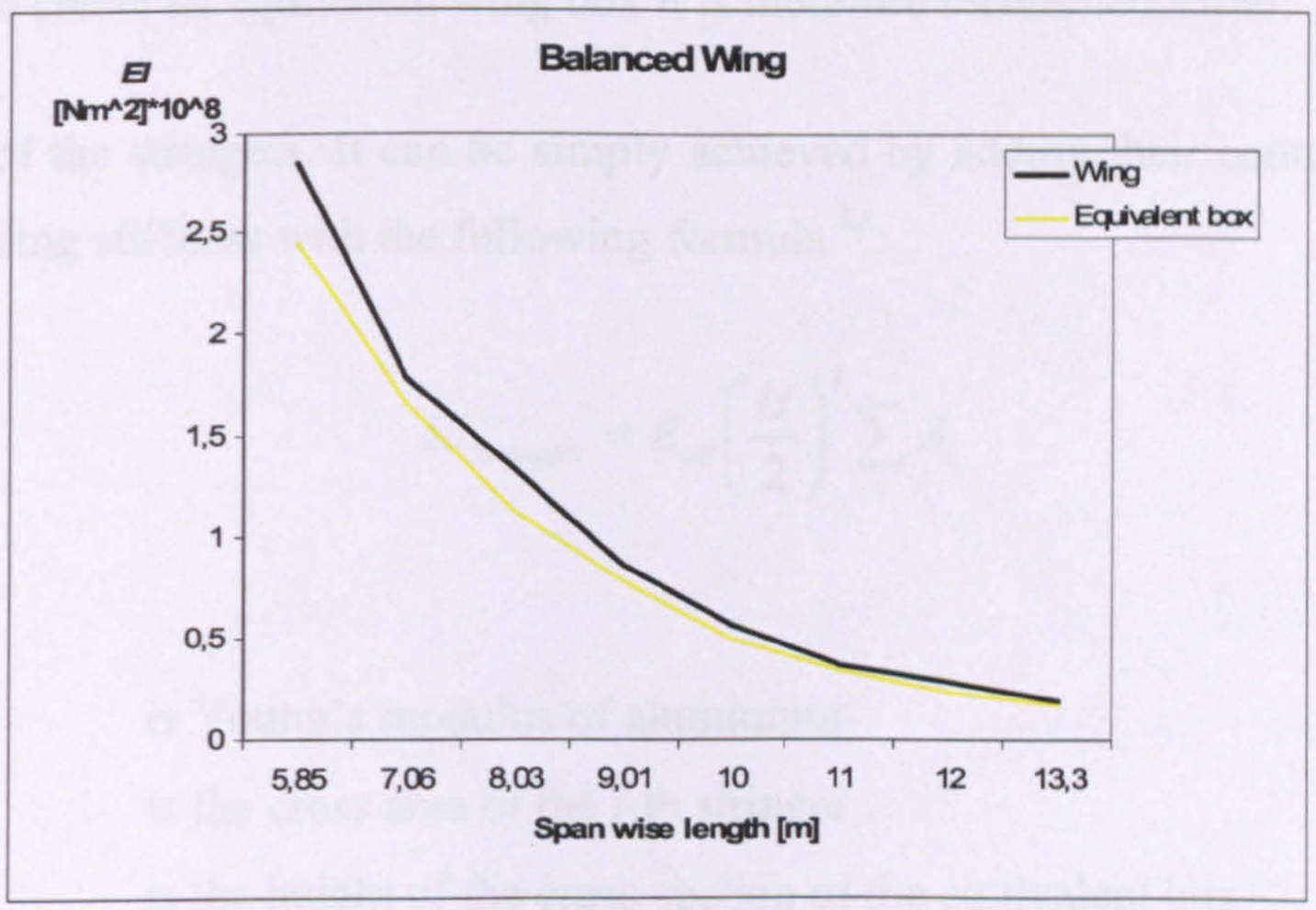

Figure 5.5: Comparison of the equivalent wing box with a wing like structure in terms of *EI* (balanced case).

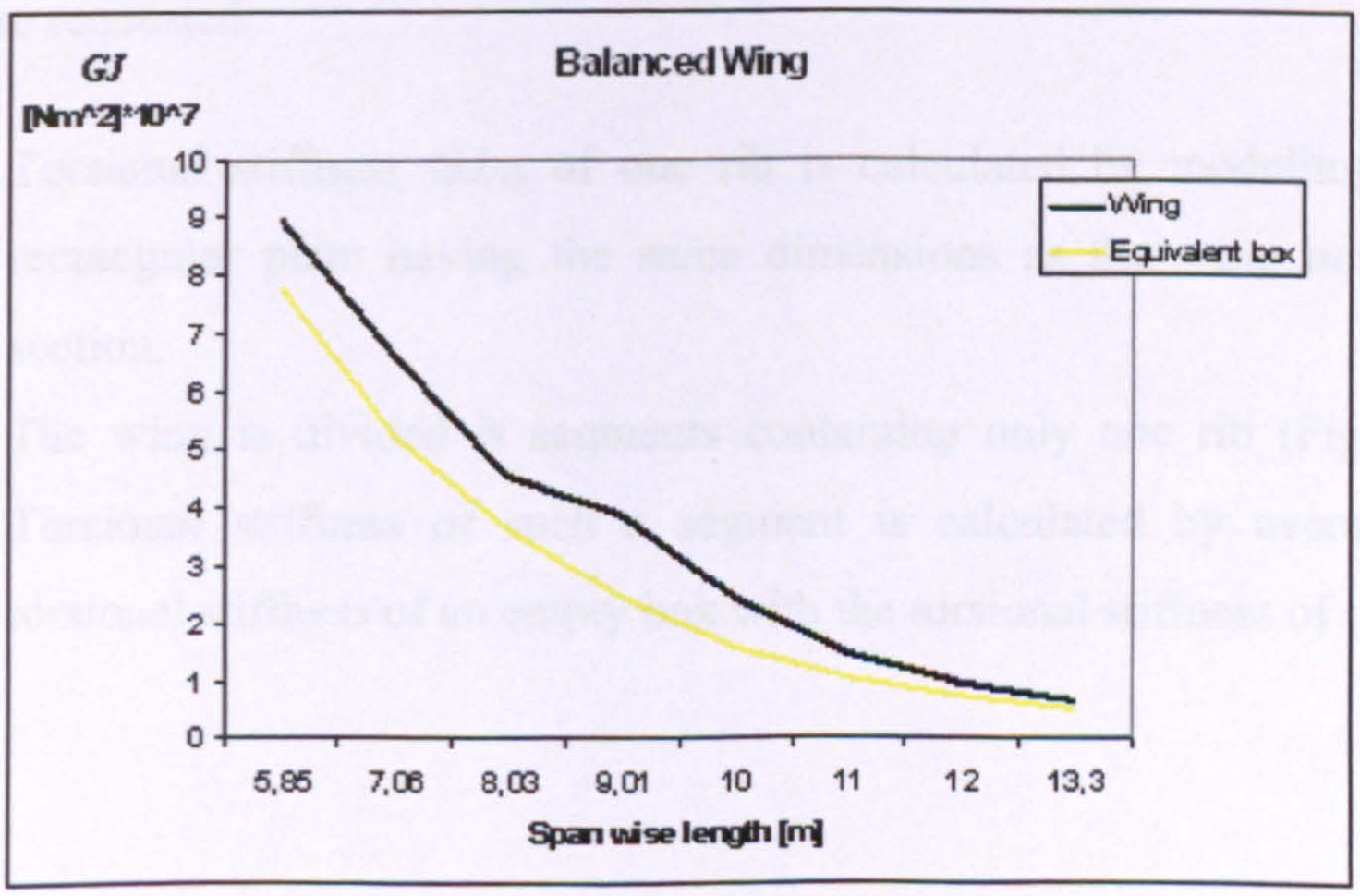

Figure 5.6: Comparison of the equivalent wing box with a wing like structure in terms of *GJ* (balanced case).

Results are quite acceptable with a margin of error less than 20%, but the presence of stringers clearly increases the bending stiffness *EI* of the real wing box, while the presence of ribs increases its torsional stiffness *GJ*. In other words, when a "real" wing like structure is compared with a prismatic box having the same walls thicknesses and the same dimensions, the latter will show lower values of stiffness.

In order to create an equivalent wing box it is therefore recommended to:

- Model of the stringers. It can be simply achieved by adding their contribution to the bending stiffness with the following formula [82]:

$$EI_{Stringers} = E_{all}\left(\frac{H}{2}\right)^2 \sum_i A_i \qquad (5.1)$$

where

E_{all}	is Young's modulus of aluminium
A_i	is the cross area of the *i*-th stringer
H	is the height of the cross section of the equivalent box.

- Model the effect of the ribs: their presence affects the torsional stiffness *GJ*. Two steps are requested:

1. Torsional stiffness GJ_{rib} of one rib is calculated by modelling it as a rectangular plate having the same dimensions as the wing box's cross section.
2. The wing is divided is segments containing only one rib (Figure 5.7). Torsional stiffness of such a segment is calculated by averaging the torsional stiffness of an empty box with the torsional stiffness of the rib.

If the following symbols are used:

l	a segment of the wing containing a rib (Figure 5.7)
GJ_{rib}	the torsional stiffness of a rib
GJ_{hollow}	the torsional stiffness of the hollow cross section of the wing
t_{rib}	the thickness of the rib

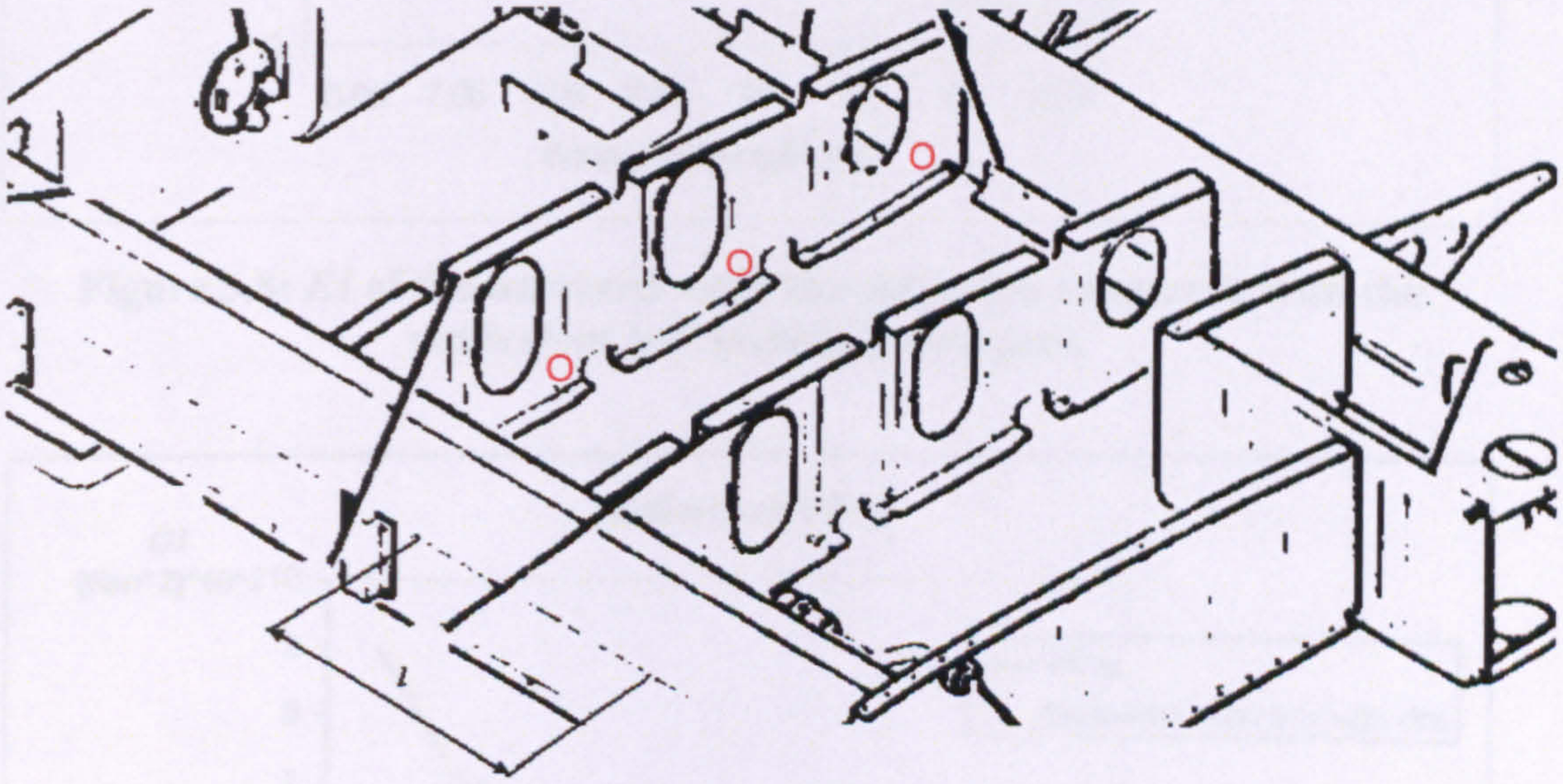

Figure 5.7: Wing segment containing only one rib. Its length is denoted by the symbol *l*.

Using a simple linear relation, for the sum of parts, the global stiffness GJ of such a section of the wing is given by:

$$GJ = \frac{(l - t_{rib})GJ_{hollow} + t_{rib}GJ_{rib}}{l} \tag{5.2}$$

When these structural elements are included, the margin of error is clearly reduced as shown in Figure 5.8-5.9.

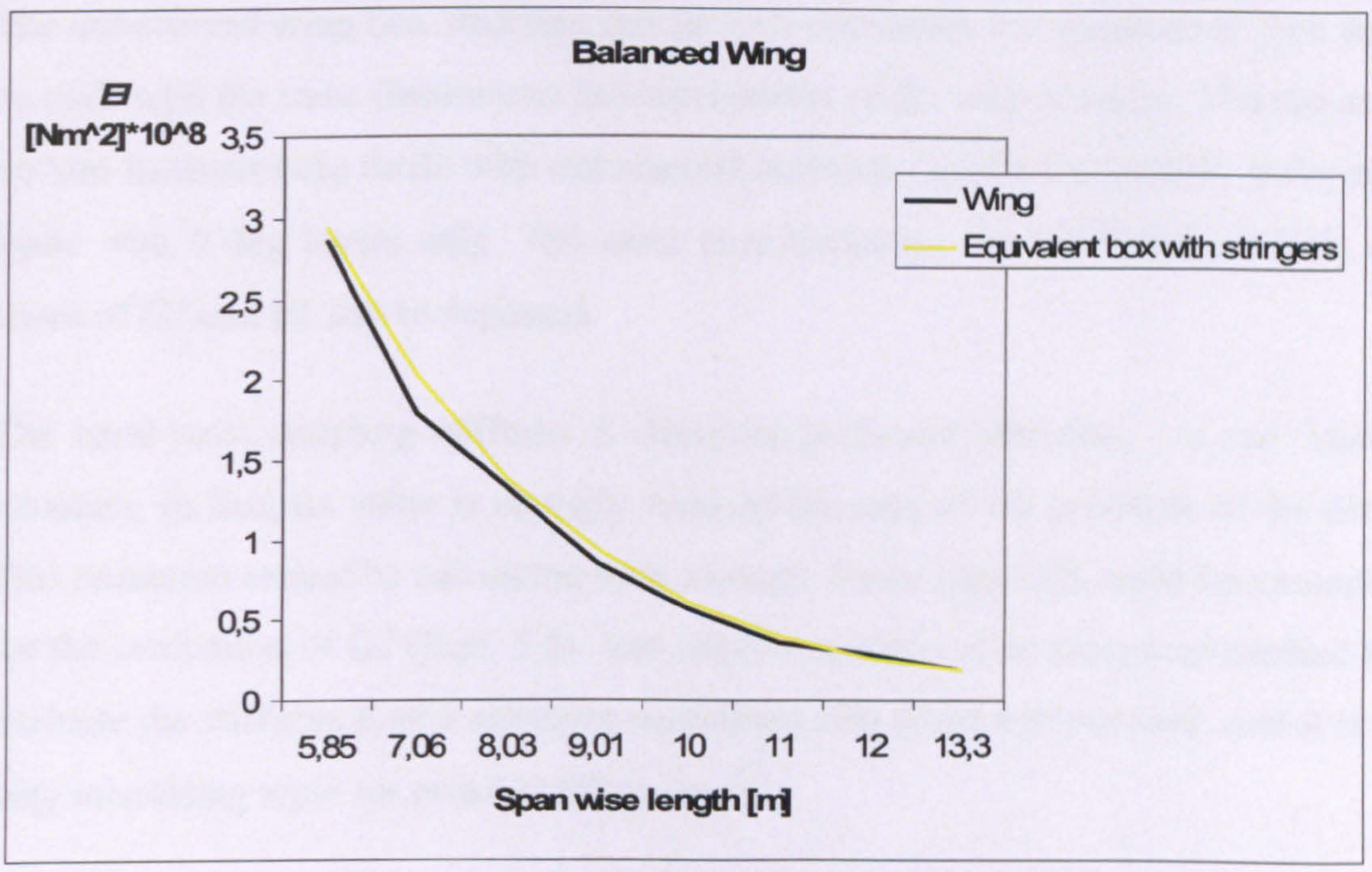

Figure 5.8: *EI* of the balanced wing like structure compared with the equivalent box including stringers.

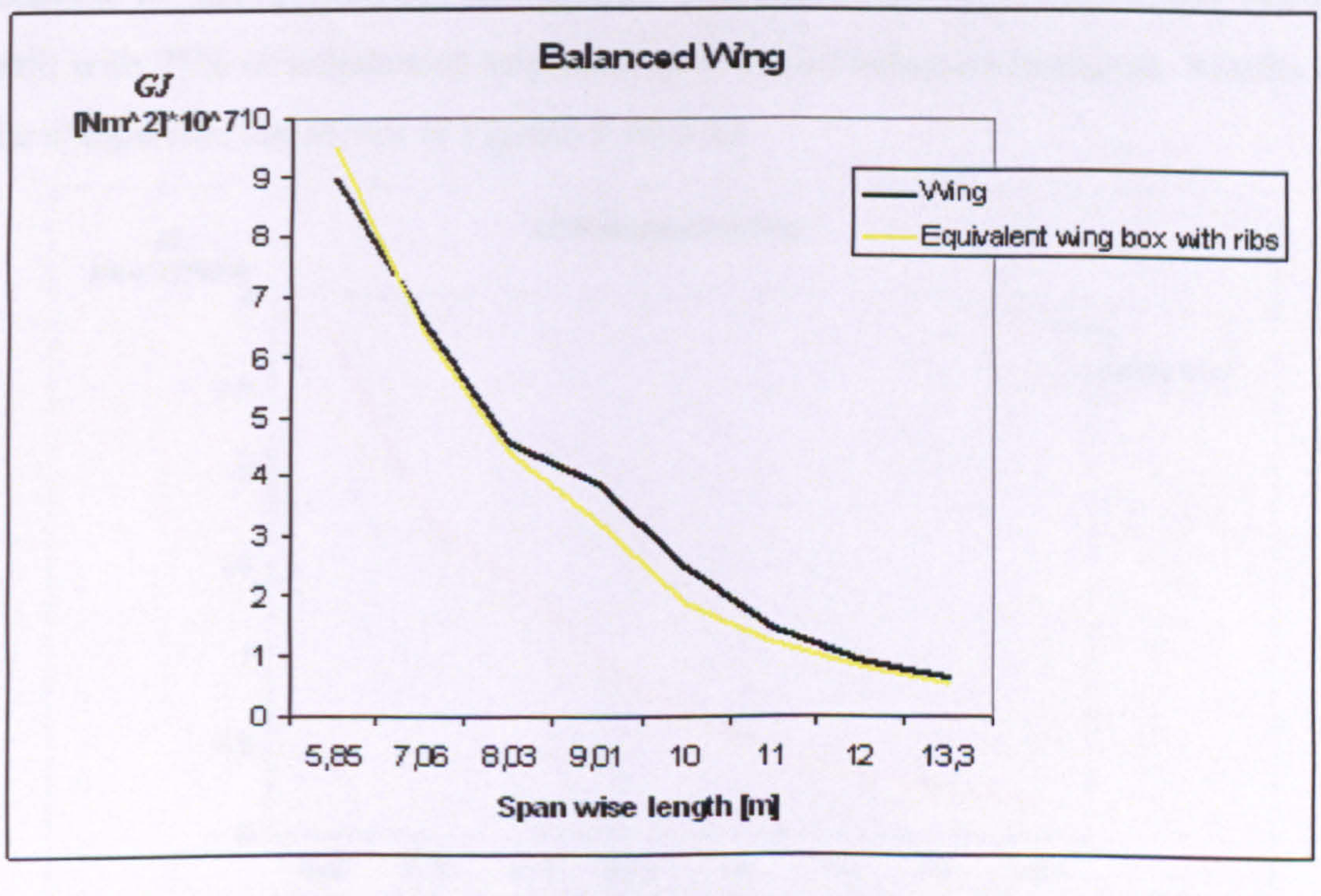

Figure 5.9: *GJ* of the balanced wing like structure compared with the equivalent box including ribs.

The unbalanced wing box structure can be now discussed. Its "equivalent" box can be built with the same dimensions and thicknesses of the real structure. The top and bottom laminates are made with unbalanced laminates whilst the vertical walls are made with 0 deg layers only. The same considerations, for the balanced case, in terms of *GJ* and *EI,* can be repeated.

The bend-twist coupling stiffness *K* deserves particular attention. In the "real" structure, in fact, its value is strongly reduced because of the presence of the ribs. This reduction cannot be calculated with a simple linear approach, used for example for the evaluation of *GJ* (Eqn. 5.2). The implementation of an analytical method to evaluate the stiffness *K* of a structure containing ribs is not a trivial task, and it is a very interesting topic for possible future work.

The reduced values of *K* can be modelled by simply reducing the percentage of unbalanced laminates of the top and bottom walls of the "equivalent" box. In the example of this section, top and bottom laminates of the "equivalent" box can be built with 25% of unbalanced laminates and 75% of balanced laminates. Results of the comparison are shown in Figures 5.10-5.12.

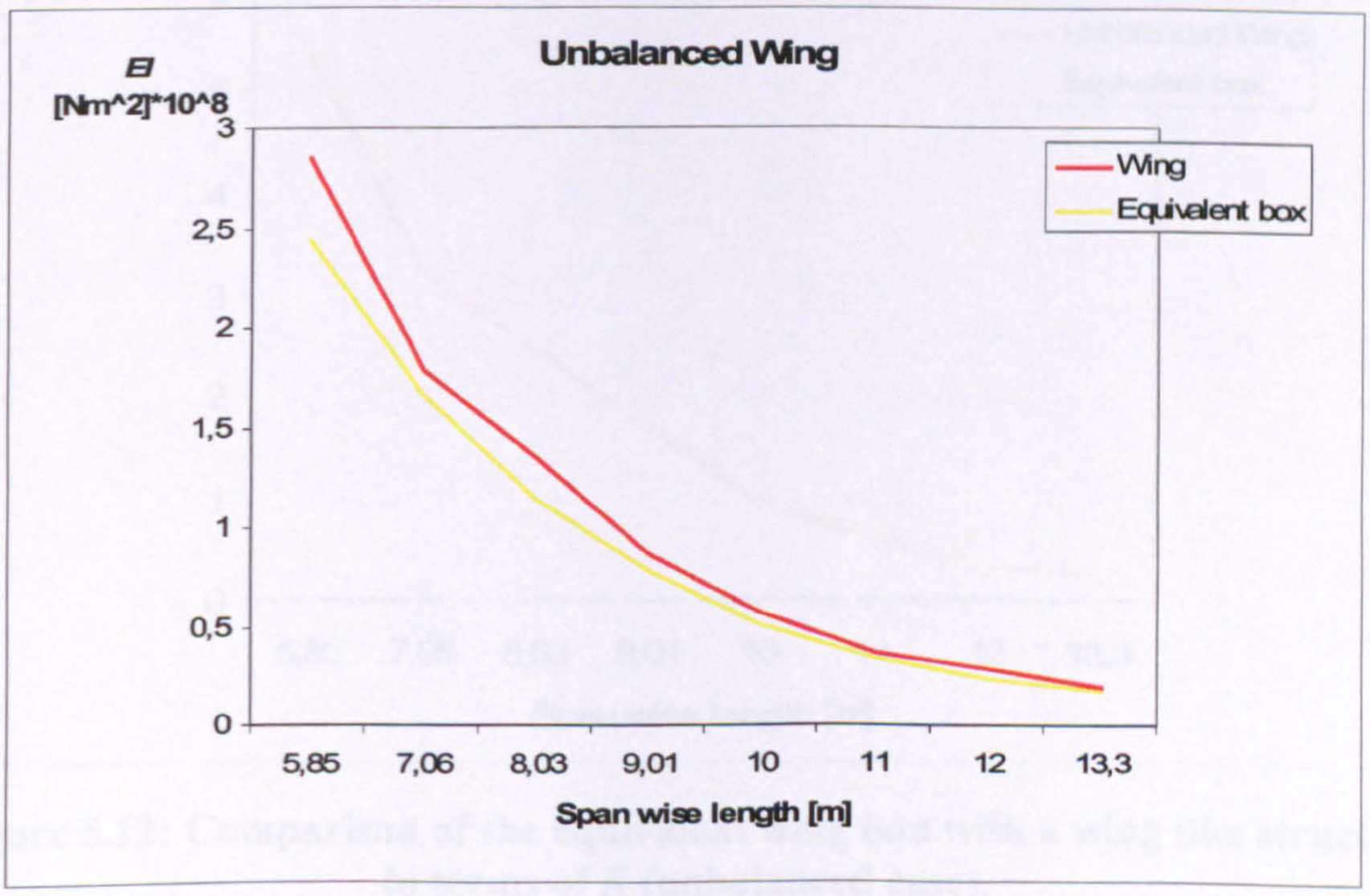

Figure 5.10: Comparison of the equivalent wing box with a wing like structure in terms of *EI* (unbalanced case).

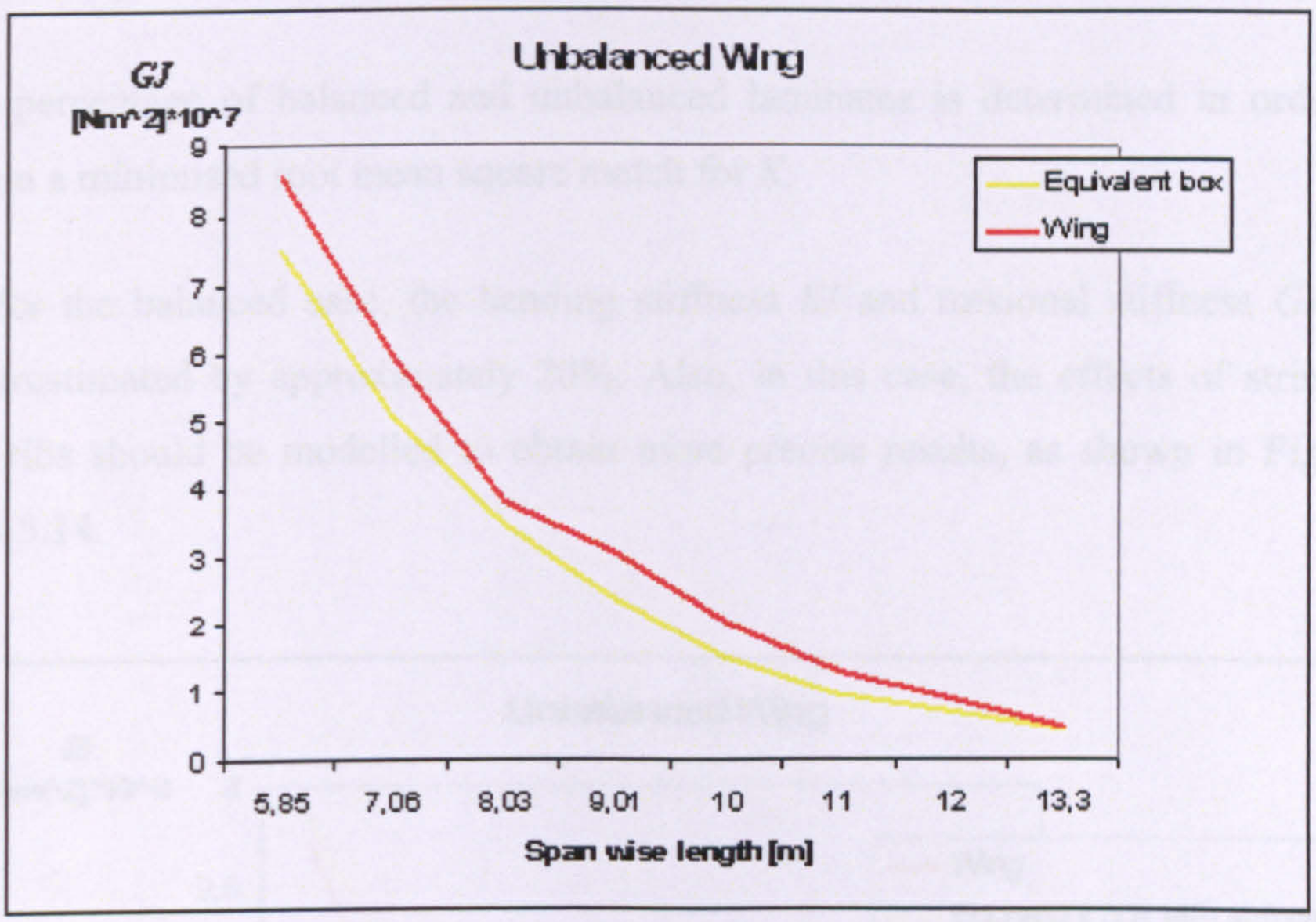

Figure 5.11: Comparison of the equivalent wing box with a wing like structure in terms of *GJ* (unbalanced case).

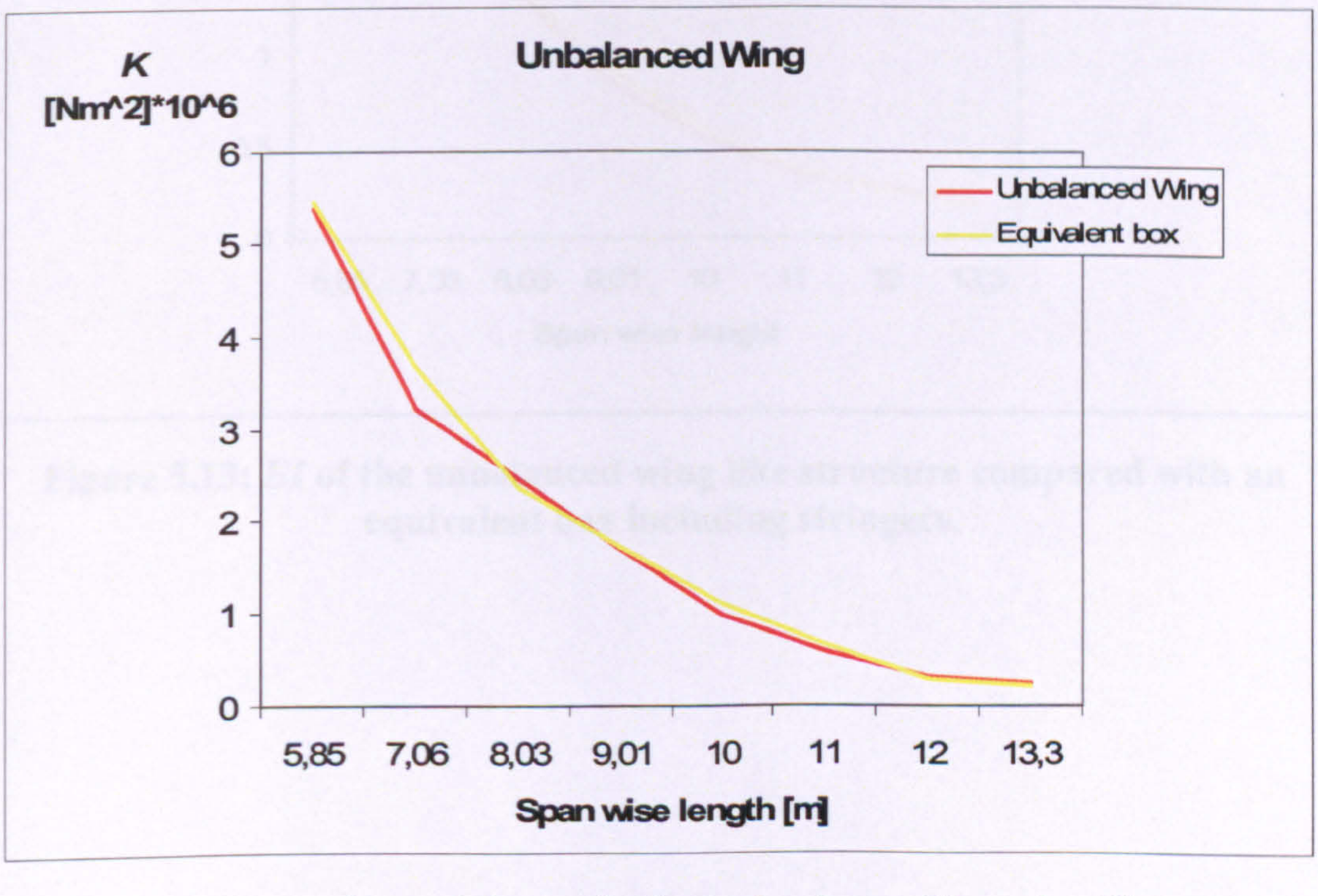

Figure 5.12: Comparison of the equivalent wing box with a wing like structure in terms of *K* (unbalanced case).

The percentage of balanced and unbalanced laminates is determined in order to obtain a minimised root mean square match for *K*.

As for the balanced case, the bending stiffness *EI* and torsional stiffness *GJ* are underestimated by approximately 20%. Also, in this case, the effects of stringers and ribs should be modelled to obtain more precise results, as shown in Figures 5.13-5.14.

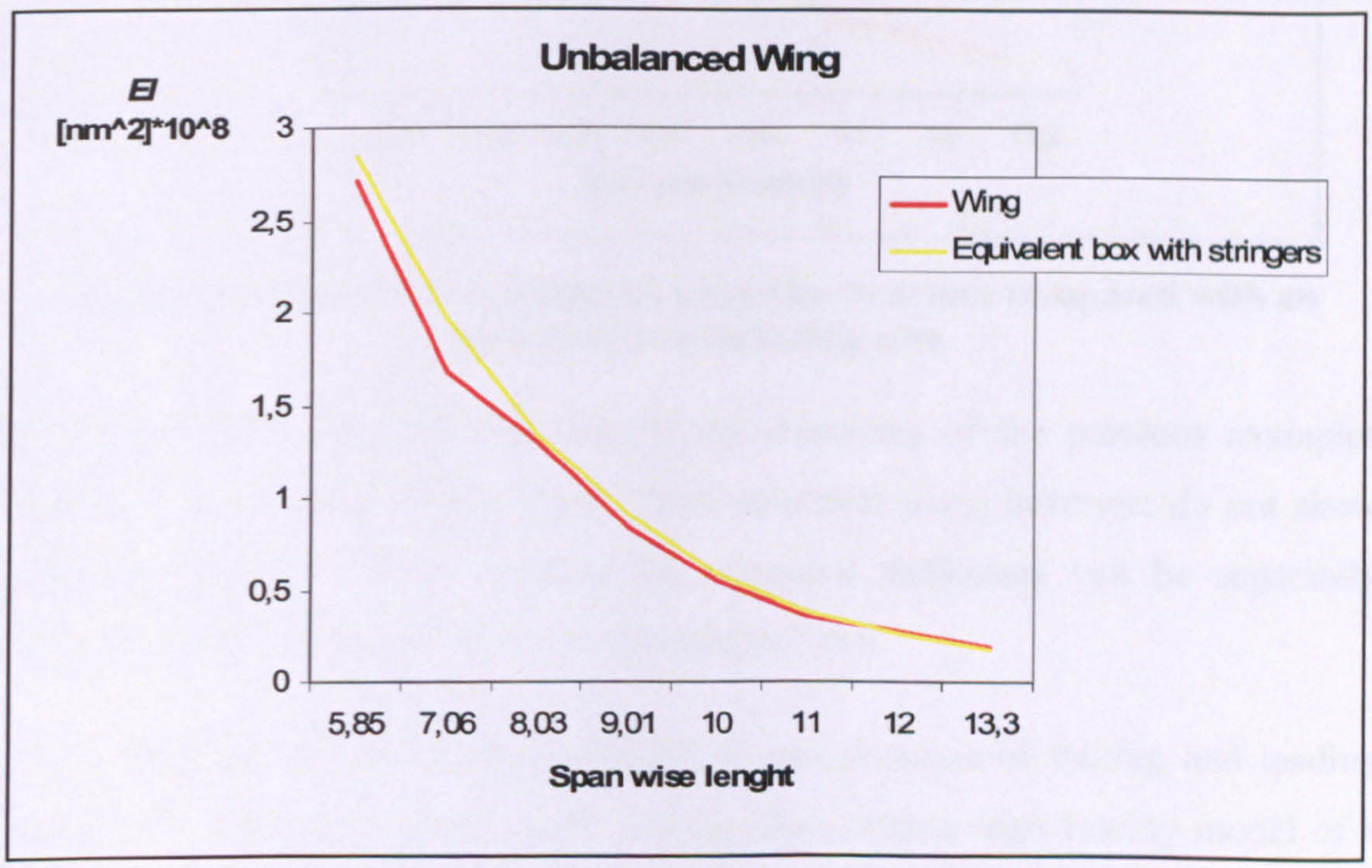

Figure 5.13: *EI* of the unbalanced wing like structure compared with an equivalent box including stringers.

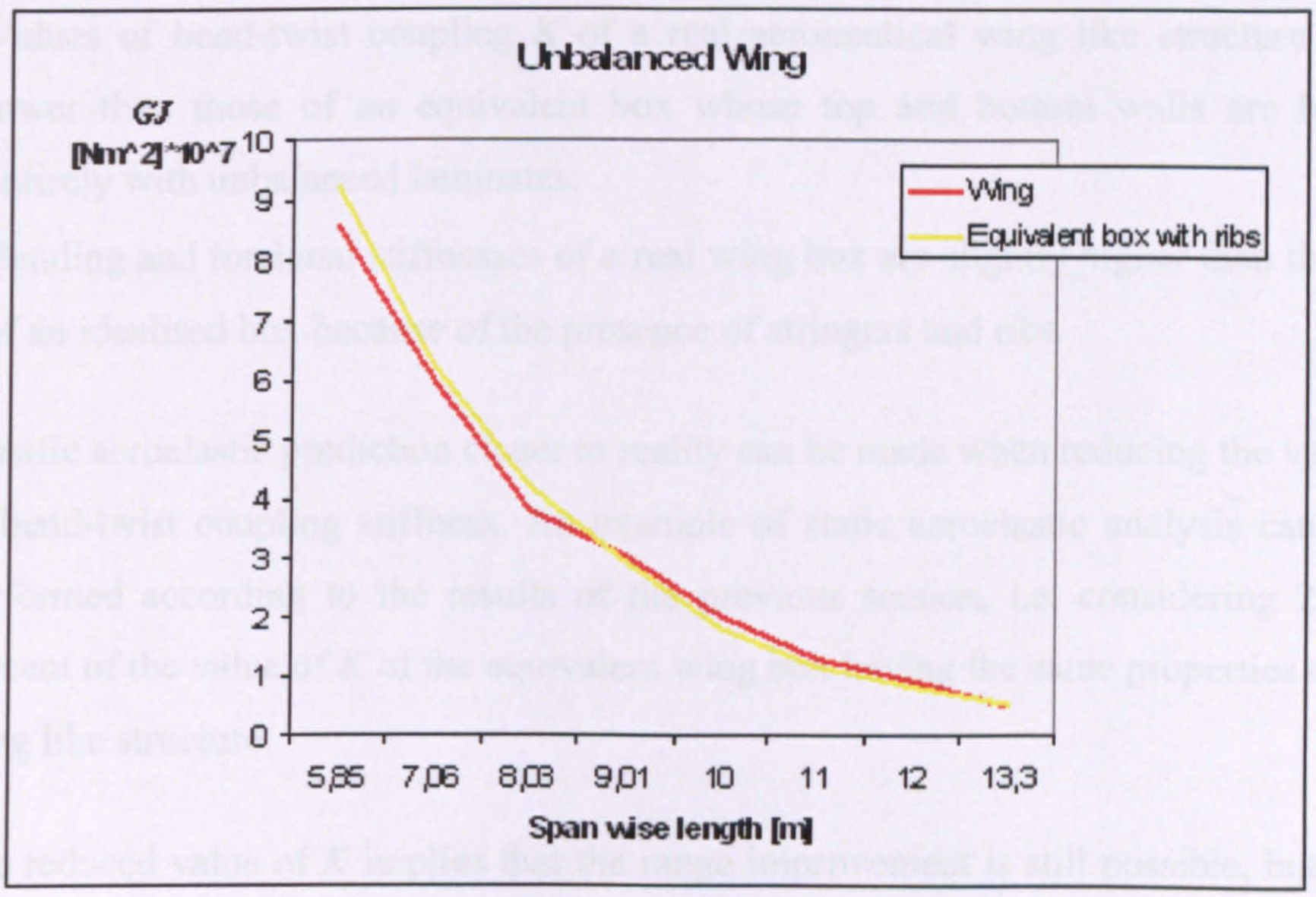

Figure 5.14: *GJ* of the unbalanced wing like structure compared with an equivalent box including ribs.

It is important to remark that none of the structures of the previous examples includes leading and trailing edges. These structural parts, however, do not show elastic anisotropies. Their bending and torsional stiffnesses can be separately calculated and added to those of the "equivalent" box.

Concerning bend-twist coupling stiffness *K*, the presence of trailing and leading edges will further reduce its value. Investigations with a high fidelity model of a complete wing structure should be performed to have a better understanding of the amount of such reduction. This is a suggestion for future research.

5.3 Consequences of a lower value of *K* on the static aeroelastic analysis

Important results have been obtained with the analyses performed in the previous section:

- Values of bend-twist coupling K of a real aeronautical wing like structure are lower than those of an equivalent box whose top and bottom walls are built entirely with unbalanced laminates.
- Bending and torsional stiffnesses of a real wing box are slightly higher than those of an idealised box because of the presence of stringers and ribs.

A static aeroelastic prediction closer to reality can be made when reducing the value of bend-twist coupling stiffness. An example of static aeroelastic analysis can be performed according to the results of the previous section, i.e. considering 25% percent of the value of K of the equivalent wing box having the same properties of a wing like structure.

The reduced value of K implies that the range improvement is still possible, but its value is diminished.

5.3.1 Numerical examples

The numerical examples of section 3.5 have been repeated here using the new values of bend-twist coupling stiffness K, i.e. 25% of their initial value. Concerning the first example, the new results can be summarised in Figure 5.15.

Thickness distribution [mm] of the horizontal walls of the "optimised" wing

9	7	7	9	7	5	4	4	3	3

Root → → → → → → → → → Span wise direction → → → → → → → → → Tip

Thickness distribution [mm] of the vertical walls of the "optimised" wing

5	5	4	7	5	4	3	3	3	2

Root → → → → → → → → → Span wise direction → → → → → → → → → Tip

Fibres angles distribution [deg] in the top and bottom laminates of the "optimised" wing

0	0	0	-30	-30	-30	-30	-30	-30	-30

Root → → → → → → → → → Span wise direction → → → → → → → → → Tip

Figure 5.15: Composite wing box designed with the new values of K. Example 1.

- The range improvement is only 0.30%. The wing, in fact, shows less "nose down" rotation, necessary to reach the point of maximum range.

- The wing is still 8% heavier than the orthotropic one.

Results of the second experiment are reported in Figure 5.16.

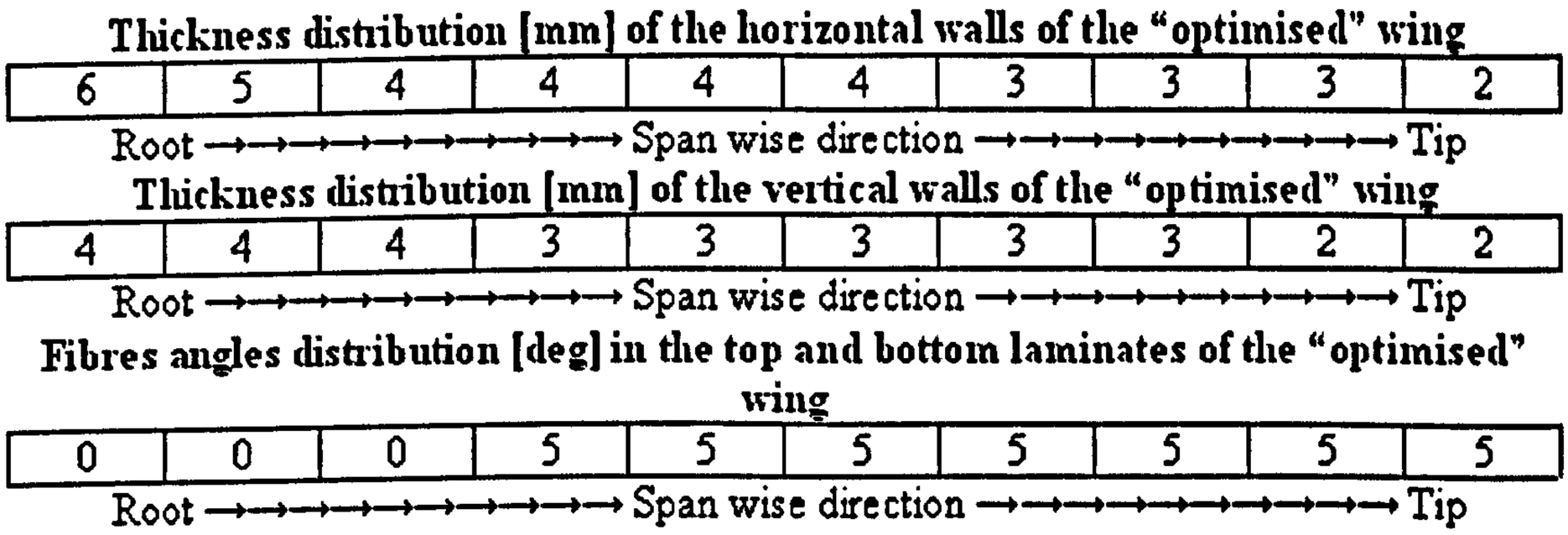

Figure 5.16: Composite wing box designed with the new values of *K*. Example 2.

- The range improvement is only 0.1%.
- There is no weight penalty because the optimum fibres angle distribution is constant along the span and the angle is only 5°, therefore, bending strength is not significantly affected.

The effect of a reduced *K* is clearly shown in the first example, but is less easy to understand in the second one. A reduced value of *K* (5° in this case instead of 20° found in Chapter 4) implies a reduced value of bend-twist coupling compliance. However, if fibre angles of 20° had also been used in this case, the structure would have been thicker and its modulus *GJ* would have been larger. This fact implies that the "nose up" rotation induced by the distance between the centre of pressure and the shear centre of each cross section would have been diminished. The result of the optimisation is a wing having only 5° fibre angle distribution. Wall thicknesses remain relatively thin. The modulus *GJ*, consequently, does not increase if compared with the orthotropic wing. The "nose up" rotation is mainly caused by the distance between the centre of pressure and the shear centre of each airfoil, rather than by the bend twist coupling effect. This rotation optimises the range, satisfying all of the constraints.

5.4 Conclusions

Analyses performed in this chapter have shown some limitations of the aeroelastic tool presented in Chapter 4. The values of bend-twist coupling K, for a real wing like structure, are significantly lower than those predicted by prismatic wing boxes models.

In order to obtain more accurate values of EI and GJ to simulate a wing like structure, models have also been proposed to include the effects of stringers and ribs.

The current chapter is the last dedicated to static aeroelasticity. In the following chapter, the potential benefits of bend-twist coupling on critical flutter speed are discussed.

6. Fundamentals of flutter analysis of boxes built with unbalanced laminates

6.1 Introduction

In this chapter, the potential beneficial effects of unbalanced composite laminates on dynamic instabilities are presented.

6.2 A brief discussion of flexural-torsional flutter

Forces of inertia are often non-negligible when analysing a structural response. When a structure is subjected to three kinds of action, aerodynamic, elastic and inertial forces, its response is dynamic. In other words, displacements of each point of the structure are a function of time, together with the forces and accelerations [103]. If the structural response does not attenuate, but is maintained or is even accentuated, it becomes unstable. The most dangerous and common dynamic instability of aeronautical structures is flexural-torsional flutter (Figure 6.1). Asymptotic air speed, measured when the instability occurs, is called the "critical flutter speed".

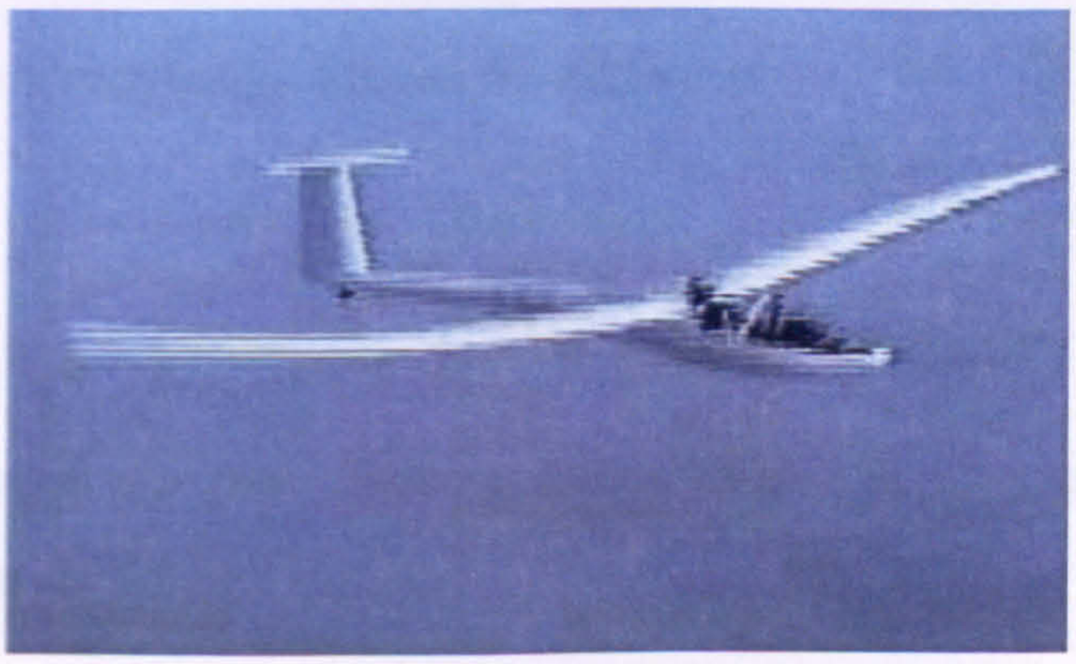

Figure 6.1: An example of flexural-torsional flutter.

Flutter cannot be obtained when a structure has only one degree of freedom [90]. In a wing, for example, the instability can only be obtained if it is able to twist and to bend. Imagine the existence of a wing only able to bend. Let $\dot{Z}$ be the vertical

speed of a cross section placed at span wise coordinate X. The reference system is shown in Figure 6.2.

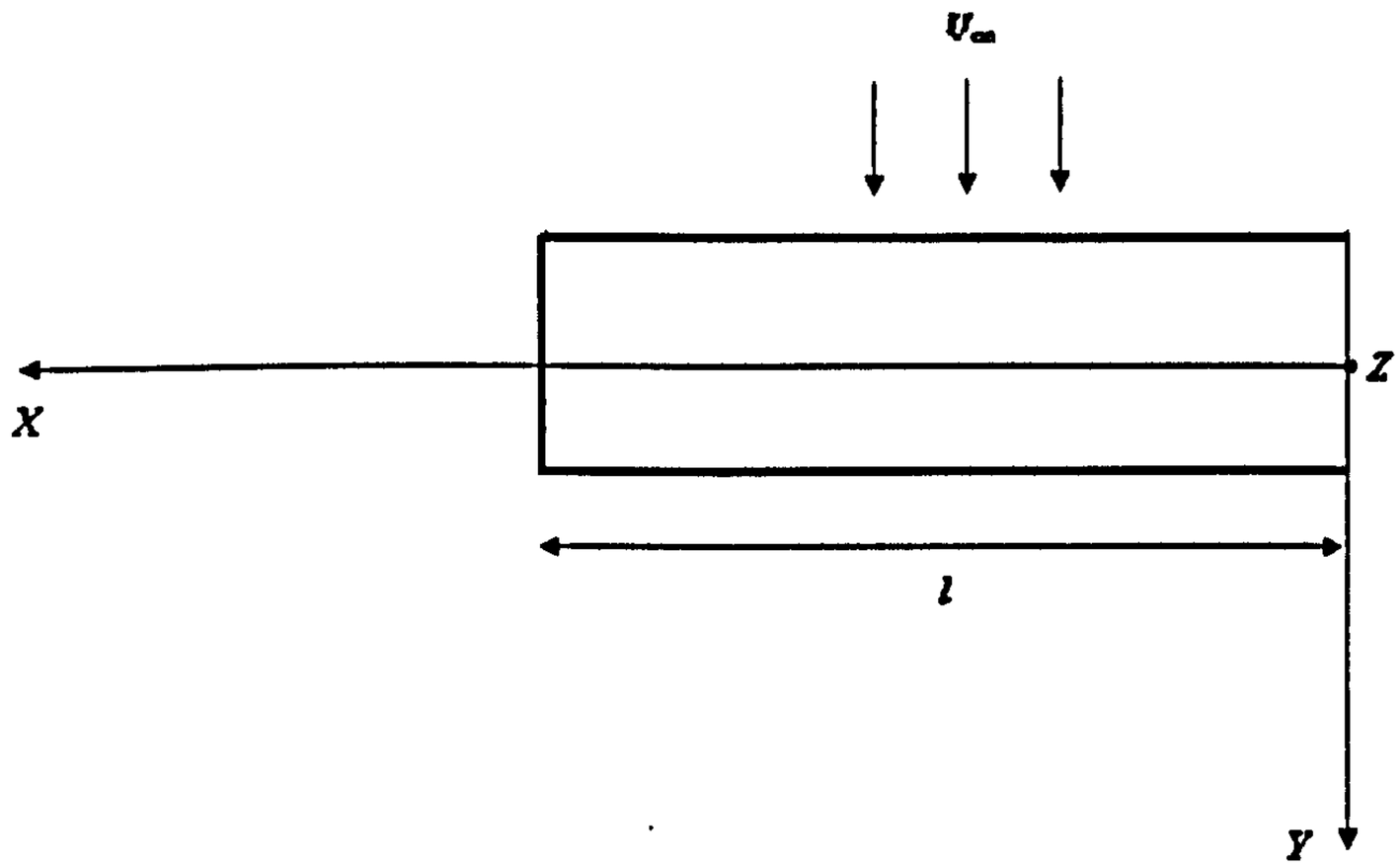

Figure 6.2: Reference frame.

The work done by the aerodynamic forces is negative. In fact, the dynamic incidence can be written as:

$$\alpha(t) = -\frac{Z}{V_\infty} = -\frac{dZ}{dt}\frac{1}{V_\infty} \tag{6.1}$$

It implies that the aerodynamic lift can be written as:

$$L = \frac{1}{2}\rho V_\infty^2 S C_{L\alpha}\alpha = -\frac{1}{2}\rho V_\infty S C_{L\alpha}\frac{dZ}{dt} \tag{6.2}$$

A positive dZ implies a negative force and vice versa. The infinitesimal work done, dW, can be written as:

$$dW = -\frac{1}{2}\rho V_\infty S C_{L\alpha}\frac{dZ}{dt}dZ \tag{6.3}$$

This work done is in a sense negative, i.e. the aerodynamic force rises against the motion of the structure. Therefore, instability cannot exist. In order to create an

instability, energy from the fluid must be transferred to the structure [104]. This is possible only when flexural and torsional degrees of freedom exist.

The main goal of this chapter is to show the potential benefits of unbalanced composite laminates on critical flutter speed. To maintain consistency for the thesis and to provide physical insight, a low-fidelity model is employed.

Both aeroelastic and structural models are required. From the structural point of view, the wing has been modelled using a FE beam approach [105]. Rotations and displacements have been eliminated at the root and bend-twist coupling effects have been included. For the sake of simplicity, the wing is considered as prismatic and the values of stiffness do not change along the span. The aerodynamic model used is based on Theodorsen's strip theory [106].

6.2.1 Determination of the natural modes

A fundamental step to study the flutter instability of a structure, is the evaluation of structural natural modes. Flutter, in fact, is generated from the "coalescence" of such modes [107].

Natural modes show different shapes (displacements) and frequencies whether the wing is orthotropic ($K = 0$) or not. Flexural and torsional modes are uncoupled only in orthotropic structures: when flexural deformation exists, torsional rotations are zero and vice-versa. This phenomenon plays an important role in flutter instability.

Natural modes have been evaluated with a finite element beam model [105]. The global mass matrix $\underline{\underline{M}}$ and global elastic matrix $\underline{\underline{K}}$ have been written for each system analyzed, taking into account the bend-twist coupling effect.

The general equation of motion, for a discrete system, can be written as follows:

$$\underline{\underline{M}}\,\ddot{\underline{u}} + \underline{\underline{K}}\,\underline{u} = \underline{F} \tag{6.4}$$

where

$\underline{F}$ is the vector of nodal forces

$\underline{u}$ is the vector of nodal displacements

Equation 6.4 can be readily re-arranged into a linear system of differential equations. Once this step has been completed, the eigenvalues and eigenvectors of the dynamic matrix [108] represent frequencies and shapes of the natural modes, respectively. The form of this matrix is:

$$\underline{\underline{Adyn}} = \begin{bmatrix} \underline{\underline{0}} & \underline{\underline{I}} \\ \underline{\underline{M^{-1}K}} & \underline{\underline{0}} \end{bmatrix} \tag{6.5}$$

where

$\underline{\underline{I}}$ is the Identity matrix, with dimensions equal to that of $\underline{\underline{M}}$ and $\underline{\underline{K}}$.

6.3 Flutter of structures with uncoupled modes

Once frequencies and shapes (displacements) of natural modes have been determined, the critical flutter speed can be calculated by using well established models. For the structure with uncoupled modes, the model proposed by Fung [52] has been used.

Let $\mu_f(X)$ denote the shape of the first flexural mode with ω_f as its frequency. The symbols $\mu_t(X)$ and ω_t are used to represent the first torsional mode and its frequency. The reference system is shown in Figure 6.2. Displacements in the vertical direction Z can be written as:

$$w(X,Y,t) = q_f(t)\mu_f(X,Y) + Yq_t(t)\mu_t(X,Y) \tag{6.6}$$

where

$q_f(t)$ describes the time progression of the flexural mode: it is the Lagrangian flexural coordinate

$q_t(t)$ describes the time progression of the torsional mode: it is the Lagrangian torsional coordinate

The motion is described by Lagrange's equations [109]:

$$\frac{d}{dt}\frac{\partial P}{\partial \dot{q}_f} - \frac{\partial}{\partial q_f}(P-U) = Q_f$$

$$\frac{d}{dt}\frac{\partial P}{\partial \dot{q}_t} - \frac{\partial}{\partial q_t}(P-U) = Q_t \qquad (6.7)$$

where

P is the kinetic energy

U is the elastic energy

Q_f, Q_t are the Lagrangian components of the force and of the torque respectively They are

$$Q_f = \frac{\partial W}{\partial q_F}$$

$$Q_t = \frac{\partial W}{\partial q_T} \qquad (6.8)$$

6.3.1 Kinetic energy

The kinetic energy P can be written as a function of the Lagrangian variables q_F and q_T as

$$P = \iiint \rho_m w^2 dX dY dZ \qquad (6.9)$$

Volume

where

ρ_m is the material density

Equation 6.6 can be substituted into Eqn. 6.9. After some manipulations, the expression for kinetic energy is written as

$$P = \frac{1}{2}\dot{q}_f^{\,2} m_{eq} + \frac{1}{2}\dot{q}_t^{\,2} J_{eq} \tag{6.10}$$

where m_{eq} and J_{eq} are the equivalent mass and torsional inertia. In other words, the mass and the inertia of the whole system are represented with these two coefficients, which average the properties along the span of the beam, by using the modal displacements. They can be written as:

$$m_{eq} = \iiint_{Volume} \rho_m \mu_f^{\,2} dXdYdZ$$

$$J_{eq} = \iiint_{Volume} \rho_m Y^2 \mu_t^{\,2} dXdYdZ \tag{6.11}$$

6.3.2 Potential elastic energy

The potential energy of the system is calculated once the natural frequencies are known. In fact, U is written as:

$$U = \frac{1}{2} q_f^2 K_f + \frac{1}{2} q_t^2 K_t \tag{6.12}$$

where K_f and K_t are the elastic constants of the flexural and torsional mode respectively. According to the definition of natural frequencies, they are:

$$\begin{aligned} K_f &= \omega_f^2 m_{eq} \\ K_t &= \omega_t^2 J_{eq} \end{aligned} \tag{6.13}$$

6.3.3 Aerodynamics

The model used is Theodorsen's strip theory [106]. Two components of aerodynamic action are modelled: the lift per unit span $\frac{dL(X)}{dX}$ and the torque per unit span $m(X)$. They are functions of the Lagrangian coordinates q_t and q_f. The aerodynamic forces are written in the frequency domain. The analytical expression, when the shear centre is located in the middle of the aerodynamic chord, is:

$$\frac{dL}{dX} = \pi\rho b^2\left[-\omega^2 q_f \mu_f(X) + j\omega V_\infty q_t \mu_t(X)\right] +$$
$$+ 2\pi\rho V_\infty b C_{th}(k)\left[j\omega q_f \mu_f(X) + \frac{1}{2} b j\omega q_t \mu_t(X) + V_\infty q_t \mu_t(X)\right] \tag{6.14}$$

$$m(X) = \frac{dL}{dX}(X)\frac{b}{2} - \pi\rho b^3\left[-\omega^2 \frac{1}{2} q_f \mu_f(X) + \frac{1}{8} b\omega^2 q_t \mu_t(X) + j\omega V_\infty q_t \mu_t\right] \tag{6.15}$$

where

ω is the frequency of the oscillation of an airfoil

b is half of the aerodynamic chord, i.e. $b = \frac{c}{2}$

The quantity $C_{th}(k)$ is Theodorsen's function and it is important to evaluate intensities and phases of the aerodynamic actions as functions of the reduced frequency:

$$k = \frac{\omega b}{V_\infty} \tag{6.16}$$

By using Eqn. 6.14 and 6.15, the Lagrangian components of the aerodynamic forces are

$$Q_f = \int_0^L \frac{dL}{dX}(X)\mu_f dX$$
$$Q_t = \int_0^L m(X)\mu_t dX \tag{6.17}$$

The Lagrangian components of Eqn. 6.17 are basically representative of lift and torque. They can be also written in matrix form as a function of the Lagrangian coordinates q_t and q_f by

$$\begin{pmatrix} Q_f \\ Q_t \end{pmatrix} = \begin{bmatrix} \tilde{Q}_{FUz} & \tilde{Q}_{F\alpha} \\ \tilde{Q}_{TUz} & \tilde{Q}_{T\alpha} \end{bmatrix} \begin{pmatrix} q_f \\ q_t \end{pmatrix} \tag{6.18}$$

This mathematical manipulation is useful when writing flutter equations.

It can be noted from Eqn. 6.18, that lift and torque depend on both the Lagrangian parameters q_f and q_t: this dependency is the origin of instability in the system.

6.3.4 Flutter Equations

The flutter equations in the time domain can be readily derived from Eqn. 6.7. They are

$$\begin{aligned} m_{eq}\ddot{q}_f + K_f q_f &= Q_f \\ J_{eq}\ddot{q}_t + K_t q_t &= Q_t \end{aligned} \tag{6.19}$$

The system of equations in (6.19) can be expressed in the frequency domain as follows:

$$-\omega^2\begin{pmatrix} m_{eq} & 0 \\ 0 & J_{eq} \end{pmatrix}\begin{pmatrix} q_f \\ q_t \end{pmatrix}+\begin{pmatrix} K_f & 0 \\ 0 & K_t \end{pmatrix}\begin{pmatrix} q_f \\ q_t \end{pmatrix}=\begin{bmatrix} \tilde{Q}_{FUz} & \tilde{Q}_{F\alpha} \\ \tilde{Q}_{TUz} & \tilde{Q}_{T\alpha} \end{bmatrix}\begin{pmatrix} q_f \\ q_t \end{pmatrix} \tag{6.20}$$

It is important to note the role of the aerodynamic forces in Eqn. 6.20. Without them, the system would oscillate indefinitely, transforming elastic energy into kinetic energy and vice-versa. Aerodynamic forces, however, are able to create a coupling that can induce the instabilities.

By means of Eqn. 6.20, it is possible to calculate the critical flutter speed, i.e. the speed that induces permanent oscillations of the system. The goal is, therefore, to find the value of reduced frequency k, and of the asymptotic speed V_∞, which satisfies these equations. It happens when:

$$\underline{\underline{H}}\begin{pmatrix} q_F \\ q_T \end{pmatrix} = \underline{0} \tag{6.21}$$

where

$$H = \begin{bmatrix} -\omega^2 m_{eq} + K_f - \tilde{Q}_{FUz} & -\tilde{Q}_{F\alpha} \\ -\tilde{Q}_{TUz} & -\omega^2 J_{eq} + K_t - \tilde{Q}_{T\alpha} \end{bmatrix} \tag{6.22}$$

Such a system has a non-trivial solution when

$$\det(\underline{\underline{H}}) = 0 \tag{6.23}$$

This eigenvalue problem can be solved by using several numerical methods [90]. The lowest value of the asymptotic speed, that satisfies Eqn. 6.23, is the critical flutter speed.

6.4 Flutter of structures with coupled modes

When flexural and torsional modes are not decoupled, the solution procedure suggested by Chiocchia [90] can be used. Each modal shape can be written as:

$$\mu_s = \mu_{fs} + Y\mu_{ts} \qquad s = 1 \ldots n \tag{6.24}$$

where μ_{fs} and μ_{ts} are the flexural and torsional components of the *s*-th mode.
The frequency of each coupled mode is denoted with ω_s. Vertical displacements of the wing, *w*, can be written as a sum of the *n* natural modes:

$$w(X,Y,t) = \sum_{s=1}^{n} q_s(t)\mu_s(X,Y) \tag{6.25}$$

where $q_s(t)$ are the modal coordinates. It can be demonstrated that, for the *s*-th mode:

$$(-\omega^2 m_s + K_s)q_s = Q_s \tag{6.26}$$

where

$$m_s = \iiint_{Volume} \rho_m \mu_s{}^2 dXdYdZ \tag{6.27}$$

is the generalized mass,

$$K_s = \omega_s^2 m_s \tag{6.28}$$

is the generalized stiffness and Q_s is the Lagrangian component of the aerodynamic force. A system of s equations analogous to Eqn. 6.26 is, therefore, be written and solved.

6.5 The beneficial effects of "nose up" fibres angles on flutter speed

The flutter model described in the previous sub-sections has been used to show the potential beneficial effects of unbalanced laminates. Also in this case, as for the static aeroelasticity, three structural stiffnesses of the wing *EI*, *GJ* and *K* have been considered. They have been assumed to represent those of the wing box. The top and bottom walls of the box are identical so as to obtain bend-twist coupling. They are made with one single layer whose fibre angle ξ varies from -30 to 30 degrees (Figure 2.1). As already mentioned, a negative angle corresponds to a "nose down" deformation, while a positive fibres angle corresponds to a "nose up" deformation. Vertical walls are made with orthotropic laminates.

For the sake of simplicity, the wing is considered to be prismatic with elastic properties constant along the span wise direction. Note, this assumption does not affect the generality of the formulation. The elastic centre is assumed to be in the same position as the geometric centre of the wing box and in the same position as the centre of mass.

Geometrical characteristics of the wing box used for the analyses are reported in Table 6.1. Elastic properties used are reported in Table 6.2.

Table 6.1: Geometric properties of the cross section.

Chord (*C*)	0.8 m
Height(*H*)	0.2 m
Wing span (*l*)	10 m
Wall thicknesses	0.01 m
Aerodynamic Chord	1.5 m

Table 6.2: Elastic properties of the composite material.

E_{11}	181 GPa
E_{22}	10.3 GPa
G_{12}	4.55 GPa
ν_{12}	0.28

The wing has been divided into 10 sections for the analysis. The mass of each section is 30 kg. The air density considered is 1.1 kg/m^3.

Three steps are required for each analysis:

- The stiffnesses *EI, GJ* and *K* are evaluated from geometric and elastic properties of the box.
- Natural modes and frequencies are evaluated.
- Finally, the critical flutter speed is calculated.

Concerning the orthotropic structure, modes are decoupled. The first four natural modes (three flexural and one torsional) are shown in Figure 6.3-6.6.

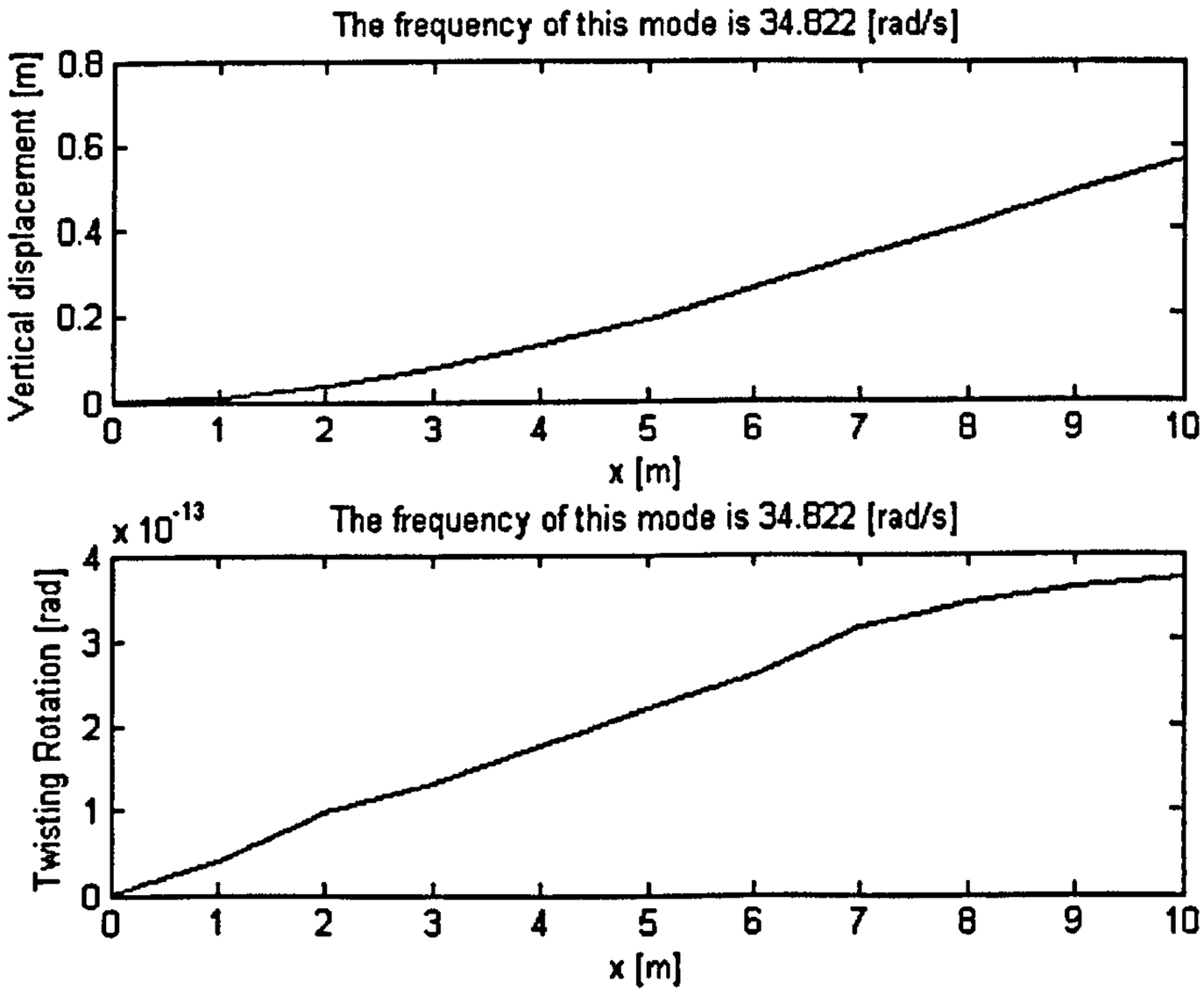

Figure 6.3: First natural mode (first flexural) of a structure with $K = 0$.

It is noted that as the order of magnitude of the torsional displacements is 10^{-13} then no torsion is observed.

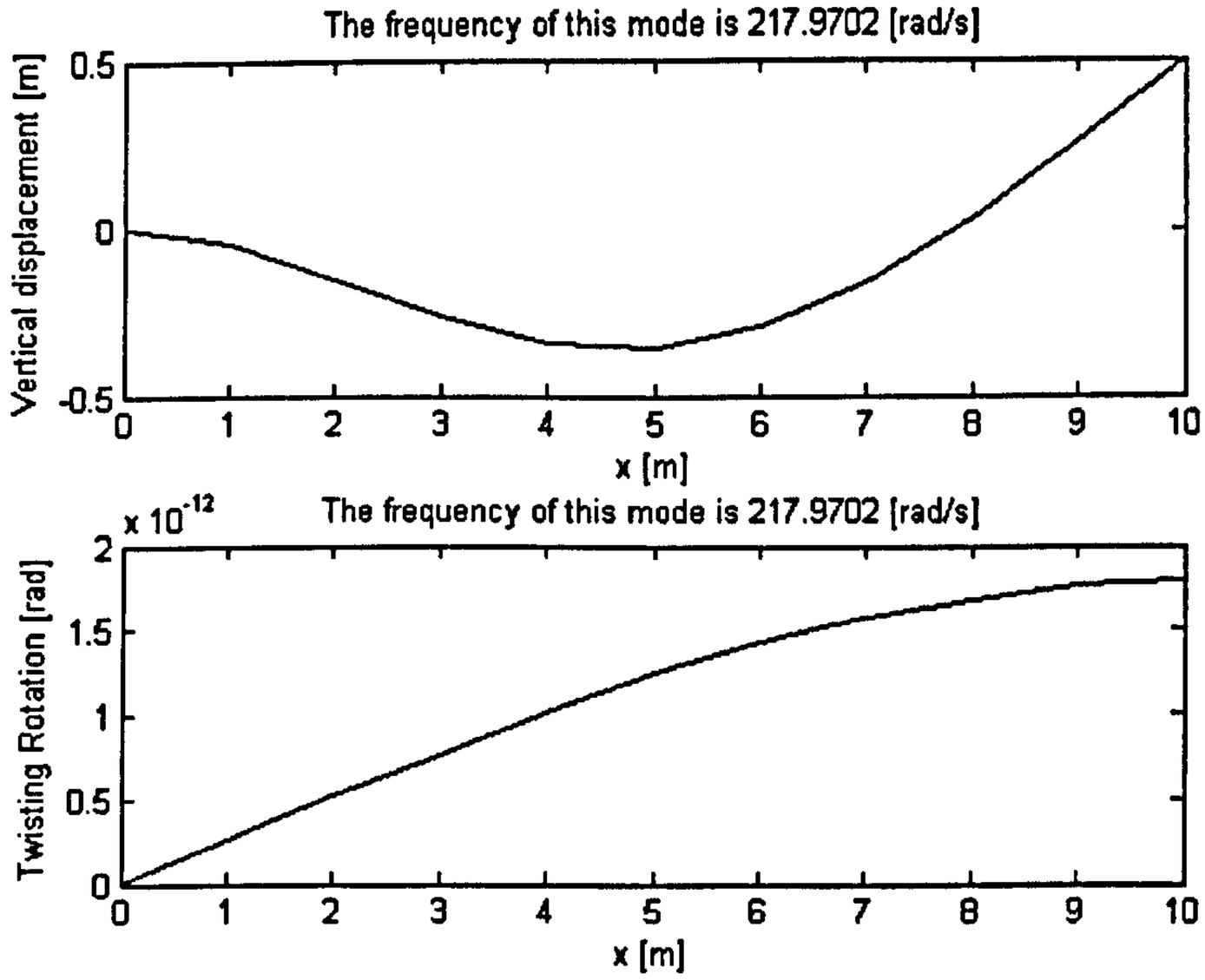

Figure 6.4: Second natural mode (second flexural) of a structure having $K = 0$.

Also in this case the torsional rotations are negligible.

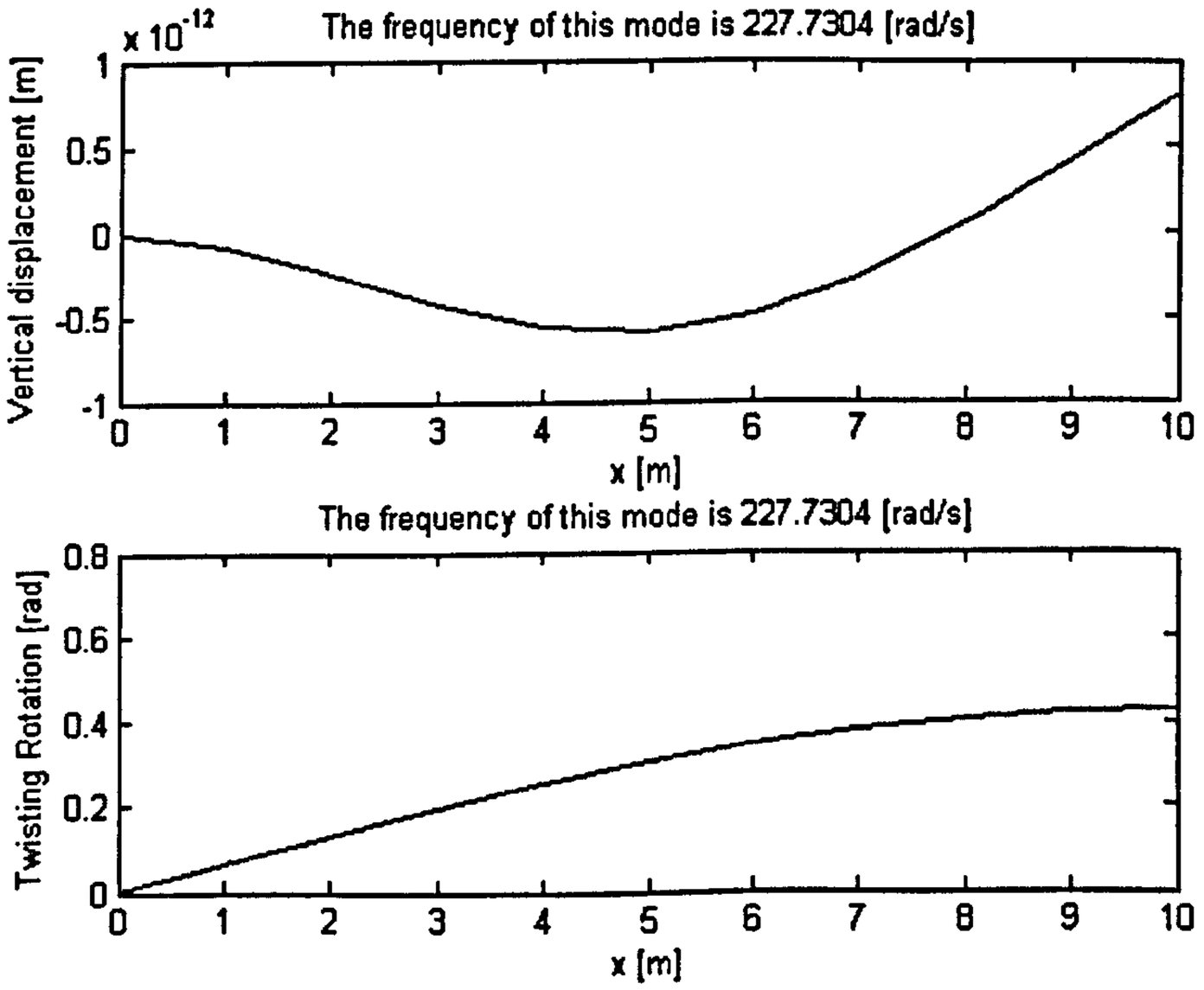

Figure 6.5: Third natural mode (first torsional) of a structure with $K = 0$.

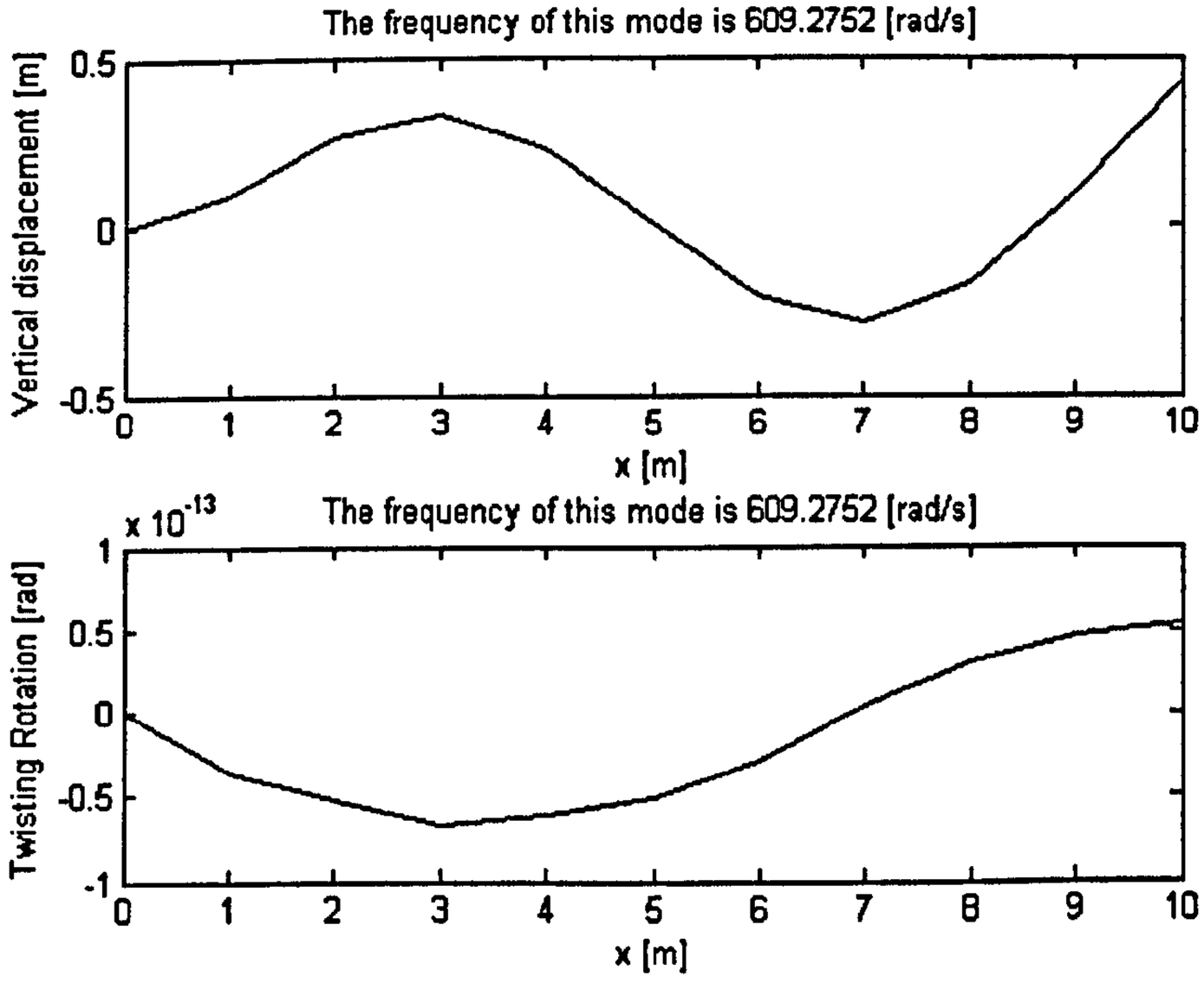

Figure 6.6: Fourth natural mode (third flexural) of a structure with $K = 0$.

On the other hand, when a composite structure exhibits bend-twist coupling, flexural and torsional natural modes are coupled. In Figures 6.7-6.8, the first two modes of a wing box with fibre angles of 30 degrees ("nose up") are shown.

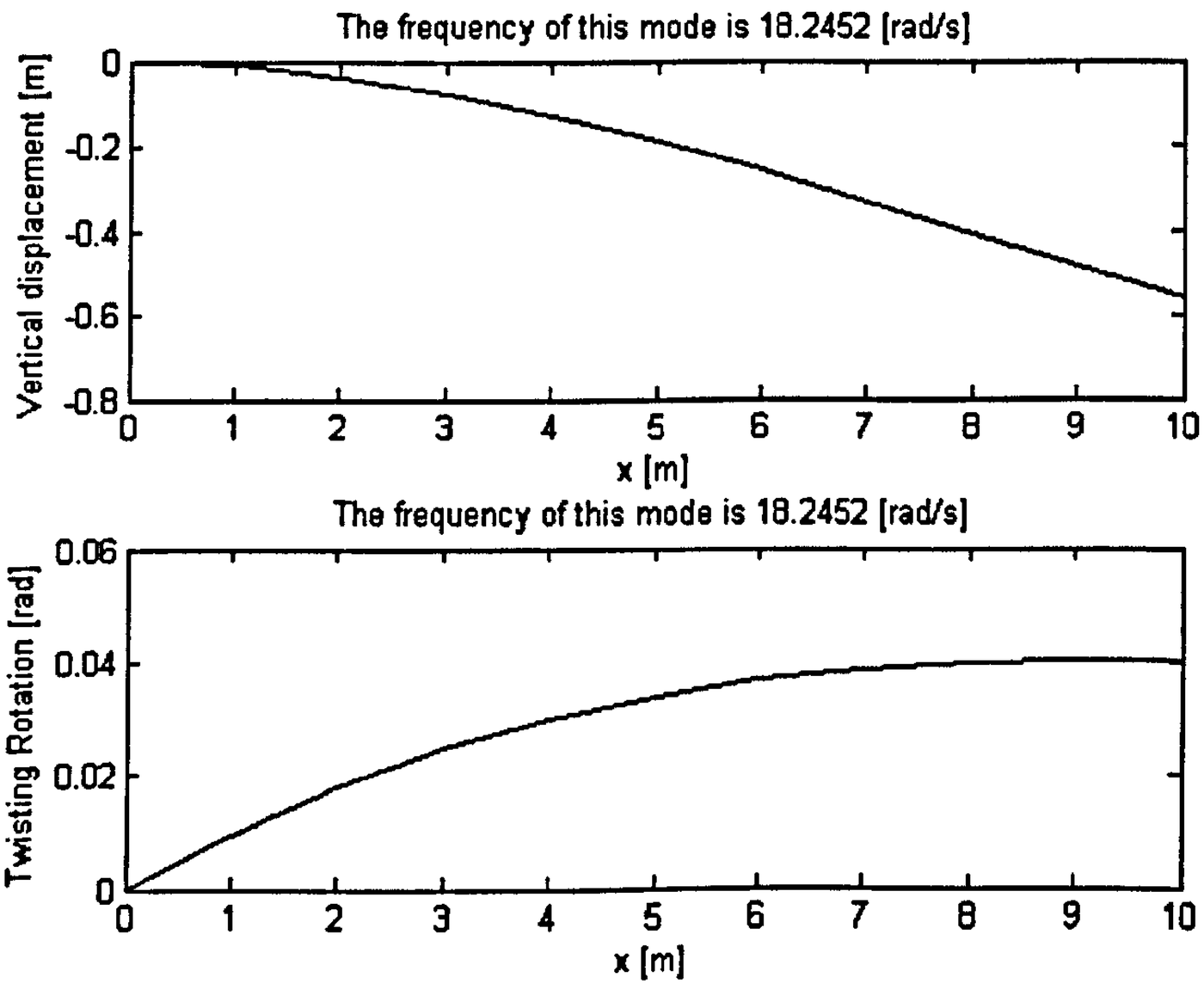

Figure 6.7: First natural mode (coupled) of a structure with $K > 0$.

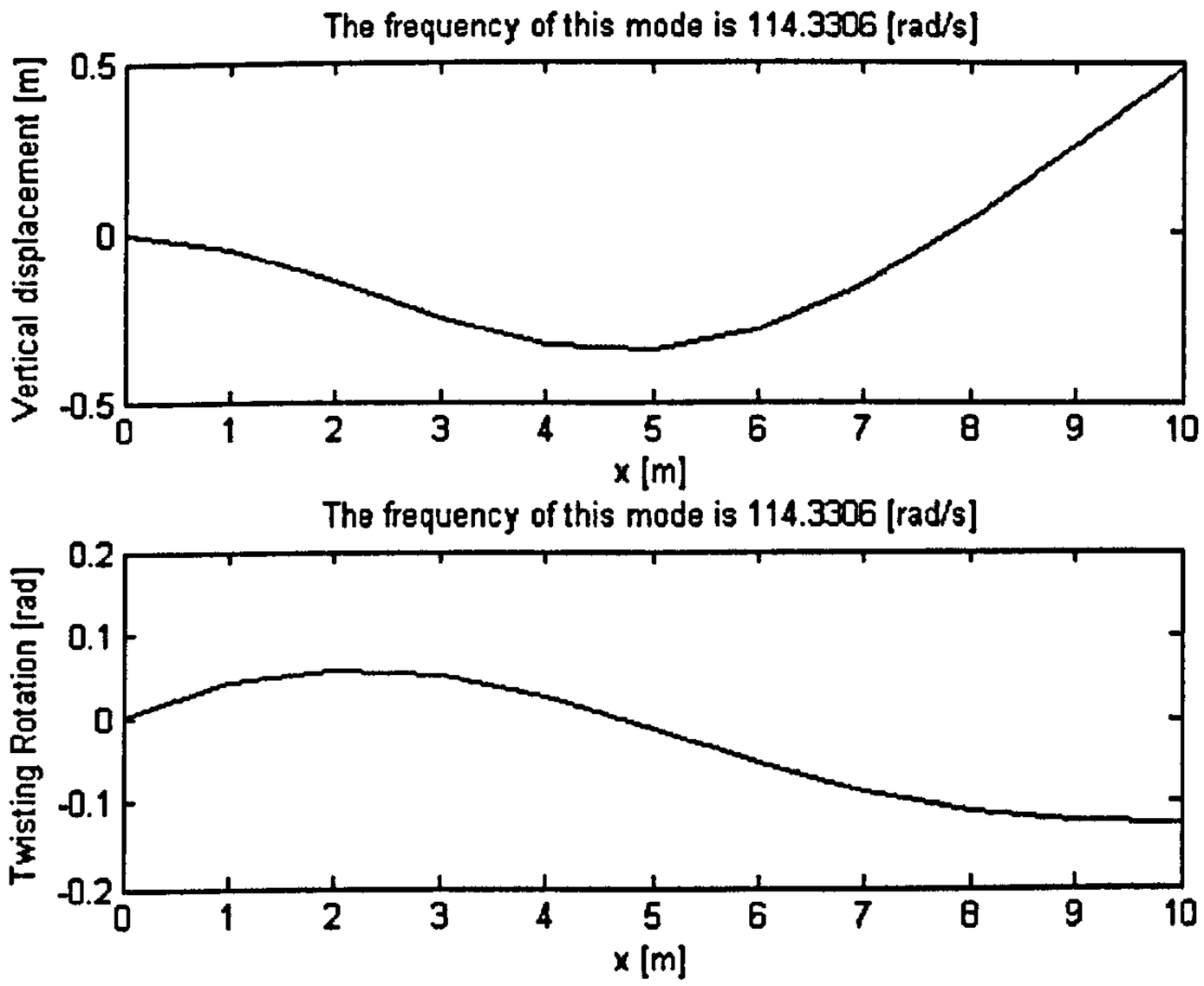

Figure 6.8: Second natural mode (coupled) of a structure with $K > 0$.

The critical flutter speed has been calculated for all of the possible wings having different ply orientations from -30 to 30 degrees, with a step of 5°. In these analyses, structural damping has not been included in order to obtain conservative results [90]. Some authors, however, have shown that increased values of structural damping may reduce flutter critical speed [52]. Such cases, on the other hand, do not concern classical flexural-torsional flutter investigations [110]. It has been observed [110] in fact that:

- The drop in flutter speed (when present) caused by an increased value of damping is very small, for practical values of damping coefficients.
- If damping is added in the same proportion in each mode (torsional and flexural), and this is the most common case, flutter speed always increases.

Results of flutter analyses are summarised in Figure 6.9. It is observed that:

- A wing with positive fibre angle ("nose up" effect) shows higher critical flutter speed than the orthotropic wing. This result has been already remarked in the literature, as mentioned in Chapter 2. A wing with negative angle of fibres ("nose

down" effect), on the other hand, shows lower critical flutter speed than the orthotropic wing.

- The minimum critical flutter speed is observed when $\xi = -10$ deg.

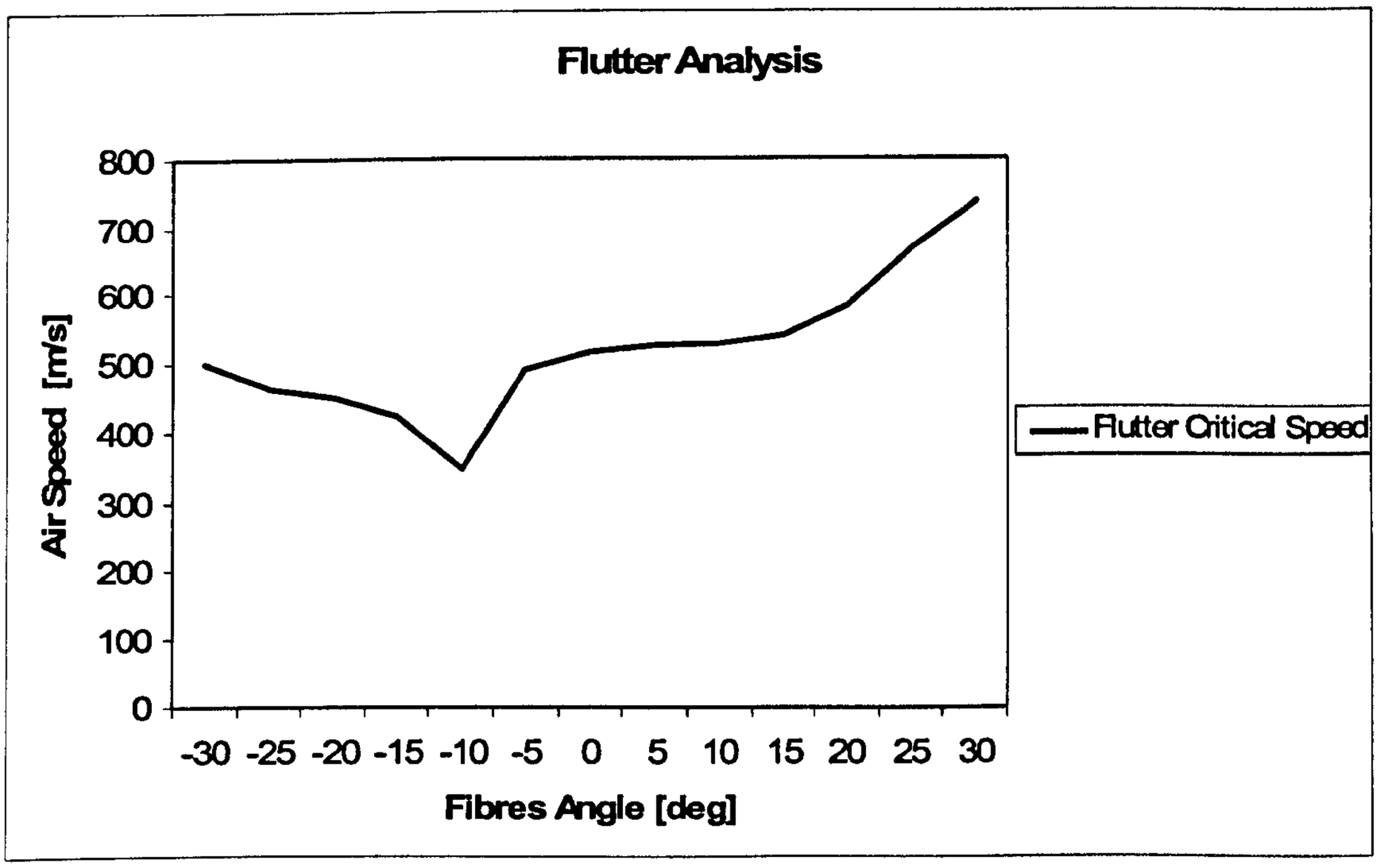

Figure 6.9: Critical flutter speed as function of fibre angles.

Such a minimum can be explained as follows. A negative fibre angle has a negative effect on critical flutter speed. However, as the absolute value of fibre angles increases, the stiffness *GJ* also increases, at least in the domain [0, -30] degrees. When *GJ* increases, an improvement of the critical flutter speed is always observed, especially in high aspect ratio wings [90]. Therefore, the worst values of critical flutter speed are observed for small values of negative angles but when the torsional stiffness increases, such effects tend to be re-balance.

The analyses undertaken suggest an interesting idea: to use positive fibre angles, even when located locally within the structure, to improve critical flutter speed. Investigations with high fidelity model are suggested (as future work) to confirm this trend.

An interesting comparison can be performed when analysing the divergence critical speeds obtained for the same structures. It has been calculated by using the analytical formulation proposed by Weisshaar [57].

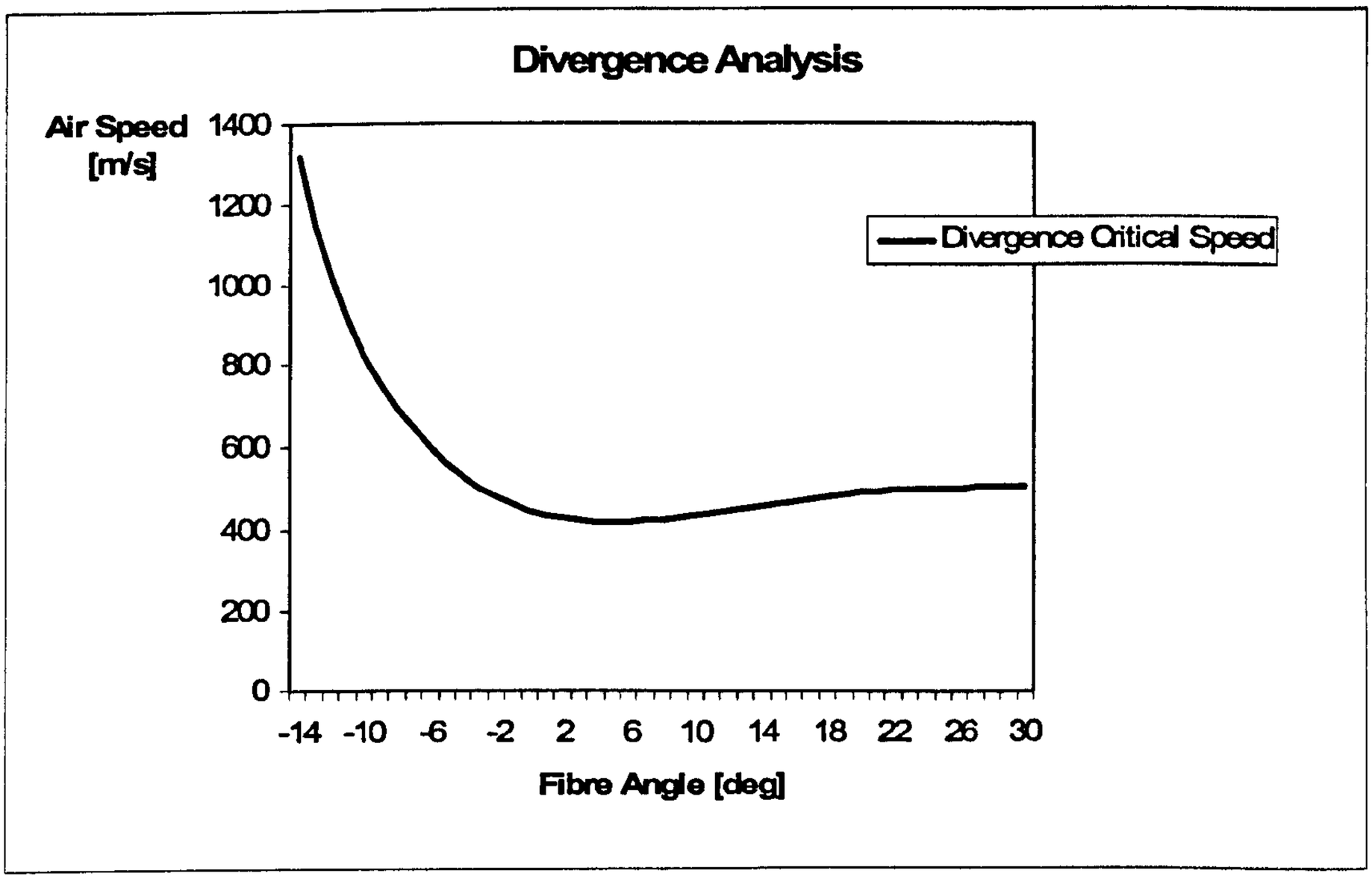

Figure 6.10: Critical divergence speed as function of fibre angles.

It can be observed that a "nose down" effect implies an increased value of critical divergence speed with respect to the orthotropic structure. A wing with a positive fibre angle ("nose up" effect), on the other hand, shows lower critical divergence speed than the orthotropic wing. As the value of the fibre angle increases, however, the torsional stiffness *GJ* increases as well and this effect tends to be re-balance.

6.6 Conclusions

Unbalanced composite laminates, when inducing "nose up" rotations, can increase critical flutter speed. However, as already discussed for the static aeroelasticity case in Chapter 5, bend-twist coupling is diminished in real wing boxes (primarily due to the presence of ribs), and to an even greater extent in a complete wing structure, because of the presence of leading and trailing edges. Thus, the magnitude of the improvement will also be diminished.

This Chapter is the last dedicated to aeroelastic tailoring. Potential benefits of bend-twist coupling effect have been shown both in the static aeroelasticity (Chapter 4) and in the flexural-torsional flutter (Chapter 6).

In the following Chapter, a new technique of combinatorial optimisation of composite plates will be described.

Chapter 7
A modified branch and bound for stacking sequence optimisation of a composite laminate

7.1 Introduction

The range and critical flutter speed improvements, discussed in Chapters 4 and 6 respectively, are strictly related to the bend-twist coupling effect and consequently to the anisotropy of the panels used in a wing box. To obtain such anisotropy, and more generally for the aeroelastic design of wings, only volume fractions of fibres are relevant. The stacking sequence of the laminae does not significantly affect the stiffnesses of the box and consequently the final aeroelastic design. In other words, bend-twist coupling stiffness K, bending stiffness EI and torsional stiffness GJ of a thin walled box, are only significantly affected by the $\underline{\underline{A}}$ matrix of each panel, but not by the $\underline{\underline{D}}$ matrix, which is a function of stacking sequence. Aeroelastic tailoring of a thin-walled wing box is, therefore, a function of membrane properties of the panels.

Once volume fractions of the layers have been fixed for aeroelastic tailoring purposes, then, stacking sequences of each panel can be optimised to improve a particular structural behaviour, related to the $\underline{\underline{D}}$ matrix. Stacking sequence optimisation can be performed without affecting the designed volume fractions.

In this chapter, a new method of stacking sequence optimisation is presented. It has been tested and compared with a heuristic technique in order to solve two different problems: the maximization of compression buckling load and the maximization of the first natural frequency of a composite laminate.

7.2 Modified Branch and Bound (MBB)

Stacking sequence optimisation of composite laminates is often formulated as a continuous optimisation problem with ply thicknesses and orientations used as design variables. In many practical applications, however, as already mentioned in the introduction, thicknesses of laminates are fixed and possible ply orientations are restricted to a small finite set. In this sense, the nature of the optimisation is inherently discrete and permutative.

A new technique for this type of stacking sequence optimisation is proposed. The starting point is a branch and bound method (BB), proposed in the literature by Kim and Hwang [111]. This algorithm is based on combinatorial calculus and it has already been successfully used in the optimisation of laminated composite structures [112].

The fundamental idea of this BB is the "ideal layer". Such an ideal lamina behaves as an optimum layer in any position of the stacking sequence. It does not exist in reality; its properties are purely abstract. The ideal lamina can be defined by using its properties:

1. A laminate consisting of n ideal layers must maximise the objective function. It can be represented as follows:

   [*id*\ *id*\ *id*\ *id*\.....\ *id*]

   where

   id is the ideal layer

   The fitness function of such laminate is the highest theoretically obtainable. In other words, this value of fitness function cannot be reached by using a real composite laminate.

2. When a single composite layer, whose fibres angle is ξ, is substituted for an "ideal lamina", a lower value of the fitness function F is always obtained. Symbolically, it can be written

$$F([\xi_1 \mid id \mid id \mid id \mid \ldots\ldots \mid id]) < F([id \mid id \mid id \mid id \mid \ldots\ldots \mid id]) \qquad (7.1)$$

This process continues until the last layer is replaced. A worst value of the fitness function is obtained every time a new composite layer replaces an "ideal" one. Therefore, the following property can be written:

$$F([\xi_1 \mid \xi_2 \mid \xi_3 \mid \xi_4 \mid \ldots\ldots \mid \xi_N]) < F([\xi_1 \mid \xi_2 \mid \xi_3 \mid \ldots\ldots \mid \xi_{N-1} \mid id]) \qquad (7.2)$$

The importance of ideal laminae will soon become clear. Next, the BB algorithm [111] is briefly described. The first step consists of selecting an initial stacking sequence S whose objective function is evaluated. The value of this function is denoted by F^S. Next, the idealized stacking sequence, denoted by ID, is also evaluated. It is important to remark that the fitness function F^S is not the fitness function of the ideal laminate. All the layers in the laminate ID are replaced with real layers, through the searching of branches, until the optimal stacking sequence is determined. Starting from the outermost ply, the k^{th} ideal layer is replaced with the real layer of ply angle ξ_k. In the example illustrated in Figure 7.1, the ply angles are restricted to 0, 90 or 45 degrees. For each stacking sequence obtained during the branching process, the objective function is evaluated. If a stacking sequence has a corresponding fitness lower than F^S, then this branch need not be branched further. According to the properties of Eqns. 7.1 and 7.2 further introduction of new composite layers, replacing "ideal" ones, would imply even lower values of the fitness function.

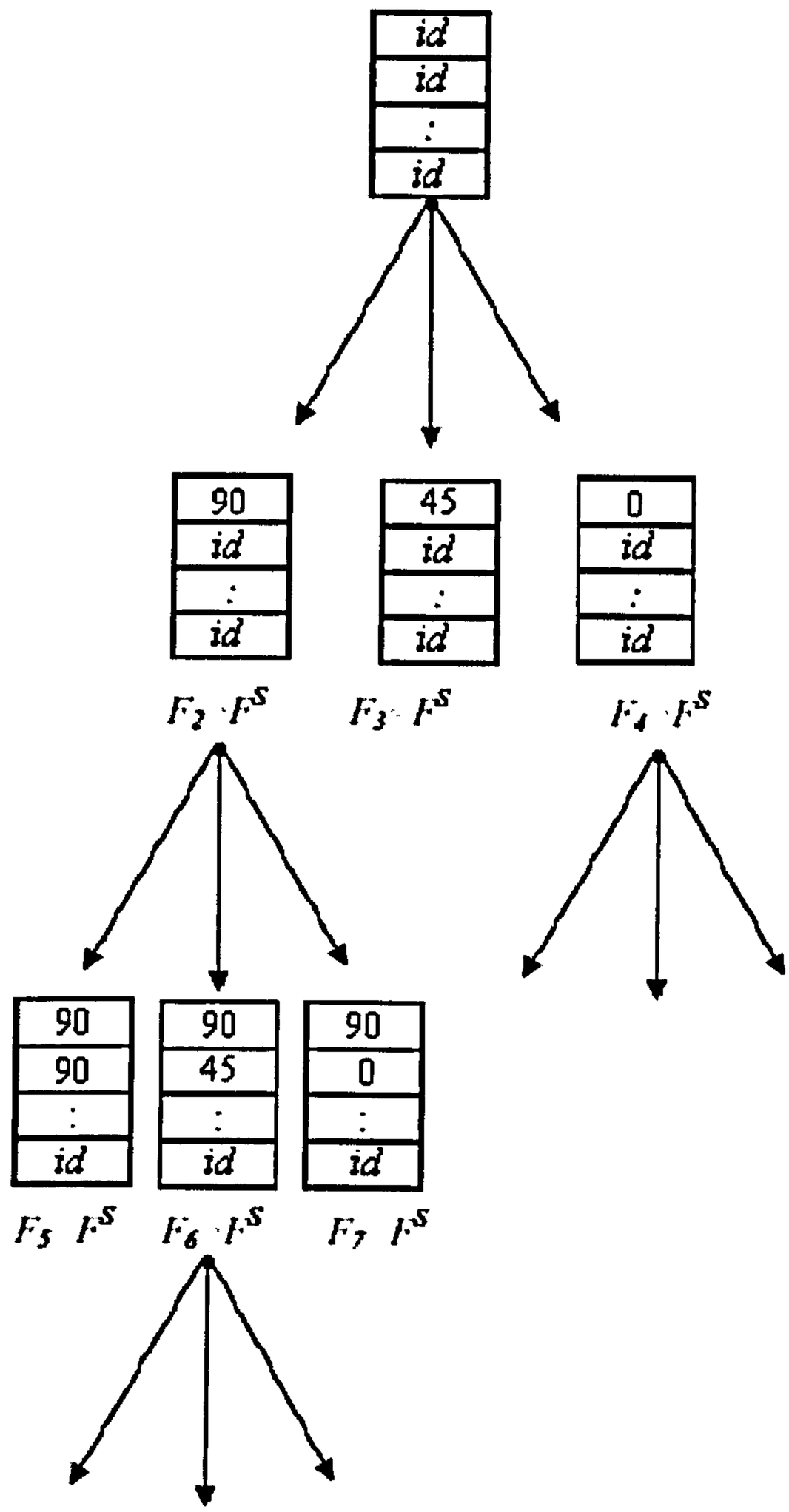

Figure 7.1: Branch and Bound model of Kim and Hwang.

The complete algorithm is effective and able to find excellent results. On the other hand, the CPU running time may be excessively long in finding a solution. Motivated by this shortfall, the following modification is proposed:

- For each ply that substitutes an ideal lamina, only the branch showing the best fitness function is investigated further. Therefore, the initial BB has been corrected by using a Greedy algorithm [113], i.e. by using the locally optimum choice at each stage of the search. The MBB is illustrated in Figure 7.2.

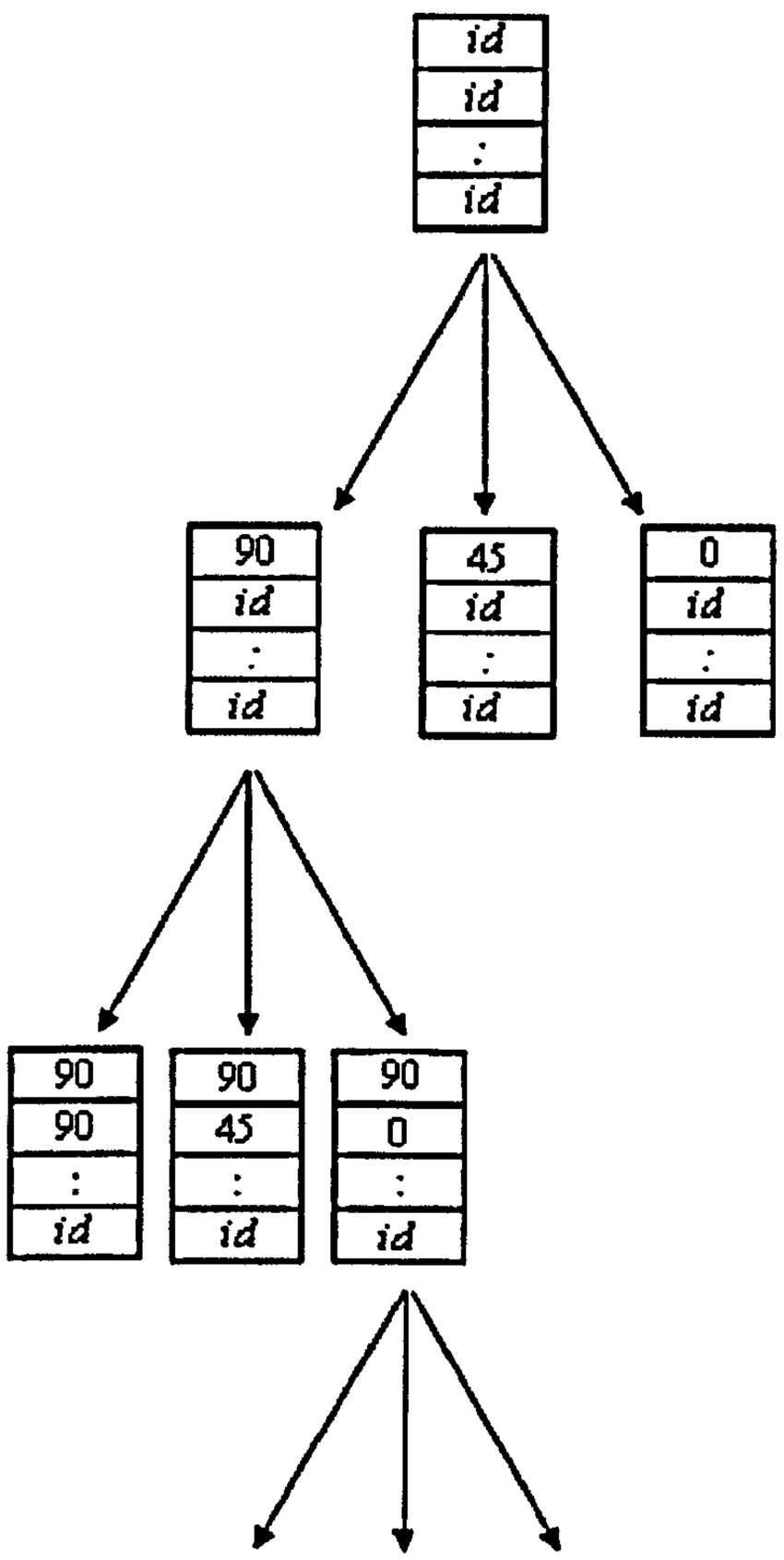

Figure 7.2: Modified branch and bound model with 3 possible plies [90/45/0].

With this modification, good solution accuracy is preserved and CPU running time is drastically reduced. The algorithm is effective when performances strictly related to the $\underline{\underline{D}}$ matrix are optimised. Ideal layers, in fact, are replaced with real layers starting from the outer to the middle of the laminate and the outermost layers are, in these problems, more relevant in the determination of the final sequence. In other words, the correct choice of the outermost layers has a larger impact on the final performance of the laminate, simply due to the larger local contribution of second moment of area from outer plies. For this reason the MBB algorithm still produces good stacking sequences.

7.3 Numerical examples

Two different problems, and consequently two different Fitness Functions, have been chosen to test the MBB algorithm. Furthermore, a comparison with a permutative GA [72], described is Chapter 2 has been performed. The first problem is the maximization of the first natural frequency of a simply supported composite plate; the second is the maximization of its compression buckling load.

For both problems, two different kinds of panels have been analysed. The first is an unbalanced laminate and, consequently, it exhibit extension-shear coupling. It is of the same type of panel used to build the wing box showing bend-twist coupling properties, described in Chapters 4 and 6. The second, is a balanced laminate, widely used in the aerospace industry. It will exhibit better performance than the analogous unbalanced laminates, both in terms of buckling and frequency. Both laminates are simply supported. They are 120 mm long and 40 mm wide. They are composed of 80 layers, but since they are both symmetrical, stacking sequence of only 40 layers are considered.

In the first panel, three different ply orientations are examined: 0, 90 and 45 degrees. The thickness of each layer is 0.2 mm. The number of layers with 90, 45 and 0 degrees is fixed as follows:

$n_{90} = 8$	is the number of 90 deg layers
$n_{45} = 16$	is the numbers of 45 deg layers
$n_0 = 16$	is the number of 0 deg layers

In the second panel 8 of 16 layers oriented at 45 deg are replaced with layers oriented at -45 deg. By fixing the number of each ply orientation, membrane properties are also fixed since the $\underline{\underline{A}}$ matrix is not a function of the laminate stacking sequence. The elastic properties of the material used are summarised in Table 7.1,

Table 7.1: Elastic properties of the composite layer.

E_1	181 GPa
E_2	10.3 GPa
G_{12}	4.55 GPa
v_{12}	0.28
density	1600 Kg/m^3
ply thickness	0.002 m

The MBB requires the definition of an ideal lamina. For the maximization of the first natural frequency and of the compression buckling load, such ideal lamina can be modelled as an isotropic one, having elastic modulus E equal to E_1 of the composite lamina and Poisson's ratio v equal to v_{12}. Furthermore, it is assumed that the density of the ideal layer is the same as a composite layer. An isotropic panel with such properties exhibits better performances than any composite plate, without regard to the stacking sequence. The explanation is quite simple. In a composite laminate, fibres are unidirectional with respect to the structural axis; consequently, the elastic strength is concentrated only in this direction. On the other hand, an isotropic material can be thought of as being made by fibres placed in all of the possible directions. When its elastic modulus is high, frequency and compression buckling load results are maximized.

However, and it is an important point to be remarked, the ideal layer may not be an isotropic one for all problems.

7.3.1 Examples with an unbalanced laminate

The maximization of the first natural frequency is first described. This problem is of general importance for two reasons:

- To avoid panel flutter, a phenomenon that can occur at supersonic speed.
- To avoid resonance and consequent amplified vibrations [114].

Due to the lack of closed form solutions for unbalanced laminates, the fitness function is evaluated by interfacing MATLAB [115 ©] and MSC Nastran [83 ©].

It is observed that the fitness function of the "ideal" laminate is $F_{max} = 2.75\ 10^5$ rad/s. It was calculated as the natural frequency of a plate of isotropic material having elastic modulus E equal to E_1 of the composite lamina and Poisson's ratio v equal to v_{12}. With respect to the aforementioned permutative GA (refer to Chapter 2), three tuning parameters are refined to ensure timely convergence. The following parameter values were used:

- Minimum number of generation before terminations: 20
- Size of initial population: 30
- Number of mutations (permutation of two layers randomly selected): one for each generation.

The improved MBB method requires no parameter tuning. It was observed that whilst the GA obtained good results, it was only able to find local minima. The fitness function obtained by the GA prior to termination was $F_{GA} = 216260$ rad/s. The average value of the fitness function of each generation is shown in Figure 7.3. A particular characteristic of GA algorithms is observed: the population is continuously improving, even if some oscillation is present.

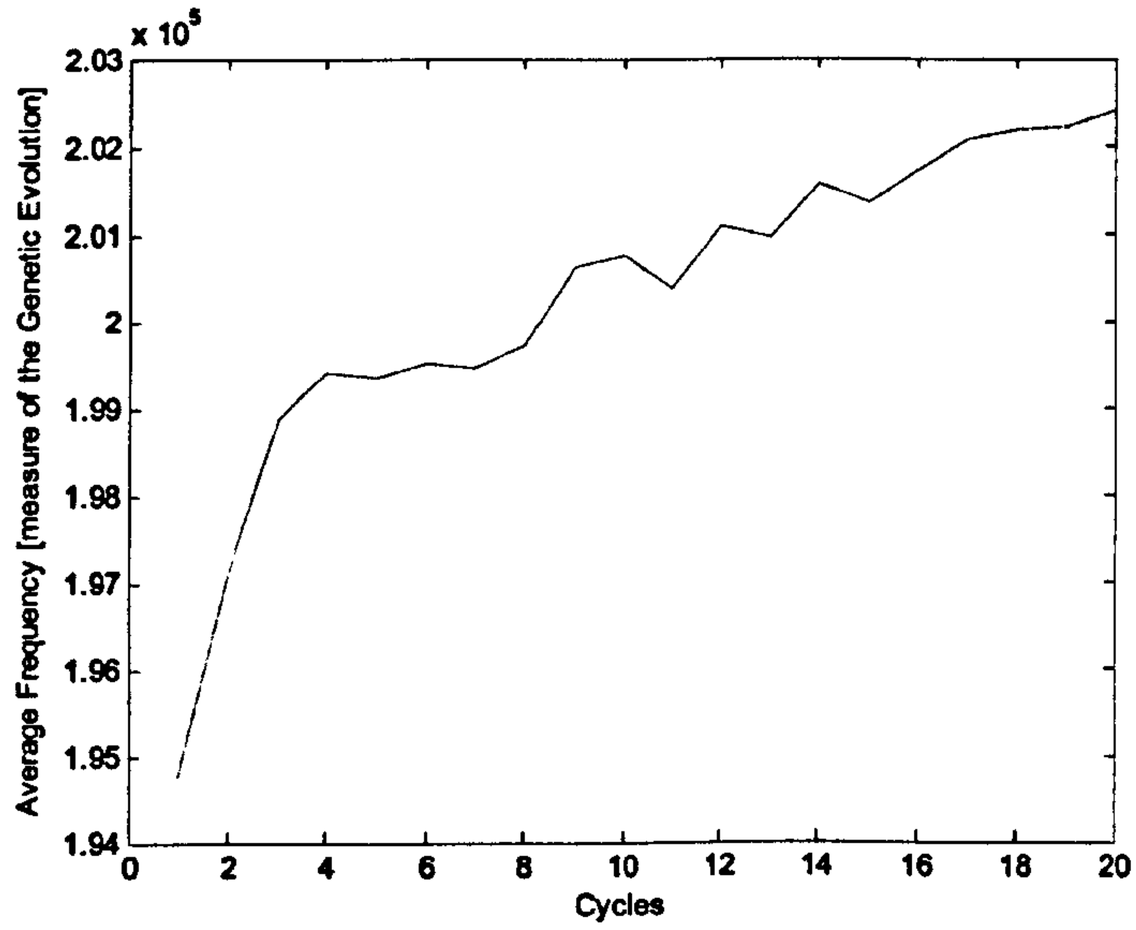

Figure 7.3: Evolution of the population. The average frequency increases with the progression of cycles (generations).

Using a GA, the stacking sequence obtained was found to be

$$[90_4\backslash 0\backslash 45_2\backslash 0\backslash 90\backslash 45\backslash 0\backslash 45\backslash 90\backslash 45_2\backslash 0\backslash 45\backslash 0\backslash 45_2\backslash 0_3\backslash 45\backslash 0\backslash 90\backslash 45\backslash 90\backslash 0\backslash 45\backslash 0_4\backslash 45_2\backslash 0\backslash 45\backslash 0\backslash 45]_s$$

Better results are obtained by using the modified MBB algorithm. Its stacking sequence was found to be

$$[90_8\backslash 45_{16}\backslash 0_{16}]_s$$

Table 7.2 details the obtained fitness values for each algorithm as well as respective CPU times.

Table 7.2: Comparison of the results of GA and MBB for the first natural frequency of an unbalanced laminate.

	GA	MBB
Value of Fitness (Frequency [rad\s])	$2.16\ 10^5$	$2.51\ 10^5$
CPU Running Time [s]	835	98

Compressive buckling loads maximization is now described. It is a common problem in the aerospace industry. When a wing is loaded in bending, for example, panels of the top skin are compressed under uplift. Even if the value of such compression load is below its critical strength it can force the panels to buckle. Due to the lack of analytical formulations for plates of general geometry with unbalanced laminates, the fitness function is evaluated by interfacing MATLAB© and MSC Nastran©. In other words, the fitness function of each laminate is evaluated by using MSC Nastran. The Nastran input file (.bdf), however, is written by using a Matlab M-file. At each iteration, a sub-routine substitutes an ideal layers of isotropic material with a real composite lamina. Results of the analyses are reported below. Using the modified branch and bound, the optimal stacking sequence was found to be

$$[45_{13}\backslash 90_8\backslash 0_{16}\backslash 45_3]_s$$

By using the permutative genetic algorithm, the optimal stacking sequence is

$[90\backslash 45\backslash 90_2\backslash 45_2\backslash 0_2\backslash 45_2\backslash 0\backslash 45\backslash 90\backslash 45\backslash 90\backslash 0\backslash 90\backslash 45\backslash 0\backslash 45\backslash 0\backslash 45_3\backslash 90\backslash 45_2\backslash 0_2\backslash 45\backslash 0\backslash 45\backslash 0_5\backslash 90\backslash 0_2]_s$

Results obtained with MBB do not differ significantly from those obtained with the GA. However, the MBB is quicker. Results are summarised in Table 7.3

Table 7.3: Comparison of the results of GA and MBB for compressive buckling load maximization of an unbalanced laminate.

	GA	MBB
Buckling compression load [N\mm]	2.25 * 10^4	2.26*10^4
CPU Running Time [s]	680	101

7.3.2 Examples with a balanced laminate

Let us now focus on the balanced laminated panel. To evaluate its first natural frequency and compressive buckling load, formulae are available in the literature [21], and have been used. Analytical formulae, in fact, avoid the interactive model using Nastran-Matlab, allowing significant CPU time savings.

Using the modified branch and bound, the optimal stacking sequence to maximize the first natural frequency is

$$[90_8\backslash \pm 45_8\backslash 0_{16}]_s$$

whilst the permutative genetic algorithm gives

$$[90_2\backslash \pm 45\backslash 90_2\backslash \pm 45\backslash 90_4\backslash 0_2\backslash \pm 45_6\backslash 0_{14}]$$

Results are summarised in Table 7.4

Table 7.4: Comparison of the results of GA and MBB for the first natural frequency of a balanced laminate.

	GA	MBB
Value of Fitness (Frequency [rad\s])	$2.45\ 10^5$	$2.54\ 10^5$
CPU Running Time [s]	41	0.5

Concerning compressive buckling loads, the results show once again how fast and reliable the modified branch and bound method appears to be. The optimal stacking sequence obtained with MBB is:

$$[\pm 45_8\backslash 90_8\backslash 0_{16}]_s$$

whilst the optimal stacking sequence obtained with the permutative GA is:

$$[\pm 45_4\backslash 0_2\backslash 90_2\backslash \pm 45_4\backslash 90_4\backslash 0_2\backslash 90_2\backslash 0_{12}]$$

Results are summarised in Table 7.5

Table 7.5: Comparison of the results of GA and MBB for compressive buckling load maximization of a balanced laminate.

	GA	MBB
Buckling compression load [N\mm]	2.82 * 10^4	2.90*10^4
CPU Running Time [s]	15	0.5

The stacking sequences proposed are quite simple, but these examples are only useful to understand the potential of the method proposed.

7.3.3 An example with the four plies rule

In order to obtain more realistic stacking sequences, empirical knowledge for avoiding large scale matrix cracking and delamination can be easily implemented. This rule is known as four plies rule [116]: stacking sequence do not have more that four consecutive layers with the same orientation. If this rule is applied to the example of the compression bucking load of a balanced laminate, the following results are obtained. The stacking sequence obtained with the GA is

$$[\pm 45_4\backslash 0_2\backslash 90_2\backslash \pm 45_4\backslash 90_2\backslash 0_2\backslash 90_2\backslash 0_4\backslash 90\backslash 0_4\backslash 90\backslash 0_4]$$

whilst the stacking sequence obtained with the MBB is:

$$[\pm 45_8\backslash 90_3\backslash 0\backslash 90\backslash 0\backslash 90\backslash 0_4\backslash 90\backslash 0_4\backslash 90\backslash 0_4\backslash 90\backslash 0_2]_s$$

The results are summarised in Table 7.6.

Table 7.6: Comparison of the results of GA and MBB for compressive buckling load maximization of a balanced laminate. Four plies rule is applied.

	GA	MBB
Buckling compression load [N\mm]	2.79 * 10^4	2.88*10^4
CPU Running Time [s]	15	0.5

7.4 Discussion and Conclusions

A new algorithm to optimise the stacking sequence of a composite plate having a fixed number of layers and possible ply orientations has been proposed and tested. Good results have been obtained, especially if the algorithm is compared with a standard GA technique. CPU running time has been drastically reduced.

Despite the success of MBB, it is important to highlight potential issues. The algorithm works well due to the inherently discrete nature of the set of ply orientations used in the optimisation. As the set of ply orientations grows, it must be questioned whether this approach remains efficient and suitable for determining laminate stacking sequences. Additionally, due to the rapid and premature pruning of branches, the obtained stacking sequence may not satisfy certain criteria. Premature pruning of branches limits an abundance of possible combinations of angles which may give improved designs. On the other hand, if the BB approach presented in the literature is used, the algorithm becomes increasing inefficient with increasing thickness and number of ply orientations.

Despite these potential shortfalls, tests have shown that the MBB obtains respectable results. Note, the optimal laminates found (if considered not satisfactory) could form part of an initial population for a heuristic optimisation method. Lastly, for different objective functions, different idealizations may be required. It is noted that the search for an idealization which satisfies the conditions outlined in Section 7.2 may be a non-trivial and time consuming task.

Chapter 8
Conclusions and Future Work

8.1 Introduction

The major results and contributions of this research are summarised in this chapter. Suggestions for future work and possible research are also included.

8.2 Main objectives and results of the research

Possible benefits of bend-twist coupling on aeroelastic performances of composite wings have been investigated. In particular, two different aspects of aeroelasticity have been studied:

1. Static aeroelasticity. A "low fidelity" aeroelastic model has been developed. Aerodynamic loads have been calculated by using a vortex-lattice method. The wing structure has been modelled as a box, i.e. a thin-walled composite beam with rectangular cross section. Static aeroelastic equilibrium has been obtained by using an iterative procedure.

2. Flexural-torsional flutter. A "low fidelity" aeroelastic model has been developed to calculate critical flutter speed. The wing has been modelled as a prismatic beam, while Theodorsen's aerodynamic model (in the frequency domain) has been used to model the aerodynamic behaviour.

Results obtained can be summarised with the following points:

- Unbalanced plates, when used in a composite wing, can improve the range of the aircraft. The improvement, measured with respect to an orthotropic wing, taken as a reference structure, was found to be less than 1%. Besides this small improvement, a negative effect is also observed, i.e. structural weight increases. The wing made with unbalanced composite materials can be up to 15% heavier than the orthotropic wing, for the representative wing that was analysed.

If a more realistic structure was considered (including structural details as stringers, ribs, webs, leading and trailing edges), the bend-twist coupling effect would be further diminished, so the improvements on range performance are significantly less.

This result could appear quite poor. However, the small improvement of range regards the whole aircraft. Furthermore, even a small improvement can imply important financial savings. On the other hand, even if the structural weight increases, the overall weight penalty on the aircraft is often small. More precise results could be obtained by using a high fidelity model.

- The use of unbalanced composite materials can improve the critical flutter speed of a composite box. A "nose up" distribution of the elastic properties is required, even if it negatively affects critical divergence speed and structural weight.

Besides the aeroelastic analyses, two sub-problems have been studied and solved. They are the point of novelty of this thesis, i.e. the main contribution of the research.

- An analytical model to evaluate the basic stiffnesses *EI* and *GJ* of a composite thin-walled box has been developed and tested, and included as part of the static and dynamic aeroelastic tools. The analytical model provides excellent results for several geometries and lay-ups. Furthermore, its form is relatively simple and provides a good understanding of the physical meaning of the stiffness. No other model, presented in the literature (to the knowledge of the author), provides such precision in the evaluation of *EI* and *GJ* for different geometries and, at the same time, can be easily implemented.

- A new algorithm (MBB) for stacking sequence optimisation has been developed. It is useful to optimise laminates whose $\underline{\underline{A}}$ matrix is predetermined: i.e. when plate thickness and number of different ply orientations are fixed "a priori". The fitness function must be strictly dependent on the $\underline{\underline{D}}$ matrix of the plate: examples

can be fundamental frequency or compression buckling load maximization. The algorithm has been developed by adapting a Branch and Bound (BB) method presented in the literature, with the integration of a Greedy algorithm. MBB gives excellent results when compared with standard heuristic techniques, such as permutative GAs. Additionally, CPU running time is drastically reduced when comparing the new algorithm with the original BB.

8.3 Future Work

Range improvement induced by anisotropic laminates offers potential financial savings while a heavier aircraft suggests financial losses (less passengers can be transported by exploiting the same lift, because the structural weight increases). Which of these two effect dominates? To know with more precision the answer to this question, high fidelity models must be used. A detailed structural model of an existing aircraft wing coupled with a transonic aerodynamic code could be investigated to find precise values of lift and drag, and consequently of range. Furthermore, weight penalties due to a heavier wing should be evaluated by using the real weight of this existing aircraft. In other words, the static aeroelastic investigation presented in this thesis could be repeated using more precise structural and aerodynamic tools in order to obtain more precise results. The basic concept developed in this thesis, however, remains unchanged.

In the same way, high fidelity models could be also investigated to understand whether "nose up" fibres could be used, even just locally, i.e. not in the whole wing span, to improve critical flutter speed without excessive weight penalties.

An analytical model could be developed to predict the bend-twist coupling stiffness K of a box including ribs. The approach proposed by Lemanski and Weaver could be used also in this case: a unitary bending deformation can be applied and the resultant twisting moment measured.

References

[1] Shirk M. H., Hertz T. J., Weisshaar T. A., "Aeroelastic tailoring-theory, practice, and promise", Journal of Aircraft, 23 Nr. 1 (1986).

[2] Weisshaar T. A., "Aeroelastic Tailoring: Creative use of unusual materials", AIAA paper 87-0976-CP, AIAA\ASME\ASCE\AHS 28th Structures, Structural dynamics and Materials conference, (1987).

[3] Krone Jr. N. J., "Forward Swept Wing Flight Demonstrator", AIAA Aircraft Systems and Technology Meeting, August 1980, Anaheim, California (USA).

[4] Krone Jr. N. J., "Divergence Elimination with Advanced Composites", AIAA Aircraft Systems and Technology Meeting, August 1975, Los Angeles, California (USA).

[5] Krone Jr. N. J., "Divergence Elimination with Advanced Composites", PhD Thesis, University of Maryland, (1974).

[6] Patil M., "Aeroelastic Tailoring of Composite Box Beams", Aerospace Sciences Meeting and Exhibit, 35th, Reno, NV, Jan. 6-9, (1997).

[7] Wu X., Sun T., "Simplified theory for composite thin-walled beams" AIAA Journal, Vol. 30, Nr 12, (1992).

[8] Massa J. C., Barbero E. J., "A strength of material formulation for thin-walled composite beams with torsion". Journal of Composite Materials, 32, Nr. 13, (1998).

[9] Rand O., "Fundamental closed-form solutions for solid and thin-walled composite beams including a complete out-of-plane warping model", International Journal of Solid and Structures, Nr. 35, Vol. 21, (1998).

[10] Hwu C., Tsai Z. S., "Aeroelastic Divergence of Stiffened Composite Multi-cell Wing Structures" Journal of Aircraft Vol.39, Nr.2, (2002).

[11] Kim C., White S. R., "Thick Walled Composite Beam Theory Including 3-D Elastic Effects and Torsional Warping", Journal of Solid Structures, Vol. 34, Nr 31-32, pp 4237-4259 (1997).

[12] Rehfield L. W., Atilgan A. R., Hodges D. H., "Non-classical behaviour of Thin-Walled Composite Beams with Closed Cross Section", Journal of American Helicopter Society 35 Nr. 2, (1990).

[13] Librescu L. and Song O., "On the Static Aeroelastic Tailoring of Composite Aircraft Swept Wings Modelled as Thin-Walled Beam Structures" Composite Engineering, Vol. 2, Nr. 5-7, pp497-512, (1992).

[14] Chandra R., Chopra I., "Structural response of Composite Beams and Blades with Elastic Couplings", Composite Engineering, Vol. 2, Nr. 5-7, pp 347-374, (1992).

[15] Berdichevsky V., Armanios E., Badir A., "Theory of anisotropic thin-walled closed cross-section beams", Composite Engineering, 2, Nr. 5-7, pp. 411-432, (1992).

[16] Kollar L. P., Pluzsik A., "Analysis of thin-walled composite beams with arbitrary layup", Journal of Reinforced Plastics and Composites, 21, Nr. 16, (2002).

[17] Pluzsik A., Kollar L. P., "Effect of shear deformation and restrained warping on the displacement of composite beams". Journal of Reinforced Plastics and Composites, 21, Nr. 17, (2002).

[18] Lemanski S., Weaver P. M., "Flap-torsion coupling in sandwich beams and filled box sections", Thin-walled Structures, Nr. 43 vol. 6, (2005).

[19] Johnson E. R., Vasiliev V. and Vasiliev D., "Anisotropic thin-walled beams with closed cross-sectional contours", AIAA Journal, 39, Nr. 12, (2001).

[20] Guo S., "Aeroelastic optimisation of an aerobatic aircraft wing structure", Aerospace Science and Technology, 11, (2007).

[21] Gurdal Z., Haftka R. T., Hajela P., "Design and Optimisation of Laminated Composite Materials", John Wiley and Sons.

[22] Stanewsky E., "Aerodynamic benefits of adaptive wing technology" Aerospace Science and Technology, 4(7): pp 439–452, (2000).

[23] Mason W. H., Papila M., Haftka R. T. and Alves R., "Tailoring wing structures for reduced drag penalty in off-design flight conditions",10th AIAA/ISSMO Multidisciplinary analysis and optimization conference, Albany, NY, USA, August 30th - September 1st, 2004.

[24] Fontanazza A., Talling R., Jackson M., Dashwood R., Dye D., Iannucci L., "Morphing Wing Technologies Research", Seas DTC Conference-Edinburg, (2006).

[25] Flick P. M., Love M. H., Zink P. S., "The impact of active aeroelastic wing technology on conceptual aircraft design", RTO AVT Specialists' Meeting on Structural Aspects of Flexible aircraft control".

[26] Voracek D., Pendleton E., Reichenbach E., Griffin K., Welch L., "The active aeroelastic wing phase I flight research through Jaunuar 2003" NASA/TM-2003-210741.

[27] Cooper J. E., " Adaptive Stiffness Structures for Air Vehicle Drag Reduction. Meeting Proceedings RTO-MP-AVT-141, paper 15. Neuilly-sur-Seine, France, (2006).

[28] Chen P. C., Sarhaddi D., Jha R., Lui D. D., Griffin K., Yurkovich R., "Variable Stiffness Spar Approach for Aircraft Manouver Enhancement Using ASTROS" AIAA J. Aircraft Vol.37 Nr 5 (2000).

[29] Hartl D. J., Lagoudas D. C., "Aerospace applications of shape memory alloys", Proceeding of IMech 2007, Vol. 221 Part G: Aerospace Engineering.

[30] Wang D. P., Bartley-Cho J. D., Martin C. A., Hallam B., "Development of high-rate, large deflection, hinge-less trailing edge control surface for the smart wing wind tunnel model", Smart Structures and Materials 2001.

[31] Strelec J. K., Lagoudas D. C., Khan M. A., Yen J., "Design and implementation of shape memory alloy actuated reconfigurable wing" Journal of Intelligent Materials, Systems and Structures, Vol. 14, (2003).

[32] Sofla A. Y. N. , Meguid S. A., Tan K. T., Yeo W. K., "Shape morphing of aircraft wing: status and challenges", Materials and Design 31, (2010).

[33] Balta J. A., Simpson J., Michaud V., Manson J.A.-E., Schrooten J., Embedded Shape Memory Alloys confer aerodynamic Profile Adaptivity", Smart Materials Bulletin, (2001).

[34] Knowles G. , Bird, R. W., "Telescopic wing system". US Patent 6834835. 28 December 2004.

[35] Mason W. P.,"Piezoelectricity, its history and applications", Journal of Acoustic American Society 70 (1981).

[36] Irshik H.,"A review on static and dynamic shape control of structures by piezoelectric actuation", Engineering Structures 24 (2002).

[37] Chee C., Tong L., Steven G. P., " Piezoelectric actuator orientation optimization for static shape control of composite plates", Composite Structures 55 (2002).

[38] Bruch Jr. J. C. , Sloss J. M., Sadek I. S., "Optimal piezo-actuator locations/length and applied voltage for shape control of beams", Smart Material Structures (2000).

[39] Cesnik C. E., Palacios, "Modelling Piezo-composite Actuators Embedded in Slender Structures" AIAA paper 2003-1803.

[40] Suleman A., Costa A. P., "Adaptive control of an aeroelastic flight vehicle using piezoelectric actuators", Computer and Structures 82 (2004).

[41] Nam C., Kim Y., Weisshaar T. A., "Optimal sizing and placement of piezo-actuators for active flutter suppression", Smart Material Structures 5, (1996).

[42] Rocha J., Moniz P., Suleman A., "Aeroelastic Control of a Wing with Active Skins Using Pizoelectric Patches", Mechanics of Advanced Materials and Structures, Vol. 14, pp. 23-32, (2007).

[43] Simpson J., Schweiger J., "Industrial Approach to Piezo-Electric Damping of Large Fighter Aircraft Components", SPIE Smart Structures and Materials Conference, (1998).

[44] Rocha J., Moniz P.A., Costa A.P. , Suleman A., "On Active Aeroelastic Control of an Adaptive Wing Using Piezoelectric Actuators", Engineering Note, Journal of Aircraft, Vol. 41, No. 6, (2004).

[45] Soykasap O., Hodges D. H., "Performance Enhancement of a Composite Tilt-Rotor Using Aeroelastic Tailoring", Journal of Aircraft Vol. 37, Nr. 5 (2000).

[46] Cesnik C. E., Hodges D. H., "VABS:A new concept for composite rotor blade cross section modelling", Journal of American Helicopter Society, Vol. 42, Nr. 1 (1997).

[47] Ganguli R., Chopra I., "Multi-Objective Optimization of a Composite Helicopter Rotor", Proceeding of 35th AIAA/ASCE/AHS/ASC Structures, Structural Dynamics, and Material Conference (1994).

[48] Lobitz D. W., Laino D. J., "Load mitigation with twist-coupled HAWT blades", 18th ASME Wind Energy Symposium (1999).

[49] Lobitz D. W., Veers P. S., "Aeroelastic Behaviour of Twist-coupled HAWT Blades", paper AIAA-98-0029.

[50] Weisshaar T. A., Foist B. L., "Vibration Tailoring of Advanced Composite Lifting Surfaces", Journal of Aircraft, Vol. 22 Nr. 2 (1985).

[51] Weisshaar T. A., Ryan R. J., "Control of Aeroelastic instabilities trough stiffness cross-coupling" Journal of Aircraft, Vol. 23, Nr. 2.

[52] Fung Y. C., "An introduction of the theory of aeroelasticity", Dover Publications (2002).

[53] Sarigul-Klijn N. and Oguz S., "Effect of aspect ratio and ply orientation on aeroelastic response of composite plates", Journal of Aircraft, Vol. 35 Nr. 4 (1998).

[54] Green J. A., "Aeroelastic Tailoring of Aft-Swept High-Aspect-Ratio Composite Wings", Journal of Aircraft Vol. 24, Nr. 11 (1987).

[55] Ehlers S. M., Weisshaar T. A., "Static Aeroelastic control of an adaptive lifting surface", Journal of Aircraft, Vol. 30 Nr. 4 (1993).

[56] Weisshaar T. A., Nam C., Baptista-Rodriguez A., "Aeroelastic Tailoring for Improved UAV Performance", AIAA Paper 98-1757. Presented at the 39th AIAA/ASME/ASCE/AHS/ASC Structures, Structural Dynamics, and Materials Conference. Long Beach, California, April. 20–23, (1998).

[57] Weisshaar T. A., "Divergence of Forward Swept Composite Wings", Journal of Aircraft Vol. 17, Nr. 6 (1980).

[58] Weisshaar T. A., Duke D. K., "Induced drag reduction using aeroelastic tailoring with adaptive control surfaces", Journal of Aircraft Vol. 43, Nr. 1 (2006).

[59] Eastep F. E., Tischler V. A., Venkayya V. B. and Khot N. S., "Aeroelastic Tailoring of Composite Structures", Journal of Aircraft Vol. 36, Nr. 6 (1999).

[60] Herencia J. E., Weaver P. M. and Friswell M. I., "Morphing wing design via aeroelastic tailoring", 48th AIAA/ASME/ASCE/AHS/ASC Structures, Structural Dynamics and Materials Conference, 23-26 April 2007, Honolulu, Hawaii, USA.

[61] Kim Y. Y., Kim J. H., "Thin walled closed box beam element for static and dynamic analysis", Journal for numerical methods in engineering 45, pp 473-490 (1999).

[62] Peng L. C., Peng T. S., "Pipe Stress Engineering", ASME Books, (2009).

[63] Giavotto V., Borri M., Mantegazza P., Ghirinelli G., "Anisotropic Beam Theory and applications", Computers and Structures 16 Nr. 1-4 (1983), pp. 403-413.

[64] Yu W., Hodges D. H., Volovoi V., Cesnik C., " On Timoshenko-like modelling of initially curved and twisted composite beams", International Journal of Solids and Structures, Nr. 39, (2002).

[65] Bruhn E. F., "Analysis and design of flight vehicle structures", Tristate Offset Company (1965).

[66] Mesquita L., Kamat M. P., "Optimisation of stiffened laminates composite panels with frequency constraints", Engineering Optimisation Nr. 11, 1987 pp 77-86.

[67] Schmidt L. A., Farshi B., "Optimum laminate design for strength and stiffness", Journal of numerical for Engineering 7 1973, 519-536.

[68] Park J. H., Hwang J. H., Lee C. S., Hwang W., "Stacking sequence design of composite laminates for maximum strength using genetic algorithms", Composite Structures Nr. 52 (2001).

[69] Gurdal Z., Hafka R. T., Nagendra S., "Genetic algorithms for the design of laminated composite panels", SAMPE J. 30(3), (1994).

[70] Le Riche R., Hafka R. T., "Optimization of laminate stacking sequence for buckling load maximization by genetic algorithm", AIAA 31, Vol. 5, (1993).

[71] Herencia J. E., Weaver P. M., Friswell M. I., "Optimisation of anisotropic composite panels with T-shaped stiffeners including transverse shear effects and out-of-plane loading" Structural Multidisciplinar Optimization, Vol.37, Nr. 2, pp165-184, (2008).

[72] Liu B., Hafka R. T., Akgun M. A., Todoroki A., "Permutation genetic algorithm for stacking sequence design of composite laminates", Computational Methods Applied Mechanical Engineering 186, 357-372 (2000).

[73] Eberhart R., Shi Y., Kennedy J., "Swarm Intelligence", Morgan Kauffman.

[74] Adali S., Verijenko V. E., "Optimum stacking sequence design of symmetric hybrid laminates undergoing free vibrations" Composite Structures, Nr. 54, (2001).

[75] Suresh S., Sujit P. B., Rao A. K., "Particle swarm optimisation approach for multi-objective composite box-beam design", Composite Structure, Nr. 81, pp 598-605, (2007).

[76] Dorigo M., "Optimization, learning and natural algorithms", PhD thesis, Politecnico di Milano, (1992).

[77] Aymerich F., Serra M., "Optimisation of laminate stacking sequence for maximum buckling load using the ant colony optimisation (ACO) metaheuristic" Composites Part A 39, pp 262-272, (2008).

[78] Manan A., Vio G. A., Harmin M. Y., Cooper J. E., "Optimisation of aeroelastic composite structures using evolutionary alogorithms", Engineering Optimization, Vol. 42, No. 2, (2010).

[79] Michalewicz Z., Dasgupta D., Le Riche R. G., Schoenauer M., "Evolutionary Algorithms for Constrained Engineering Problems" Computers and Engineering Vol. 30, Nr. 4, (1996).

[80] Cesnik C. E. S., Hodges D. H., Patil M. J., "Aeroelastic Analysis of Composite Wings", AIAA paper-96-1444-CP AIAA/ASME/ASCE/AHS/ASC Structures, Structural Dynamics and Materials Conference and Exhibit, 37th, Salt Lake City, UT, Apr. 15-17, (1996).

[81] Jones R. M., "Mechanics of Composite materials", Taylor and Francis, (1999).

[82] Viola E., "Scienza delle Costruzioni", Pitagora Editrice, Bologna, (1983).

[83] MSC Patran/Nastran Software"-MSC Software Corporation, Santa Ana, CA, USA, (2005).

[84] Bathe K. J., "Finite Element Procedures", Prentice-Hall, (1996).

[85] Paidoussis M.P., Issid N. T., "Dynamic instability of pipes conveying fluid", Journal of Sound and Vibrations, Vol. 33, Nr. 3, (1974).

[86] Collar A. R., "The expanding domain of aeroelasticity", Journal of the Royal Aeronautical Society, Vol. L, (1946).

[87] Lanchester F. W., "Torsional vibration of the tail of an airplane", ARC R&M 276, Part 1, (1916).

[88] Friedmann P.P., "The renaissance of aeroelasticity and its future", Journal of Aircraft, Vol. 36, Nr. 1, (1999).

[89] Livne E., "Future of airplane aeroelasticity", Journal of Aircraft, Vol. 40, Nr. 6, (2003).

[90] Chiocchia G., "Principi di Aeroelasticità" Levrotto & Bella, (1999).

[91] Monegato G., "Fondamenti di calcolo numerico", CLUT (1998).

[92] Bertin J. J., "Aerodynamics for Engineers", Prentice Hall.

[93] Katz J., Plotkin A., "Low Speed Aerodynamics", Cambridge University Press (2001)

[94] Thomas R. W., "Analysis of Aircraft Stability and Control Design Methods", AFWAL-TR-84-3038, Vol. 2, App. B, "Evaluation of Aerodynamic Panel Method", by Koegler, (1984)

[95] Clancy L. J., "Aerodynamics", John Wiley and Sons (1975).

[96] Lausetti A., "Elementi di meccanica del volo", Levrotto &Bella.

[97] Anderson J. D., "Fundamentals of aerodynamics", McGraw Hill (2001).

[98] Roskam J., "Airplane Design, part V, component weigh estimation" Roskam Aviation and Engineering Corporation, (1985).

[99] Svoboda C.,"Aluminium Structural weigh components as a function of wing loading", Aircraft Design 2, (1999).

[100] Seebass A. R., "Shock-Free configurations in two and three dimensional flows" Arizona University Tucson engineering experiment Station, (1981).

[101] Prananta B. B., Tjatra I. W., Spekreijse S.P., Kok J. K., Meijer J. J., "Static aeroelastic simulation of military aircraft configuration in transonic flow", Technical Report, National Aerospace Laboratory NLR (The Netherlands), (2001).

[102] Canale G., Weaver P. M., " A simple model to evaluate aeroelastic tailoring of a wing box", Proceedings of Royal Aeronautical Society Conference on Aircraft structural design, Liverpool, (2008).

[103] Wright J. R., Cooper J. E., " Introduction to Aircraft Aeroelasticity and Dynamic Loads", Wiley and Sons, (2007).

[104] Hancock G. J., Wright J. R., "On the teaching of the principles of wing flexure-torsional flutter" Aeronautical Journal, Vol. 89, Nr. 88, (1985).

[105] Senett R. E., "Matrix analysis of Structures" Waveland Pr Inc, (2005).

[106] Kargarnov M. H., Mamandi A., "Aeroelastic Response for pure plunging motion of a typical section due to sharp edged gust, using Jones approximation aerodynamics", Word Academy of Science, Engineering and Technology, Nr. 36, (2007).

[107] Butler R., Banerjee J. R., "Optimum design of bending-torsion coupled beams with frequency or aeroelastic constraints" Computers and Structures, Vol. 60, Nr. 5, (1996).

[108] Etkin B., "Dynamics of atmospheric flight", Dover, (2005).

[109] Grioli G., "Lezioni di meccanica razionale" Cortina, (2000).

[110] Broadbent E. G, Williams M., "The effect of structural damping on binary flutter", Aeronautical Research Council-Reports and Memoranda (1960)

[111] Kim Tae-Uk, Hwang In Hee, "Optimal design of composite wing subjected to gust loads", Computers and Structures 83, (2005).

[112] Matsuzaki R., Todoroki A., "Stacking-sequence optimization using fractal branch-and-bound method for unsymmetrical laminates", Composite Structures 78, (2007).

[113] Kozen D., "The design and analysis of algorithms", Spring, (1992).

[114] Narita Y., "Layerwise optimisation for the maximum fundamental frequency of laminated composite plates", Journal of Solid and Vibrations 263, (2003).

[115] Matlab Software", Version 7.1, The Mathworks, (2007).

[116] Todoroki A., Sasada N., Miki M., "Object-Oriented Approach to optimize composite laminated plate stiffness with discrete ply angles", Journal of Composite Materials, Vol. 30 Nr. 9, (1996).